Thermal Characterization of Lithium-ion Cells with Positive Electrode Materials $LiNi_xMn_{0.8-x}Co_{0.2}O_2$ and their Components

Zur Erlangung des akademischen Grades einer

DOKTORIN DER INGENIEURWISSENSCHAFTEN (Dr.-Ing.)

von der KIT-Fakultät für Maschinenbau des

Karlsruher Instituts für Technologie (KIT)

angenommene

DISSERTATION

von

M. Sc. Wenjiao Zhao

Tag der mündlichen Prüfung	22. Juni 2021
Hauptreferent	Prof. Dr. Hans Jürgen Seifert
Korreferent	Prof. Dr.-Ing. habil. Torsten Markus

Abstract

Nowadays, Lithium-ion batteries (LiBs), due to the high energy density, long cycling life and the maturity in manufacture, are widely adopted as electrical energy storage systems for stationary applications, portable electronic devices, as well as electric vehicles (EVs). However, safety issues of LiBs raise concerns regarding the daily usage of battery powered devices. For instance, EVs catching fire when parking and charging were repeatedly reported in recent years [1, 2]. In order to improve the electrochemical performance as well as the safety of the batteries, the thermal properties and thermal behavior of LiBs have to be investigated thoroughly.

The thermal stability of LiBs can be improved internally and externally. Internal development implies the development of battery design and components, especially the positive electrode. External development implies the development of a thermal management system, such as temperature monitoring or a cooling system. In respect to the internal development, in this work NMC positive electrode materials were intensively investigated in terms of varying chemical composition and thermal properties of delithiated positive electrode materials. Regarding external development, the thermal behavior of NMC-based LiBs during cycling and thermal runaway were investigated, which can provide useful experimental data that can be utilized for thermal management systems.

$LiNi_xMn_{0.8-x}Co_{0.2}O_2$ (x=0.4, 0.5, 0.6, 0.7, 0.8) series positive electrode materials were synthesized using the sol-gel method. The calcination temperatures were optimized and the electrochemical properties of $LiNi_{0.4}Mn_{0.4}Co_{0.2}O_2$ (NMC442) positive electrode materials were tested and compared with commercially available NMC442 material. In order to obtain different Li contents, chemical delithiation was performed by using $(NH_4)_2S_2O_8$ solution as oxidizing agent. With different solution amounts and various reacting times, various Li contents in samples were achieved. Along with extraction of lithium, transition metals were also dissolved in oxidizing agent. The thermal properties of selected specimens with compositions of $Li_yNi_{0.4}Mn_{0.4}Co_{0.2}O_2$ (y=1.11, 0.76, 0.48) were studied in regard to phase transitions and formation enthalpies. The phase transitions are accompanied with gases release and were investigated using simultaneous thermal analysis (STA) and mass spectroscopy. The formation enthalpies were measured by high temperature oxide melt drop solution calorimetry.

Furthermore, thermal behavior and thermal runaway events of commercially available coin cells with $LiNi_{0.6}Mn_{0.2}Co_{0.2}O_2$ (NMC622) positive electrode material were investigated using a Tian-Calvet calorimeter (C80) and an accelerating rate calorimeter (ARC). Heat flow rates of coin cells with NMC622 during charging and discharging at various C-rates were investigated using the C80 calorimeter. Heat generation from LiBs during cycling consists of reversible heat contributions, which can be correlated to reversible reactions and irreversible heat contributions, which can be correlated to internal resistances and irreversible reactions. The internal resistances were investigated using galvanostatic intermittent titration technique (GITT) measurements, and the reversible entropy change was determined by measuring the

dependence of open circuit voltages (OCVs) on temperatures. Consequently, the total generated heat could be calculated based on the experimental results. As the heat flow rates during cycling at 25 °C and 30 °C were measured directly by a C80 calorimeter, the total heat generation can be determined by integration of measured heat flow rate over time. The difference between the calculated and measured heat was compared and discussed. Thermal runaway events observed in the ARC were analyzed from component to complete cells from room temperature to thermal runaway. This work presents a whole picture of the thermal runaway event, which might contribute to the development of thermal management systems.

Zusammenfassung

Heutzutage werden Lithium-Ionen-Batterien (LiBs) aufgrund ihrer hohen Energiedichte, ihrer langen Lebensdauer und der Herstellungsreife zunehmend als Energiespeicher in stationären Anlagen Elektrofahrzeugen (EVs) und tragbaren elektronischen Geräten eingesetzt. Jedoch gibt es weiterhin Bedenken hinsichtlich der Sicherheit von LiBs. In den letzten Jahren wurden in den Medien regelmäßig Fälle bekannt, in denen Elektrofahrzeuge beim Parken oder während des Ladevorgangs in Brand gerieten [1,2]. Aus diesem Grund sind die thermischen Eigenschaften und das thermische Verhalten im Rahmen der Entwicklung von Sicherheitsmaßnahmen für LiBs sehr interessant, um die elektrochemische Leistung sowie die thermische Stabilität zu verbessern.

Die thermische Stabilität von LiBs kann durch interne und externe Entwicklungen verbessert werden. Interne Entwicklungen implizieren die Verbesserung des Batteriedesigns und der Komponenten, insbesondere der positive Elektrode. Bei externen Entwicklungen handelt es sich um die Entwicklung eines Wärmemanagementsystems, unter anderem durch eine Temperaturüberwachung oder durch ein Kühlsystem. In Bezug auf interne Entwicklungen wurden in dieser Arbeit NMC positive Elektrodenmaterialien intensiv hinsichtlich der chemischen Zusammensetzung und der thermischen Eigenschaften delithiierter positiver Elektrodenmaterialien untersucht. In Bezug auf externe Entwicklungen wurde das thermische Verhalten von LiBs während des Zyklierens und des „Thermal Runaway“ untersucht. Die gewonnenen Daten können zum Beispiel als Eingangsdaten für ein Wärmemanagementsystem dienen.

Zunächst wurden NMC Elektrodenmaterialien mit den Zusammensetzungen $LiNi_xMn_{0,8-x}Co_{0,2}O_2$ (x=0,4; 0,5; 0,6; 0,7; 0,8) unter Nutzung der Sol-Gel Methode synthetisiert. Die Kalzinierungstemperaturen wurden optimiert, die elektrochemischen Eigenschaften von $LiNi_{0,4}Mn_{0,4}Co_{0,2}O_2$ (NMC442) getestet und mit kommerziellem NMC442 Material verglichen. Weiterhin wurden NMC-positive Elektrodenmaterialien unterschiedlicher Lithium-Gehalte durch chemische Delithiierung unter Verwendung von $(NH_4)_2S_2O_8$-Lösung als Oxidationsmittel durchgeführt. Durch Verwendung unterschiedlicher Lösungsmengen und Reaktionszeiten konnten aus dem Delithiierungsprozess Materialien mit unterschiedlichen Lithium-Gehalten erhalten werden. Neben der Extraktion von Lithium wurden auch Übergangsmetalle im Oxidationsmittel gelöst. Die thermodynamischen Eigenschaften von Proben ausgewählter Zusammensetzungen $Li_yNi_{0,4}Mn_{0,4}Co_{0,2}O_2$ (y=1,11; 0,76; 0,48) wurden hinsichtlich der Phasenübergänge und Bildungsenthalpien untersucht. Die Phasenübergänge, bei denen Gas freigesetzt wird, wurden durch Simultane Thermische Analyse (STA) und Massenspektroskopie untersucht. Die Bildungsenthalpien wurden mittels Hochtemperatur-Einwurflösungskalorimetrie gemessen.

Darüber hinaus wurden das thermische Verhalten und der „Thermal Runaway“ von handelsüblichen Knopfzellen mit $LiNi_{0,6}Mn_{0,2}Co_{0,2}O_2$ positive Elektrodenmaterial mit einem Tian-Calvet Kalorimeter (C80) und einem Accelerating Rate Calorimeter (ARC) untersucht. Dabei wurde die Wärmeentwicklung aus reversiblen Wärmebeiträgen, welche aus reversiblen

Reaktion resultieren, und irreversiblen Wärmebeiträgen, die aufgrund von Innenwiderständen und irreversiblen Reaktionen entstehen, untersucht. Die Innenwiderstände wurden unter Verwendung von Galvanostatischer intermittierender Titrationstechnik (GITT) untersucht, und die reversible Entropieänderung wurde durch Messungen der Abhängigkeit der Leerlaufspannungen (OCVs) von den Temperaturen ermittelt. Daraufhin konnte die gesamte Wärmeentwicklung aus den durchgeführten experimentellen Ergebnissen berechnet werden. Da die Wärmestromraten während des Zyklus bei 25 °C und 30 °C direkt mit einem C80-Kalorimeter gemessen wurden, kann die gesamte Wärmeerzeugung durch Integration der gemessenen Wärmestromrate über die Zeit bestimmt werden. Die Differenz zwischen der berechneten und der gemessenen Wärmeentwicklung wurde ermittelt und diskutiert. Mittels ARC wurde der „Thermal Runaway“ ausgehend von den einzelnen Komponenten bis hin zur vollständigen Zelle untersucht. Diese Arbeit zeigt somit ein Gesamtbild des „Thermal Runaway“, das zur Entwicklung von Wärmemanagementsystemen verwendet werden kann.

Publication list

1. Article title: Experimental analysis of thermal runaway in 18650 cylindrical Li-ion cells using an accelerating rate calorimeter.
   Publication year: 2017.
   Journal: batteries.
   Authors: B. Lei, W. Zhao, C. Ziebert, N. Uhlmann, M. Rohde and H. J. Seifert.
   Independently working on: thermal runaway measurements on 18650 cells with $LiMn_2O_4$ materials: including internal/external pressure change and temperature change measured by an accelerating rate calorimeter.
2. Presentation title: battery calorimetry of Li-ion cells to prevent thermal runaway and develop safer cells.
   Publication year: 2018.
   Conference: aabc Europe, 8^{th} international advanced automotive battery conference.
   Authors: C. Ziebert, N. Uhlmann, S. Ouyang, B. Lei, W. Zhao, M. Rohde, H. J. Seifert.
   Independently working on: thermal runaway measurement on 18650 cells, providing input parameters and validation for the pressure change simulation.
3. Presentation title: Combined thermal runaway analysis of coin cells with C80 and ARC calorimeter.
   Publication year: 2018.
   Conference: MSE 2018 conference.
   Authors: W. Zhao, C. Ziebert, M. Rohde, H. J. Seifert.
   Independently working on: measurements and analyze for thermal behaviors of coin cells and their components using ARC and C80 calorimeter.
4. Poster title: Calorimetric studies of the thermal behavior of Li-ion cells: calibration and measurements with a Tian-Calvet calorimeter.
   Publication year: 2019.
   Conference: Kalorimetrietage 2019 conference.
   Authors: W. Zhao, C. Ziebert, N. Uhlmann, C. Gebert, M. Rohde, H. J. Seifert.
   Independently working on: calibration on the calorimeter, specific heat capacity of coin cells measurements, and measurements of heat generation from coin cells, as well as the analysis of these results.
5. Article title: Heat generation in NMC622 coin cells during electrochemical cycling: separation of reversible and irreversible heat effects.
   Publication year: 2020.
   Journal: batteries.
   Authors: W. Zhao, M. Rohde, I. Mohsin, C. Ziebert, H. J. Seifert.
   Independently working on: measurements of heat generation from coin cells during cycling, electrochemical tests and entropy measurements as well as the analysis of these results.

Acknowledgement

This dissertation was completed at Institute for Applied Materials-Applied Material Physics (IAM-AWP) from April 2016 to December 2019. I am very grateful for all the support during this period, and without the helps this dissertation cannot be presented here.

I appreciate the support of Professor Dr. Hans Jürgen Seifert, who enables and guides this work. He also gave me countless valuable advices and inspired me with the professional discussions. I learned and still am learning from him to do the research with solid foundation and reliable methods. I also would like to thank Professor Dr. Torsten Markus for the corrections and advices to optimize my work.

Dr. Magnus Rohde is advising and supporting me especially in the difficult phase, when I started a new topic in the middle of the promotion. The professional guidance and kind advice were so helpful for me to get through the difficulties. Many thanks.

Dr. Carlos Ziebert guides my work as supervisor since my Master thesis at IAM-AWP. He always shares plenty of novel researches. Since he collaborates closely with industry, his opening mind and practical thoughts provide a new view to solve problems. I am benefited a lot from his supervision, and I would like to express my gratefulness for that.

Dr. Dajian Li inspires me by innumerable ideas and innovation methods, which contributes to this work in many ways. Dr. Damian Cupid gave me his professional suggestions and support in the researches of cathode materials synthesis and delithiation. He helped me as a fresh PhD student, to land in the institute. Dr. Peter Frank's creativity and widely professional knowledge encourage me to learn more and be curious to other fields as well. I sincerely thank them for the inspiration and support. Dr. Nicolas Mayer offers sincerely and unselfish help to me when he was PhD student in our group and after he has finished his promotion. I would like to thank him to be a reliable friend and colleague. I would also like to thank Dr. Thomas Reichmann and Dr. Petronela Gotcu, who helped me with XRD measurements and electrochemical characterization.

Mr. Nils Uhlmann, Mr. Christoph Gebert and Ms. Judith Jung support this work in the laboratory with the experimental instruments. I appreciate our companionship, and the memories of funny lunch breaks and summer/ Christmas excursion. Thanks for the enjoyable collaboration and generous help.

Dr. Thomas Bergfeldt and the chemical analysis group help me to perform ICP-OES measurements, and advised me about chemical delithiation. Dr. Martin Steinbrück helps me with measuring samples on the STA-MS instrument and offered professional opinions on the analysis. Dr. Harald Leiste helps me with XRD measurement and its analysis. Thank them all for the measurement supporting.

For PhD fellows Dr. Maryam Masoumi, Dr. Maximilian Rank, Mr. Joel Fels, Mr. Ingo Markel, Mr.

Christian Poltorak, I thank them for all the discussions and nice accompanying.

Moreover, thank for the financial supporting by Deutsche Forschungsgemeinschaft (DFG). Thank for my family's financial as well as mentally support, which helps me go through all the difficult phases. Especially my husband Ding, Ming gives me a lot of support and encourage me to overcome challenges.

The promotion at IAM-AWP was definitely an important and wonderful time. Thank all fellow doctoral candidates and colleagues from IAM-AWP.

Braunschweig, 08. 03. 2021 Wenjiao Zhao

List of abbreviations

A	Surface area
ARC	Accelerating rate calorimeter
ALD	Atomic layer deposition
BMS	Battery management system
C	Capacity
c, C_p	Specific heat capacity
CC	Constant current
CCCV	Constant current and constant voltage
CO	Carbon monoxide
d	Inter-plane distance of layers
DEC	Diethyl carbonate
DMC	Dimethyl carbonate
DOD	Depth of discharge
DSC	Differential scanning calorimetry
DTA	Differential thermal analysis
EC	Ethylene carbonate
EIS	Electrochemical impedance spectroscopy
EV	Electric vehicle
F	Faraday constant
G	Gibbs free energy
GC-MS	Gas chromatography with mass selective detection
GITT	Galvanostatic intermittent titration technique
h	Heat transfer coefficient
H	Enthalpy
HEV	Hybrid electric vehicle
HWS	Heat wait seek
i	Current density
I	Current
ICP-OES	Inductively coupled plasma optical emission spectroscopy
IR-ATR	Infrared spectroscopy with attenuated total reflectance
k	Thermal conductivity
LCO	Lithium cobalt oxide, $LiCoO_2$
LCSU	Local coordination structure unit
LFP	Lithium iron phosphate, $LiFePO_4$
LiB	Lithium-ion battery
LMC	Lithium methyl carbonate, $C_2H_3LiO_3$
LMO	Lithium manganese oxide, $LiMn_2O_4$
MAUD	Material analysis using diffraction
MS	Mass spectrometer
n	Number of electronic charges
n	Order of the diffraction peak

NCA	Lithium cobalt aluminum oxide, $LiNi_xCo_yAl_zO_2$
NIST	National institute of standard and technology
NMC	Lithium nickel manganese cobalt oxide, $LiNi_xMn_yCo_zO_2$
NMP	N-methyl-pyrrolidone
NMR	Nuclear magnetic resonance
NO_x	Nitrogen oxides
OCV	Open circuit voltage
P	Pressure
PE	Polyethylene, $(C_2H_4)_n$
PP	Polypropylene, $(C_3H_6)_n$
PVDF	Polyvinylidene fluoride, $(C_2H_2F_2)_n$
Q	Heat
$\dot{Q}$	Heat flow rate
R_{th}	Thermal resistance
R_Ω	Ohmic resistance
S	Entropy
SADT	Self-accelerating decomposition temperature
SEI	Solid electrolyte interface
SEM	Scanning electron microscope
SOC	State of charge
STA	Simultaneous thermal analysis
t	Time
T	Temperature
TG	Thermogravimetry
TGA	Thermogravimetric analysis
TM	Transition metal
U^0	Equilibrium voltage
XPS	X-ray photoelectron spectroscopy
XRD	X-ray diffraction
Z	Impedance
ε	Emission ratio
σ	Stefan-Boltzmann constant
Ø	Electronic potential
λ	wavelength
θ	Bragg angle
η	Overpotential
$\Delta_{trs}h$	Entropy in phase transition in J/g
$\Delta_{trs}H$	Entropy in phase transition in J/mol

Contents

Abstract III
Zusammenfassung V
Publication list VII
Acknowledgement VIII
List of abbreviations X
1 Introduction 1
2 Fundamentals and principles 5
2.1 Working principle of a Lithium-ion battery 5
2.2 Positive electrode material $LiNi_xMn_yCo_zO_2$ 6
2.3 Thermodynamic principles of LiB operation 10
2.4 Heat effects during LiB's operation 11
2.4.1 Heat generation during LiB's operation 11
2.4.2 Heat dissipation during LiB's operation 15
2.5 Thermal runaway of LiBs 16
2.6 Measurement condition in calorimeters 18
3 Characterization and measurement methods 21
3.1 Characterization methods 21
3.1.1 X-ray diffraction (XRD) 21
3.1.2 Inductively coupled plasma with optical emission spectroscopy (ICP-OES) 21
3.1.3 Scanning electron microscopy (SEM) 22
3.1.4 Electrochemical impedance spectroscopy (EIS) 22
3.1.5 Galvanostatic intermittent titration technique (GITT) 23
3.2 Calorimetric methods applied in this work 24
3.2.1 C80 3D Tian-Calvet calorimeter 24
3.2.2 Accelerating rate calorimeter (ARC) 35
3.2.3 High temperature oxide melt drop solution calorimetry 37
3.2.4 Simultaneous thermal analysis (STA) 40
3.3 Evaluation of uncertainties 42
3.3.1 Type A evaluation of standard uncertainty 42
3.3.2 Type B evaluation of standard uncertainty 43
3.3.3 Combined uncertainty example: an uncertainty evaluation for a specific heat capacity measurement 43
4 Positive electrode material NMC synthesis and chemical delithiation 45
4.1 Literature review 45
4.2 Synthesis of $LiNi_xMn_{0.8-x}Co_{0.2}O_2$ 50
4.2.1 Synthesis of $LiNi_xMn_{0.8-x}Co_{0.2}O_2$ (x=0.4, 0.5, 0.6, 0.7, 0.8) 50
4.2.2 Comparison with commercial $LiNi_{0.4}Mn_{0.4}Co_{0.2}O_2$ (NMC442) 56
4.3 Chemical delithiation of NMC442 positive electrode materials 58

4.3.1 Chemical delithiation process and characterization 58
4.3.2 Results and discussion 60
4.4 Conclusion 85
Synthesis of $LiNi_xMn_{0.8-x}Co_{0.2}O_2$ 85
Evaluation of chemical delithiation with $(NH_4)_2S_2O_8$ 86
5 Thermal behavior studies of LiB under normal operation and thermal abuse scenarios 87
5.1 Literature review 87
5.1.1 Heat generation and entropy measurements 87
5.1.2 Thermal runaway studies 94
5.2 Measurements for thermal behavior study 99
5.2.1 Heat generation determination 99
5.2.2 Thermal runaway measurements 99
5.3 Investigated coin cells 99
5.4 Measurements of the specific heat capacity of coin cells 100
5.4.1 Continuous method 100
5.4.2 Step method 102
5.5 Heat generation during cycling 103
5.5.1 Heat generation determined by temperature measurement 104
5.5.2 Heat generation determined by heat flow rate measurement 107
5.5.3 Measurement of internal resistances 112
5.5.4 Measurement of entropy change 119
5.5.5 Comparison of calculated heat generation with measured data 127
5.5.6 Conclusion 137
5.6 Combined thermal runaway investigation with ARC and C80 calorimeter 138
5.6.1 Thermal runaway investigation for a large temperature range using ARC 139
5.6.2 Investigation of early stages of thermal runaway using C80 calorimeter 151
5.6.3 Conclusion 156
6 Summary and outlook 157
6.1 NMC active material investigations 157
6.2 Coin cell investigations 158
6.3 Outlook 159
Bibliography 162
List of Figures 171
List of Tables 177
Appendix 178
Appendix I The parts of C80 calorimeter 178
Appendix II The raw data of ICP-OES results 179
Appendix III The raw data of the function of ΔH, ΔS and SOCs in Fig. 5.38 180

1 Introduction

Most international metropolises benefit from the urban population growth but also suffer by related environmental problems. One of the most important issues is high emission of air pollutants. In Germany, for instance, the emissions of carbon monoxide (CO) and nitrogen oxides (NO_x) are the main air pollutants. The emissions of CO and NO_x due to motor traffic contribute more than half the total emissions in Germany [3].

The increasing pressure of replacing the fossil fuels drives the booming growth of "green energy". Alternatives for road transport are hybrid electric vehicles (HEVs) and electric vehicles (EVs). For the interest of long time development, several countries put the popularizing of EVs as a policy in schedule. Netherlands' and Norway's government plans are to ban the sale of internal combustion engine vehicles by 2040. In 2020, EV market of Europe grew to the largest in the world. High specific energy, long durability and reliable safety performance are critical properties for power sources of EVs and HEVs. Lithium-ion battery (LiB) fulfills the most requirements. In the year 2030, the total LiB market is predicted as large as 390 GWh/y, in which road-transport market consumes 245 GWh/y [4].

Positive electrode materials are crucial for the electrochemical performance and thermal stabilities of LiB. In Fig. 1.1 [4], five commercially applied positive electrode materials are compared regarding affordability, energy, power, safety, performance, durability, materials and maturity. $LiCoO_2$ (LCO) is the first positive electrode material applied in commercialized LiB, which is now widely used in computer, communication and consumer electronic (3C) products. However, as the Co consumption growing and the limitation of Co source, the raw materials price of Co is increasing dramatically. Layered structured Li(Ni, Mn, Co)O_2 (NMC) and Li(Ni, Co, Al)O_2 (NCA) due to their outstanding performance, spinel type materials $LiMn_2O_4$ (LMO) and olivine type materials $LiFePO_4$ (LFP) due to their low costs, are alternative positive electrode materials for commercial LiB [5-11]. The LMO battery has a low internal resistance, leading to a relatively high power. The thermal stability and cycle life of LMO are also excellent. However, its energy density is notably lower than energy density of NMC and NCA, which is the main problem for LMO application. The LFP battery has the best safety performance and its raw materials are environment friendly and abundant in resources. Similar to LMO, energy density of LFP needs to be improved. The Ni-based layered positive electrode materials such as NMC and NCA are the most promising candidates thanks to their high capacities and low cost comparing with $LiCoO_2$ [7-9], which currently dominate in EV and HEV's batteries market. The increasing of Ni content in NMC can improve the specific capacity effectively. Since the synthesis process of NMC/NCA is similar to LCO, the materials' production is highly industrialized, comparing to other positive electrode materials. Hence, Ni-rich NMC/NCA positive electrode materials are especially attractive in large-scale automotive applications. Despite their outstanding electrochemical performances, the thermal stability, in aspect of safety issue, remains to be the main drawback in the use of Ni-rich NMC/NCA materials as presented in Fig. 1.1, which has been discussed in some literature [12-13].

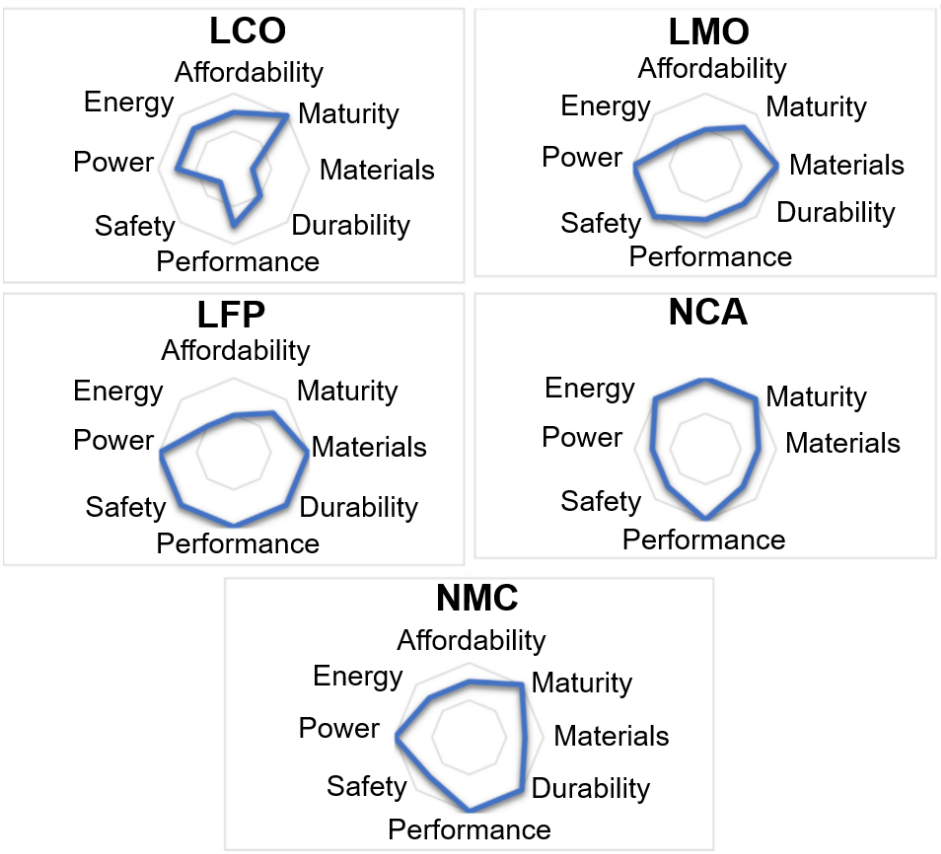

Fig. 1.1: Spider diagrams of main characteristics of commercial Li-ion batteries [4].

As shown in Fig. 1.1, layered materials LCO, NMC and NCA have safety issues in comparison to LMO and LFP. For instances, laptop on fires [14], airplane transport incidents [15] and Tesla Model S safety event [16], have raised the concerns for our daily applications. In some abusive situations, e.g. short circuit, fast charging, and working at high ambient temperature, the exothermic reactions could be triggered. These will cause an overheating and/or thermal non-uniformity in the battery pack, which can lead to a thermal runaway, fire and finally to an explosion [17-25]. In addition, thermal behavior during operation of the battery is important knowledge to design “thermal management systems” for regular use of the batteries.

In order to understand and solve the safety problems, the intrinsic properties, thermal behavior and the battery thermal simulation are investigated and developed in this work. A comprehensive and better understanding of thermal properties of LiB with positive electrode materials Ni-rich NMC aims to be achieved. The thermal behavior of LiB during operation, is analyzed and computed under different scenarios, which is a rudiment of battery thermal management. Safety issues related to Lithium-ion battery are analyzed in this work step by step according to the production structure in Fig. 1.2. Firstly, the materials manufactures produce positive/negative electrode materials etc.. In the cell component’s level, positive/negative electrodes are produced after slurry preparation, coating, and calendaring. Furthermore, components are assembled to single cell then to battery pack. Thus, the key properties showed in Fig. 1.1 can be addressed at three levels: inherent materials, cell design, and battery management system (BMS).

Fig. 1.2: Production structure of the Li-ion battery industry [4].

This work mainly focuses on the problem in inherent materials level, and the results can contribute to BMS design. First of all, on inherent materials level, NMC positive electrode materials should be synthesized and chemically delithiated to investigate the thermal stability of NMC with selected delithiated states. Exothermic reactions can take place accompanying with heat generation and gases production which will increase the temperature and internal pressure of the batteries. Secondly, on components level, the early stage of thermal runaway have to be investigated in aspects of cell components, such as electrodes, electrolyte and separator. Thirdly, on cell's level, the thermal runaway events should be analyzed on cells with various SOCs. Thermal properties such as enthalpy change and entropy change are of interest for tested cells. In addition, the internal resistances cause thermal effects, which are also critical in operation. Heat effects during cycling should be measured by a Tian-Calvet calorimeter, and heat development to be calculated based on the thermal properties. The experimental determined thermal properties can be used as input values in thermal management systems.

On the material's scale, following experiments have to be performed:

- The cathode materials $LiNi_xMn_{0.8-x}Co_{0.2}O_2$ (x=0.4, 0.5, 0.6, 0.7, 0.8) are synthesized via sol-gel method. The calcination temperatures need to be adjusted in consideration of Ni content.
- Chemical delithiation on cathode materials NMC is performed with various oxidizing agent amounts and operating times.
- The formation enthalpies of selected delithiated samples should be measured by a high temperature oxide melt drop solution calorimeter.
- The thermal stability of NMC with different delithiation degrees are investigated by a simultaneous thermal analysis calorimeter. Simultaneously, the gases development are analyzed.

In the scope of cell components, the early stage of thermal runaway should be investigated in detail by the calorimeter on electrodes, separator and electrolyte. Full cells experiments are designed as following:

- The cells with selected SOCs to be tested under thermal abuse conditions in an accelerating rate calorimeter. The temperatures and temperature changes are measured during thermal runaway events.
- The early stages of thermal runaway are analyzed with a Tian-Calvet calorimeter.
- Entropy changes and enthalpy changes during reversible reactions of LiB have to be determined experimentally. The heat generation due to internal resistances are studied

based on various resistances' sources.

- Calorimetric study on heat generation during LiB’s cycling, and the heat development should be calculated with help of the thermal properties' parameters.

2 Fundamentals and principles

2.1 Working principle of a Lithium-ion battery

A battery converts chemical energy into electric energy. Secondary batteries enable the conversion process in both directions [26], as the electrochemical reactions are reversible. LiB is one of the successfully commercialized secondary batteries, due to its high energy density and stable performance.

During LiB's charging, an external power source drives the electrons flowing from the positive electrode to the negative electrode through an external circuit. Meanwhile, Li ions move from positive electrode to negative electrode internally through electrolyte. The term "delithiation" describes the process of extracting Li ions from positive electrode during charging. Due to the Li ions movement similar to a rocking chair, this reaction is called "rocking chair" reaction, visualized in Fig. 2.1. A characteristic value "state of charge" (SOC) defines the available capacity in percentage, i.e. SOC100 is fully charged state.

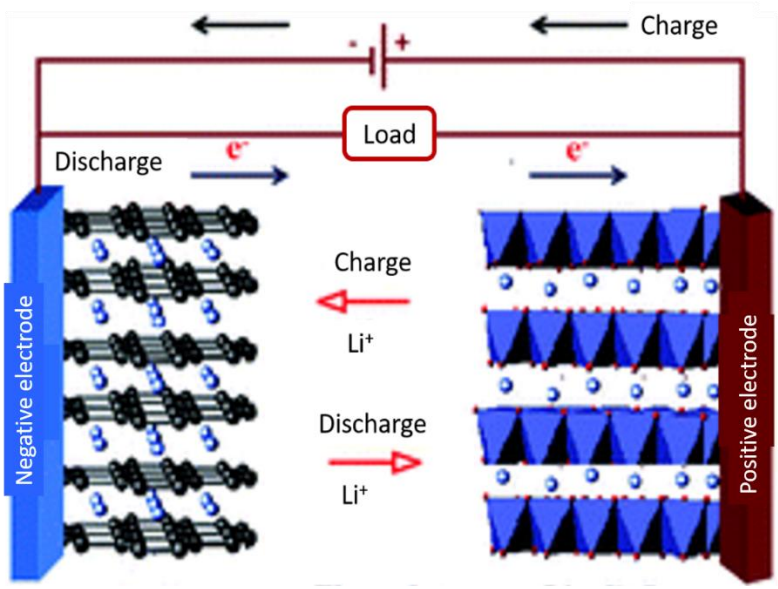

Fig. 2.1: Schematics of a Li-ion battery during charge [27].

In discharge process, reduction reaction takes place on positive electrode in Fig. 2.1, which represents a layered structure material. The negative electrode active materials are oxidized simultaneously, representing graphite in Fig. 2.1. The most commonly used electrolyte is an organic solvent containing Li salt, which enables the movement of Li ions between positive and negative electrodes. The separator is a porous membrane, normally consisting of polymer film which separates the negative and positive electrodes but allows ions to flow through it. During the first cycle, a solid-electrolyte layer (SEI) is formed at the interface of the negative electrode and electrolyte. Although the formation of SEI causes initial capacity loss, SEI stabilizes the battery by preventing further interface reactions between negative electrode and electrolyte. According to international convention the terms "anode" and "cathode" are

used for cell discharge situation. The oxidation reaction takes place on anode, while, reduction reaction on cathode in this case.

2.2 Positive electrode material $LiNi_xMn_yCo_zO_2$

As mentioned in Chapter 1, layered structure NMC materials are promising candidates for LiB's positive electrode materials. In the following text, pros and cons of lithium transition metal oxides $LiTMO_2$ (TM = Co, Ni, Mn) are explained in detail. At the end of this section, advantages of the combination of these three transition metals are discussed.

$LiCoO_2$ is a successfully commercialized positive electrode material for LiBs, with reversible capacity 140 mAh/g - 145 mAh/g and charge voltage 4.1 V - 4.2 V. However, one drawback is its poor thermal stability especially under high SOCs. The reactivity of the material arises from uncharged considerably to higher delithiation degree. Therefore, an overcharge must be carefully avoided [28]. With high octahedral-site stabilization energy, Co has excellent structural stability [29]. Fig. 2.2 shows the number of states N(E) of some redox couples, whose energy bands (E) lie between Li/Li^+ and O^{2-} energy bands. $Co^{3+/4+}$: t_{2g} band overlaps with O^{2-} band, causing the oxidation of O^{2-} when the positive electrode materials are delithiated to more than 50 %, which ends up in release of oxygen [30]. Additionally, problems such as high cost, toxicity and child labour in cobalt mines, limit the application of $LiCoO_2$ [31].

$LiNiO_2$ has relatively high specific capacity (185 mAh/g at 4.1 V, or 210 mAh/g at 4.2 V), and lower cost than $LiCoO_2$. However, the synthesis of $LiNiO_2$ is problematic since a second phase nickel over-stoichiometry with formulation $Li_{1-\delta}Ni_{1+\delta}O_2$, is prone to appear in the sample [28]. The lack of lithium in cathode material results in poor electrochemical performance and poor reversibility. Moreover, the capacity of $LiNiO_2$ batteries fades dramatically with cycling. The thermal stability problem is another critical barrier for the application of $LiNiO_2$. The oxygen release from delithiated nickel-rich sample $Li_{0.3}NiO_2$, took place at 150 °C [32]. As shown in Fig. 2.2, $Ni^{3+/4+}$ band locates just above O^{2-} band. Since Ni^{3+} has octahedral-site stabilization energy higher than Mn^{3+} but lower than Co^{2+}, stability of Ni is ranking between Mn and Co in both structural and chemical stabilities. Unlike Co^{3+}, Ni^{3+} can be fully oxidized to Ni^{4+} without the loss of oxygen. However, at deep charge, significant amount of lithium ions will be removed from lattice due to phase transition. Ni^{4+} is highly oxidizing and reactivity to electrolyte leading to the formation of a thick SEI, rising the impedance as well [29].

$LiMnO_2$ has a reversible capacity of 132 mAh/g and charge voltage reaches the range of 3.5 V - 4.0 V. Comparing with the above two materials, its chemical stability is outstanding. As shown in Fig. 2.2, the $Mn^{3+/4+}$: e_g band lies well above O^{2-}: 2p band [29]. As Li ions are intercalating into the orthorhombic structure, a second phase with spinel structure appears and subsequently grows. There is thus a continuous one-phase plateau at 3 V, followed by a two-phase voltage plateau at 4 V for $LiMnO_2$ battery due to structural change [28, 33]. This non-continuous manner and multi-phase reaction hinder its practical application. Since Mn^{3+} has low octahedral-site stabilization energy, $LiMnO_2$ suffers structural transition [29].

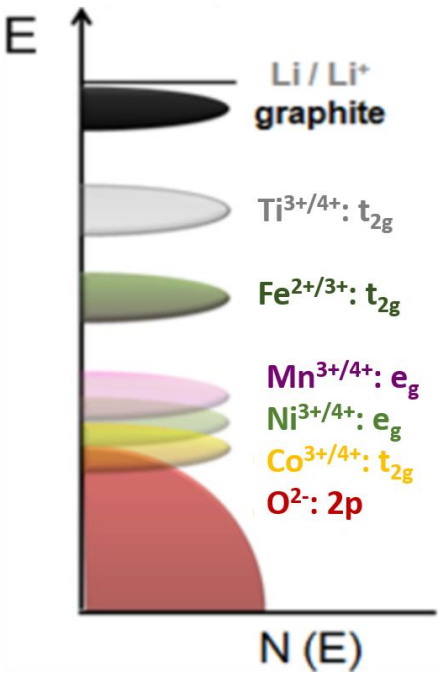

Fig. 2.2: Positions of the various redox couples relative to the oxygen 2p band [29].

NMC Since these three materials $LiCoO_2$, $LiNiO_2$, and $LiMnO_2$ have essentially similar crystal structure, the $LiNi_xMn_yCo_zO_2$ (NMC) solid solution can optimize the performances in regard of the thermal stability and specific energy. NMC crystallizes in the space group $R\bar{3}m$ (No. 166) with the α-$NaFeO_2$ structure. Lithium, transition metal and oxygen occupy the Wyckoff positions of 3a, 3b, and 3c, respectively. The octahedral sites are alternatively occupied by lithium cations and transition metal cations, which are the face-centers of oxygen anions in cubic array (Fig. 2.3). Along the $[111]_{FCC}$ direction, LiO_2 and MO_2 sheets are stacking regularly [34], demonstrated in Fig. 2.3 for $LiNi_{1/3}Mn_{1/3}Co_{1/3}O_2$ (NMC111). The oxidation states of Ni, Co and Mn are 2+, 3+ and 4+. After delithiation, the oxidation states of Ni and Co increase to 3+/4+ and 4+, respectively; and Mn remains 4+.

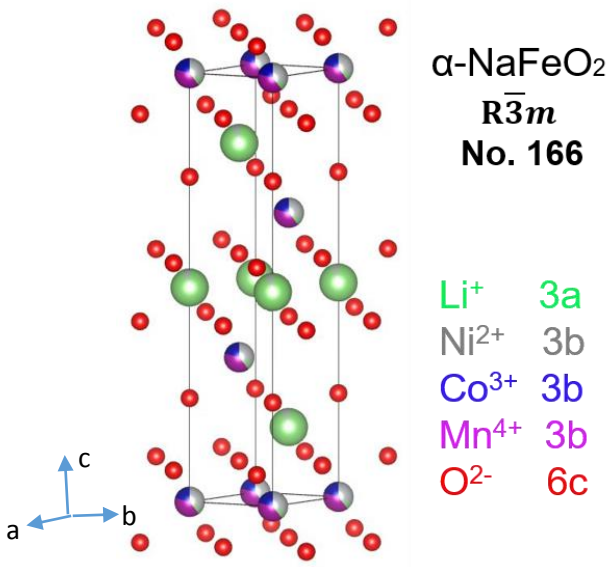

Fig. 2.3: Ideal layer structure of NMC111 (space group R$\bar{3}$m).

As shown in Fig. 2.1, during charging, the oxidation reaction takes place at positive electrode side:

$$0 < x \leq \frac{2}{3} \quad \mathrm{LiNi}_{\frac{1}{3}}^{2+}\mathrm{Mn}_{\frac{1}{3}}^{4+}\mathrm{Co}_{\frac{1}{3}}^{3+}\mathrm{O}_2 - x\mathrm{Li}^+ - xe^- \rightarrow \mathrm{Li}_{1-x}\mathrm{Ni}_{\frac{1}{3}-y}^{2+}\mathrm{Ni}_y^{3+/4+}\mathrm{Mn}_{\frac{1}{3}}^{4+}\mathrm{Co}_{\frac{1}{3}}^{3+}\mathrm{O}_2 \tag{2.1}$$

$$\frac{2}{3} \leq x \quad \mathrm{LiNi}_{\frac{1}{3}}^{2+}\mathrm{Mn}_{\frac{1}{3}}^{4+}\mathrm{Co}_{\frac{1}{3}}^{3+}\mathrm{O}_2 - x\mathrm{Li}^+ - xe^- \rightarrow \mathrm{Li}_{1-x}\mathrm{Ni}_{\frac{1}{3}}^{4+}\mathrm{Mn}_{\frac{1}{3}}^{4+}\mathrm{Co}_{\frac{1}{3}-z}^{3+}\mathrm{Co}_z^{4+}\mathrm{O}_2 \tag{2.2}$$

In equation 2.1 and 2.2, y and z represent the amount of oxidized Ni cations and oxidized Co cations, respectively. x is the amount of Li ions de-intercalating from NMC. The oxidizing reaction of TMs takes place in the order of Ni^{2+} to $Ni^{3+/4+}$, and then Co^{3+} ions were oxidized to Co^{4+}, during delithiation in low Ni content NMC [35]. Ni^{3+} is an unstable state, so in equation 2.2, all Ni^{2+} ions were oxidized to Ni^{4+}. In equation 2.1, the ratio of $Ni^{3+/4+}$ cations is difficult to be determined. With increasing Ni content, the energy bands of Ni and Co begin to overlap and it's difficult to distinguish the contribution for the capacity. At high voltage > 4.7 V in half cell with NMC111, anion redox reaction is tending to occur, leading to oxygen gas release [36]. During charging, at negative electrode side, the following reaction occurs:

$$6\mathrm{C} + x\mathrm{Li}^+ + xe^- \rightarrow \mathrm{Li}_x\mathrm{C}_6 \tag{2.3}$$

Thus, the overall redox reaction during charging is expressed:

$$\mathrm{LiTMO}_2 + 6\mathrm{C} \rightarrow \mathrm{Li}_{1-x}\mathrm{TMO}_2 + \mathrm{Li}_x\mathrm{C}_6 \tag{2.4}$$

Table 2.1: Comparison of the characteristics of Mn, Co, and Ni in NMC active materials of positive electrode [30].

Parameter	**Trend**
Chemical stability	Mn>Ni>Co
Structural stability	Co>Ni>Mn
Electrical conductivity	Co>Ni>Mn
Abundance	Mn>Ni>Co
Environmental benignity	Mn>Ni>Co

Table 2.1 qualitatively compares the chemical stability, structural stability, electrical conductivity, abundance and environmental benignity of Mn, Co and Ni. Ni has the performance between Co and Mn in all aspects [30]. Additionally, with higher Ni content capacity increases. Although high Ni content is favorable, there are a lot of challenges to overcome.

With higher Ni content, the cation mixing of Ni cations (with ionic radius of 0.69 Å) and Li cations (with ionic radius 0.76 Å) is prone to take place severely. Especially, when Li is absent in positive electrode material during delithiation, 3a sites will be occupied by Ni cations. The cation intermixing is suggested to be the main cause for the poor electrochemical performance of high Ni content NMC [37-38]. To inhibit these structural disorders in initial materials, the annealing temperature and duration must be carefully controlled. Another important role is the proportion of transition metals. In addition, the electrochemical and thermal stability decrease [37, 39], and the synthesis with increasing Ni content becomes more and more difficult. Dahn's group investigated the influence of Co content in the solid-solution $LiNi_xCo_{1-2x}Mn_xO_2$ with $0 \leq x \leq 0.5$. With increasing Co content (above 20 at.%), the cation mixing is suppressed effectively [35]. Moreover, according to the investigation of Shizuka et al. [40], the cell performance was improved effectively with 20 at.% Co substitution. Therefore, this work investigated the compositions $LiNi_xMn_{0.8-x}Co_{0.2}O_2$ (x=0.4, 0.5, 0.6, 0.7, 0.8) with increasing Ni content up to 80 at.%, illustrated in Fig. 2.4. One dotted line indicates the NMC with constant Co content of 20 at. %. The investigated compositions are $LiNi_{0.4}Mn_{0.4}Co_{0.2}O_2$ (NMC442), $LiNi_{0.5}Mn_{0.3}Co_{0.2}O_2$ (NMC532), $LiNi_{0.6}Mn_{0.2}Co_{0.2}O_2$ (NMC622), $LiNi_{0.7}Mn_{0.1}Co_{0.2}O_2$ (NMC712) and $LiNi_{0.8}Co_{0.2}O_2$ (NMC802). To maintain the electron neutrality of NMC, the oxidation states of Ni cations increase with decreasing fraction of Mn cations. The other dotted line shows the variation of the overall compositions when $LiCoO_2$ is mixed with $LiNi_{0.5}Mn_{0.5}O_2$. The positive electrode material $LiNi_{0.4}Mn_{0.4}Co_{0.2}O_2$ on both dotted lines, is further chemically delithiated and compared with commercial materials $LiNi_{0.4}Mn_{0.4}Co_{0.2}O_2$. The classical material $LiNi_{0.33}Mn_{0.33}Co_{0.33}O_2$ is on the vertical line too.

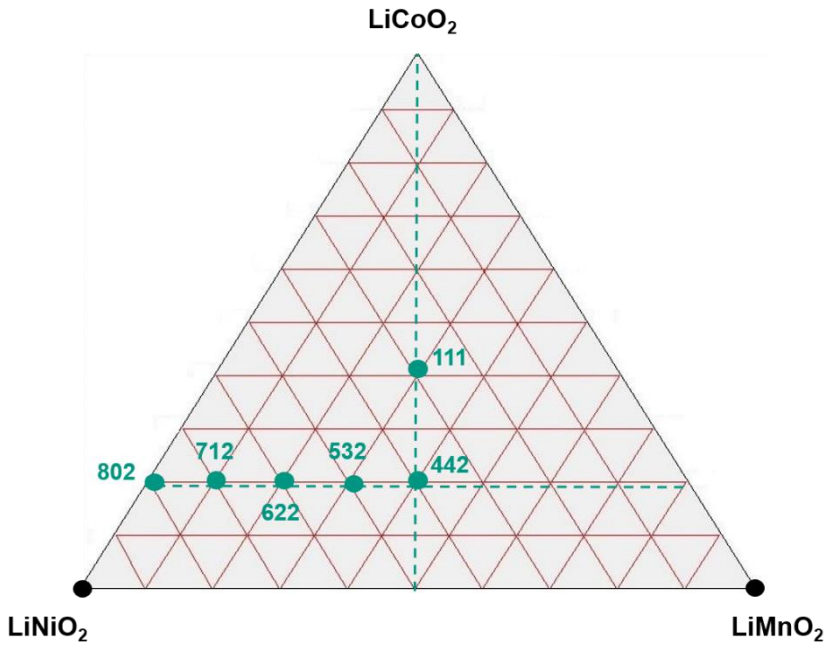

Fig. 2.4: Locations of NMC compositions on the Gibbs triangle, showing 20 at.% - $LiCoO_2$ and $LiNi_{0.5}Mn_{0.5}O_2$ concentration lines.

2.3 Thermodynamic principles of LiB operation

As described before in equation 2.4, the redox reaction during charging is:

$$\mathrm{LiTMO_2} + 6\mathrm{C} \rightarrow \mathrm{Li_{1-x}TMO_2} + \mathrm{Li}_x\mathrm{C}_6 \tag{2.4}$$

To analyze the reaction with respect to thermodynamics, some thermodynamic parameters and relations need to be introduced firstly. Gibbs free energy of the full-cell reaction ΔG gives the maximum amount of chemical energy that can be converted into electrical energy in the battery, and vice versa. The relation between equilibrium voltage and ΔG can be described as:

$$\Delta G(x, \mathrm{T}) = -n\mathrm{F}U^0(x, T) \tag{2.5}$$

where *n* represents number of exchanged electronic charges, F is Faraday constant, 96485 Coulomb per equivalent. An equivalent is one molar (Avogadro's number) of electronic charge. U^0 represents equilibrium voltage of the cell in unit Volt. An open-circuit voltage (OCV) displays the difference between the negative and positive electrode chemical potential. The chemical potential is a function of the composition x, pressure P, and temperature T. Pressure normally doesn't vary, hence, the equation 2.6 has two variations x and T. According to the laws of thermodynamics, if the reactants and products are all in their thermodynamic standard states, the Gibbs free energy of the reaction is:

$$\Delta G(x, \mathrm{T}) = \Delta H(x, \mathrm{T}) - \mathrm{T} \cdot \Delta S(x, \mathrm{T}) \tag{2.6}$$

The enthalpy of reaction ΔH characterizes the enthalpy difference between reactants and products. The product of temperature and entropy change $\mathrm{T} \cdot \Delta S$ represents the energy loss or gain in form of heat under equilibrium condition in the chemical or electrochemical process.

2.4 Heat effects during LiB's operation

As described in Chapter 1, in LiB, electrical energy is converted from chemical energy of reactants. Beside expected reactions, cycling process also involves side reactions and Joule heating. Overall heat effects of the cell consist of heat generation within the cell and heat dissipation to the environments. The temperature change ΔT of the cell indicates the correlation between heat generation Q_{gen} and heat dissipation Q_{diss}, determined by following equation:

$$m \cdot \mathrm{c}_{cell} \cdot \Delta T = Q_{gen} - Q_{diss} \tag{2.7}$$

The temperature change rate equals to the heat flow rates' difference divided by heat capacity:

$$m \cdot \mathrm{c}_{cell} \cdot \frac{dT}{dt} = \dot{Q}_{gen} - \dot{Q}_{diss} \tag{2.8}$$

where m, $\mathrm{c_{cell}}$, $\dot{Q}_{gen}$ and $\dot{Q}_{diss}$ stand for mass of the cell, specific heat capacity of the cell, generated heat rate and dissipated heat rate between the cell and surrounding environment, respectively.

2.4.1 Heat generation during LiB's operation

Heat generation consists of two parts [41]:

- The *reversible heat effect*, caused by electrochemical reactions in cells, is one of thermodynamic parameters, which is introduced by equation:

$$Q_{rev} = T \cdot \Delta S \tag{2.9}$$

  where *T* and *ΔS* represent temperature and entropy of the reactions, respectively.
- The *irreversible heat effect* is caused by current flow through conducting objects, including the positive and negative electrodes, electrolyte and separator. The polarization against the external electrical field is also part of internal resistance $\mathrm{R_i}$ (the sum of ohmic, activation and diffusion polarization resistances). A voltage disparity between open circuit and under current potentials can be observed in electrochemical cells. Fig. 2.5 shows galvanostatic intermittent titration technique (GITT) measurements for $LiFePO_4$ half-cell, establishing the voltage curves under current pulses. In Fig. 2.5, the black and red dash lines are the voltages measured when no current applied, known as equilibrium states. The solid lines are the voltages measured under current. The black lines are measured voltages during charging, while red lines for discharging process.

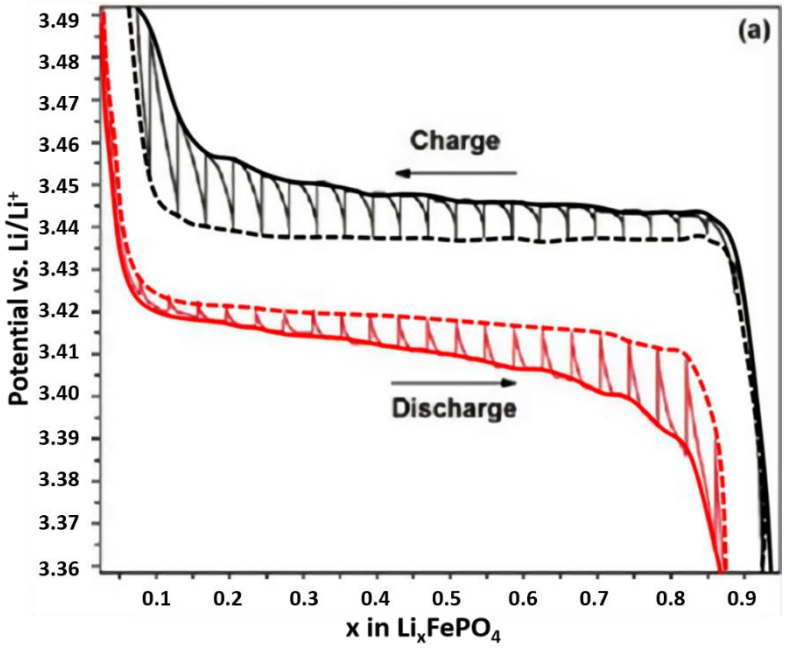

Fig. 2.5: An example of charge/discharge GITT curves [42].

- The generated heat is proportional to the voltage difference:

$$\dot{Q}_{irr} = \Delta U \cdot i \tag{2.10}$$

Where $\dot{Q}_{irr}$: generated heat rate due to irreversible reactions (W), ΔU: voltage difference of under current status and open circuit (V), i: current (A). This irreversible heat effect is named Joule effect or Joule heating, which is the irreversible energy loss to the system.
Therefore, the total heat generation rate $\dot{Q}_{tot}$ during battery's cycling consists of irreversible heat flow rate $\dot{Q}_{irr}$ and reversible heat flow rate $\dot{Q}_{rev}$ [26]:

$$\dot{Q}_{tot} = \dot{Q}_{rev} + \dot{Q}_{irr} \tag{2.11}$$

Reversible heat effect

Reversible heat effect can be the heat absorption or heat emission, accompanying with electrochemical reactions. This heat effect is independent from charge/discharge rate, and is defined to be proportional to entropy change (equation 2.9). From the equation 2.5 and equation 2.6, following relationships are derived:

$$\frac{\partial U^0}{\partial T} = -\frac{1}{n\mathrm{F}} \cdot \frac{\partial \Delta G}{\partial T} = -\frac{1}{n\mathrm{F}} \cdot \frac{\partial (\Delta H - T\Delta S)}{\partial T} \tag{2.12}$$

where the charge number *n* equals to 1 for Li^+. The following equation 2.13 is yielded from the equation 2.12. Combining equation 2.12, 2.13 and 2.14 is obtained [41, 43-44]:

$$\Delta S(x) = \mathrm{F} \cdot \left(\left. \frac{\partial U^0(x,T)}{\partial T} \right|_x \right) \tag{2.13}$$

$$\Delta H(x) = \mathrm{F} \cdot \left(-U^0(x,T) + T \cdot \left. \frac{\partial U^0(x,T)}{\partial T} \right|_x \right) \tag{2.14}$$

According to equation 2.13, $\left. \frac{\partial U^0(x,T)}{\partial T} \right|_x$ denotes the slope of U^0 changing with temperatures at constant composition x, which enables to determine entropy and enthalpy change via measurements. At constant composition x of electrode materials, the temperature dependence of open circuit voltage OCV (U^0) can be experimentally determined. The total change in entropy during delithiation/lithiation process between compositions x_1 and x_2 can be obtained from integration of ΔS from composition x_1 to x_2 according to the following equation 2.15 [45]. Similarly, the total enthalpy change of the cell reaction between compositions x_1 and x_2 can be obtained from integration of equation 2.14 [44]:

$$\Delta S|_{x_1}^{x_2} = F \cdot \left(\int_{x_1}^{x_2} \left. \frac{\partial U^0(x,T)}{\partial T} \right|_x \cdot dx \right) \tag{2.15}$$

$$\Delta H|_{x_1}^{x_2} = \mathrm{F} \cdot \int_{x_1}^{x_2} \left(-U^0(x,T) + T \cdot \left. \frac{\partial U^0(x,T)}{\partial T} \right|_x \cdot dx \right) \tag{2.16}$$

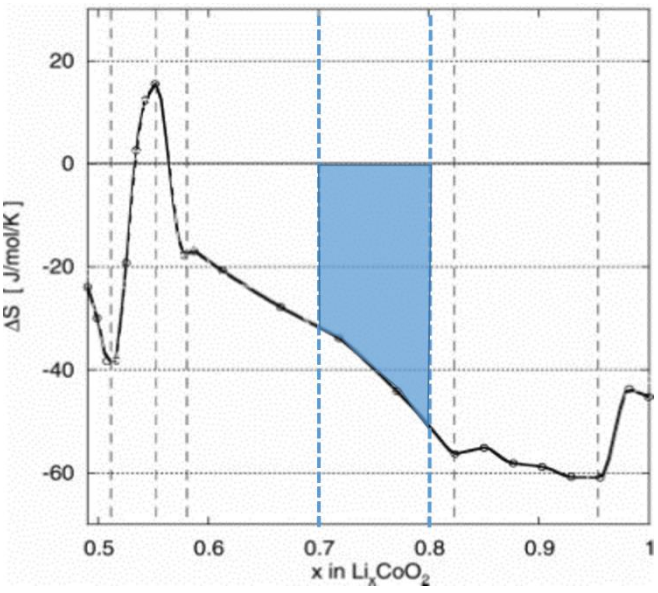

Fig. 2.6: Entropy of lithium intercalation into Li_xCoO_2 [44].

From equation 2.9, the reversible heat flow rate $\dot{Q}_{rev}$ is given by the following equation [41, 43]:

$$\dot{Q}_{rev} = T \cdot \Delta S \cdot \frac{i}{F} \tag{2.17}$$

Thus, the reversible heat Q_{rev} generated between composition x_1 and x_2 equals to the integration of the reversible entropy change ΔS from composition x_1 to x_2 multiplying with temperature according to equation 2.9 and 2.15:

$$Q_{rev}|_{x_1}^{x_2} = T \cdot \Delta S|_{x_1}^{x_2} \tag{2.18}$$

For example, Fig. 2.6 establishes an entropy change curve in discharge process versus various Li content in positive electrode material Li_xCoO_2. When Li content is changing from 0.7 to 0.8, normalizing the electrode composition to the full compositional range Li=1, the total entropy change during the process $\Delta S|_{0.7}^{0.8}$ is showed as the blue area. The reversible heat during lithiation x from 0.7 to 0.8 equals to $\Delta S|_{0.7}^{0.8}$ multiplying with temperature (equation 2.18). For the measurement of OCVs at different temperature, potential error sources are: side reactions, conductor resistances and chemical depletion. In order to define the composition accurately, especially the Li content, the side reaction such as self-discharge must be carefully avoided [44]. Osswald et al. [45] had the similar observation: when ambient temperature is higher than 40 °C, the ageing process was accelerated due to side reactions. Therefore the temperature of measurement is adjusted carefully in this work.

Irreversible heat effect

Irreversible heat flow rate $\dot{Q}_{irr}$ is generated due to the internal resistance $\mathrm{R_i}$ (the sum of ohmic, activation and diffusion polarization resistances), which is proportional to the voltage difference as showed in equation 2.10.
To avoid the positive/negative values in voltage differences during discharge / charge process, the absolute voltage difference is taken in equation 2.19:

$$\dot{Q}_{irr} = \Delta U \cdot i = |U_i - OCV| \cdot i \tag{2.19}$$

where U_i (V) represents the voltage under current i (A), and the irreversible heat flow rates $\dot{Q}_{irr}$ are given in Watt.

The voltage disparity exits in both charging and discharging processes. The voltage drops/jumps during charging/discharging in Fig. 2.5 indicate the related irreversible heats: $U_i - OCV$ in equation 2.19. Therefore, the irreversible heats for both processes are not identical, when the voltage disparities during charging/discharging are not identical. There are several reasons. The electron-active ions and related atomic species are transported for charging and discharging in opposite direction, resulting in different impedances. Furthermore, the impedance exists in the time–dependent reactions because of solid state diffusion [26], which also varies from charge/discharge process. Therefore, the voltage difference should be defined corresponding to charge and discharge process. Under constant current i, the voltage difference $U_i - OCV$ as showed in Fig. 2.5 are varying all the time. Therefore, the irreversible

heat Q_{irr}, which is generated in the period of t_1 to t_2 is obtained by integration of heat flow rates over time:

$$Q_{irr} = \int_{t_1}^{t_2} (|U_i - OCV|) \cdot dt \cdot i \tag{2.20}$$

Electrochemical impedance in LiB

When the current flows through an electrochemical cell, the voltage diverges from OCV, because of the resistances of electrolyte to ionic transport, electrodes, and electrode/electrolyte interfaces. Instead of "resistances", the term "impedance" can better identify the time-dependent and composition-dependent manner of resistances. Under DC conditions, the impedance is equivalent to resistance, and the electronic impedance Z_e can be calculated by following equation [26]:

$$Z_e = E_{appl}/I_e \tag{2.21}$$

E_{appl} represents a voltage applying on the circuit elements, and its corresponding current I_e across the circuit elements.

2.4.2 Heat dissipation during LiB's operation

In general, heat dissipates into surrounding via the three paths: thermal conduction, radiation and air convection. Heat dissipation affects the measurement system dramatically, which will be discussed in Section 2.6. In coin cells' cycling tests, cables have to be used in the measurement system. The heat transfers mainly through air convection, which is discussed further in Chapter 5. Following equations have to be considered:

1. Heat dissipation rate by thermal conduction can be described as:

$$\frac{dQ}{dt} = \frac{k \cdot A \cdot \Delta T}{L} \tag{2.22}$$

   k stands for thermal conductivity of coin cell shell W/(m·K). A indicates surface area of coin cells in m^2, and L is the thickness of the coin cell shell in unit m. ΔT characterizes the temperature difference between contacted interface in K.

2. Heat dissipation rate by radiation according to Stefan-Boltzmann law can be described as:

$$\frac{dQ}{dt} = \varepsilon \cdot \sigma \cdot (T_{surf}^4 - T_{amb}^4) \tag{2.23}$$

   σ represents the Stefan-Boltzmann constant 5.67×10^{-8} W/(m^2·K^4). ε is the emission ratio of the cell surface comparing with black body ($\varepsilon_{usual\ container\ material} = 0.95$, $\varepsilon_{black\ body} = 1$). T_{surf} is surface temperature of cells, and T_{amb} represents ambient temperature.

3. Heat transfer rate by air convection from known surface area:

$$\frac{dQ}{dt} = h \cdot A \cdot \Delta T \tag{2.24}$$

h stands for heat transfer coefficient, W/(m^2·K), and A indicates surface area in unit m^2. ΔT represents difference of temperatures between the solid surface and air, K.

2.5 Thermal runaway of LiBs

For daily application of LiBs, short circuit, high temperature circumstances, and failure of a single cell etc., could lead to catastrophic hazardous events, such as violent venting, smoke, fire or explosion [23, 46-48]. Thermal runaway is described as the event in which the cell generates a significant amount of heat and gases due to exothermic reactions. It could be extremely dangerous when the thermal runaway on a single cell causes the thermal runaway of neighboring cells in a battery pack [49-50]. With growing thermal runaway incidents, involving airplanes, automotive and batteries' storage or transport [47] the safety issues become more and more urgent to be solved.

The temperature, caused by the heat balance between dissipation and generation, affects the thermal runaway conformation and its process extremely. When the temperature of a cell is higher than the onset temperature of thermal runaway reactions, the exothermic reaction enhances the temperature, which accelerates the reaction rate in return. Furthermore, the heat generation exceeds the heat dissipation capacity, then the thermal runaway event is under a quasi-adiabatic condition.

To visualize this temperature change process, Semenov plot [51] is introduced in Fig. 2.7, which demonstrates that the heat generation (curve 4) due to the exothermic reactions follows the exponential function (assuming Arrhenius law), while the heat dissipating lines (line 1, 2 and 3) are linear functions according to Newton's law of cooling at different coolant temperatures A, B and C. Three lines indicate three possible relationships of heat generation/dissipation rates: intersection, a tangent and non-intersection. For line 1, two intersection points E and F are stable and unstable isothermal operation, respectively. If the temperature is lower than point E, the heat generation rate is higher than heat dissipation, which rises temperature to point E. When temperatures is between point E and F, cooling rate is higher than heating rate, resulting in a temperature decrease to point E. Above point F, the heat generation rate increases fast and the thermal runaway is inevitable at temperature T_1. For line 2, T_{NR} means the "Temperature of No Return", since it is above the tangent point D, where is the critical equilibrium, the thermal runaway would take place. The temperature B is defined as the self-accelerating decomposition temperature (SADT) [23, 52]. The temperature C has totally no cooling impacts on the system.

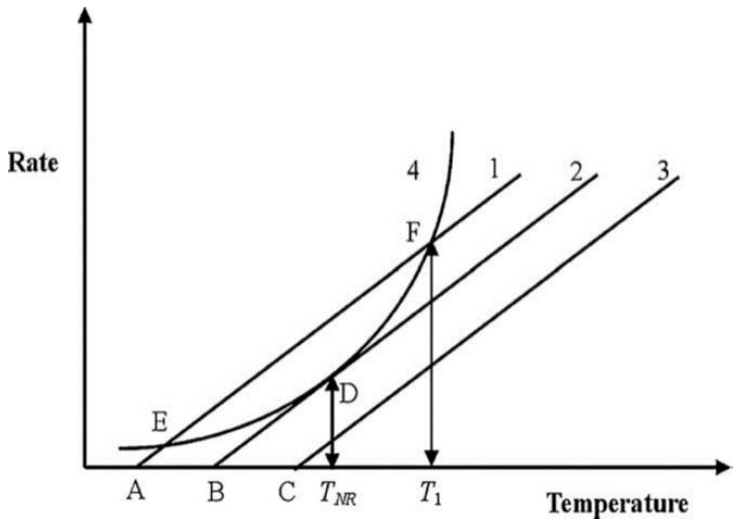

Fig. 2.7: Heat balance between heat due to an exothermic reaction and heat loss from a vessel, at variant ambient temperatures A, B, and C [51].

Comparing the energy balance of the thermal runaway event with LiB's cycling, the additional part is the heat generated rate from abuse chemical reaction $\dot{Q}_{ab-chem}$ inside a unit volume [23, 53-55]:

$$\frac{\partial(\rho \cdot c_{batt} \cdot T)}{\partial t} = -\nabla(k \cdot \nabla T) + \dot{Q}_{ab-chem} + \dot{Q}_{Joule} + \dot{Q}_S + \dot{Q}_P + \dot{Q}_{ex} + \cdots \qquad (2.25)$$

Where ρ: the average mass per unit volume of the battery (g/cm^3), c_{batt}: the specific heat capacity of the battery (J/(g·K)), T: the temperature (K), t: the time (s), k: the thermal conductivity of the studied unit (W/(cm·K)). $\dot{Q}_{Joule}$: Joule heating rate in the battery (W), $\dot{Q}_S$: the heat rate due to entropy change (W), $\dot{Q}_P$: the heat rate due to over-potential effect (W) and $\dot{Q}_{ex}$: the heat exchange rate between the surrounding and the system (W).
The exothermic reactions include the decomposition of solid electrolyte interface (SEI), the inter-reaction of electrodes and electrolyte and the decomposition of electrodes. The detailed description will be given later. The heat generation for an individual exothermic reaction is defined as following [23, 56]:

$$\dot{Q}_{ab-chem-individual} = \frac{dH}{dt} = \Delta H \cdot M^n \cdot A \cdot \exp(-\frac{E_a}{RT}) \qquad (2.26)$$

where ΔH is the individual reaction heat. M is the mass of reactant in the individual reaction, and n is the individual reaction order. A is a pre-exponential factor of individual reaction. E_a is activation energy of the individual reaction and R is gas constant. $Q_{ab-chem}$ is the summary of all reactions. The Joule heat is generated when a current flows through conductive components. Therefore, the overall Joule heat is the summarized value in all phases as:

$$\dot{Q}_{Joule} = \sum\nolimits_j |\emptyset_j \cdot i_j| \qquad (2.27)$$

where $\emptyset_j$: electric potential in phase j (V), i_j: current density in phase j (A/cm^2).

2.6 Measurement condition in calorimeters

To study the thermal behavior of the battery, it is essential to define the operating conditions in the calorimeter. The adiabatic, isoperibolic and isothermal conditions are introduced. The term “scanning” regarding calorimeter operation is explained in this section, which is controlled by heating system. Simutaneously, the temperature in a calorimeter needs to be controlled carefully, so that the measuring system is under isothermal or adiabatic condition.

The adiabatic condition

The adiabatic condition refers to operation in an adiabatic manner when no heat exchange between measuring system and surrounding exists. Fig. 2.8 illustrates a measuring system and surroundings. No. 1 is environment. No. 2 represents furnace, which is the surrounding for measuring system with temperature T_F. No. 3 is the measuring system with temperature T_M. Under ideal circumstances, no heat exchange whatsoever occurs between the measuring system and its surroundings: $T_F = T_M$. In reality, the measurements in calorimeter can create an adiabatic condition through following three ways [57]:

1. The sample reacts so rapidly that no appreciable quantity of heat released or absorbed during the measuring interval.
2. The thermal resistance R_{th} (No. 4 R_{th} in Fig. 2.8) between surroundings and the measuring system is infinitely large.
3. The temperature of surroundings is controlled in every moment to be equal to the measuring system $T_F(t)=T_M(t)$.

In this work, accelerating rate calorimeter (ARC), is the one we used as a quasi-adiabatic calorimeter having a large thermal resistance and heating jacket to minimize the temperature difference between surroundings and measuring system. Moreover, "thermal runaway" measurements even satisfy point 1., in which heat generation in battery increases fast. Thus, the thermal balance cannot be reached and all generated heat remains within the battery, which indicates the following relationship for dissipation heat rate from the battery to surrounding:

$$\frac{dQ_{diss}}{dt} = 0 \tag{2.28}$$

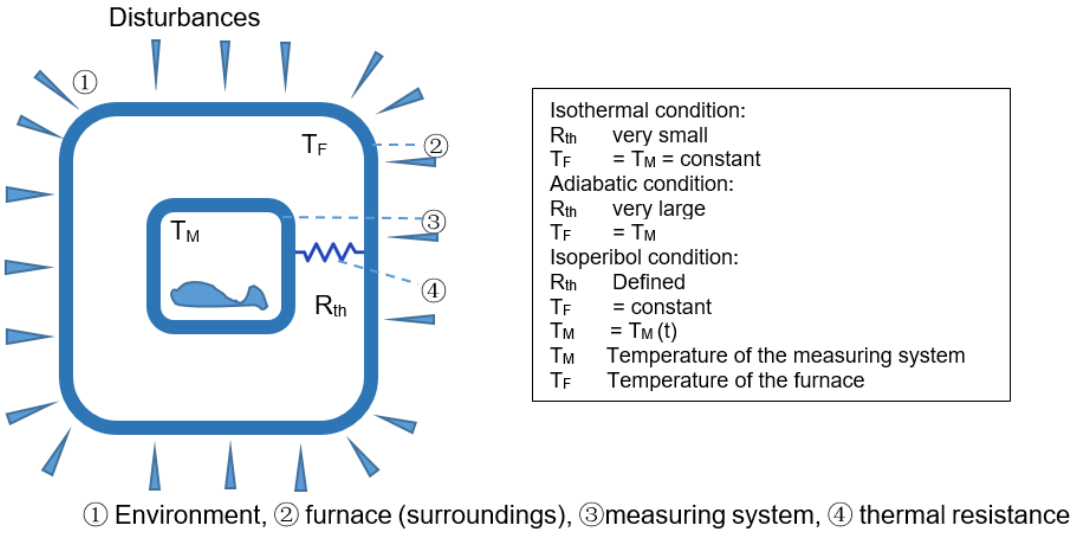

Fig. 2.8: Schematic design of a calorimeter and its surroundings under isothermal/adiabatic/isoperibolic conditions [57].

The isoperibolic condition

The isoperibolic condition describes a measuring system with possible temperature changes while the temperature of the surrounding maintains constant. As in Fig. 2.8 shown, during the measurement, the furnace temperature T_F is kept constant. The measuring system's temperature T_M is a function of time, T_M=T_M(t). In this work, the isoperibolic condition is adopted in measurements of heat generation during cell's cycling in a Tian-Calvet calorimeter (C80). The temperature of measured cells are varied with charge/discharge process. The surrounding temperature is controlled by furnace and thermal resistance, so that there are no disturbances to measuring system. The heat flow rate between the measuring system and the reference can be measured, and higher accuracy is achieved.

The isothermal condition

The isothermal condition refers to that the surroundings and the measuring system have the same constant temperature, which means: T_F=T_M=constant as written in Fig. 2.8. The description of the isotherm state in phenomenological thermodynamics is: the heat exchange between system and surroundings takes place via an infinitesimally low thermal resistance R_{th} and surrounding has an infinite heat capacity. Strictly saying, there are no truly isothermal conditions, since no heat transport would be possible when no temperature difference occurs.

The scanning condition

"Scanning" refers to the condition in which the temperature of the surroundings or of the measuring system is changed according to a set temperature program with respect to time. In Fig. 2.9, the conditions for a scanning case are listed. A defined thermal resistance R_{th}, and furnace temperature T_F is controlled by a scanning rate β. For instance, the furnace temperature is increased with heating rate β (constant scanning rate), therefore: T_F=$T_{F,ini}$+β·t. $T_{F,ini}$ denotes the initial temperature of furnace. t refers to the time. In this work, the

temperature calibration of C80 calorimeter and the investigation for early stage of thermal runaway events on cells and components are performed under scanning operation.

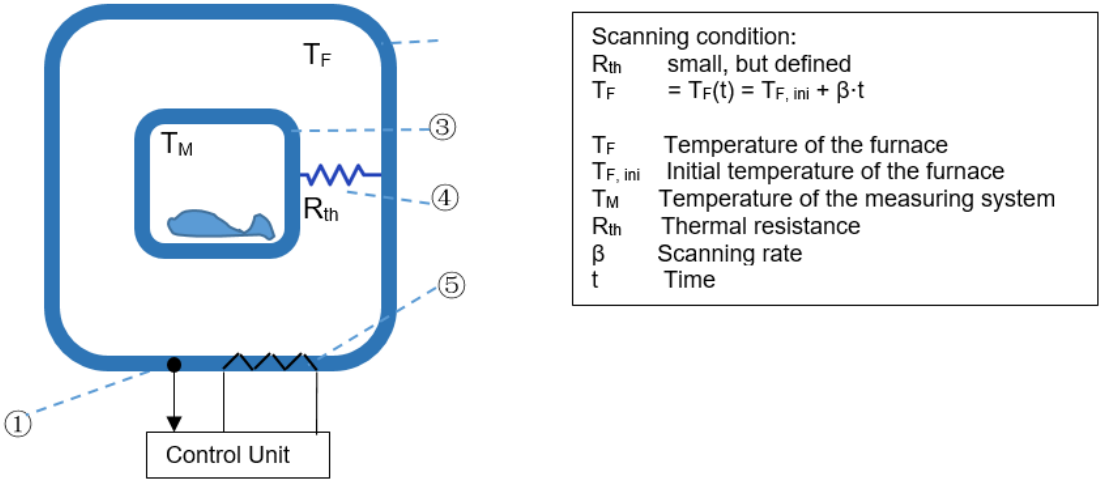

Fig. 2.9: Schematic design of a calorimeter under scanning operation [57].

3 Characterization and measurement methods

3.1 Characterization methods

In this work, several physical, chemical and electrochemical analyses were performed. The crystal structure, composition and morphology of samples were investigated by X-ray diffraction measurements, inductively coupled plasma with optical emission spectroscopy and scanning electron microscopy. In order to determine the irreversible heat, the impedance and resistance are investigated by electrochemical impedance spectroscopy and galvanostatic intermittent titration technique.

3.1.1 X-ray diffraction (XRD)

X-ray diffraction is commonly utilized in crystalline phases identification and analysis. It can be also applied in details investigation such as strain state, crystallographic texture and grain size [58]. The results after carefully refinement, can provide the information of lattice parameter and phase amount.

The high-energy electromagnetic waves of X-rays ranges from 10^{-3} nm to 10 nm wavelength. Since X-rays have a much shorter wavelength compared to visible light, the diffraction of X-rays can be observed when applied on periodic planes of crystals. The behavior of waves diffraction obeys the Bragg's law proposed in 1912:

$$2\mathrm{d} \cdot \sin\theta = n \cdot \lambda \qquad (3.1)$$

Where λ represents wavelength, and θ denotes the Bragg angle. n is an integer representing the order of the diffraction peak and d is inter-plane distance of atoms, ions or molecules, respectively. As the values of wavelength and the scattering angle are known, the inter-plane distance d is determined by equation 3.1.

In this work, for the phase and structure identification, the samples were measured by using powder X-ray diffraction (powder-XRD) using a D8 Advance flat-plate Bragg-Brentano diffractometer (Bruker-AXS GmbH, Germany) with a copper target X-ray tube.

3.1.2 Inductively coupled plasma with optical emission spectroscopy (ICP-OES)

The chemical compositions of solid/liquid specimens are quantitatively investigated by Inductively Coupled Plasma with Optical Emission Spectroscopy (ICP-OES). The segmented-array charge-coupled detector is equipped on an OPTIMA 4300 DV (Perkin Elmer) with an Echelle spectrometer. Echelle based spectrometers provide high spectral resolution and high light throughput. Argon gas is ionized by the electromagnetic field, which is created by high frequency current applying on the torch tube. Then plasma is generated with high electron density and temperature (6000 - 8000 K). The component elements (atoms) in analytic solution are excited in the inductively coupled plasma, and then the excited atoms turn back to low energy level. The emission rays are detected and the elements are identified via characteristic emission spectrum and the intensity of emission lines exhibit the amount of the elements.

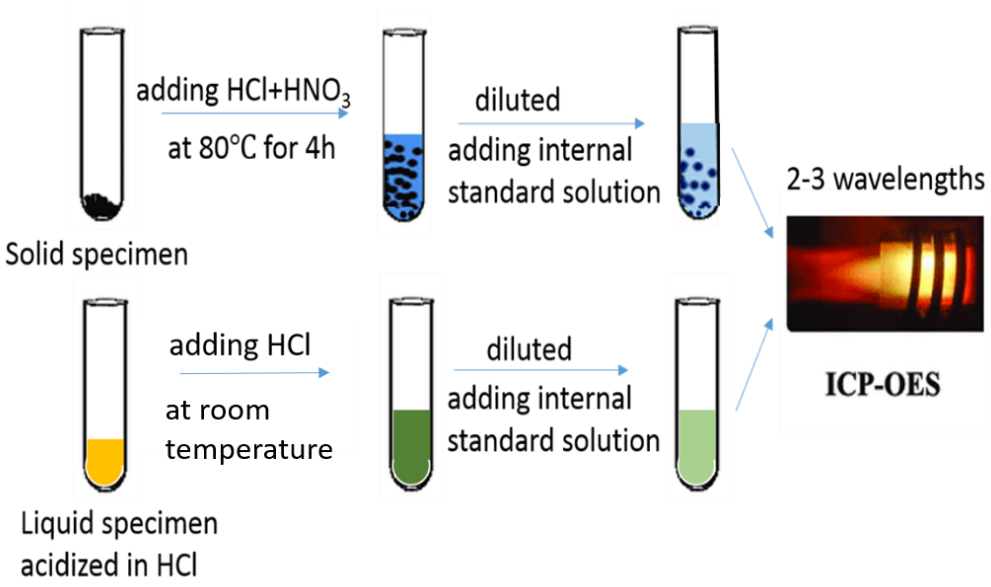

Fig. 3.1: Solid/liquid specimen's preparation for ICP-OES measurements.

In this work as shown in Fig. 3.1, solid specimens were mainly NMC active materials of positive electrode, and liquid specimens were reagent solution from chemical delithiation. The preparing procedure for solid specimens, included adding HCl and HNO_3, storing at 80 °C for 4 h, diluting and adding internal standard solution. Liquid specimens were acidized using HCl in order to dissolve MnO_2 powders. The diluted solid/liquid specimens were tested. Two to three different wavelengths were applied in ICP-OES measurements to define elements.

3.1.3 Scanning electron microscopy (SEM)

A scanning electron microscope (SEM) is a useful material analysis method to produce images of a sample's surface by focused beam of electrons. When the beam is scanning the surface of the sample, the electrons interact with atoms to produce secondary electrons. The detector will collect the signals, and the intensity depends on specimen topography. The resolution can be better than 10 nm.

In this work, a FEI XL30S (Philips, Netherlands) was utilized to investigate the morphological properties of separator samples of tested cells. The separator was specially prepared by sputtering with gold before the measurement. The negative and positive electrodes were observed by a JEOL JSM-840 scanning electron microscope with a tungsten cathode.

3.1.4 Electrochemical impedance spectroscopy (EIS)

Electrochemical Impedance Spectroscopy is used to study kinetics of electrode processes and complex interfaces between electrodes and electrolyte. EIS measurement can reveal physical properties of electrodes, the structure and the chemical reactions of interfaces.

When a sinusoidal alternative potential or current applied on a battery, the responding current or potential would have a phase shift. When the frequency changes, the frequency-dependent impedance can be analyzed from the response. Different processes dominate the electrochemical reactions for a frequency range. Fig. 3.3 shows an interface of electrode and electrolyte, where a double layer is formed, illustrated by the inner Helmholtz plane (IHP) and

outer Helmholtz plane (OHP). When the electrons are transferred across the interface, both faradaic and nonfaradaic components exist. The faradaic part is due to an appropriate activation barrier of the reactions, known as polarization resistance (R_p). The uncompensated solution resistance (R_s) also has to be overcome as an energy barrier. The double-layer capacitor (C_d) leads to the nonfaradaic component. Another key process is the mass transfer, which determines the rate of the charge transfer [59, 60]. Warburg impedance Z_w refers to the impedance in diffusion process. An electrical equivalent circuits is developed from the EIS results showing in Fig. 3.2 a) and b). WE and CE stands for a working-electrode and a counter-electrode, respectively.

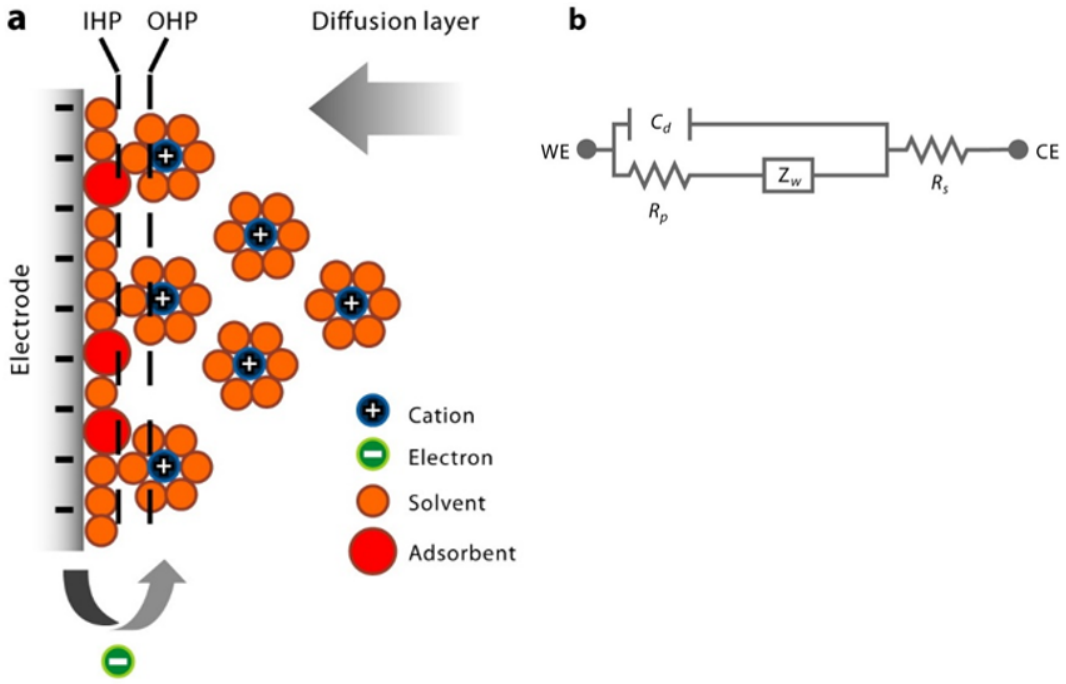

Fig. 3.2: Interface of electrode and electrolyte: a) Schematic diagram of double-layer structure. b) An electrical equivalent circuit accordingly [59].

In this work, the coin cells were firstly fully charged by CCCV method with 42.5 mA (0.5 C) current, then relaxing for 3 h to reach a stable open circuit potential. Afterwards, EIS measurement was carried out by electrochemical analysis instrument (Gamry, Canada) at ambient temperature. The impedance was measured by 140 µA alternating current with frequency ranging from 20 kHz to 0.01 Hz. The cells were discharged by 85 mA (1 C) for 6 minutes to measure impedance for every 10 % SOC, and the procedure was repeated until the cells were fully discharged. The corresponding voltages were measured, and then Nyquist plots were analyzed to determine the ohmic resistance.

3.1.5 Galvanostatic intermittent titration technique (GITT)

Another method of analyzing the internal resistances and separating the contributions is galvanostatic intermittent titration technique (GITT). As shown in Fig. 3.3, a 42.5 mA (0.5 C) current was applied on the cells for 12 minutes, and the potential increases instantaneously. The IR drop is the sum effect related to the ohmic resistance (R_Ω) and charge transfer resistance (R_{CT}). Since the ohmic overpotential is the product of the resistance and applied current, the charge transfer overpotential is yielded by [61]:

$$\eta_{\mathrm{CT}} = \eta_{\mathrm{IR}} - \eta_{\Omega} = \eta_{\mathrm{IR}} - \mathrm{I} \cdot \mathrm{R}_{\Omega} \tag{3.2}$$

Then the potential decreases relatively slowly due to the time-dependent diffusion at interfaces, in electrolyte, and bulk. The diffusion overpotential η_D is thus determined, as shown in Fig. 3.3 (a measurement from this work).

Comparing to the elements in Fig. 3.2, overpotential η_{Ω} is the driving force for R_s and R_p. Overpotential η_D is for Warburg impedance, and η_{CT} is mainly for capacitance. Unlike EIS measurements, GITT measurement supplements the impedances under operating current (not small current as in EIS measurements).

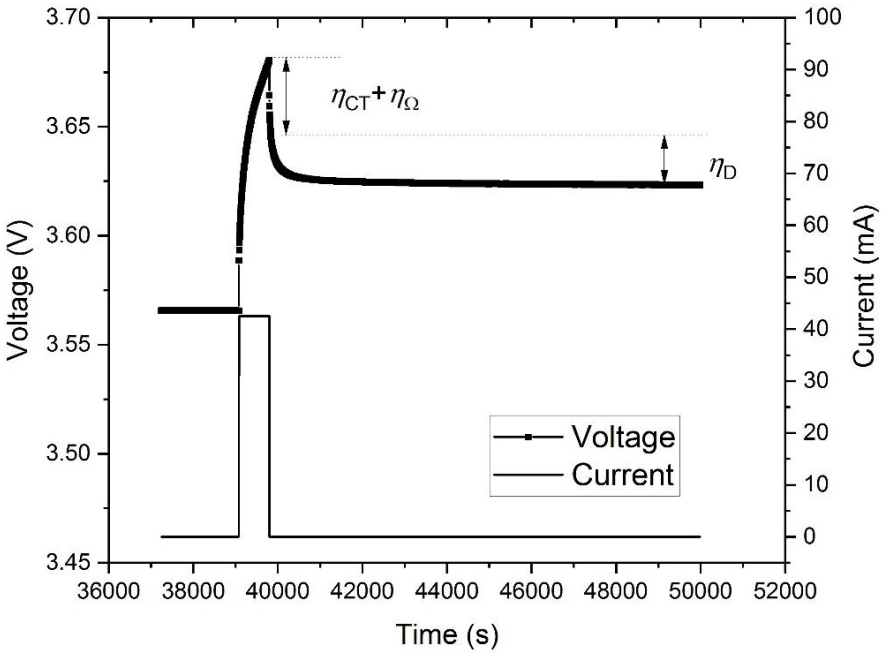

Fig. 3.3: Charging pulse followed by a relaxation time of 3 h in this work [62].

3.2 Calorimetric methods applied in this work

The thermal properties and thermal behaviors of LiBs and their components are investigated by means of C80 calorimeter (Setaram, France), accelerating rate calorimeter (THT, England), high temperature oxide melt drop solution Alexsys-1000 calorimeter (Setaram, France) and simultaneous thermal analysis (NETZSCH, Germany).

3.2.1 C80 3D Tian-Calvet calorimeter

Introduction to a C80 3D Tian-Calvet calorimeter

In year 1948, Calvet extended the design of Tian's calorimeter (1923), which has two equal systems in an isothermal block instead of a single system. C80 calorimeter is adapted to isothermal calorimetry, mixing calorimetry and temperature scanning calorimetry, which was designed to study the sample's thermal properties or reactions over the temperature range from ambient temperature up to 300 °C.

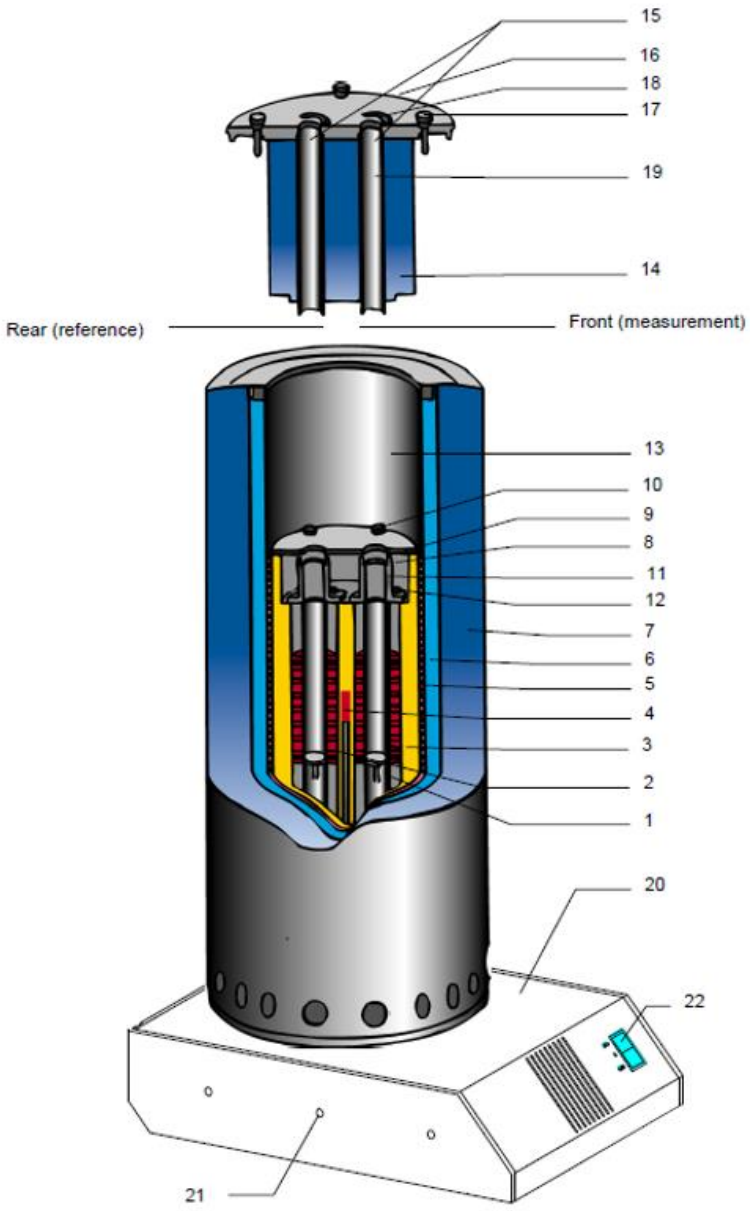

Fig. 3.4: Internal view of C80 calorimeter, detailed information for all the sections is introduced in the appendix.

The functional principle of C80 is similar to differential scanning calorimetry (DSC), as shown in Fig. 3.4. No. 1 and 2 are measurement and reference fluxmeter respectively. No. 3 is the calorimetric block, which is the thermostat. A sleeve (No. 6) surrounds it, and around No. 6, No.7 is a heat insulator. Inside the sleeve, cooling air can circulate, pulsed by a fan. Between No. 3 and No. 6, there is a peripheral heating element (No. 5). No. 4 is a Pt100 platinum thermal sensor to measure the calorimetric sample's temperature with an accuracy of ±0.1 °C and a precision of ±0.05 °C. Another thermal element Pt200 platinum locates in the block to control the temperature. No. 8, 9, 10 and 11 are upper sections of the block, a cover, screws and two support guides. No. 13, 14 and 15 are cylindrical space, heat insulating stopper and two wells, respectively. No. 19 are two metallic tubes which connect directly the upper plate to the No. 11. The thermic plugs in Fig. 3.6 are used in the two tubes to insulate fluxmeters.

Other parts are listed in the appendix.

The advantages of C80 calorimeter over DSC is the application of the latest evolution of the Calvet design calorimetric detector. All heat evolved (or adsorbed) including radiation, convection or conduction can be detected. The design of 3D heat flow sensor is shown in Fig. 3.5. Each fluxmeter is surrounded by 3D heat flow sensor. The sensor is formed by 7 rings, and each ring has 19 thermal couples. These Calvet detectors can measure the heat flow rate with an efficiency of 94 %. Whereas, this value of typical plate DSC amounts to 20 - 40 %.

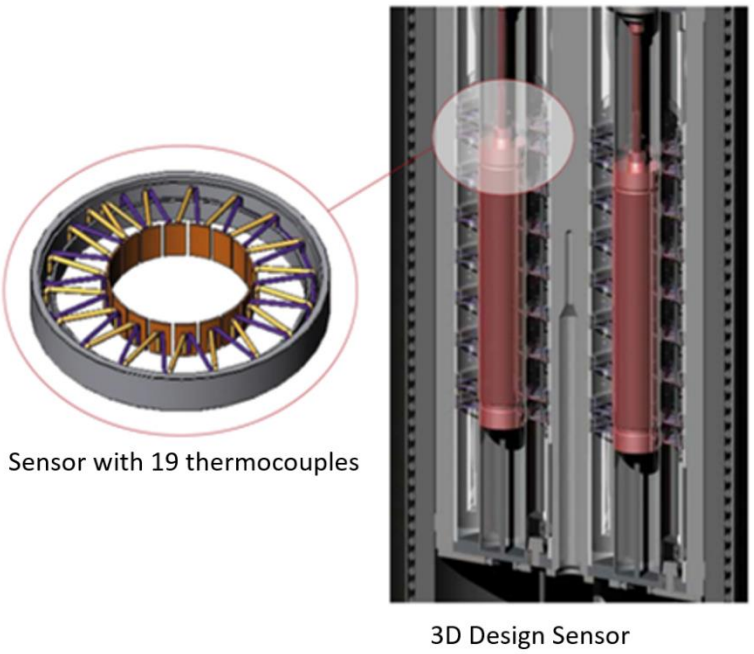

Fig. 3.5: 3D heat flow sensor of C80 calorimeter: each sensor with 19 thermocouples; two identical systems.

The heating rate of C80 calorimeter can be controlled in extremely small range -- from 0.001 °C/min to 2 °C/min, and the resolution is 0.10 µW. The twin-type design of the fluxmeters, has the decisive advantage of excluding the disturbances such as temperature variations and compensating the difference between the individual signals [63]. The quantities that can be determined by C80 calorimeter, are temperature (e.g., of transition or fusion), enthalpy (e.g. of transition or fusion) and heat flow rate (e.g., for determination of the heat capacity of a substance and its change with temperature or for studies of reaction kinetics). Hence, the calibration is performed to calibrate temperature measurements, enthalpy measurements and heat flow rates, which is described in this section.

Two set-ups for C80 measurements used in this work are shown in Fig. 3.6. Set-up 1 was adopted in specific heat capacity measurement and early stage study for thermal runaway. These measurements don't need to connect with cables using set-up 1. For the measurements of heat flow rates during cycling, set-up 2 were used. For set-up 1, the thermic plugs fill the space of two tubes (No. 19 in Fig. 3.4) to insulate the measuring part from surroundings. The thermic plug of set-up 1 sitting above the vessel has three heat shields. A stainless steel vessel is a container for samples, putting in fluxmeters. This design helps to reduce the heat exchange between the chamber and the ambient. Set-up 2 in Fig. 3.6 b) has a special hollow design,

which allows introducing cables into the vessel, but having lower insulation performance. Since the part placing above vessel is designed by Setaram, 60/0519 the name is adopted from Setaram handbook. Thermic plug and 60/0519 in principle have the same function to prevent the heat exchange between sample and surrounding. In Fig.3.6 a), set-up 1, is adopted for the thermal properties' measurements and other measurements which don't need to introduce cables into the vessel. While, Fig. 3.6 b), set-up 2, is used for the batteries' cycling measurements to connect the coin cell with cycling device outside C80 calorimeter. Since the heat exchange of these two set-ups may be different, calibration is performed on both set-ups. Additionally, a Joule effect calibration is performed to determine the calibration factor to exclude the heat effect of cables under current. Details and results are discussed in following text.

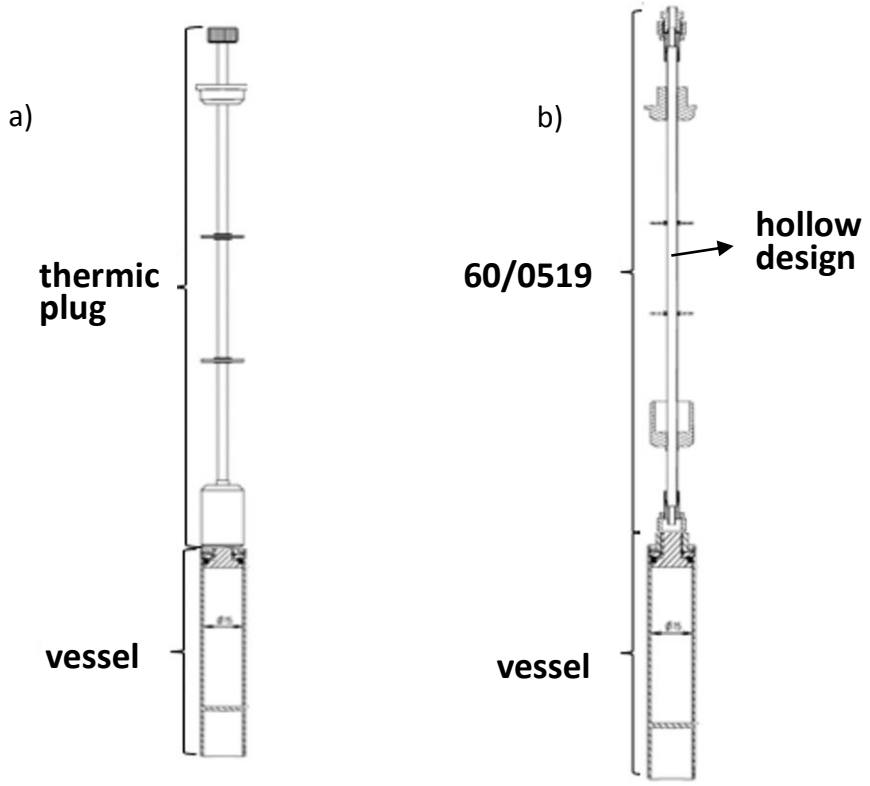

Fig. 3.6: Two set ups for C80 measurements: a) set-up 1 for no cable measurements, b) set-up 2 for cable needed measurements.

Sensitivity calibration of C80 calorimeter

The term sensitivity refers to the transformation of original outputs (voltages in µV) of C80 calorimeter to heat flow rate in mW. The value of sensitivity factor is the reciprocal of calibration factor [57], which equals to 1/K with unit of µV/mW. Sensitivity calibration is performed by the supplier Setaram before shipping. They assume a C80 calorimeter as a Joule Effect calibration module, which can emit a perfectly calibrated impulse. The applied power is the upper curve shown in Fig. 3.7. Simultaneously, C80 calorimeter outputs voltages, which are the measuring signals. The corresponding voltages curve are plotted below in Fig. 3.7. Knowing voltages and time, energy is calculated, which is proportional to heat. The sensitivity factors under selected temperatures can be immediately determined by comparing the values of energy and heat. Furthermore, a calibration polynomial is developed as shown in Fig. 3.8.

The coefficients in polynomial function are embedded in the software of C80 calorimeter.

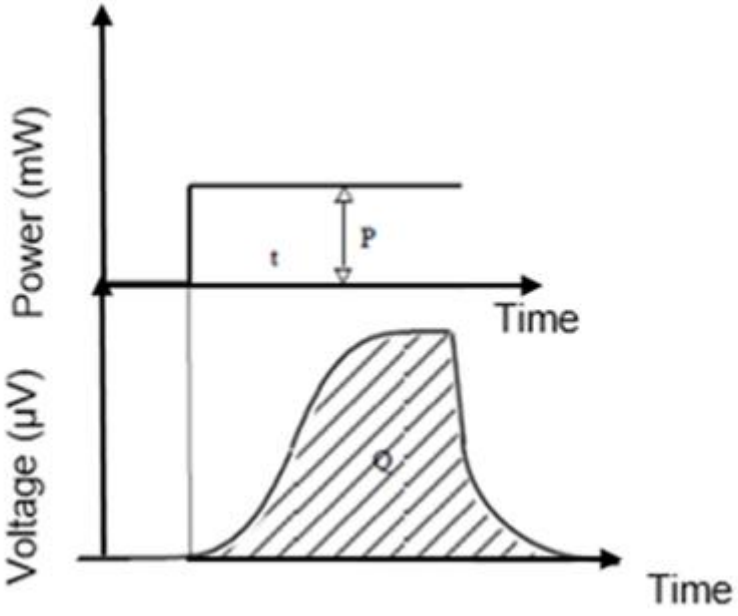

Fig. 3.7: Applied power externally and corresponding voltages outputs of C80 calorimeter against time.

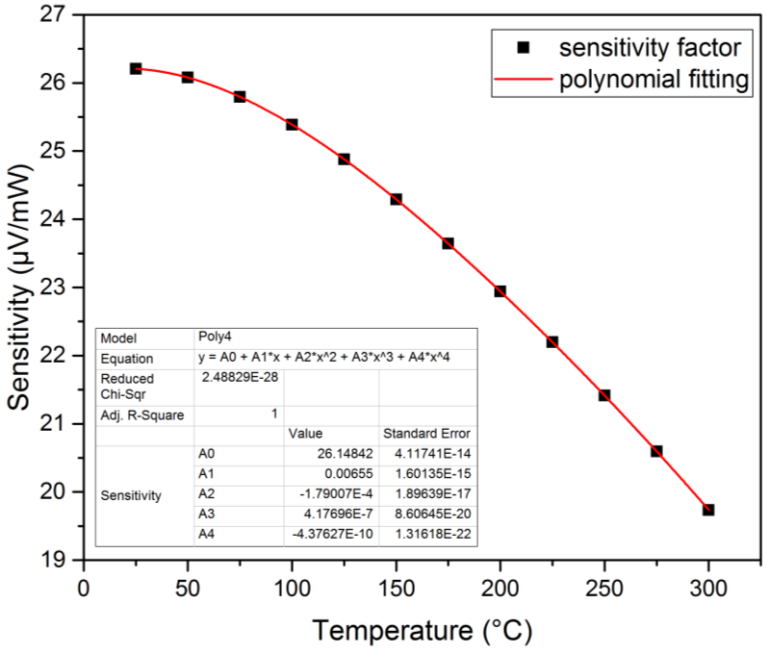

Fig. 3.8: Sensitivity factors under selected temperatures and polynomial fitting.

Reference materials

Since the operating temperature range of C80 calorimeter is from ambient temperature to 300 °C, and the adopted measuring vessels can withstand till 220 °C, calibration temperature range is from ambient temperature to 220 °C. Beside the temperature range, other essential properties should be fulfilled by reference materials [64]:

- Represent a fixed point of phase transition/melting which is thermodynamically well defined.
- Available in high purity (at least 5N).
- Chemically and physically stable. There should be no reaction with atmospheric moisture or the carrier gas, especially with crucibles and C80 chambers.
- Easy to handle and of low toxicity, which should be recognized as physiologically safe.

According to these requirements, Ga, KNO_3 and In (Table 3.1) are selected as reference materials for temperature and enthalpy calibration.

Table 3.1 Reference materials: the transition temperatures T_{trs} and enthalpies $\Delta_{trs}h$ in J/g and $\Delta_{trs}H$ in J/mol.

	Ga [65-68]	KNO_3 [69]	In [65-68]
Molar mass (g/mol)	69.723	101.103	114.818
T_{trs} (°C)	29.7646	129±2	156.5985
$\Delta_{trs}h$ (J/g)	80.07±0.13	48.49±1.26	28.62±0.04
$\Delta_{trs}H$ (J/mol)	5583±9	4902±127	3287±5

Temperature calibration for C80 calorimeter

The aim of temperature calibration is to determine the temperature correction in operating temperature range. Temperature correction refers to the difference between the measured temperature and the "true" temperature. Firstly, the onset temperature of transition or fusion should be carefully defined. Fig. 3.9 shows a typical measurement in temperature scanning calorimeter, from which the critical terms are well defined [68, 70-71]:

T_{st}: starting temperature, where the temperature program starts.
T_{end}: ending temperature, where the temperature program ends.
T_i: initial peak temperature, where the curve of measured values begins to deviate from the interpolated baseline.
T_f: final peak temperature, where the curve of measured values meets the final baseline.
T_e: extrapolated peak onset temperature, where the auxiliary line (the inflectional tangent) of the ascending peak slope intersects the linear baseline.
β: heating rate, increasing/decreasing of the temperature with time.

Fig. 3.9 shows the heat flow and temperature program against time during the measurement. The temperature was set a constant value, and then heating with a steady scanning rate. At end, the temperature was hold at a higher constant value. The heat flow doesn't change when the temperature was constant. The heat flow increased at the beginning of the temperature increase and then stabilized under a constant scanning rate till a reaction took place. The peak indicates the thermal effect during reactions. At ending of the reactions, the heat flow rate curve was stable again. When the temperature program switched from increasing to a constant value, the heat flow rate changed from one stable value to another.

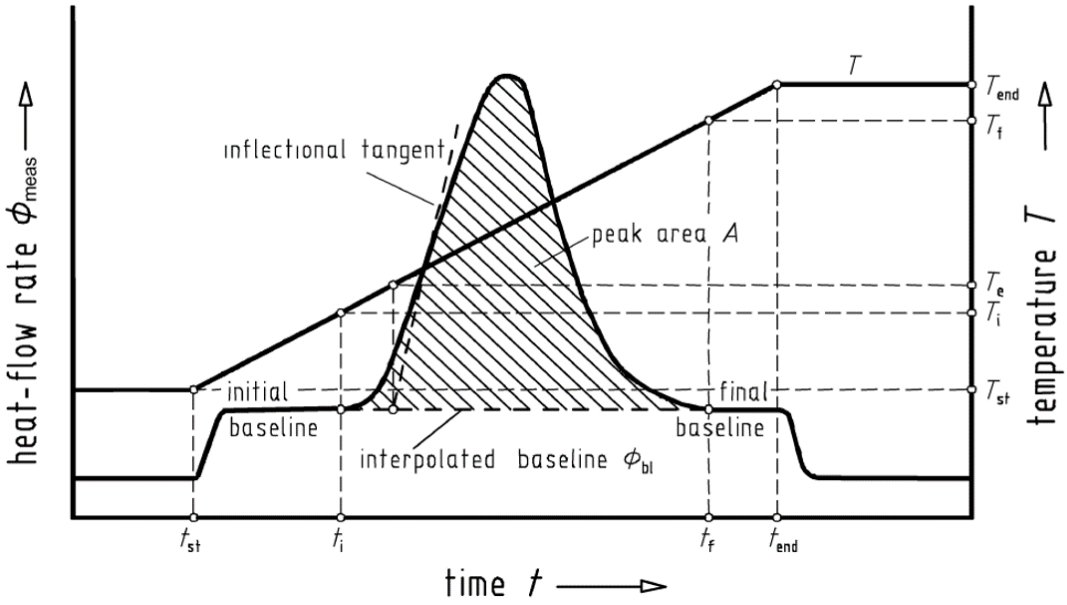

Fig. 3.9: Definition of terms for describing measured curves with the peak representing a transition or reaction in the sample (subscript 'meas' denotes measured quantities) in a plot of heat flow rate and temperature against time, [68] page 1460.

The reaction temperature is determined usually by the extrapolated onset temperature T_e, where the auxiliary line (the inflectional tangent) of the ascending peak slope intersects the linear baseline. There are two reasons for choosing T_e over T_i as onset temperatures. First reason is that the detectable deviation from baseline T_i varies from observers, the absolute value hard to be determined. Second reason is that T_e depends less on sample parameters (thickness, mass etc.). However, in Boettinger's opinion, picking the T_i temperature actually has a smaller deviation from the true melting point and smaller heating rate dependence than the T_e [72]. This method specially suits alloy studies, because alloy usually has a melting range instead of melting with a linear section. Therefore, they used the first detectable deviation from baseline T_i for the calibration.

In this work, the tested coin cell and its components are neither a simple substance nor an alloy. The investigation focuses on the overall thermal properties, reactions, and thermal behavior. The measured heat effects are the results of all interactions not a single reaction. T_e is considered as onset temperature for the measurements as well as for temperature calibration. The peak area A is determined for the enthalpy calibration (Fig. 3.9).

As the heating rate increases, the measured onset temperature increases linearly. The temperature correction term (ΔT_{corr}) is obtained by subtracting the measured onset temperature of transition T_e ($\beta \rightarrow 0$) from the true transition temperature T_{trs} [68, 71].

$$\Delta T_{corr} = T_{trs} - T_e(\beta \rightarrow 0) \tag{3.3}$$

where β refers to heating rate.

In order to perform the calibration at ambient temperature, the start temperature must be much lower. C80 calorimeter is thus put in cooling incubators (BINDER GmbH, Germany), which is set at 10 °C. Each reference material is measured twice to determine the mean onset temperatures with three heating rates.

Calibration with In

Fig. 3.10 shows the heat flow rate versus temperatures during the phase transition of In at heating rate 0.1 K/min. The heating range is from 30 °C to 170 °C. A tantalum crucible is used. The masses of two samples are 1027.8 mg and 1023.1 mg. The sample was taken with a mass of the value calculated from the product of heat (similar value as the heat effects in coin cells' investigation) divided by material's specific heat capacity, so that the heat of In calibration is in the same range. With the evaluation software provided by Setaram, T_e, and the enthalpy of phase transition are determined. In Fig. 3.10, the software interface is shown, where heat amount can be integrated, and T/t represents the temperature/time for phase transition. Temperature of peak maximum and the peak height are given too. Onset/offset temperatures/times are determined, and the mass of sample is shown.

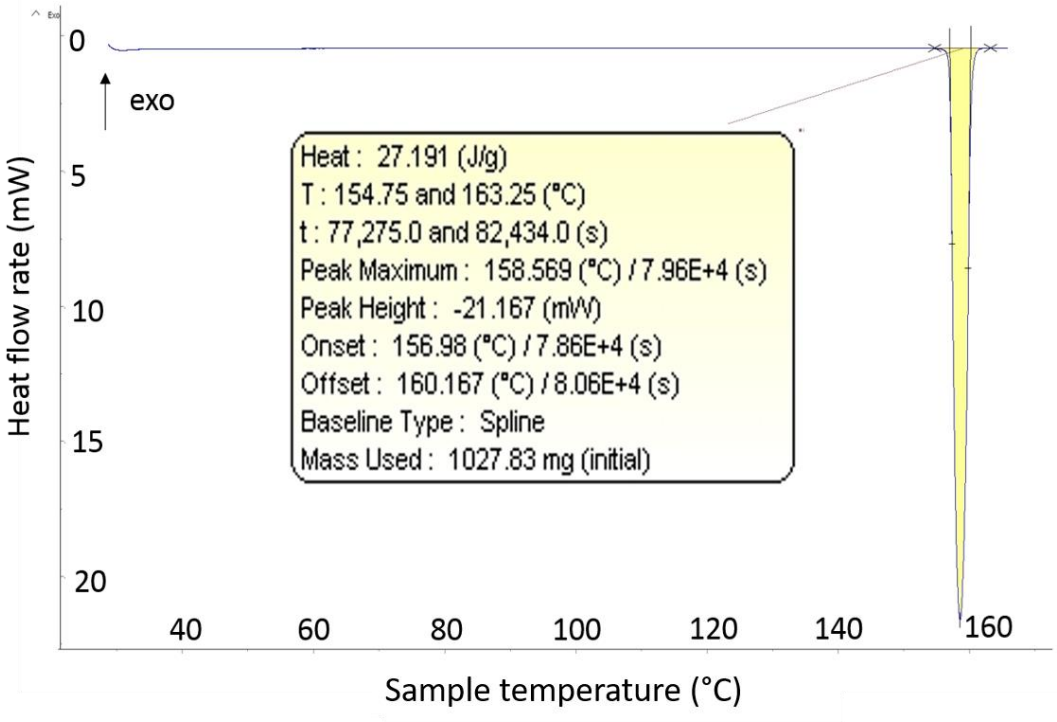

Fig. 3.10: Interface of Setaram software for evaluation of heat flow rate (subtracted baseline).

The onset temperatures T_e at other heating rates are likely measured for set-ups which are introduced in Fig. 3.6. A linear relationship between T_e and heating rates is found, and the intercept of the y axis is obtained (Fig. 3.11). In Fig. 3.11, onset temperatures T_e are plotted against heating rates. The blue points and green points are measured by set-up 1 and set-up 2, the corresponding fitting curves in blue and green, respectively.

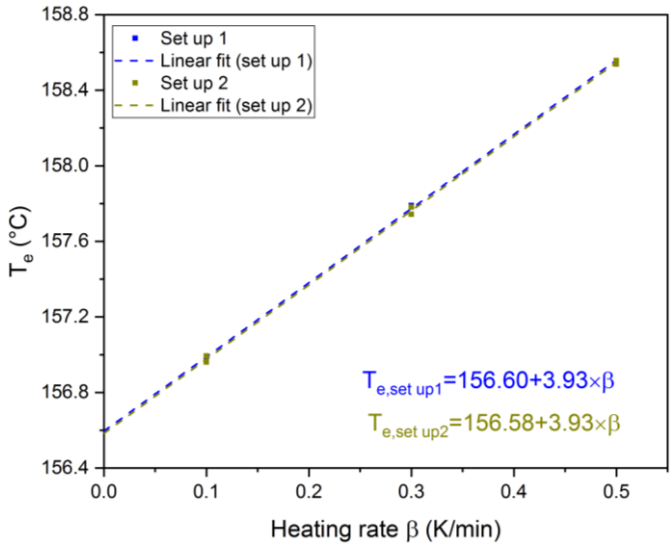

Fig. 3.11: Extrapolated peak onset temperature T_e as a function of heating rate β and measured T_e values of In for both set-ups.

The temperature correction term of C80 is yielded by equation 3.4:

$$\Delta T_{corr} = 156.6\ ℃ - (156.6 \pm 0.4)\ ℃ = 0 \pm 0.4\ ℃ \quad (3.4)$$

The results of two set-ups show no detectable difference in In temperature calibration. Setaram has calibrated C80 calorimeter with In before shipping, hence, in our calibration the temperature correction term equals to zero. This C80 calorimeter demonstrates a good operating state and stable performance. Moreover, another measurement on In with mass 433.8 mg in Al crucible is performed to investigate the stability of C80 calorimeter against the change of crucibles and mass. The comparison is shown in Fig. 3.12, which compares to the measured temperatures of Al/Ta crucible with different masses. These results indicate a relatively small influence on the temperature determination. The uncertainties were from the deviation of three repeated measurements.

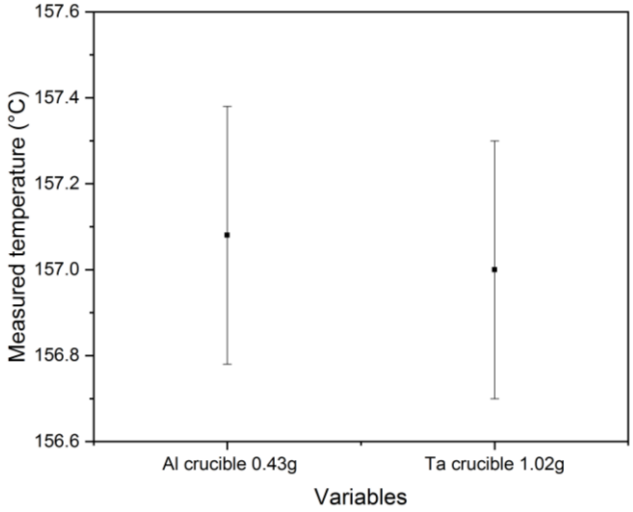

Fig. 3.12: Measured temperatures and their uncertainties of In calibration with different masses and crucibles.

Calibration with KNO_3

The similar calibration is carried out on approximately 540 mg potassium nitrate (KNO_3). The extrapolated peak onset temperatures for both set-ups are determined under heating rate 0.1 K/min, 0.3 K/min, and 0.5 K/min (Fig.3.13). In Fig. 3.13, onset temperatures T_e vary with heating rates linearly. The fitting functions are plotted in blue and green for set-up 1 and 2, respectively. Similar to In calibration, the temperature correction term ΔT_{corr} is obtained by equation 3.5:

$$\Delta T_{corr} = (129 \pm 2)℃ - (129.2 \pm 0.6)\,℃ = -0.2 \pm 2.6\,℃ \tag{3.5}$$

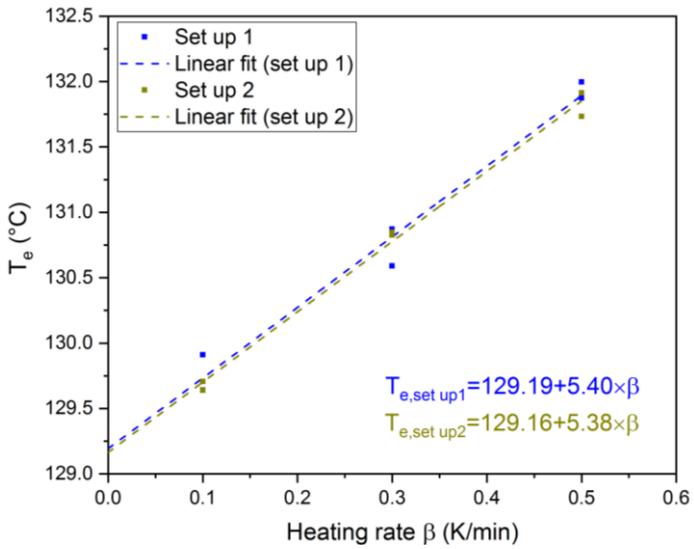

Fig. 3.13: Extrapolated peak onset temperature T_e as a function of heating rate β and measured T_e values of KNO_3 for both set-ups.

Calibration with Ga

As introduced before, C80 calorimeter has only a fan to cool down, so the lowest operating temperature for measurements is ambient temperature. Since the transition temperature of Ga is approximately 29 °C, the ambient temperature has to be as low as 10 °C - 15 °C. To create such surroundings, a cooling incubator (Binder GmbH, Germany) is used to place C80 calorimeter. In Ga calibration, the heating rates have to be lower than for In and KNO_3, due to the small temperature difference between T_{st} and T_e, Otherwise, Ga calibration method is same as for In and KNO_3. The mass of Ga is chosen to perform similar heat effects as cell cycling's heat effects.

The transition of approximately 250 mg Ga is measured to calibrate in temperature range of 15 °C to 40 °C. The heating rates are selected: 0.01 K/min, 0.05 K/min, and 0.1 K/min. Ta crucible is used in the calibration. Onset temperature T_e versus heating rates and the corresponding linear fittings are exhibited in Fig. 3.14. Blue and green results represent measurements of set-up 1 and 2, respectively. In comparison with other two materials' calibration, the two curves of two set ups derive from each other more. That indicates the C80 calorimeter at low temperature range is not as stable as at high temperature range. Similar to In calibration, the temperature correction term ΔT_{corr} is obtained by equation 3.6:

$$\Delta T_{corr} = 29.8\,℃ - (29.6 \pm 0.7)\,℃ = 0.2 \pm 0.7\,℃ \tag{3.6}$$

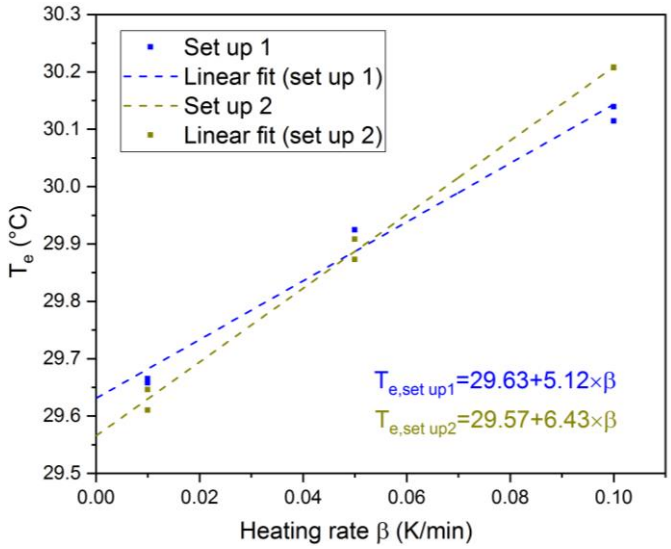

Fig. 3.14: Extrapolated peak onset temperature T_e as a function of heating rate β and measured T_e values of Ga for both set-ups.

Enthalpy calibration

In Fig. 3.9, the peak area is integrated and conversed to the enthalpy change by a conversion factor. This factor is obtained through a calibration with reference material by comparing the measured peak area to the known enthalpy. The enthalpy calibration of In has been done before shipping, so a factor is set in the evaluation software of C80 calorimeter.

In this work, C80 calorimeter is applied to measure the heat generation during coin cell's cycling as well as the heat effects due to the reactions of coin cell's components. In order to achieve reliable results, the measured enthalpy changes are carefully calibrated according to the methods proposed by Della Gatta [68]. Enthalpy and temperature calibration with In, KNO_3, and Ga are performed simultaneously. The enthalpy calibration factor K_H at the transition temperature T_{trs} is yielded by equation 3.7.

$$K_H(T_{trs}) = \Delta_{trs}H / \Delta_{meas}H \tag{3.7}$$

where $\Delta_{trs}H$ and $\Delta_{meas}H$ denote the known transition enthalpy and measured enthalpy change respectively. As the measured enthalpy change might change with different heating rates, $K_H(T_{trs})$ for different heating rates are shown in Fig. 3.15.

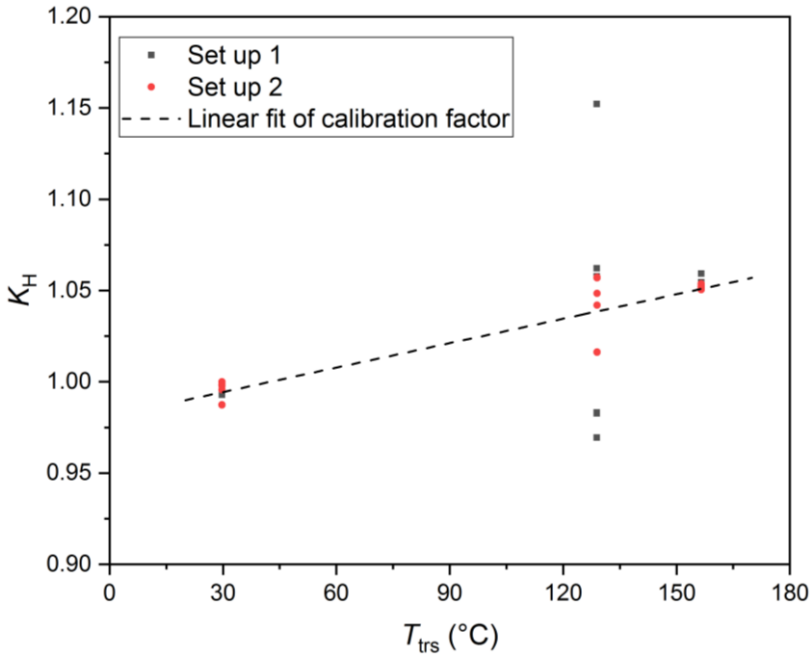

Fig. 3.15: Enthalpy calibration factor plotted against the transition temperature T_{trs} for two set-ups, and a K_H(T) function of the transition temperature.

In Fig. 3.15, the calibration factors determined at about 30 °C (Ga calibration) and 156 °C (In calibration) are in good agreement. However, the measured enthalpy changes of KNO_3 calibration at about 130 °C, are scattering points. The calibration material KNO_3 has the solid phase transition at 129 °C, and the accuracy is not as good as solid-liquid phase transition, such as In and lead [73]. KNO_3 calibration has scattered calibration factors. The development of a linear fitting is more reasonable than non-linear fitting, which indicates the mean values of the repeated calibration at different temperatures. In addition, the heat flow rate calibration is carried out for specific heat capacity measurements, which is introduced in Chapter 5. Therefore, the calibration factors are determined by linear function (dash line in Fig. 3.15).

3.2.2 Accelerating rate calorimeter (ARC)

ARC was firstly developed in the 1970's by the Dow Chemical Company of Midland, Michigan, USA. It was designed to meet the potential needs for hazardous runaway reactions that may occur during the chemical processing, to detect and record the measurement values of time-temperature-pressure. Furthermore, ARC provides a safe and adiabatic environment for the operation and storage. To get better adiabatic conditions, the temperature of the reaction chamber is controlled to be the same as the temperature of the sample.

As shown in Fig. 3.16 a), ARC consists of three parts: containment vessel (with associated hardware and the calorimeter vessels), electronics enclosure (including the PC/work-station), and user interface (monitor, keyboard and mouse). Containment vessel is where the reaction takes place and made of steel. It will be locked during the experiments to ensure the safety in laboratory. Fig. 3.16 b) indicates the internal view of set up in coin cells' tests. Tested coin cell is fixed on the steel holder on the lid, so that tested coin cell is located in the middle of the chamber. Bomb sensor is a thermal element fixed on surface of cells, which indicates the temperature of sample. Top sensor measures the temperature near the lid, and middle sensors

measured the temperature around chamber. Bottom sensor measures the temperature near the bottom. All temperatures are monitored, so heaters will work to eliminate temperature differences in the chamber.

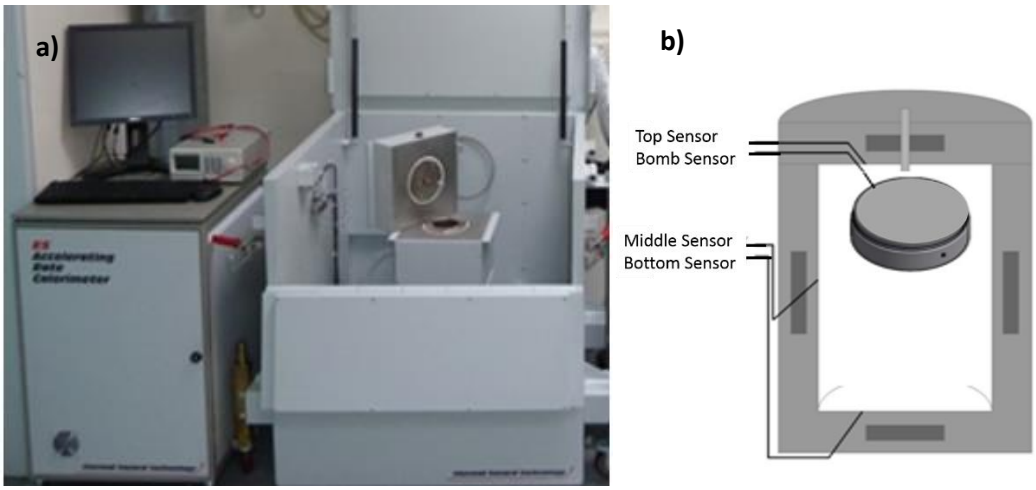

Fig. 3.16: Accelerating rate calorimeter: a) overview; b) Internal view of the calorimeter's chamber.

Heat-Wait-Seek Method

The "Heat-Wait-Seek" (HWS) mode was applied in the thermal runaway measurement. The measurement process is shown in Fig. 3.17, which switches from Heat mode to Wait mode and then to Seek mode. When there is no reaction taking place, the HWS-HWS loop will continue. In Heat mode, the temperature increases almost linearly until reaching "Start Temperature" (manually entered into the set-up software), then slow down linearly to zero. From "Start Temperature", the heater will work to reach each "Temperature Step" e.g. 5 °C.

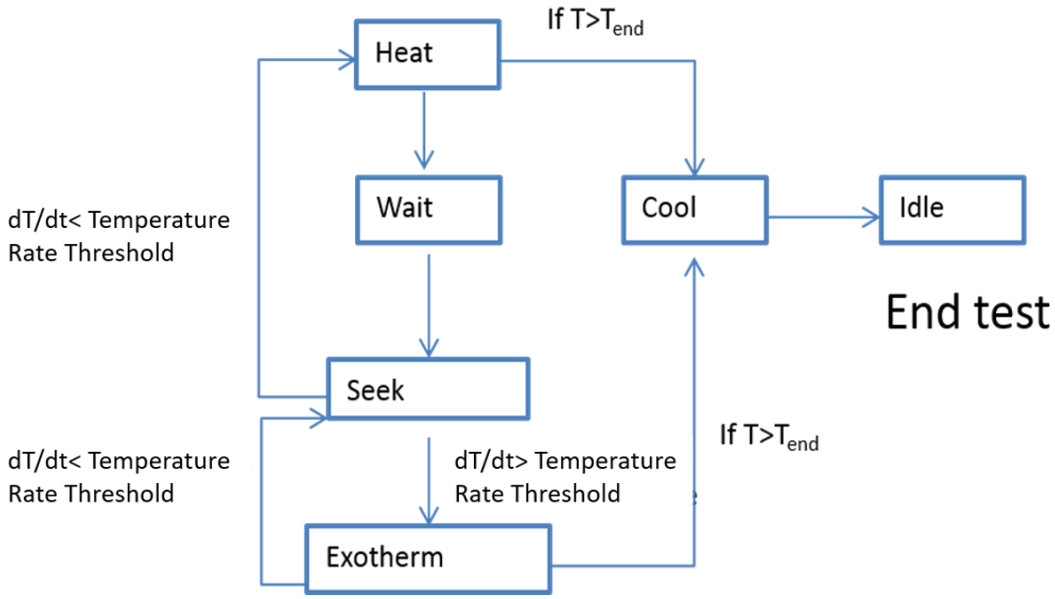

Fig. 3.17: Processes of heat-wait-seek method in ARC.

When temperature span is reached, the Wait mode will be activated till reaching thermal

equilibrium over a certain time. After reaching thermal equilibrium, the system switches to Seek mode, which detects the temperature change rates (dT/dt in Fig. 3.17). When an exothermic reaction takes place (dT/dt > Temperature Rate Sensitivity), HWS loop will stop, switching to exotherm mode instead of Heat mode. Exotherm mode means the measuring system switching to a quasi-adiabatic condition, and more measuring data of the temperature rates and temperatures are recorded. Temperature Rate Threshold is the threshold temperature rate considering exothermic reaction occurring. Temperature drift exits during measurements in ARC, which will lead to faults of detecting temperature changes and temperature rate. Therefore, a calibration test is necessary to be performed.

Calibration

The calibration is performed to ensure the stability of ARC system when no reaction takes place. After Wait mode, the system is supposed to reach the thermal equilibration, therefore, all thermal sensors should show same temperature value. However, there sometimes exits temperature drift/offset larger than the “Temperature Rate Threshold”. The aim of calibration is to determine the temperature drift and minimize or even eliminate the temperature drift. The temperature drift might not be below the sensitivity after one time correction, thus an iteration is designed for calibration test. That means, after determination of an offset/drift, the correction is applied to measure the temperature drift again. Only when the temperature drift is smaller than “Temperature Rate Threshold”, a further small modification will be applied to reduce the drift closer to zero. When these two consecutive drifts are both lower than the sensitivity, next heat step will occur. The calibration is performed on a dummy cell, and the dummy cell is the coin cell after thermal runaway test in this work. The dummy cell should have replicate mass and dimensions of tested cell and no reaction occurring during the calibration. “Temperature Rate Sensitivity” of calibration is set as 0.01 °C/min, which is the half value of the measurement (0.02 °C/min), so that a good thermal stability is achieved in measurements. The calibration is in temperature range from 50 °C to 250 °C. Since the maximum operation of coin cells are 60 °C, no reaction should take place below 60 °C, so the beginning of calibration is set as 50 °C.

3.2.3 High temperature oxide melt drop solution calorimetry

A Setaram Alexsys-1000 Tian-Calvet calorimeter was used to measure enthalpies of drop solution in oxide melts. This high temperature oxide melt drop solution calorimetry is constructed according to the specifications introduced by Navrotsky [74, 75]. The schematic diagrams (Fig. 3.18 a), b), c)) demonstrate the internal structure of Alexsys-1000 calorimeter, which consists of an isoperibolic twin calorimeter system (right and left identical measurement cells) of Calvet-type. The blue part and red part in Fig. 3.18 a) represent isolator and heating elements of the chamber, respectively. In order to heat the system equally, the furnace (red part) is separated to three-zone heaters: upper, middle and lower heating elements. The yellow part in the middle of calorimeter consists of three parts too, which are thermal block cover, thermal block body and thermal block at bottom. The thermal blocks serve to stabilize the measurement environment, where two thermopiles with 8 rings are set. The thermal signals are detected by the thermopiles around the reference and measurement cells. Each ring has 8 thermal couples connected in series in a star-like form as shown in Fig. 3.18 b).

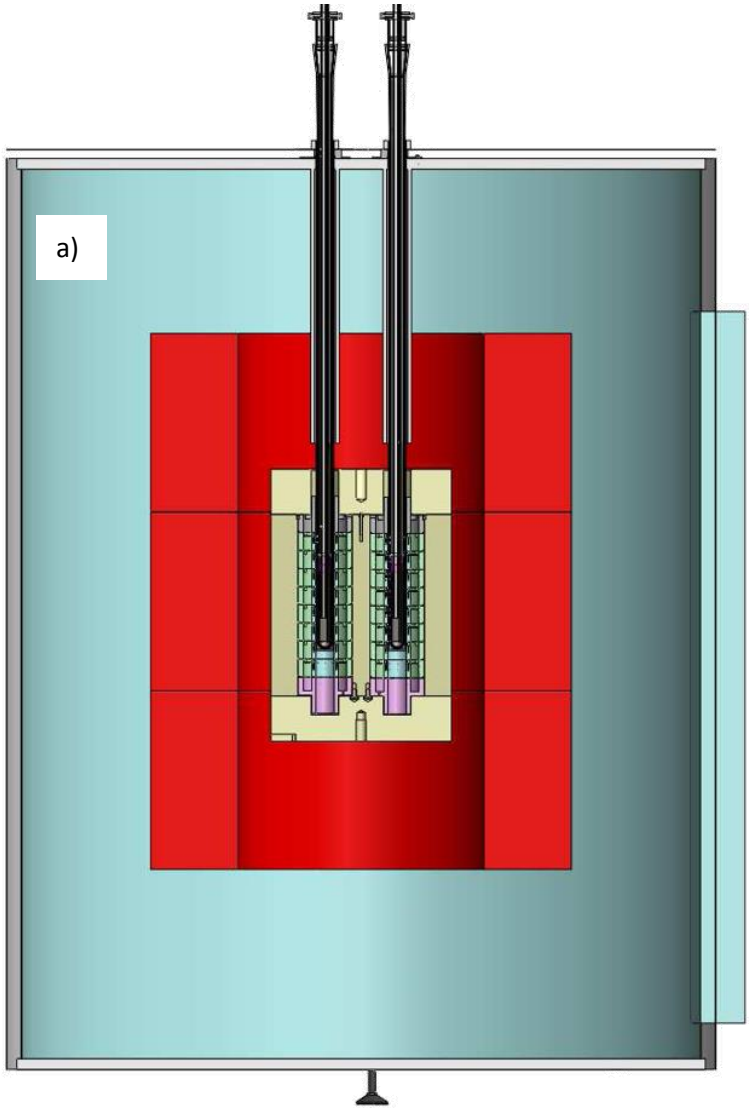

b)

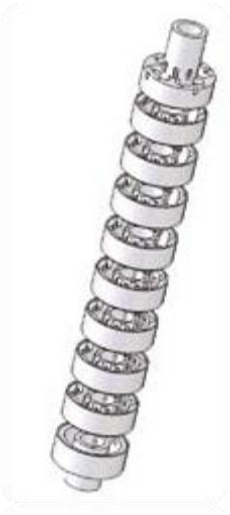

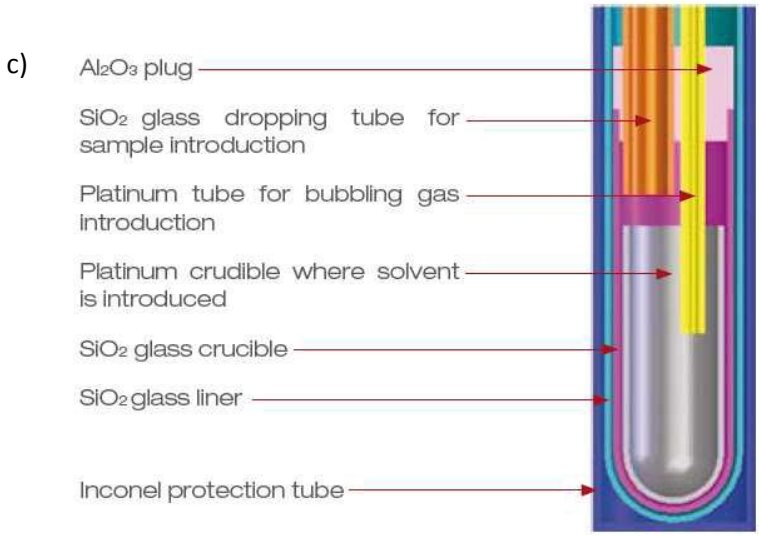

Fig. 3.18: Alexsys-1000 calorimeter (a) internal view, (b) schematic diagram of one thermopile with 8 rings, surrounding by 8 Pt-Pt13Rh-thermal couples (c) enlargement diagram of calorimeter cell [76, 77].

As established in Fig. 3.18 c), the Al_2O_3 plug isolates the solvent from the surrounding. The SiO_2 glass dropping tube is used to introduce the samples from top of the calorimeter into the solvent. The glass tube avoids the dissipation via thermal radiation. The yellow tube is platinum tube inserting in solvent to introduce bubbling gas to stir the solvent, which helps to dissolve the sample homogeneously during measurements.

In order to ensure the stability of the measured heat flow signal, the calorimeter is installed carefully in a thermally-stable and no rapid airflow room. For this three-zone furnace, the set-point temperatures are adjusted to keep a flat temperature profile, which has an average temperature of 701 °C in the 10 cm length platinum crucibles in the calorimeter. The oxide solution is prepared firstly by thoroughly mixing sodium molybdate dihydrate ($Na_2MoO_4{\cdot}2H_2O$) and molybdenum (IV) oxide with the amount so that the final molar ratio of Na_2O and MoO_3 is 3:4. Then the mixture is melted at 700 °C in air for 5 h. Furthermore, the mixture is cooled down in furnace and grounded into powder. Approximately 28 g of sodium molybdate powder ($3Na_2O{\cdot}4MoO_3$) is used in platinum crucibles for each side of twin calorimeter [78]. The chemicals are listed in Table 3.2 with purity and producers.

Table 3.2 Chemicals table of high temperature oxide melt drop calorimeter's measurements.

Raw material	**Chemical formula**	**Source**	**Initial mass fraction purity**
Sodium molybdate dihydrate	$Na_2MoO_4{\cdot}H_2O$	Merck KGaA	≥0.99
Molybdenum trioxide	MoO_3	Merck KGaA	≥0.99
Sapphire spheres	Al_2O_3	Alfa Aesar	0.9999
Argon	Ar	Air Liquide	0.99999[a]

[a] Purity expressed in mole fraction.

Moreover, before the high temperature drop solution measurements, both sides are calibrated using sapphire spheres of approximately 7 mg with diameter of 1.5 mm (seeing Table 3.2). The sapphire spheres are dropped from ambient temperature into the empty platinum crucibles at 701 °C [78]. Argon atmosphere is adopted as flush gas in all measurements to maintain a constant environment above the oxide solution. The enthalpy of drop solution of specimens are measured on both sides, which is described in Chapter 4.

3.2.4 Simultaneous thermal analysis (STA)

Generally speaking, Simultaneous Thermal Analysis (STA) denotes a combination of differential thermal analysis and thermogravimetric analysis. The heat fluxes and mass changes are measured simultaneously by STA calorimeter. Fig. 3.19 shows the internal schematic view of STA 449 F3 Jupiter (NETZSCH, Germany). The atmosphere in the oven can be controlled and defined for various measurements, as shown in Fig. 3.19 b). The protective gas can be introduced from yellow screw on the back side of STA, as shown in Fig. 3.19 a). The gas gets out from the top of STA, which is the green part in Fig. 3.19 a). Under the same temperature program, the temperature difference between the reference and sample is detected by thermal couples, which are located in the bottom of the crucibles, shown in Fig. 3.19 b). DTA signals are collected by the thermal couples. The heating elements are located around the crucibles. Twin-crucibles system is built ideally symmetric, and the thermal radiation from surrounding must be prevented by radiation shield, seeing Fig. 3.19 a) and b). Therefore, when an endothermic or exothermic reaction takes place, the signals of heat fluxes which are proportional to temperature differences, are plotted against time or temperature.

With help of thermogravimetric analysis, the mass changes of samples are measured by balance in the bottom of system seeing Fig. 3.19 b). There are always gases involved in the reactions, either gases releasing leading to a mass loss or a mass gain due to oxidation. At end, a mass change curve can be obtained versus time or temperature by collecting the TGA signals. In conclusion, STA calorimeter, combination of DTA and TGA, is a very effective and multi-functional method to investigate phase transitions and reactions, especially when gases are involved in reactions.

The specimens are heated from ambient temperature to 800 °C with heating rate 5 K/min, and cooled down at same rate. Ar gas with purity of 99.9999 % was adopted as protection gas, flowing rate 50 ml/min. The protective gas is introduced through the protective at bottom behind and goes in arrows direction out from gas outlet on the top of STA, as described before. In this work, a simultaneous TG-DTA apparatus was used to investigate thermal characters of the delithiated specimens. The produced gases in the reaction were collected and analyzed by a mass spectrometer (QMS 403C, NETZSCH Germany). Since the oxygen releasing from active materials of positive electrode is essential to trigger thermal runaway, the released oxygen was investigated by an extra sensor as oxygen detector (SGM 5T, Zitrox Sensoren und Elektronik GmbH Germany) beside mass spectroscopy.

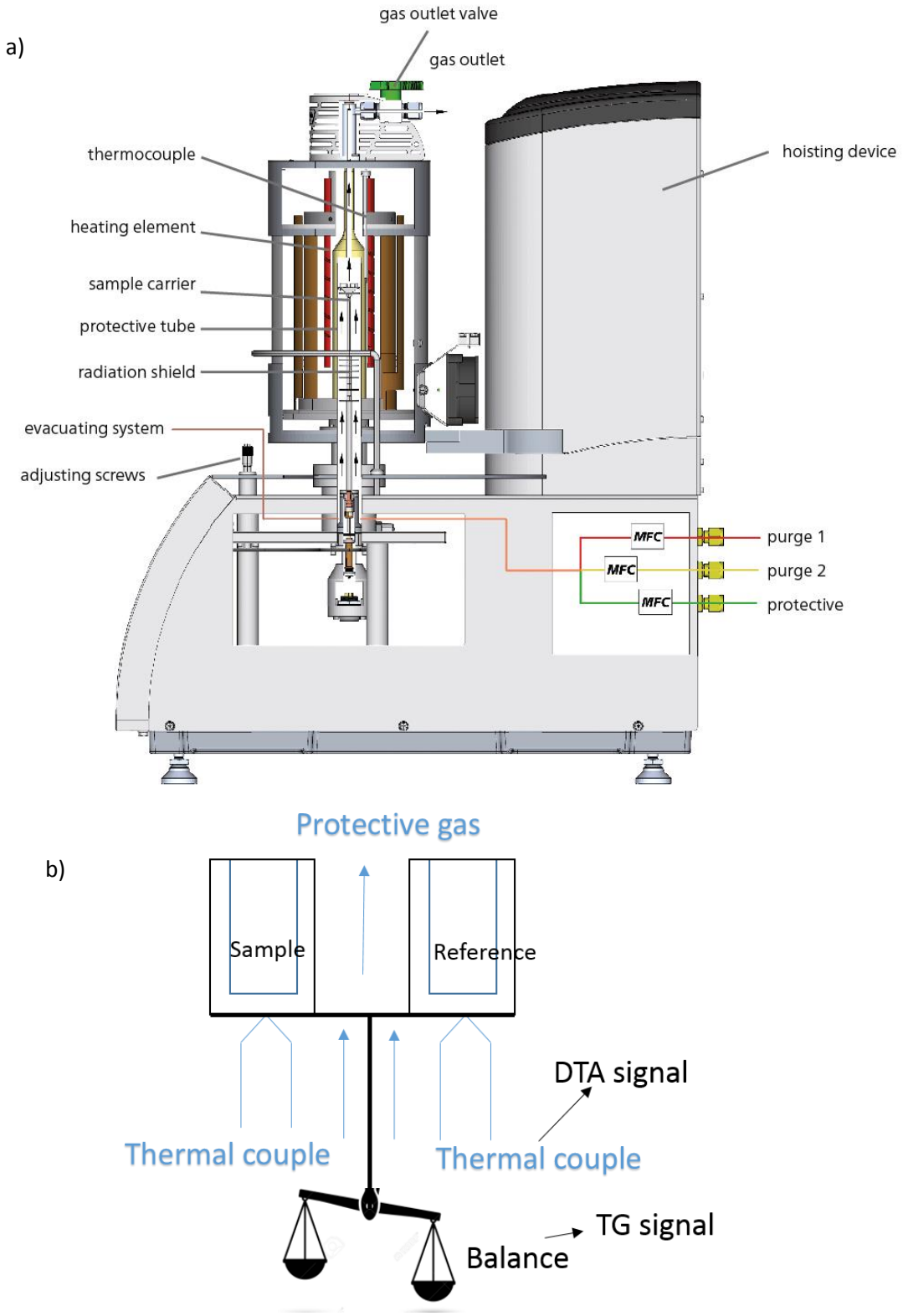

Fig. 3.19: Schematic views of simultaneous thermal analyzer STA-449 F3 Jupiter: (a) the internal sectional view, (b) combination of DTA and TGA simplified schematic diagram.

3.3 Evaluation of uncertainties

For a measurement, the objective is to determine the value of the measurands. In fact, the measurement result is only an approximation or estimation of the true value. Here the true value denotes the value with a quantity that is believed to satisfy fully the definition of the measurand [79]. In order to complete the measurement results, the uncertainty of the estimate must be given. The definition of uncertainty of measurement, according to literature [79], is "parameter, associated with the result of a measurement, that characterizes the dispersion of the values that could reasonably be attributed to the measurand". Uncertainty of measurement is the sum of many evaluations in aspects of i.e. the statistical distribution of the results of series of measurements or systematic effects. In order to evaluate the uncertainty, two types "A" and "B", both based on probability distribution were proposed by recommendation INC-1 (1980) of the Working Group on the Statement of Uncertainties [79]. Type A standard uncertainty is yielded from a probability density function derived from an observed frequency distribution. Type B standard uncertainty is evaluated by an assumed probability density function, which is based on the degree of belief that an event will occur [79]. Following text, these two methods to evaluate standard uncertainty as well as the methods adopted in this work for uncertainty determination of calorimetric studies (specific heat measurement) are introduced.

3.3.1 Type A evaluation of standard uncertainty

In a measurement to determine a quantity X, the estimates x_i from n independent observations are obtained under the same conditions. Thus, the arithmetic mean or average $\bar{x}_i$ is yielded by:

$$\overline{x}_i = \frac{1}{n}\sum_{i=1}^{n} x_i \tag{3.8}$$

The individual observation x_i varies due to random effects, and the probability distribution of *X* can be obtained via the experimental variance s^2 of the observation:

$$s^2 = \frac{1}{n-1}\sum_{i=1}^{n}(x_i - \overline{x})^2 \tag{3.9}$$

The best estimate of the variance is the mean value, hence, a Type A standard uncertainty $u(x_i)$ equals to the experimental standard deviation of the mean $s(\bar{x})$, which is given by:

$$s(\overline{x}) = \sqrt{\frac{s^2(x_i)}{n}} \tag{3.10}$$

Since the standard deviation has the same dimension as the quantity x, the standard

deviation serves as the standard uncertainty in practice rather than the more fundamental quantity $s^2(\overline{x})$. The more observations are done, the better estimate and lower uncertainty would be achieved. In this work, the measurement were performed normally for three times, thus, the Type B evaluation is more reliable based on a comparatively small number of statistically independent observation [79].

3.3.2 Type B evaluation of standard uncertainty

The non-statistical Type B evaluation, also known as systematic uncertainty, is evaluated by scientific judgment, based on all of available information except statistics. This includes information from past experience of the measurement, from the behavior and properties of relevant materials and instruments, from manufacturer's specifications, from calibration and other certificates, and from handbooks or other published information [79]. In Section 3.3.3, the evaluation method is introduced step by step with an evaluation of specific heat capacity measurement by means of a Tian-Calvet C80 calorimeter.

3.3.3 Combined uncertainty example: an uncertainty evaluation for a specific heat capacity measurement

The procedure to determine uncertainty of specific heat capacity results performed on a Tian-Calvet C80 calorimeter, consists of four steps:

1. Consider all relevant physical quantities and based on their relationship develop the function to calculate the specific heat capacity of the sample, commercial coin cells in this work. Since the measurement consists of the empty(0), calibration sample (Ref), and sample (S) measurements, capacity of sample's function is given by [63]:

$$\mathrm{C_{p,S}(T)} = \frac{\Phi_{\mathrm{S}}(\mathrm{T}) - \Phi_0(\mathrm{T})}{\Phi_{\mathrm{Ref}}(\mathrm{T}) - \Phi_0(\mathrm{T})} \cdot \frac{\mathrm{m_{Ref}}}{\mathrm{m_S}} \cdot \mathrm{C_{p,Ref}(T)} \qquad (3.11)$$

   Φ stands for heat flow rate, in equation heat flow rate of reference (Φ_{Ref}), empty (Φ_0) and sample (Φ_s). The main sources of uncertainty can be identified: masses of sample m_s and mass of calibration material m_{Ref}, heat flow rates of all three measurements, and the specific heat capacity of the calibration material c_{Ref}.
2. The uncertainty contributions $u(x_i)$ of the relevant physical quantities X_I must be identified, which are the uncertainty of analytical balance, the uncertainty of c_{Ref} from literature, and the uncertainties of heat flow rates measured by C80 calorimeter.
3. Calculation of the specific heat capacity of sample and the uncertainty propagation to determine the standard uncertainty $u_i(c_S)$ according to $u_i(c_S) = \frac{\partial c_S}{\partial X_I} \cdot u(x_i)$. For uncorrelated quantities X_I, the combined uncertainty is calculated by following equation [79]:

$$u(c_S) = \sqrt{\sum_{i=1}^{N} (\frac{\partial c_S}{\partial X_I} \cdot u(x_i))^2} \qquad (3.12)$$

4. After repetition of the measurement on other samples, the average value of specific heat capacity as well as the corresponding uncertainty should be calculated.

$$\left(\frac{u(c_{s,mean})}{C_{s,mean}}\right)^2 = \left(\frac{u(c_{s,1})}{c_{s,1}}\right)^2 + \left(\frac{u(c_{s,2})}{c_{s,2}}\right)^2 + \left(\frac{u(c_{s,3})}{c_{s,3}}\right)^2 \quad (3.13)$$

In order to enlarge the range of confidence of the uncertainty, an expanded uncertainty *U* is obtained by:

$$U = k \cdot u(c_{s,mean}) \quad (3.14)$$

where *k* is a coverage factor. Most commonly, the overall uncertainty by the coverage factor *k*=2 is used, which gives a level of confidence of 95 percent. For other measurements, the uncertainties are evaluated according to the same process.

4 Positive electrode material NMC synthesis and chemical delithiation

4.1 Literature review

As introduced in Section 2.2, Fig. 2.4, the composition x= 0.4, 0.5, 0.6, 0.7, 0.8 for $LiNi_xMn_{0.8-x}Co_{0.2}O_2$ are synthesized through sol-gel method in this work. There are different approaches to synthesize $LiNi_xMn_{0.8-x}Co_{0.2}O_2$. This literature review demonstrates sol-gel method, solid-state reaction and co-precipitation method, which is summarized in Table 4.1. Table 4.1 establishes composition, first discharge capacity, capacity retention, particle sizes of end products, synthesis approaches and raw materials.

The very first synthetic pathway was solid-state reaction. The raw materials (Table 4.1) were mixed and calcinated. Mixing step takes about 48 h. With this method, the stoichiometry and cation arrangement are extremely difficult to control, depending on temperature, residence time and oxygen partial pressure [80]. Later, "soft chemistry" methods were developed, which have the advantages of better stoichiometry control, end products with smaller particle size and particle size in narrow distribution. In Caurant et al.'s work [81], the synthesis of $LiNi_xCo_{1-x}O_2$ materials for positive electrode were performed by the classical powder mixing ceramic method and the soft chemistry route, which was based on hydroxides co-precipitation followed by heat treatment. Similar electrochemical properties were achieved via both methods, but soft chemistry method was improved by shortening the synthesis time. For the samples with increasing Ni content, heat treatment had to be in strong oxidizing atmospheres to maintain the oxidation states of Ni and lower temperatures to avoid the cation mixing. Higher temperature will intensify the exchange of Li ions on 3a sites and Ni cations on 3b sites. Moreover, at higher temperature (≥800 °C) the substantial micro-strain was formed due to anisotropic volume variation in positive materials $LiNi_{0.76}Mn_{0.14}Co_{0.10}O_2$ [82]. Sol-gel process is another generally adopted method to prepare NMC active materials of positive electrode [83-87]. The particle's diameters of $LiNi_{1/3}Mn_{1/3}Co_{1/3}O_2$ (NMC111) were between 300 nm to 400 nm, smaller than the particles prepared by co-precipitation method, which were 1 µm - 2 µm [83] (seeing the data in Table 4.1). NMC111 with smaller particle sizes demonstrated a higher discharge capacity but poorer capacity retention [83]. The smaller particle sizes result in higher surface area, which leads to shorter diffusion length but increasing side reactions. The calcination process and heat-treatment temperature were found to affect the crystal structure and particle formation. NMC111 active material of positive electrode were prepared via sol-gel method followed by pre-calcination at 700 °C, 800 °C, 900 °C and 1000 °C, respectively for 24 h and subsequent heat-treatments at 1100 °C [88]. In their research, the crystallization of NMC111 was developed better at higher temperatures, but the particle distribution was in a wide range. At lower temperature calcination, the opposite phenomenon was found: not-well crystallized but homogeneous distribution. The comparisons of NMCs' prepared by different methods were summarized in aspects of capacity retention and first discharge capacity and particle's size in Table 4.1. The sol-gel made NMC111 positive electrode material in Ref. [85] shows the highest specific discharge capacity of 200.67 mAh/g and a high coulombic efficiency

of 93 %. Another sol-gel made in Ref. [84] had a comparably high specific capacity of 198 mAh/g and a low capacity retention of 58 % after 10 cycles due to the partial reduction reactions and Jahn-Teller distortion of Mn. The NMC622 active materials of positive electrode prepared by solid state reaction show a relatively low specific capacity of 142 mAh/g [89], while the sol-gel made and co-precipitation samples had a higher capacity of 158 mAh/g and 168 mAh/g, respectively [83].

Sol-gel method is a low cost, easy preparation method to obtain homogeneous and spherical as well as faceted growth of well-defined shapes particles [83-84]. Therefore, sol-gel process is utilized to prepare NMC with various transition metals (TM) composition, and the sintering temperature is optimized for varying the stoichiometric proportions.

In this work, as in Fig. 2.4 established, $LiNi_xMn_{0.8-x}Co_{0.2}O_2$ active materials of positive electrode were synthesized, where x varies from 0.4, 0.5, 0.6, 0.7 to 0.8. SEM, XRD and ICP-OES were used to analyze the samples' morphology, crystalline structure and composition. The electrochemical properties of sol-gel made and commercial NMC442 powders were investigated by half cells.

Table 4.1 Characteristics of NMC prepared by different synthetic pathways.

Composition of end product	synthetic pathway	Raw materials Transition metal (TM) and Li source	Particle's diameter	Voltage window V	1st discharge capacity (mAh/g)	capacity retention (%) at cycl. No.
$Li_{1.05}Ni_{1/3}Mn_{1/3}Co_{1/3}O_2$	Sol-gel	$Mn(CH_3COO)_2{\cdot}4H_2O$, $Ni(CH_3COO)_2{\cdot}4H_2O$, $Co(CH_3COO)_2{\cdot}4H_2O$, $Li(CH_3COO)_2{\cdot}2H_2O$	300-400 nm	2.5-4.3	168	87 (50 cycl.) [83]
$Li_{1.05}Ni_{1/3}Mn_{1/3}Co_{1/3}O_2$	Co-precipitation	$Mn(CH_3COO)_2{\cdot}4H_2O$, $Ni(CH_3COO)_2{\cdot}4H_2O$, $Co(CH_3COO)_2{\cdot}4H_2O$, $LiOH/NH_4OH$	1-2 µm	2.5-4.3	158	95 (50 cycl.) [83]
$0.4LiNi_{0.375}Mn_{0.375}Co_{0.25}O_2$-$0.6Li(Li_{1/3}Mn_{2/3})O_2$	Sol-gel	$Mn(CH_3COO)_2{\cdot}4H_2O$, $Ni(NO_3)_2{\cdot}6H_2O$, $Co(NO_3)_2{\cdot}6H_2O$, $Li(CH_3COO)_2{\cdot}2H_2O$	-	2.0-4.8	198	58 (10 cycl.) [84]
$LiNi_{1/3}Mn_{1/3}Co_{1/3}O_2$	Sol-gel	$Mn(CH_3COO)_2{\cdot}4H_2O$, $Ni(CH_3COO)_2{\cdot}4H_2O$, $Co(NO_3)_2{\cdot}4H_2O$, $Li(CH_3COO)_2{\cdot}H_2O$	200 nm	2.5-4.6	200.67	92 (8 cycl.) [85]
$LiNi_{1/3}Mn_{1/3}Co_{1/3}O_2$	Sol-gel	$Mn(CH_3COO)_2{\cdot}4H_2O$, $Ni(CH_3COO)_2{\cdot}6H_2O$, $Co(CH_3COO)_2{\cdot}6H_2O$, CH_3COOLi	100-200 nm	2.5-4.6	129.3	86 (200 cycl.) [86]
$LiNi_{1/3}Mn_{1/3}Co_{1/3}O_2$	Sol-gel	$Mn(CH_3COO)_2{\cdot}4H_2O$, $Ni(CH_3COO)_2{\cdot}4H_2O$, $Co(CH_3COO)_2{\cdot}4H_2O$, $Li(CH_3COO)_2{\cdot}2H_2O$	300-500 µm	3-4.2	149	97 (10 cycl.) [87]
$Li_{1.2}Ni_{0.6}Mn_{0.2}Co_{0.2}O_{2+\delta}$	Solid-state reaction	MnO_2, NiO, Co_3O_4, Li_2CO_3	-	3-4.4	170	97 (40 cycl.) [89]

As described in Section 2.2, the delithiation process takes place on the positive electrode during charging.
In this process, lithium cations are extracted from 3a positions (in space group $R\bar{3}m$) and the other atoms maintain their positions. In two dimensions, the lithium cations hop between octahedral sites through an intermediate tetrahedral site. The activated tetrahedral sites share the face formed by oxygen ions with the adjacent transition metal octahedron [90], as schematically shown in Fig. 4.1.

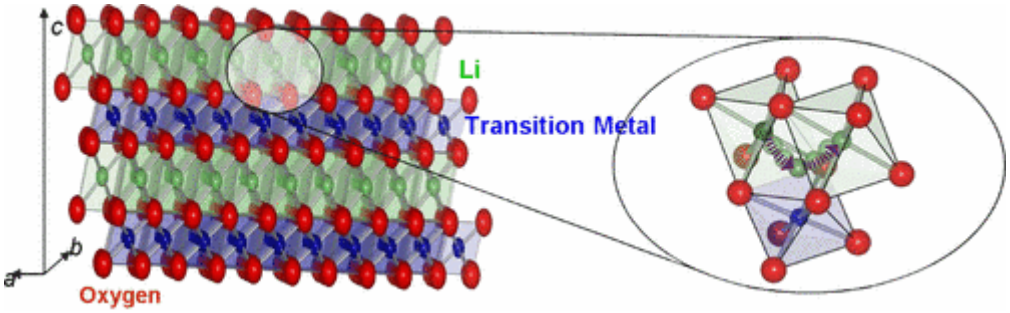

Fig. 4.1: Schematic diagram of Li^+ movement's path in electrochemical delithiation process [90].

Vice versa, during discharging, lithiation process occurs on the positive electrode. The state of charge (SOC), which indicates the degree of delithiation on the positive electrode, represents the percentage of the stored energy in the battery. The thermal stability of LiBs is significantly affected by SOCs [91-92]. Moreover, the oxygen produced from phase transition of delithiated active materials in positive electrode plays an important role in thermal runaway events. In the year of 1994, Dahn et al. proposed a typical reaction of delithiated layered Li_xCoO_2 (x<1) [32] at high temperatures:

$$Li_xCoO_2 \rightarrow \frac{1-x}{3}Co_3O_4 + xLiCoO_2 + \frac{1-x}{3}O_2 \tag{4.1}$$

This reaction was optimized with more detailed investigations by Sharifi-Asl et al. [93]. They proposed that the decomposition of delithiated layered Li_xCoO_2 is expressed by the following reactions:

$$\begin{aligned} Li_xCoO_2(\text{layered}) &\xrightarrow{\geq 100^\circ C} aLi_xCoO_2(\text{layered}) + (1-a)Li_xCo_{3-x}O_4(\text{spinel}) + \varepsilon O_2 \\ &\xrightarrow{\geq 250^\circ C} bLi_xCoO_2(\text{layered}) + cLi_xCo_{3-x}O_4(\text{spinel}) \\ &\quad + (1-b-c)Li_xCo_{1-x}O\ (\text{rock}-\text{salt}) + \delta O_2 \end{aligned} \tag{4.2}$$

The parameters a, b, c in equation 4.2, indicate phase formation taking place partially. The phases can be co-existing. Values of ε and δ are affected by the surface fraction and the morphology [93].
Bak et al. [94] utilized the synchrotron X-ray diffraction and mass spectroscopy to scrutinize the phase transitions of charged NMC positive electrode with a series of compositions, as demonstrated in Fig. 4.2. When heating up to 600 °C, the phase transition took place accompanied by oxygen release. As Fig. 4.2 shows, onset temperature and the amount of oxygen production were impacted by the nickel content considerably, and higher Ni content in NMC active materials show worse thermal stability with lower onset temperature of phase transition and larger amount of O_2 released. The NMC532 composition positive electrode material might be the optimized composition in terms of thermal stability and electric capacity.

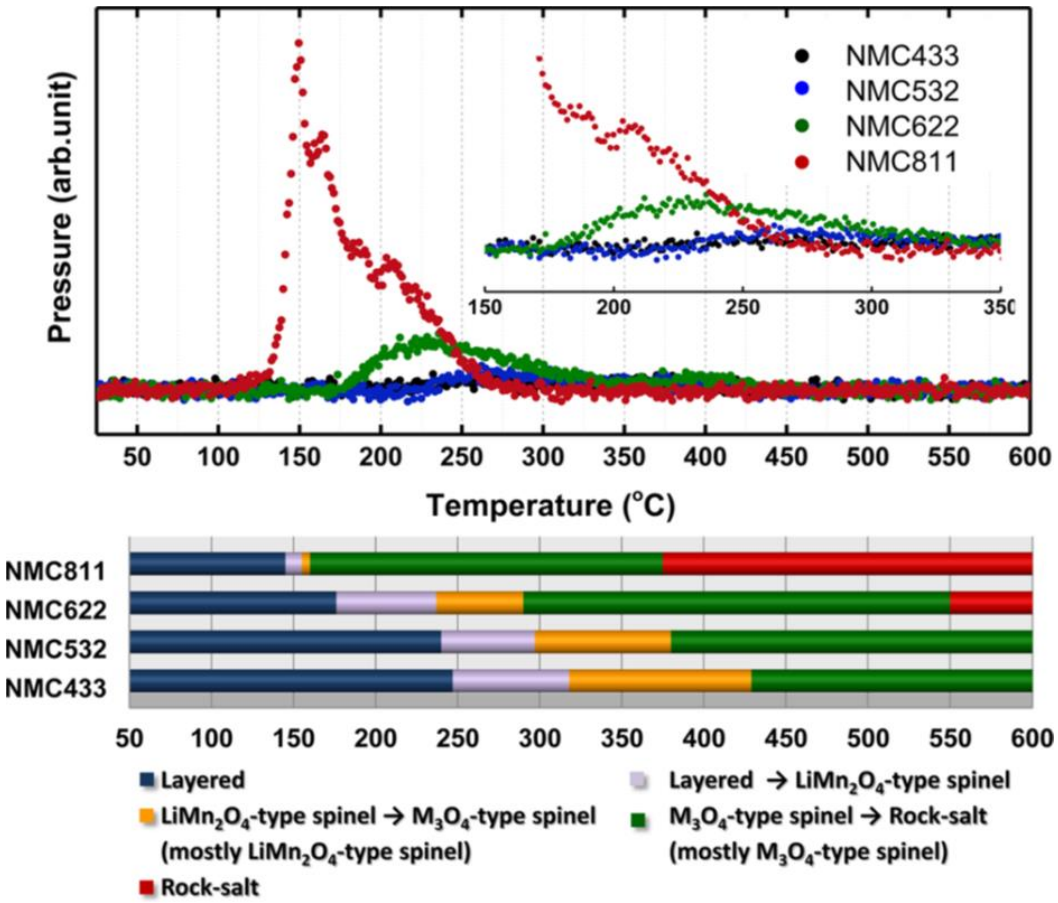

Fig. 4.2: Above: during measurement, the pressure of oxygen was measured and analyzed by mass spectroscopy; below: the phase transition temperatures were defined by in situ time-resolved X-ray diffraction (TR-XRD) measurements [94].

Delithiation methods

Beside electrochemical delithiation, chemical delithiation is another method to extract Li from active materials in positive electrode. After electrochemical delithiation, the dissembled positive electrode is mixed with carbon black and binder, which cannot be separated or washed from active material, e.g. NMC. In this work, the electrochemical delithiated positive electrode is unfortunately not ideal for further investigations, such as STA and DSC. Thus, we attempted to obtain the delithiated positive electrode active material (NMC442) via chemical delithiation. Besides pure delithiated active material can be obtained, another benefit of chemical delithiation is that larger amount of delithiated specimens can be achieved by chemical delithiation than electrochemical delithiation. The delithiated specimens would be investigated by using simultaneous TG-DTA apparatus (STA) and high temperature oxide melt drop solution calorimeter (Alexsys-1000), respectively.

In general, there are two approaches to preparing delithiated specimens via chemical methods: one utilizes acids via ion exchange reactions and the other utilizes redox reagents via redox reactions. In the former approach, undesired hydrogen ions could be introduced into the specimens. In the latter method, a number of candidates could serve as oxidizing reagent, both organic and inorganic reagents [95-97]. In the present work, $(NH_4)_2S_2O_8$ was adopted as oxidizing reagent [95]. Initially, the chemical delithiation on NMC is assumed to be similar to LCO, in which only Li was extracted. But for NMC samples in this work, the transition metals in NMC samples were dissolved in oxidizing reagent meanwhile. The redox reaction of chemical delithiation on LCO is supposed to be as follows [97]:

$$2\mathrm{LiCoO_2} + (1-x)(\mathrm{NH_4})_2\mathrm{S_2O_8} \rightarrow 2\mathrm{Li}_x\mathrm{CoO_2} + (1-x)(\mathrm{NH_4})_2\mathrm{SO_4} + (1-x)\mathrm{Li_2SO_4} \quad (4.3)$$

4.2 Synthesis of $LiNi_xMn_{0.8-x}Co_{0.2}O_2$

4.2.1 Synthesis of $LiNi_xMn_{0.8-x}Co_{0.2}O_2$ (x=0.4, 0.5, 0.6, 0.7, 0.8)

$LiNi_xMn_{0.8-x}Co_{0.2}O_2$ series samples were synthesized via sol-gel process in following manner. Firstly, stoichiometric amounts of lithium acetate di-hydrate, nickel acetate tetrahydrate, manganese acetate tetrahydrate and cobalt acetate tetrahydrate, adipic acid powders were dissolved in distilled water. Since adipic acid powder was relatively difficult to dissolve, deionized water had to be heated to 40 °C in advance. As Li tends to be lost significantly during synthesis [98], the amount of raw material was designed to be 3 at.% extra Li to compensate the loss. After proper mixing the solution, the pH value was adjusted to 7.0 with ammonium hydroxide. The solution was stirred and heated to 80 °C until gel formation. Gel was dried in vacuum condition at 120 °C for 12 h. Afterwards, the sample was grounded and pre-calcined at 450 °C, heating from room temperature at 2 K/min. The residential time was 3 hours, samples cooling in furnace. Before and after calcination the powder was grinded. The sintering process was performed at 800 °C to 900 °C for 12 h in air, and then the samples were quenched to ambient temperature. The origin and purity of the chemicals are listed in following Table 4.2.

Table 4.2 Chemicals of NMC synthesis via sol-gel method in this work.

Raw material	Chemical formula	Source	Initial mass fraction purity
Lithium acetate di-hydrate	$Li(CH_3COO)_2{\cdot}2H_2O$	Alfa Aesar	≥0.999
Manganese (II) acetate tetrahydrate	$Mn(CH_3COO)_2{\cdot}4H_2O$	Merck KGaA	≥0.99
Nickel acetate tetrahydrate	$Ni(CH_3COO)_2{\cdot}4H_2O$	Sigma-Aldrich	≥0.99
Cobalt acetate tetrahydrate	$Co(CH_3COO)_2{\cdot}4H_2O$	Merck KGaA	≥0.99
Adipic acid	$C_6H_{10}O_4$	Merck Schuchardt OHG	≥0.99

ICP-OES, SEM and XRD measurements

The electrochemical characterization of sol-gel made and commercial NMC442 powders were examined in a CR2032 type coin cell with Li metal negative electrode. The positive electrode and a lithium metal negative electrode (99.9 %, Sigma Aldrich, Germany) separated by glass separator (GF/A filtration, diameter: 15 mm, thickness: 260 µm, Whatman, Great Britain) were assembled in glovebox (MBraun, Germany, O_2 < 0.1 ppm, H_2O < 0.1 ppm). The electrolyte was 1 M $LiPF_6$ in 1:1 (by weight) ethylene carbonate (EC)/ dimethyl carbonate (DMC) (LP30, BASF, Germany). The slurry of sol-gel made positive electrode consisted of mass ratio 70 % NMC442 powders, 20 % carbon black and 10 % polyvinylidene fluoride (PVDF) on aluminum foil. While, mass ratio of active material versus carbon black versus PVDF was 85:7.5:7.5 for the commercial NMC442 powders. In comparison with commercial coin cells, the mass ratio of sol-gel made NMC materials is lower because of the no coating or doping applied in sol-gel sample and to achieve functional coin cells more conductive agent and binder were needed. The

powders were dissolved in the solution of N-methyl-pyrrolidinone (NMP). The mixture was stirred overnight. With help of a coating machine (Coatmaster 509 MC, Erichsen, Germany), the slurry was homogeneously coated on Al foil. Firstly, the vacuum pump of coating machine was turned on so that Al foil fixed on the platform. Then the slurry was placed in the middle of it. After adjusting the coater with thickness of 150 µm, the coating was done by pushing the coater forward on the Al foil. The electrode sheet was dried in vacuum oven at 120 °C for 24 h. The positive electrode sheet was cut into round form with diameter of 13 mm. One piece of lithium metal with diameter of 13 mm was punched on a steel disc. After placing separator on negative electrode, 45 µL electrolyte was added by a pipette. The cells were cycled with a current of 34 µA in voltage window of 3 V - 4.3 V using an Arbin battery testing system.

Influence of sintering temperature on NMC synthesis

As mentioned before, after pre-calcination of the samples at 450 °C, all compositions were calcinated at 800 °C. SEM images show in Fig. 4.3, with increasing Ni content, the samples were better crystallized and the particles grew larger. This phenomenon is also confirmed by the observation in XRD measurements (Fig. 4.4).

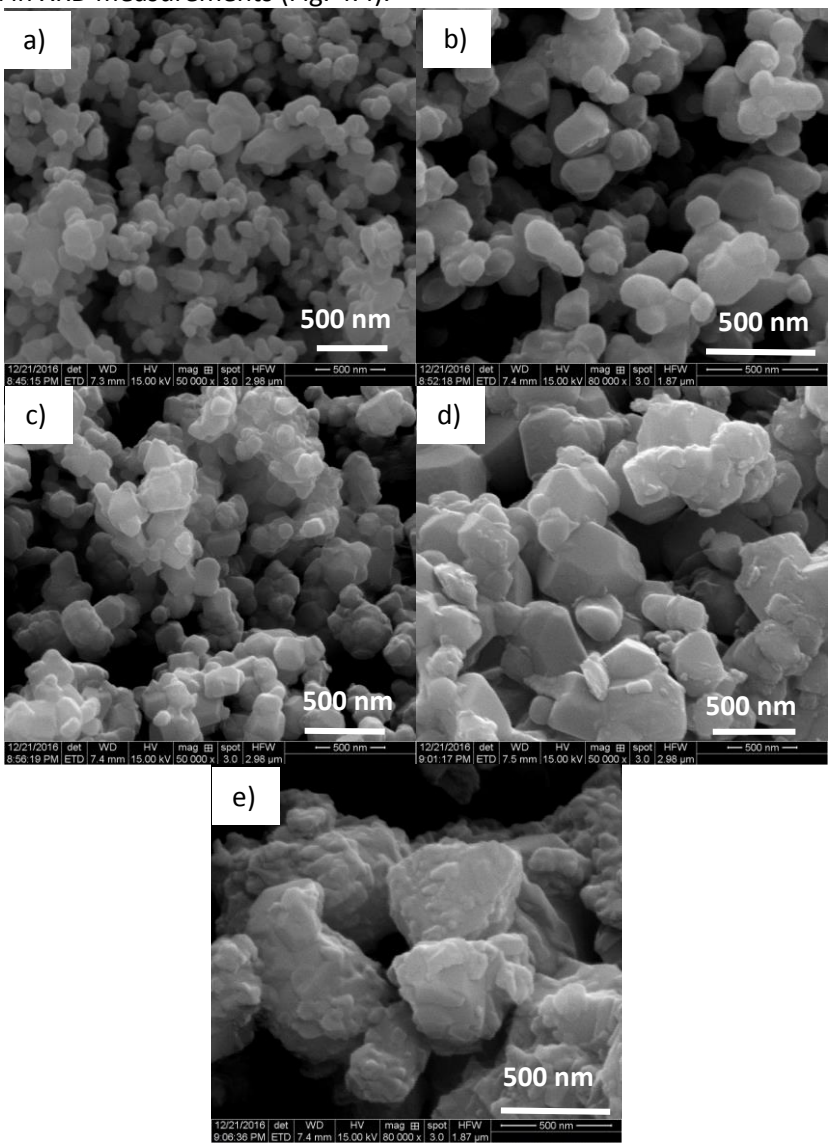

Fig. 4.3: SEM images of specimens sintering at 800 °C: a) NMC442 b) NMC532 c) NMC622 d) NMC712 e) NMC802.

In Fig. 4.4, the black curve for NMC442 material shows an unfully developed structure, (018) and (110) reflexions merging to one. So do the red pattern of NMC532 sample and the blue pattern of NMC622 sample. The pink pattern of NMC712 sample and green pattern of NMC802 sample show well developed $R\bar{3}m$ layered structures. The high intensity and sharp reflexions in XRD pattern of NMC802 sample imply that calcination temperature 800 °C is very suitable for NMC802 materials. The calcination temperatures have to be optimized especially with low Ni content. For nickel-rich samples, the temperature is lower to prevent lithium deficiency and cation mixing [82].

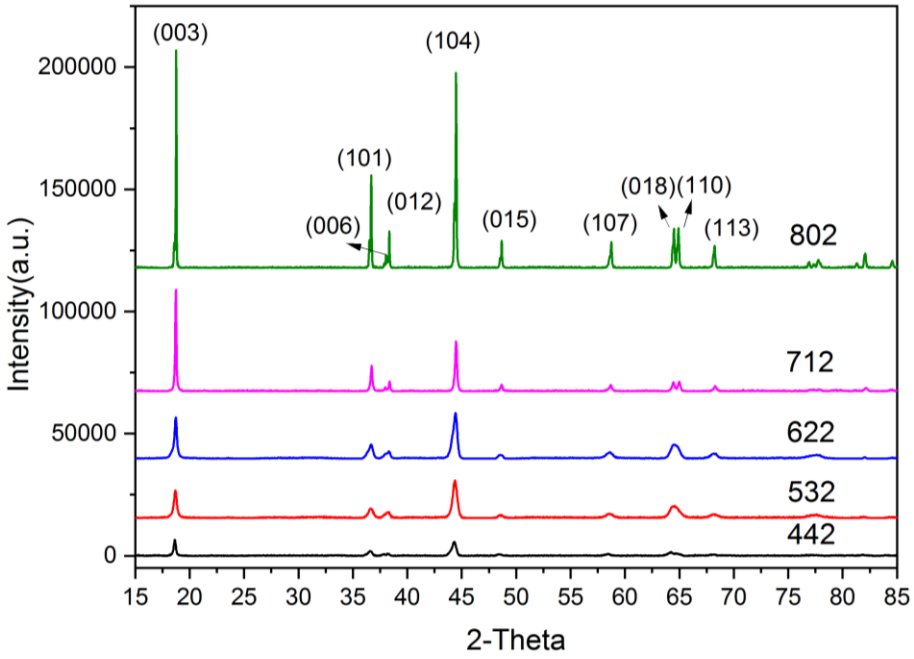

Fig. 4.4: XRD patterns of NMC specimens calcination at 800 °C with increasing Ni content NMC442 to NMC802.

Since the crystallization degree decreases with lower Ni content in NMC materials for calcination at 800 °C, the calcination temperatures are raised for lower Ni content NMC materials. The selected calcination temperatures are 900 °C for NMC442 sample, 875 °C for NMC532 sample, 850 °C for NMC622 sample, 825 °C for NMC712 sample and 800 °C for NMC802 sample, respectively. Similar synthesis processes are performed for all compositions. The XRD results in Fig. 4.5 establish obvious improvements in aspect of crystallization for all samples. The reflections (006)/(012) and (018)/(110) are splitting clearly for all compositions NMC442, NMC532, NMC622 and NMC712, which suggests a better crystallized structure. The reflexions of all optimized samples have higher intensity and sharp form, which also implies that calcination step is improved. When the ratio of the reflection (003)/(104) is lower than 1.2, it indicates the undesirable Li (3a site)-Ni (3c site) cation mixing. That indicates a high structural deviation from hexagonal towards cubic symmetry [99]. For NMC442 sample, NMC532 sample and NMC622 sample, the ratio of the reflection (003)/(104) enhances, which indicates a better layered ordering with less inter-layer mixing. NMC712 material presents more inter-layer mixing at 825 °C than at 800 °C. Ni occupying Li position might be due to Li loss, which is found by ICP-OES in Fig. 4.7 b).

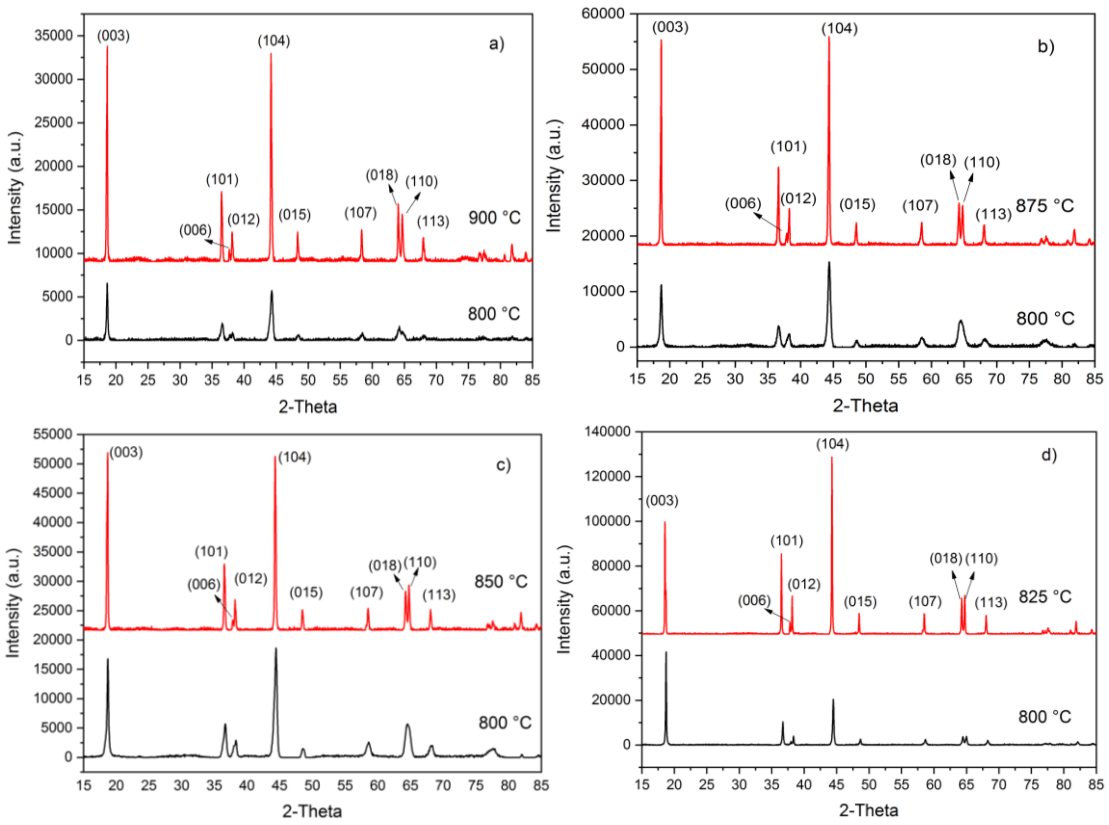

Fig. 4.5: XRD patterns of specimens after calcination at 800 °C and optimized calcination a) NMC442 samples at 900 °C and 800 °C, b) NMC532 samples at 875 °C and 800 °C, c) NMC622 samples at 850 °C and 800 °C, d) NMC712 samples at 825 °C and 800 °C.

Rietveld refinement was carried out to analyze the XRD patterns in Fig. 4.5, and the lattice parameters are listed in Table 4.3 and visualized in Fig. 4.6. The lattice parameter *c* decreases significantly with the decline of Mn content and the rise of Ni content. As Fig. 2.3 shows, TM layers and O layers are alternatively placed in the NMC's structure, and lattice parameter *c* is determined by layer distance. As Mn^{4+} content declining, Ni ions must have higher oxidation state 3+ to maintain the electroneutrality. Increasing amount of Ni^{3+} ions from NMC442 to NMC802, results in the decrease of TM/O layers' distance (decline of lattice parameter *c*) due to a smaller diameter of Ni^{3+} ions (0.56 Å) than Ni^{2+} ion (0.69 Å). The lattice parameters *a* of all compositions are similar and after optimization there is no big change.

Table 4.3 Lattice parameters of sol-gel made NMC materials with various compositions.

Lattice parameter	*a* (Å)	*b* (Å)	*c* (Å)	Unit volume (Å^3)
NMC442 800 °C	2.8777(0)	14.2672(3)	0.2017(0)	102.32199(8)
NMC442 900 °C	2.8774(3)	14.2762(3)	0.2015(5)	102.3654(3)
NMC532 800 °C	2.8761(7)	14.2482(5)	0.2018(6)	102.0754(6)
NMC532 875 °C	2.8774(4)	14.2539(1)	0.2018(7)	102.2058(9)
NMC622 800 °C	2.8743(0)	14.2108(0)	0.2022(6)	101.6745(3)
NMC622 850 °C	2.8767(8)	14.2371(4)	0.2020(6)	102.0392(0)
NMC712 800 °C	2.8741(8)	14.1870(3)	0.2025(9)	101.4959(8)
NMC712 825 °C	2.8764(8)	14.2243(5)	0.2022(2)	101.9259(4)
NMC802 800 °C	2.8690(1)	14.1782(1)	0.2023(5)	101.0685(9)

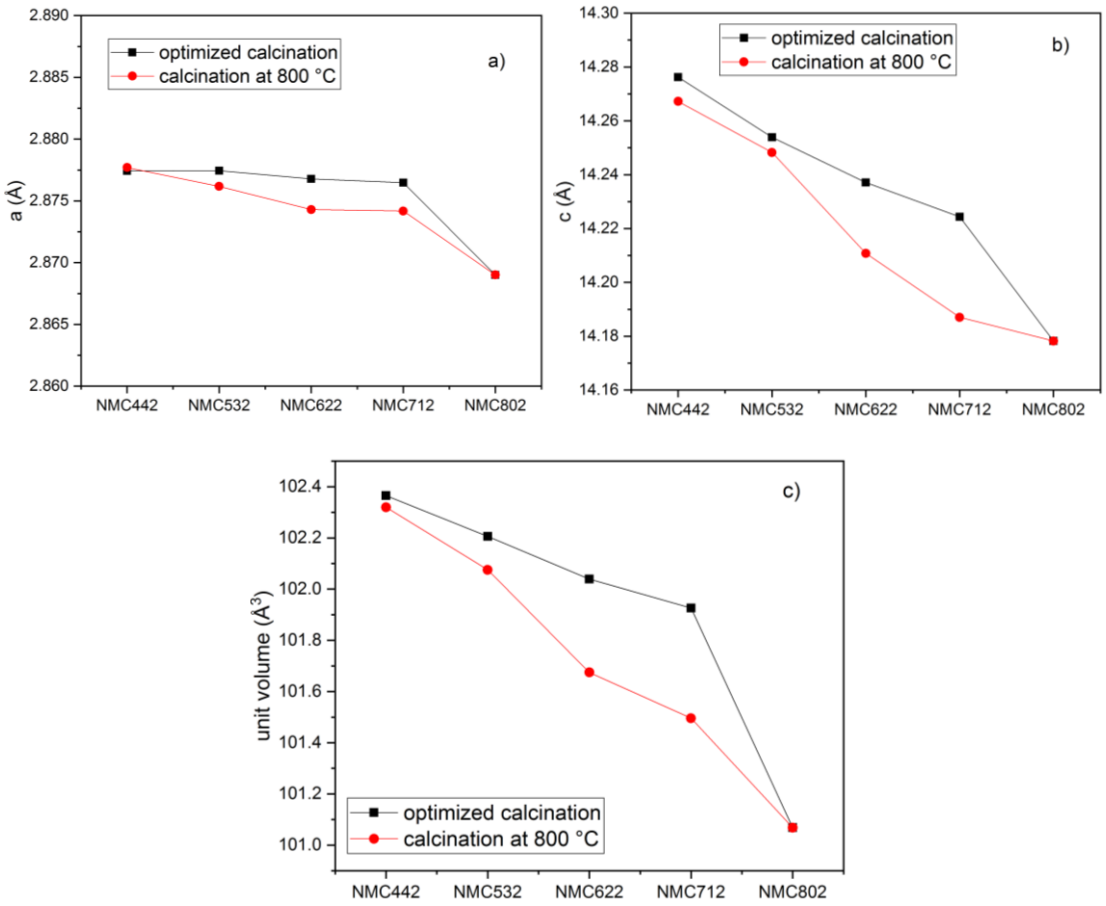

Fig. 4.6: Rietveld refinement results of specimens after calcination at 800 °C and optimized calcination a) lattice parameter *a*, b) lattice parameter *c*, c) crystal unit volume.

Fig. 4.7 a) shows the composition of samples after pre-calcination at 450 °C. The ICP-OES results reveal that the composition of samples after pre-calcination maintain the stoichiometric proportion well. Fig. 4.7 b), c), d) and e) establish the ICP-OES results, which are listed in Table 4.4. Table 4.4 lists Li content and transition metals' (TM) contents in the samples. The Li content is calculated with assumption of composition of TM=1 in the samples. In Fig. 4.7 a) and Table 4.4 shown, Li content after calcination decreases especially in Ni-rich samples, because Li is prone to form Li_2CO_3 and LiOH on particle's surface. Lithium deficiency is found to be more severely with nickel content, which can be improved by increasing the oxygen flow in the oven [81]. The Ni/Mn/Co contents in Fig. 4.7 c), d) and e) and Table 4.4 are in good agreement with the initial composition. In conclusion, the optimization on calcination temperature improves the crystalline growth of NMC442 samples, NMC532 samples and NMC622 and NMC712 samples. However, NMC712 samples represent more Li loss when calcination at 825 °C than at 800 °C, which may need more excess of Li.

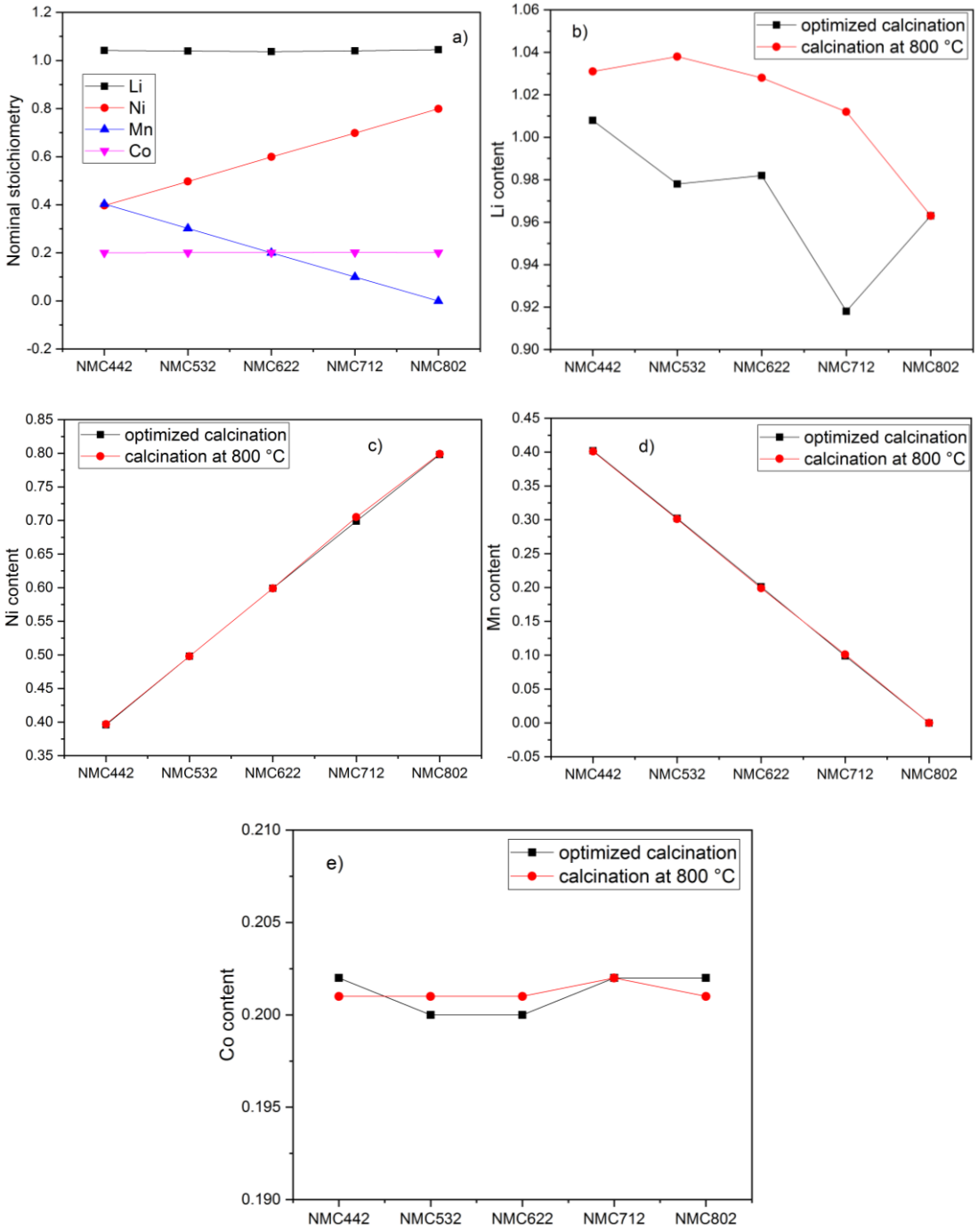

Fig. 4.7: Li and TM contents measured by ICP-OES of specimens: a) Nominal stoichiometry of samples after pre-calcination at 450 °C. Samples of various compositions after calcination at 800 °C and optimized calcination: b) Li contents, c) Ni contents, d) Mn contents, e) Co contents.

Table 4.4 Nominal stoichiometry of NMC materials with various compositions.

Nominal stoichiometry (sum TM=1)	Li content	Ni content	Mn content	Co content
NMC442 800 °C	1.03	0.40	0.40	0.20
NMC442 900 °C	1.00	0.40	0.40	0.20
NMC532 800 °C	1.04	0.50	0.30	0.20
NMC532 875 °C	0.98	0.50	0.30	0.20
NMC622 800 °C	1.03	0.60	0.20	0.20
NMC622 850 °C	0.98	0.60	0.20	0.20
NMC712 800 °C	1.01	0.70	0.10	0.20
NMC712 825 °C	0.92	0.70	0.10	0.20
NMC802 800 °C	0.96	0.80	0	0.20

4.2.2 Comparison with commercial $LiNi_{0.4}Mn_{0.4}Co_{0.2}O_2$ (NMC442)

In regard of composition, crystal structure and electrochemical performance, the sol-gel made NMC442 powders are compared with commercial NMC442 (MTI, USA) material.

Composition and crystal structure

In Fig. 4.8, XRD patterns of both commercial and sol-gel made NMC442 samples demonstrate a well-developed α-$NaFeO_2$ type structure with the space group $R\bar{3}m$. The ratio of reflection (003)/(104) of commercial sample is higher than sol-gel made sample, indicating less cation mixing of Li and Ni [99-100]. The lattice parameters are obtained by Rietveld refinement, listed in Table 4.5, which are considerably similar. The chemical analysis results were used to calculate molar ratio in solid specimens. Li content is shown as a ratio of Li atoms/ the sum of TM atoms. The Ni, Mn, Co molar ratios are also calculated and listed in Table 4.5. 11 at.% exceeding Li is found in commercial sample, while only 2 at.% exceeding Li in sol-gel made samples. Co content of commercial NMC442 sample, however, is slightly lower than sol-gel made materials.

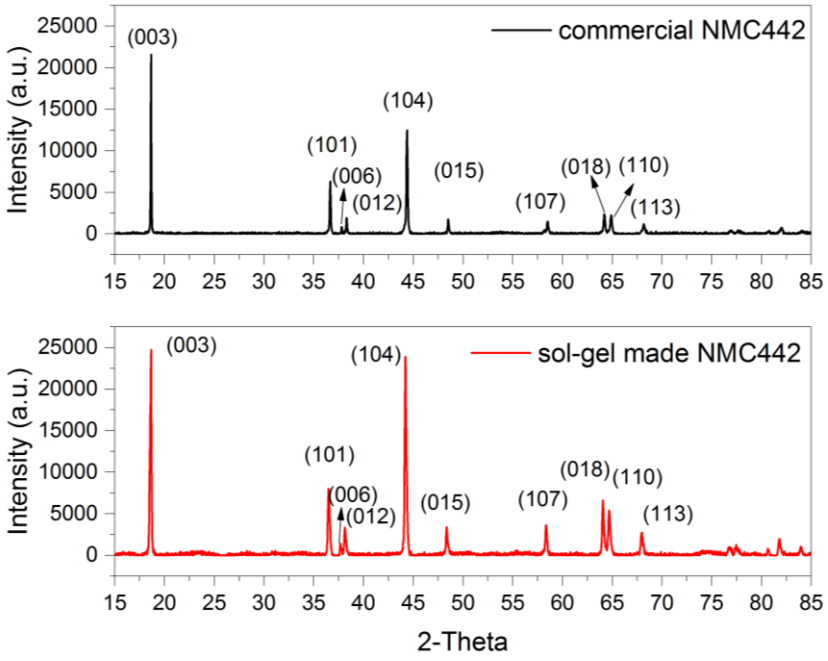

Fig. 4.8: XRD pattern of commercial NMC442 and sol-gel made NMC442.

Table 4.5 The lattice parameters and analytical compositions of commercial and sol-gel made NMC442 active materials of positive electrode.

Lattice parameter	**Commercial NMC442**	**Sol-gel made NMC442**
a (Å)	2.8701(1)	2.8774(3)
c (Å)	14.2495(7)	14.2762(3)
volume (Å^3)	101.6553(0)	102.3654(3)
Chemical analysis results		
Li wt.%	7.68±0.27	7.24±0.25
Ni wt.%	24.4±0.6	23.8±0.6
Mn wt.%	22.5±0.6	22.6±0.6
Co wt.%	10.1±0.3	12.1±0.3
Molar ratio in solid specimens		
Li/sum TM	1.11	1.02
Ni/sum TM	0.42	0.40
Mn/sum TM	0.41	0.40
Co/sum TM	0.17	0.20

Electrochemical performance

As described before, CR2023 coin cells were built to test the electrochemical performance of both NMC442 positive electrode materials. 3 cells for each sample were cycled between 3.0 V - 4.3 V at 36 µA (0.05 C) for 5 cycles. The average specific discharge capacities are 161 mAh/g and 154 mAh/g for commercial and sol-gel made NMC442, materials, respectively (Fig. 4.9), the commercial cells show larger capacities. In Fig. 4.9 a), voltages of coin cells are plotted against specific capacity for charging and discharging. The sol-gel cell has lower specific capacity in both charge and discharge processes. The black curves represent charging and discharging curves of commercial NMC442 positive electrode materials, and red curves for sol-gel made materials. The comparison of 3 coin cells is shown in Fig. 4.9 b). All commercial cells (black points) show slightly higher capacity than sol-gel made cells (red points).

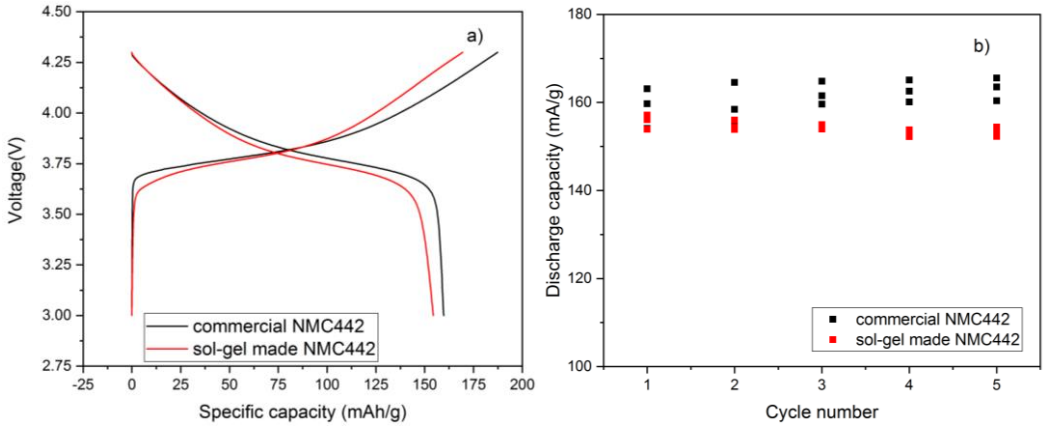

Fig. 4.9: Electrochemical tests on commercial and sol-gel made NMC442: a) Typical charge-discharge characteristics of commercial and sol-gel made NMC442, b) Cycle performance of commercial and sol-gel made NMC442 at 0.05 C.

The three coin cells with commercial NMC442 positive electrode materials were continuously cycled at various C-rates (0.05 C, 0.1 C, 0.2 C, 0.5 C and 1 C), and the cycle retentions are shown in Fig. 4.10. Cell 1 (black points) and cell 3 (red points) failed at 51 st and 38 th cycling respectively, and the coulombic efficiency of the last cycle was 83.7 % which dropped from 98.5 %, the coulombic efficiency of one cycle before. Comparing the specific discharge capacity

in last cycling with first cycling, the retention were 82 %, 96 % and 91 % for cell 1, cell 2 (blue points) and cell 3 respectively.

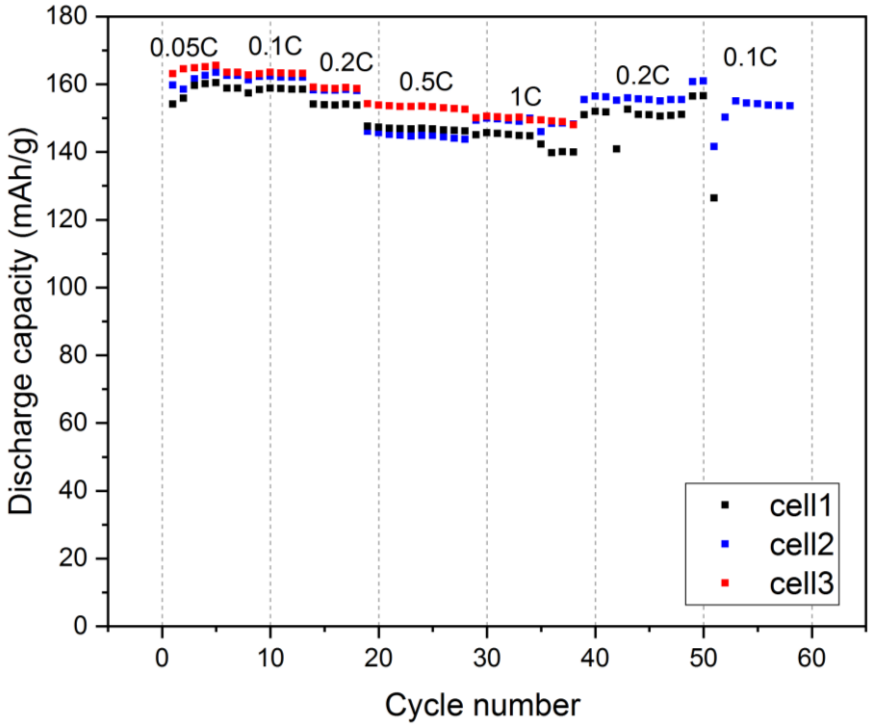

Fig. 4.10: Cycle retention of coin cells with commercial NMC442 positive electrode material at various C-rates.

As chemical delithiation on NMC samples demands a large amount of powder in order to produce adequate delithiated samples to investigate the thermal properties etc., the commercial NMC442 materials were used in the following experiments.

4.3 Chemical delithiation of NMC442 positive electrode materials

In order to investigate the thermal stabilities of delithiated $LiNi_{0.4}Mn_{0.4}Co_{0.2}O_2$, chemical delithiation was performed on sol-gel made and commercial NMC442 powders. The compositions of delithiated samples were determined by ICP-OES, and the crystal structure was investigated by XRD. Based on these results, some samples were selected, whose composition doesn't deviate from atomic ratio Ni: Mn: Co of 4:4:2 (nominal deviation ≤ 2 at.%) and the crystal structure maintains α-$NaFeO_2$ type structure. The formation enthalpy and phase transition of selected samples were measured by Alexsys 1000 and Simultaneous Thermal Analysis (STA), respectively.

4.3.1 Chemical delithiation process and characterization

Chemical delithiation process

The origin and purity of commercial $Li_{1.11}Ni_{0.42}Mn_{0.41}Co_{0.17}O_2$ (NMC442) and the oxidizing reagent are listed in Table 4.6.

The oxidizing reagent was prepared by dissolving $(NH_4)_2S_2O_8$ powders in distilled water, with a density of 0.5 mol/L. The commercial NMC442 positive electrode materials were chemically delithiated by immersing the powders into oxidizing reagent with various amounts for selected reaction times [95]. The reaction times were set as 4 h, 16 h, 24 h, 48 h, 72 h, and 96 h.

Table 4.6 Chemical specification: commercial NMC442 positive electrode materials and oxidizing reagent $(NH_4)_2S_2O_8$.

Raw material	Chemical formula	Source	Initial mass fraction purity
Lithium nickel manganese cobalt oxide	$Li_{1.11}Ni_{0.42}Mn_{0.41}Co_{0.17}O_2$	MTI	0.9776
Ammoniumpersulfat	$(NH_4)_2S_2O_8$	Alfa Aesar	0.98

1 g specimens were immersed into 250 mL and 500 mL oxidizing reagent, which are termed as one- and double-portion delithiation, respectively. After the redox reactions, the products were filtered from oxidizing reagent, and then washed 3 times with distilled water, and at the end, dried in a vacuum oven at 120 °C for 24 h. By changing the reaction time, different degrees of delithiation were achieved. In addition, in order to quantify the influence of water on the delithiation process, the same delithiation experiments were performed by using water instead of oxidizing reagent as the solvent, where the amount of Li concentration in the water was measured.

The compositions of the delithiated specimens as well as the oxidizing reagent filtrate were quantitatively determined by ICP-OES measurements. Thermal characters of selected delithiated specimens were investigated by simultaneous thermal analysis (STA) and the Alexsys 1000 calorimeter. Since the oxygen release from positive electrode materials is essential in phase transitions, a high oxygen-sensitive sensor technique was employed instead of mass spectroscopy.

Characterization methods

ICP-OES analysis

For solid specimen, the analytic solution was prepared as follows. Approximately 5 mg solid specimen was dissolved in 6 mL hydrochloric acid, 2 mL nitric acid at 80 °C for four hours. To measure the contents of transition metal elements (Ni, Co and Mn) and lithium, the chemical digestion solution was diluted and thereafter an internal standard solution was added. For each element analysis, a calibration curve was adopted, which was determined by four selected concentrations. The calibration was done within one decade.

Two to three wavelengths of each element have been used for the analysis of the composition. In this work, the components of the oxidizing reagents' filtrate were also measured by ICP-OES. The oxidizing reagents were firstly acidified with HCl and then the measurement for Li and transition metal elements took place analogously to the solid specimens.

XRD analysis

The measurements were made in the 2θ angle range of 10 ° - 110 °, with a step size increment of 0.02, and the data was collected in every 6 s. Rietveld profile refinements were carried out using the software Maud and Jade.

Simultaneous thermal analysis and oxygen release study

The phase transition of the specimens was studied by using a combination of simultaneous thermal analysis (STA, NETZSCH, Germany), mass spectroscopy, and oxygen detector (SGM 5T, Zitrox Sensoren und Elektronik GmbH Germany). Ar gas (purity 99.9999 %) with a flow rate of 50 mL/min was adopted as protective gas. The produced gases and Ar were collected and investigated by a mass spectrometer (QMS 403C NETZSCH, Germany) and an oxygen detector (SGM 5T, Zirox Sensoren und Elektronik GmbH, Germany). The specimens were heated up to 800 °C with 5 K/min. The masses of the selected specimens Li_xNMC442 with Li content x=1.11, x=0.76, and x=0.48 were 58.62 mg, 56.90 mg, and 59.59 mg (±0.005 mg), respectively.

Alexsys-1000 calorimeter measurement

As described in Section 2.5, the measurements for the enthalpies of drop solution of lithiated

and delithiated specimens were performed by Alexsys-1000 calorimeter. 5 mg - 8 mg powder specimen was pressed into pellet with a diameter of 3 mm. The mass of the specimen was carefully controlled to ensure the heat effects in the range of 5 J - 10 J, where one drop took approximately 45 minutes. Between drops it would take about 1.5 hours for the stabilization of the baseline [78]. The specimens were dropped right and left alternately from the ambient temperature to 701 °C. At meantime, Ar gas was introduced as a flushing gas to maintain a constant atmosphere with a flow rate of 40 mL/min. Moreover, Ar gas was also used to stir the solution and to prevent the local solvent saturation by bubbling into the solution with a flow rate of 5 mL/min.

4.3.2 Results and discussion

ICP-OES analysis

The following Table 4.7 tabulates the results of the ICP-OES measurements for one portion delithiated NMC materials, where TM stands for transition metals. The metals' contents and measured compositions of samples with selected reaction times are listed, and plotted in Fig. 4.11. Since molar ratios can indicate Li loss as well as TM loss clearly, Li content was calculated with assumption of atomic sum of transition metals (TM=1).

Table 4.7 Analytical composition of $Li_xNi_yMn_zCo_\delta O_\eta$ delithiated by one-portion oxidizing reagent, and measured composition was nominalized by the assumption sum of transition metals equaling to 1 (sum TM=1).

Reaction time [h]	Molar ratio in solid specimens				Nominal stoichiometry
	Li/sum TM	Mn/Co	Mn/Ni	Co/Ni	
0	1.11	2.35	0.96	0.41	$Li_{1.11}Ni_{0.42}Mn_{0.41}Co_{0.17}O_{2.08}$
4	1.01	2.36	0.91	0.41	$Li_{1.00}Ni_{0.42}Mn_{0.40}Co_{0.17}O_\eta$
16	0.88	2.35	0.96	0.41	$Li_{0.88}Ni_{0.42}Mn_{0.41}Co_{0.17}O_\eta$
24	0.87	2.40	0.99	0.41	$Li_{0.87}Ni_{0.42}Mn_{0.41}Co_{0.17}O_\eta$
48	0.83	2.51	1.06	0.42	$Li_{0.83}Ni_{0.40}Mn_{0.43}Co_{0.17}O_\eta$
72	0.76	2.60	1.11	0.43	$Li_{0.76}Ni_{0.39}Mn_{0.44}Co_{0.17}O_\eta$
96	0.74	2.57	1.09	0.43	$Li_{0.74}Ni_{0.40}Mn_{0.43}Co_{0.17}O_\eta$

In Fig. 4.11 a), the Li/TM ratios in samples with different reacting times are plotted. With further delithiation, a decrease of Li ions in NMC442 sample is clearly observed. The delithiation in first 4 h is most effective, about 10 at.% Li extracted. For 16 h delithiation, about 23 at.% Li is extracted from NMC442. However, in long term delithiation from 24 h to 96 h, the delithiated amount rises relatively slow. Li content in 96 h sample is 0.74, extracting 35 at.% Li. In Table 4.7 the molar ratios between TM elements were shown: Mn/Co, Mn/Ni and Co/Ni ratios of samples with different reacting times. The molar ratios of TM can help to compare the losses of Mn, Ni and Co with initial composition. The initial ratios of Mn/Co Mn/Ni and Co/Ni are 2.35, 0.96 and 0.41. The molar ratios of Mn/Co, Mn/Ni and Co/Ni maintain the same as initial ratios in 4 h and 16 h samples. However, in 24 h, 48 h, 72 h, and 96 h samples, TM ratios derive, especially Mn/Co and Mn/Ni shifting to higher values. That implies Mn ions were dissolved less than Ni and Co ions. Therefore, there are higher Mn contents in the samples for 24 h, 48 h, 72 h and 96 h, than initial composition.

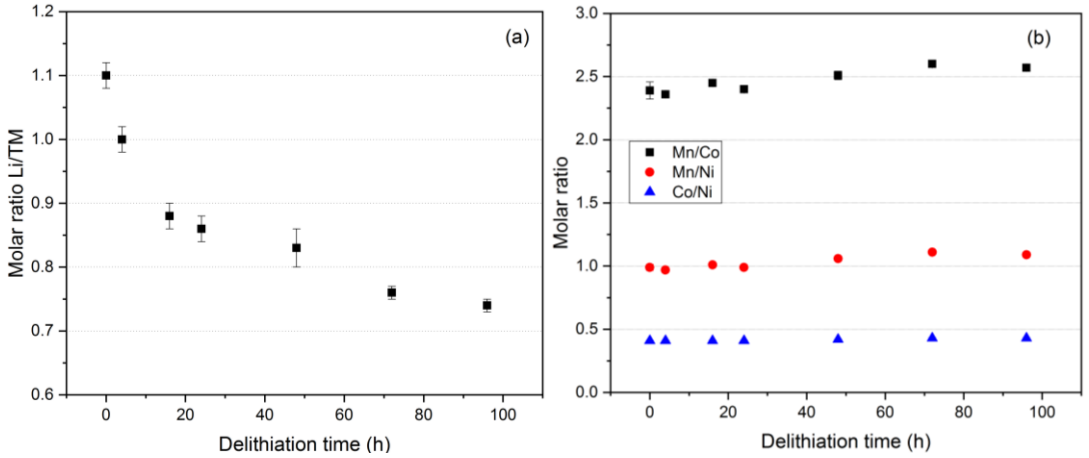

Fig. 4.11: Delithiated specimen by one-portion oxidizing reagent a) molar ratio of Li/summation of transition metals versus delithiation time. b) Molar ratio of Mn/Co, Mn/Ni and Co/Ni versus delithiation time.

As can be seen in Fig. 4.11, with the delithiation time rising from 4 h, 12 h, 24 h, 48 h, 72 h to 96 h, the amount of Li ions extraction soars. Moreover, the chemical delithiation also affects the content of transition metals in the samples, as depicted in Fig. 4.11 b). The molar ratios of Mn/Co are presented by black points, Mn/Ni red points and Co/Ni blue points. The molar ratios of the transition metals indicate the loss of transition metal elements in samples. For instance the 96 h sample, Mn/Co (black points) and Mn/Ni (red points) increase from 2.35 to 2.57, and from 0.96 to 1.09, respectively. In long chemical delithiation, TM is prone to dissolve. There is no clear relationship between TM dissolving and chemical delithiation. The 72 h sample has the largest deviation from initial ratios of Mn/Co (black points) and Mn/Ni (red points), and molar percentage of Mn in 72 h samples is the largest among all delithiated samples. As Co/Ni (blue points) ratios remain the initial ratio between 0.41 - 0.43 over delithiation time, it suggests that both Ni and Co ions are dissolved in solvent in similar amount. The molar ratio of Ni:Mn:Co deviates from initial ratio, especially in long term delithiation.

In water dissolvent, only 0.001 at.% Li ions were found, and transition metals were dissolved even far less than Li ions. This observation indicates that commercial NMC442 positive electrode materials were not dissolved in water. Table 4.8 demonstrates the molar ratios of the composition for the selected delithiation times. Besides Li, the transition metal elements Ni, Co and Mn were also found in the oxidizing reagent filtrate. This phenomenon was reported in Ref. [101] as well. In their research, Li element was chemically extracted from $LiCoO_2$ by various oxidizing reagents Cl_2, Br_2, I_2 and acid treatment, and the specimen was found to be dissolved during chlorine oxidation. By using $(NH_4)_2S_2O_8$ solvent as oxidizing reagent in this work, the dissolving of not only Li ions but also transition metal ions occurred during chemical delithiation. Three Li cations at 3a positions were extracted accompanied by one transition metal cation dissolving from 3b positions, since molar ratios of Li/sum TM are about 3 in all three samples. In Table 4.8, molar ratios of Mn/Co and Mn/Ni for 4 h filtrate are 2.45 and 1.00, respectively which are larger than initial 2.35 and 0.96, indicating Mn dissolving more than Ni and Co in first 4 h. With longer reaction time, the dissolving amounts are Ni>Co>Mn for long term delithiation, and the comparison is based on the deviation from initial ratios. The small amount of Mn dissolved in the oxidizing reagents can be due to the MnO_2 formation, which could be too small amount to be defined by XRD analysis.

The oxygen contents in selected samples are measured. As Table 4.7 for one-portion delithiation, Table 4.9 demonstrates the molar ratios of Li and TM elements, as well as measured compositions of samples delithiated with double-portion oxidizing reagent.

Table 4.8 Analytical composition of the oxidizing reagent filtrate.

Reaction	Molar ratio in solid specimens			
[h]	Li/sum TM	Mn/Co	Mn/Ni	Co/Ni
4	2.90	2.45	1.00	0.41
16	2.87	2.40	0.97	0.40
48	3.06	1.94	0.74	0.38

Table 4.9 Analytical composition of $Li_xNi_yMn_zCo_\delta O_\eta$ delithiated by double-portion oxidizing reagent, measured composition with assumption sum of transition metals equaling to 1 (sum TM=1).

Reaction time	Molar ratio in solid specimens				Measured composition
[h]	Li/sum TM	Mn/Co	Mn/Ni	Co/Ni	
0	1.11	2.35	0.96	0.41	$Li_{1.11}Ni_{0.42}Mn_{0.41}Co_{0.17}O_{2.08}$
4	0.90	2.32	0.94	0.41	$Li_{0.90}Ni_{0.42}Mn_{0.41}Co_{0.17}O_\eta$
16	0.80	2.55	1.06	0.42	$Li_{0.80}Ni_{0.40}Mn_{0.43}Co_{0.17}O_\eta$
24	0.72	2.54	1.07	0.42	$Li_{0.72}Ni_{0.40}Mn_{0.43}Co_{0.17}O_\eta$
48	0.61	2.76	1.20	0.43	$Li_{0.61}Ni_{0.38}Mn_{0.46}Co_{0.16}O_\eta$
72	0.60	2.50	1.04	0.42	$Li_{0.60}Ni_{0.41}Mn_{0.42}Co_{0.17}O_\eta$
96	0.48	2.83	1.23	0.43	$Li_{0.48}Ni_{0.38}Mn_{0.46}Co_{0.16}O_\eta$

Comparing with one-portion delithiation, more Li ions are extracted for same reaction time, seeing Fig. 4.12 a). Comparing between Li content's curves in Fig. 4.11 a) and Fig. 4.12 a), the shapes are similar. For first two experiments 4 h and 16 h delithiation, Li ions were extracted in amounts of 10 at.% and 21 at.%. The delithiation process slows down from 24 h delithiation till 96 h delithiation. As mentioned before, the initial ratios of Mn/Co, Mn/Ni and Co/Ni are 2.35, 0.96 and 0.41. With more Li extracted from NMC materials, transition metals are dissolved more severely. The samples of 48 h and 96 h have molar ratios Mn/Co (black points in Fig. 4.12 b)) of 2.76 and 2.83. The ratios of Mn/Ni are 1.20 for 48 h and 1.23 for 96 h, deviating from initial value 0.96 mostly. For 48 h and 96 h delithiation, Mn ions were dissolved much less than Ni and Co. In summary, the relative dissolving amounts are Co>Ni>Mn for long term delithiation, and comparison is based on the deviation from initial ratios.

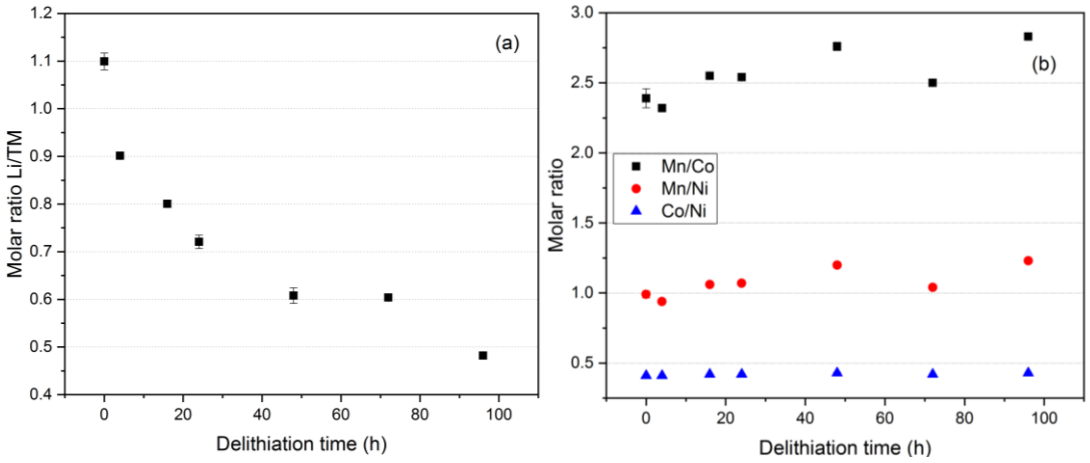

Fig. 4. 12: Delithiated specimen by double-portion oxidizing reagent. a) Molar ratios of Li/summation of transition metals versus delithiation time. b) Molar ratios of Mn/Co, Mn/Ni and Co/Ni varying with delithiation time.

Fig. 4.12 b) visualizes the values of molar ratios, and ratios of Mn/Co and Mn/Ni (black and red points) are mostly larger than initial ratio's values. That suggests Mn element dissolving less than Ni and Co, same as one-portion experiments. Only for 4 h delithiation, Mn is dissolved more than Ni and Co, which is observed in Fig. 4.11 b) as well as Mn concentration in filtrate in Table 4.8. For double-portion delithiation, the ratios of Co/Ni are similar to one-portion, relatively stable in between of 0.41 to 0.43.

XRD analysis

One-portion delithiated specimen

The XRD patterns of commercial samples, which are chemically delithiated for the selected times, are shown in Fig. 4.13 and Fig. 4.14. The structure was refined in a hexagonal lattice of α-$NaFeO_2$ type structure with the space group $R\bar{3}m$ (No. 166). Li, the transition metal ions (Ni, Mn, Co), and O are located at Wyckoff positions 3a, 3b and 6c, respectively. The XRD patterns in Fig. 4.13 show that the chemical delithiated NMC remains the layered structure. Oxygen anions at 3c positions might be lost during chemical delithiation as well, engendering oxygen vacancies. The black curves in Fig. 4.13 are XRD patterns, and red curves are plotted according to Rietveld refinement. The lattice parameters of delithiated samples are plotted in Fig. 4.15. The intensity ratio of (003)/(104) in Fig. 4.13 d) indicates a layered mixing (about 1 at.%) between 3a and 3b sites. $I_{(003)}/I_{(104)}$ is considered as a sensitive parameter to determine the cationic distribution [99]. When Li ions were chemically extracted from the NMC powder, a change in the oxidation state of the transition metals took place.

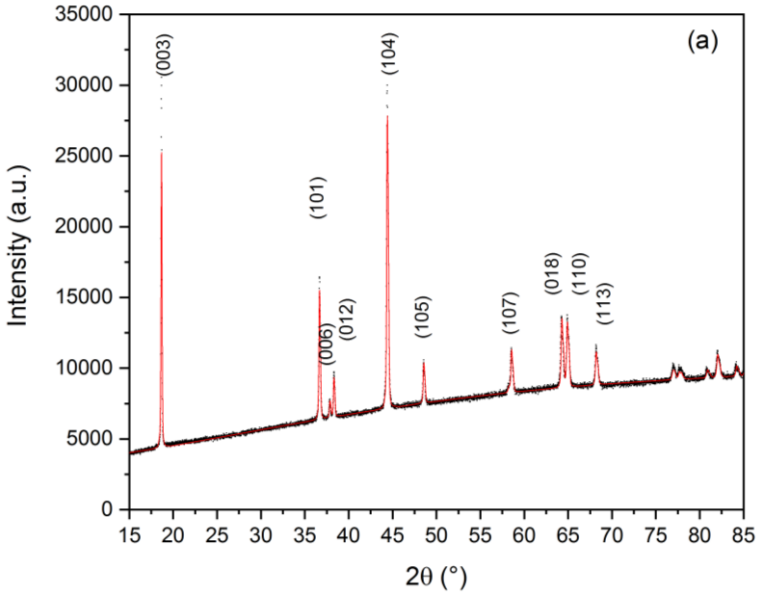

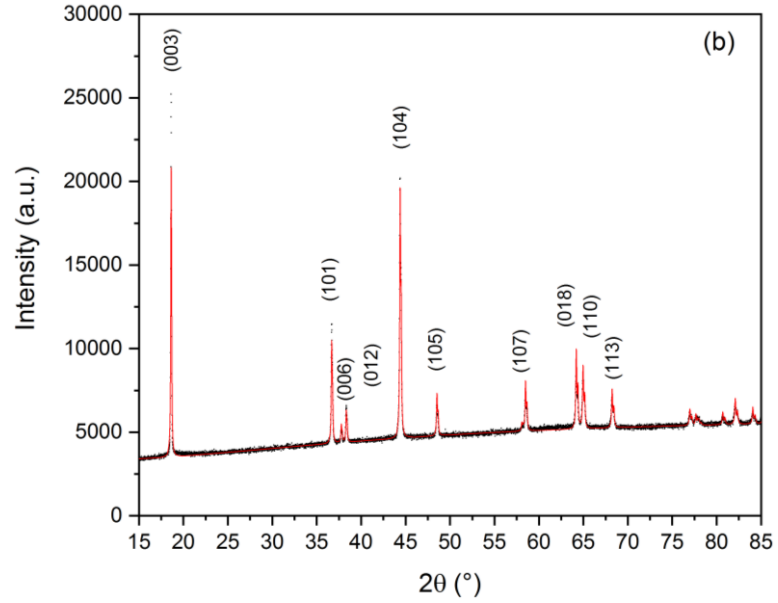
(b)
Intensity (a.u.)
2θ (°)
(003)
(101)
(006)
(012)
(104)
(105)
(107)
(018)
(110)
(113)

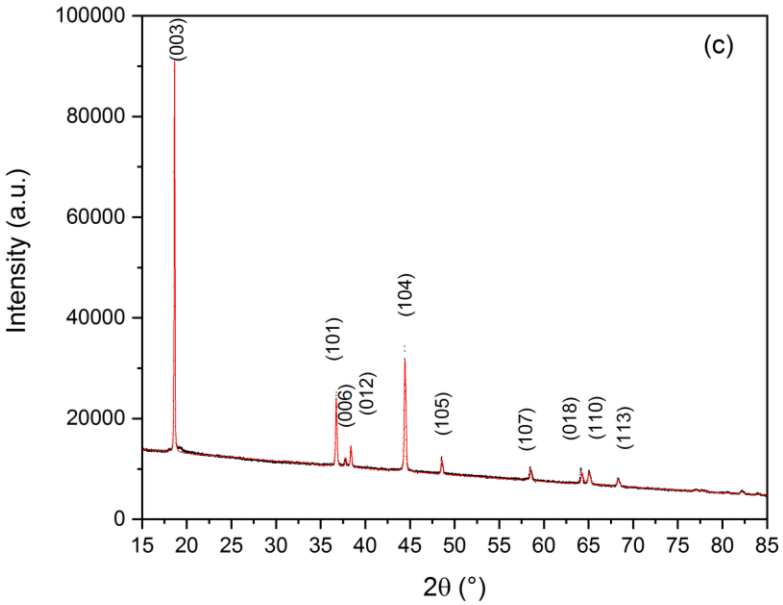
(c)
Intensity (a.u.)
2θ (°)
(003)
(101)
(006)
(012)
(104)
(105)
(107)
(018)
(110)
(113)

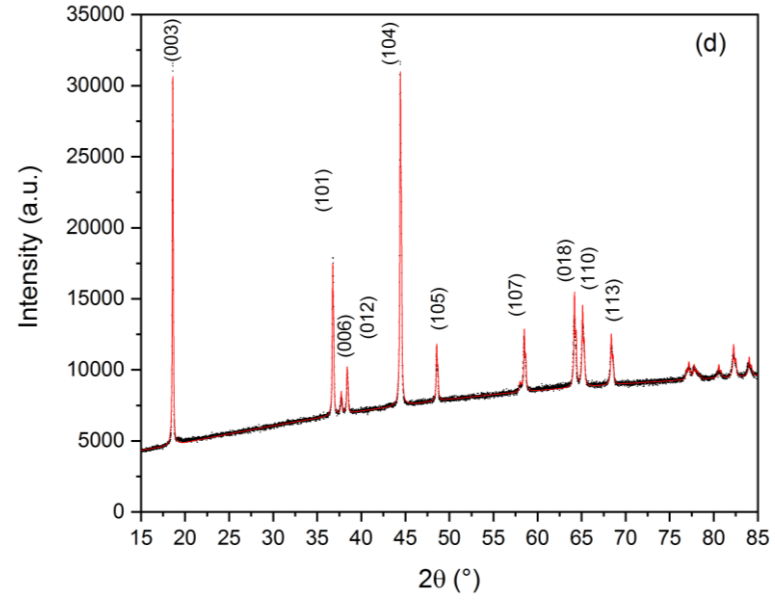
(d)
Intensity (a.u.)
2θ (°)
(003)
(101)
(006)
(012)
(104)
(105)
(107)
(018)
(110)
(113)

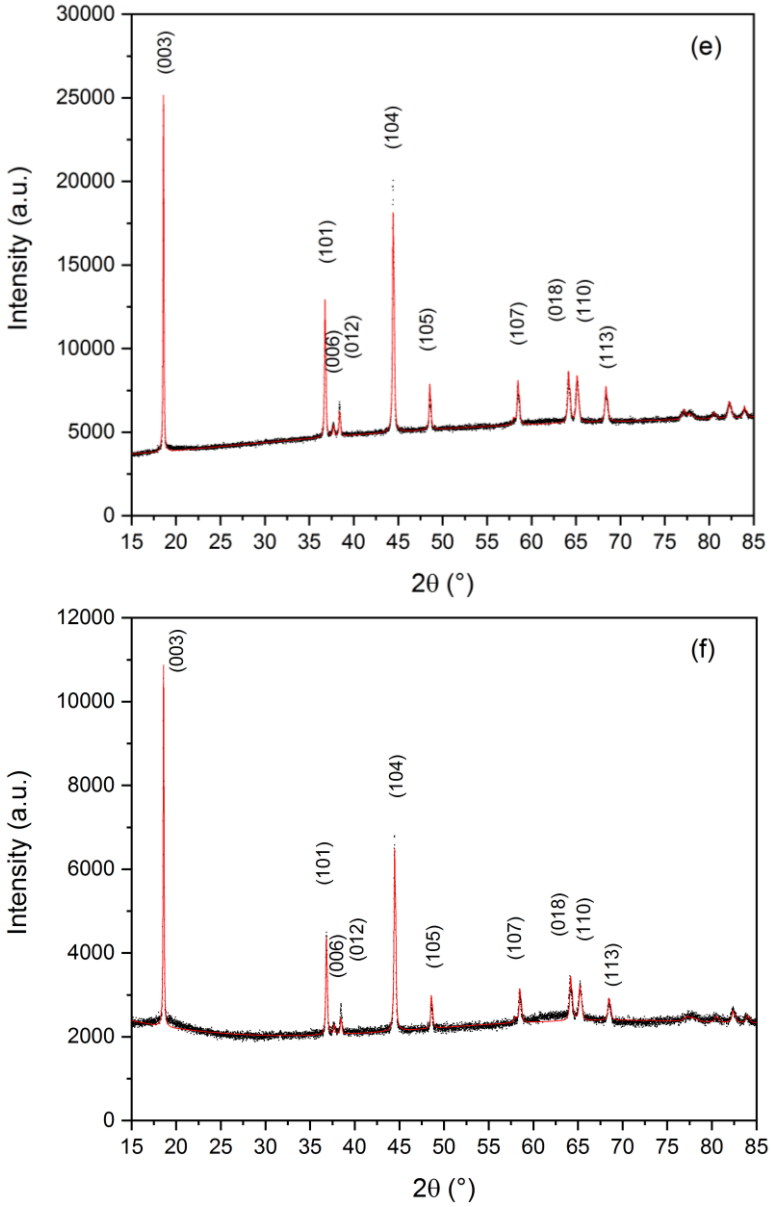
(e)
Intensity (a.u.)
2θ (°)
(003)
(101)
(006)
(012)
(104)
(105)
(107)
(018)
(110)
(113)
(f)
Intensity (a.u.)
2θ (°)
(003)
(101)
(006)
(012)
(104)
(105)
(107)
(018)
(110)
(113)

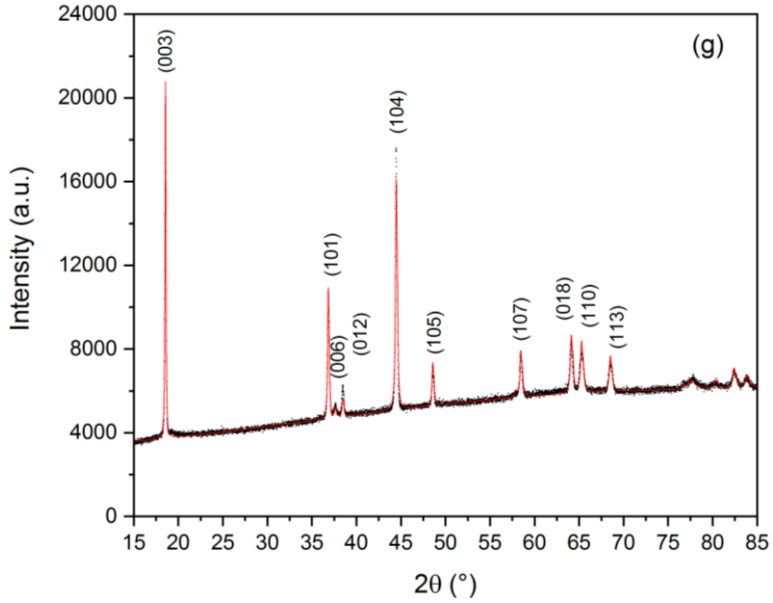

Fig. 4.13: The XRD patterns and Rietveld refinement curves of pristine and chemically delithiated commercial NMC442 materials by one-portion oxidizing reagent (black curve: measured, red curve: refined): a) pristine material; delithiated samples: b) 4 h, c) 16 h, d) 24 h, e) 48 h, f) 72 h, g) 96 h.

Enlargement specimens' XRD patterns of the reflection (003) are exhibited in Fig. 4.14 a). As the chemical delithiation proceeds with time, the reflection (003) shifts towards lower 2θ angles. The shifting of (003) is related to the increase in c_{hex}, caused by the repulsion between the oxygen layers. In addition, the increasing FWHM of (003) suggests a decline in the particle size. In Fig. 4.14 b), with further delithiation, the splitting of the (018) and the (110) reflections reveals an increase in *c/a* ratio, and the similar results were obtained in Ref. [102].

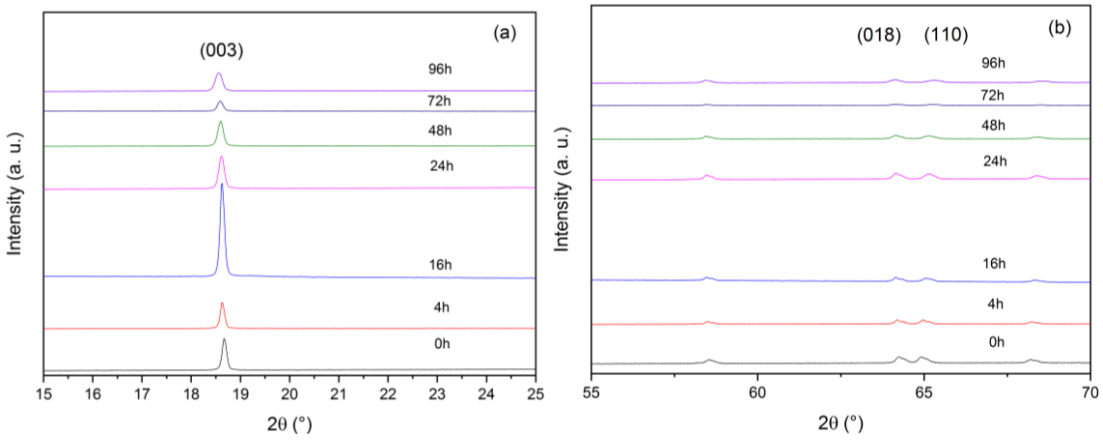

Fig. 4.14: Comparison of local XRD patterns for pristine and chemically delithiated commercial NMC442 by one-portion oxidizing reagent: a) selected 2θ regions of the reflection (003), b) selected 2θ regions of the reflections (018) and (110).

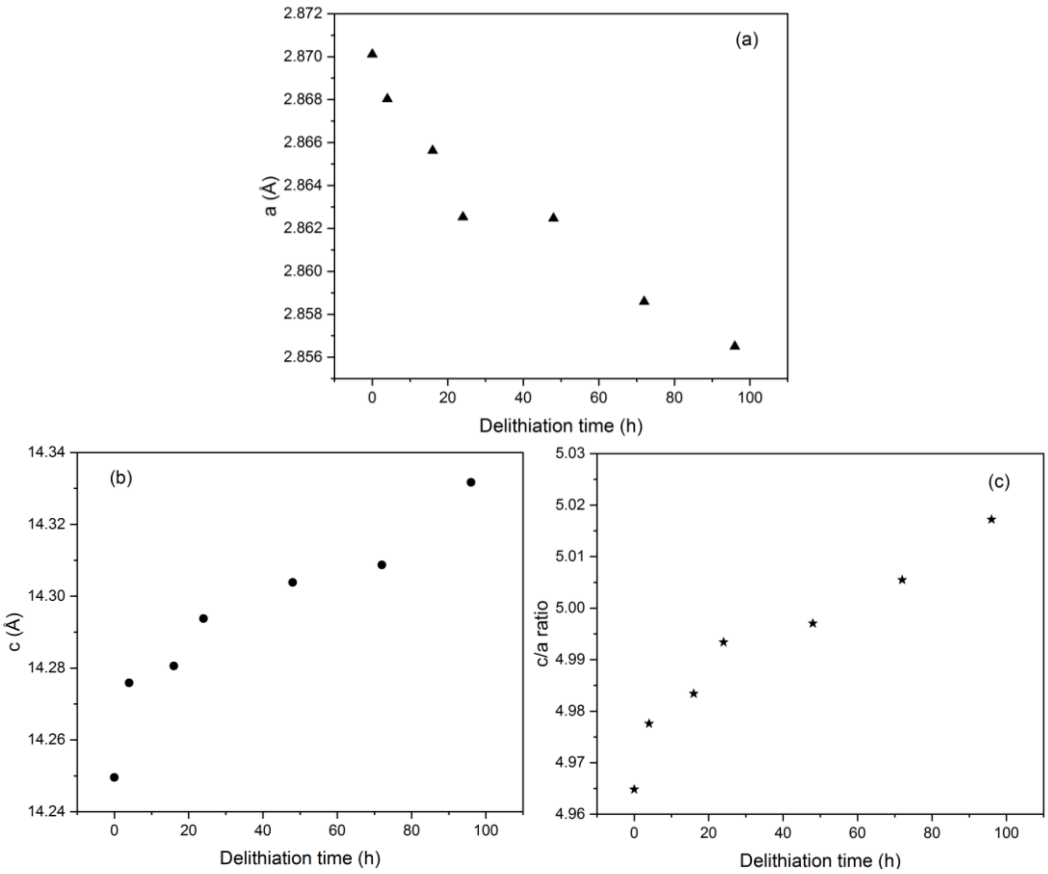

Fig. 4.15: The lattice parameters of delithiated commercial NMC442 samples by one-portion oxidizing reagent: a) a_{hex} varying with the chemical delithiation time. b) c_{hex} varying with the chemical delithiation time. c) c/a ratio versus chemical delithiation time.

Fig. 4.15 a), b) and c) demonstrate the changes of lattice parameters *a*, *c* and ratios of *c/a* against chemical delithiation time, which are in good agreement with previous work [103]. In pristine NMC442 sample, the oxidation states of Ni, Mn, and Co in the compound are 2+, 4+, and 3+, respectively. During charging, the redox process is assigned to the $Ni^{2+/3+/4+}$ couples at a relatively low voltage and then to the $Co^{3+/4+}$couples at a higher voltage [35]. In Abdel-Ghany et al.'s work [104], they found Co^{3+} was oxidized only at very deep delithiation and oxidation of Ni^{2+} was the mainly redox reaction. Similarly, in the chemical delithiation, a redox process occurs and oxidation states of transition metal increase, leading to a decrease in their ionic radius. The removal of Li ions can also cause an enlargement in the repulsion between adjacent oxygen layers. Both effects result in a variation in the lattice parameters [34].
Fig. 4.15 a) shows that the metal-metal distance, indicated by a_{hex}, decreases when the Li ions were chemically extracted. With delithiation proceeding, Ni^{2+} ions are oxidized to $Ni^{3+/4+}$ ions, therefore, the ionic radius is decreasing (radius of Ni^{2+} : 0.83 Å, radius of Ni^{4+}: 0.62 Å). In Fig. 4.15 b), the increase of c_{hex} upon chemical delithiation might be due to the increase in the electrostatic repulsion between the oxygen layers [105]. In Fig. 4.15 c), the ratio of *c/a* is increasing during chemical delithiation as analyzed from the reflections of (018) and (110).

Double-portion delithiated specimen

In order to compare with the one-portion solution, the XRD patterns and refinement results of double-portion are shown in Fig. 4.16. In the XRD patterns of the delithiated specimens for 16 h, 24 h, 48 h and 72 h, a second phase is observed, which is determined to be $NiCo_2S_4$ by the Jade (XRD analysis software) database. The main phase is of layered structure type with space group $R\bar{3}m$. The loss of the element Ni in NMC442 sample is also observed in ICP-OES measurements, and the following reaction is supposed to take place.

$$[Ni(NH_3)_4]^{2+} + 2[Co(NH_3)_4]^{2+} + 4S^{2-} \rightarrow NiCo_2S_4 + 12NH_3 \quad (4.4)$$

Moreover, in the 96 h delithiated specimen, there is a shoulder at 2θ of 19.327 °, and the second phase is $Li_{0.3}MnO_2$ according to the Jade database. In the deep delithiated samples for 72 h and 96 h, the main phase remains the layered structure, but with much lower intensities than other samples. The change in unit cell might be caused by Li vacancies. Since TM metals are dissolved severely in long term delithiation, the crystal size could be smaller, which leads to lower and wider reflexions. Additionally, element Ni is extracted more in the deep delithiation, which might be due to the cation mixing, and Ni is extracted from 3a positions.

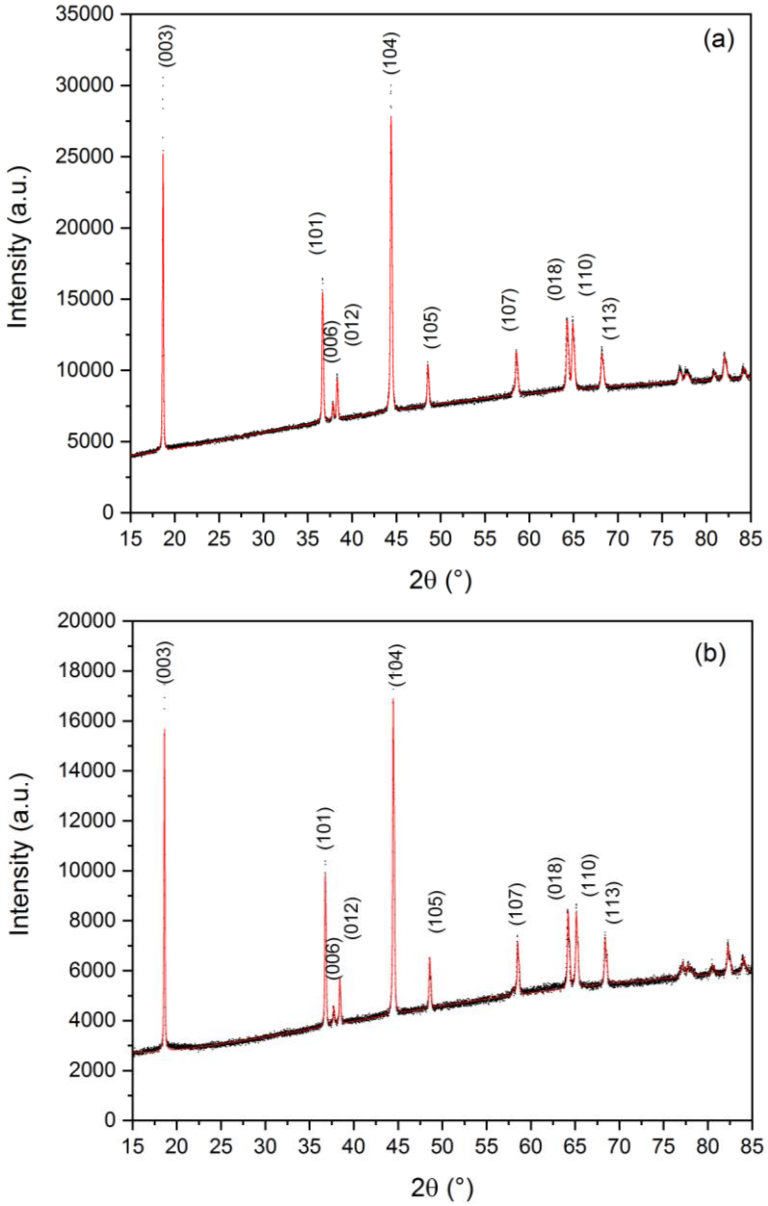

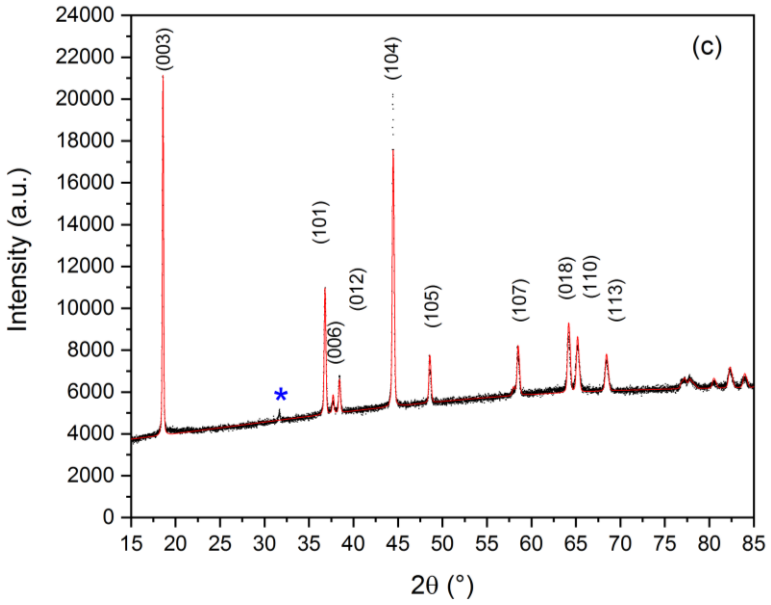
(c)
Intensity (a.u.)
2θ (°)
(003)
(101)
(006)
(012)
(104)
(105)
(107)
(018)
(110)
(113)
*

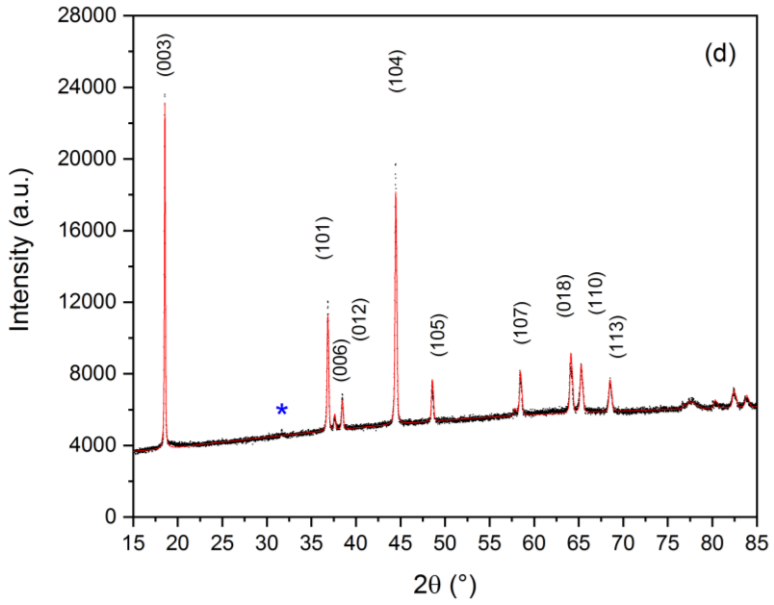
(d)
Intensity (a.u.)
2θ (°)
(003)
(101)
(006)
(012)
(104)
(105)
(107)
(018)
(110)
(113)
*

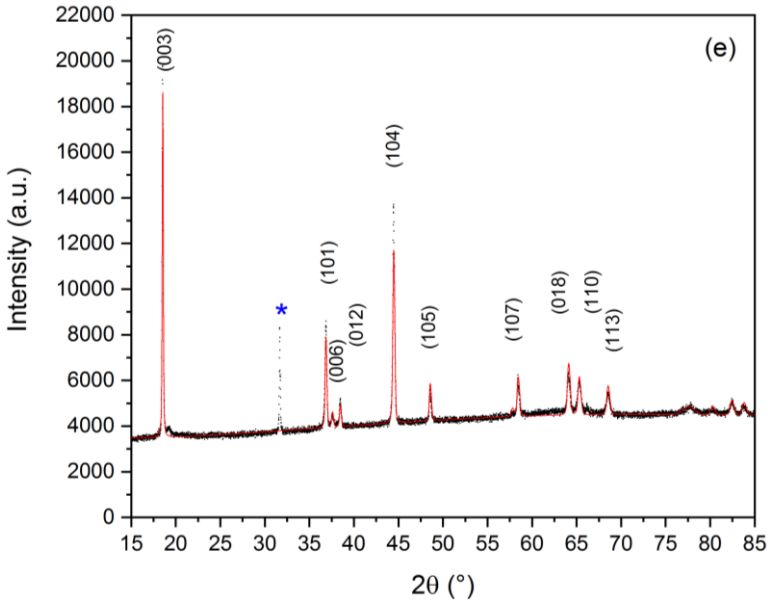
(e)
Intensity (a.u.)
2θ (°)
(003)
(101)
(006)
(012)
(104)
(105)
(107)
(018)
(110)
(113)
*

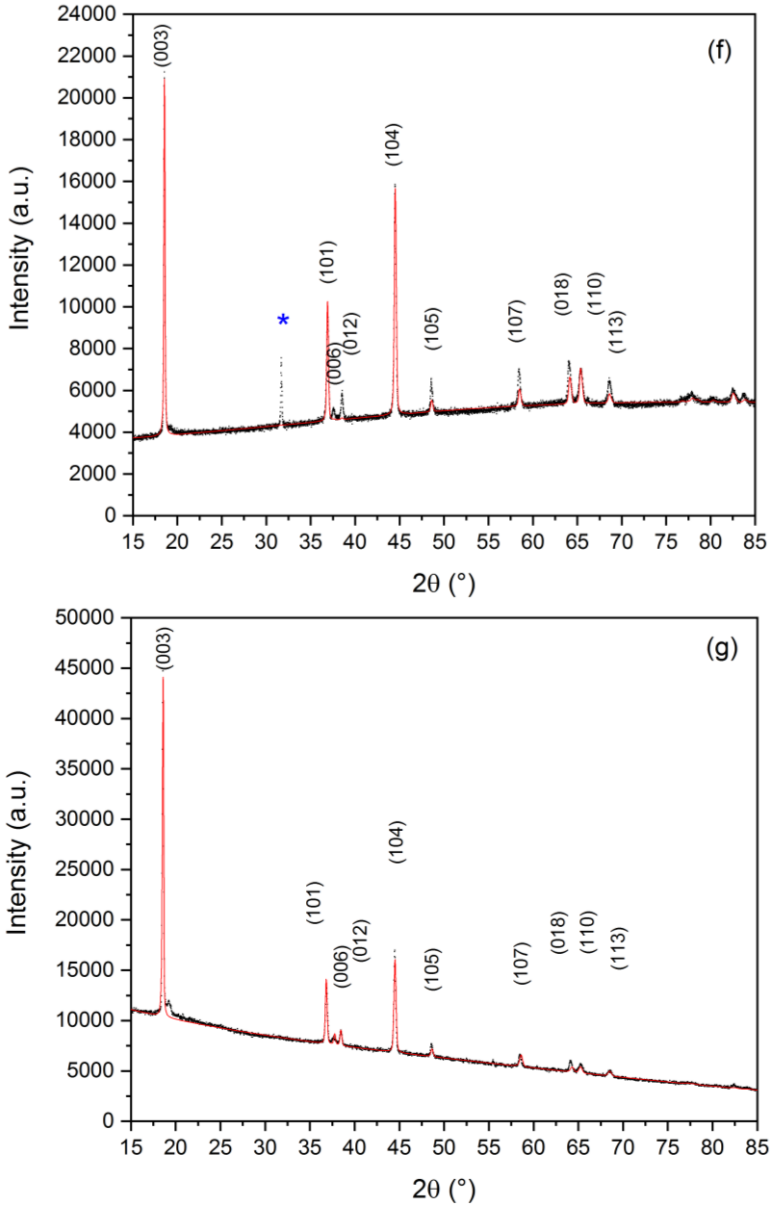

Fig. 4.16: The XRD patterns and Rietveld refinement curves of pristine and chemically delithiated commercial NMC442 by double-portion oxidizing reagent (black curve: measured, red curve: refined, *: $NiCo_2S_4$): a) pristine material, b) 4 h delithiated sample, c) 16 h delithiated sample, d) 24 h delithiated sample, e) 48 h delithiated sample, f) 72 h delithiated sample, g) 96 h delithiated sample.

Selected specimens for thermal properties investigation

Reimers and Dahn [106] observed an order/disorder phase transition with hexagonal/monoclinic structures during charging of Li_xCoO_2 by in-situ X-ray diffraction. The phase diagram in terms of temperature as well as cell voltage is shown in Fig. 4.17. As delithiation proceeding, phase I transfers to phase II partly. In region $0.75<x<0.93$, Li_xCoO_2 has both phases I and II. With further delithiation, phase I transfers to phase II completely. When $0.45<x<0.55$, the monoclinic phase exists.

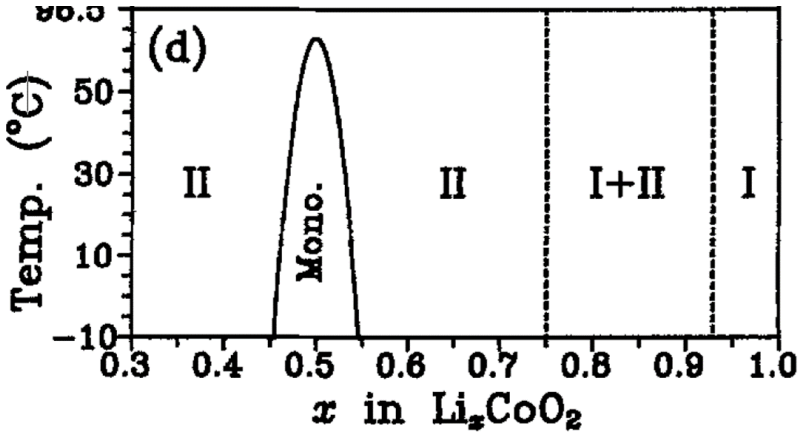

Fig. 4.17: Phases found by in-situ X-ray diffraction for the lithium ion ordering/disordering phases in Li_xCoO_2 in terms of temperature and cell voltage [106].

In delithiation process, phase transitions of NMC442 materials are similar. Fig. 4.18 demonstrates XRD patterns of a) pristine commercial material sample $Li_{1.11}Ni_{0.42}Mn_{0.41}Co_{0.17}O_{2.08}$, b) medium degree delithiated sample $Li_{0.76}Ni_{0.41}Mn_{0.42}Co_{0.17}O_{2.10}$, which was prepared with one portion for 65 hours, and c) high degree delithiated sample $Li_{0.48}Ni_{0.38}Mn_{0.46}Co_{0.16}O_{2.07}$ (see Table 4.11). The reflections (003) have shoulders in Fig. 4.18 b) and c), which implies a second phase, and the lattice parameters and percentages of phases are listed in Table 4.10. The XRD patterns were further refined by Maud to define the hexagonal (space group $R\bar{3}m$) and monoclinic (space group No. 28 P2/mb) phases. The parameters are listed in Table 4.10.

Fig. 4.17 shows co-existing phase I and phase II in LCO when x = 0.75 - 0.93. However, in delithiated sample $Li_{0.76}Ni_{0.41}Mn_{0.42}Co_{0.17}O_{2.10}$, there exist hexagonal and monoclinic phases. One reason could be the different redox reactions in NMC and LCO. In NMC materials, Ni^{2+} is oxidized instead of Co^{2+} in early delithiation. As further delithiation taking place, Co^{2+} in NMC will be oxidized and the phases are similar to delithiated LCO. Comparing the phases in sample $Li_{0.48}Ni_{0.38}Mn_{0.46}Co_{0.16}O_{2.07}$: hexagonal and monoclinic phases, to the phases in Fig. 4.17, when x=0.48 at 25 °C, it matches to each other perfectly. The boundary of hexagonal and monoclinic phases indicates a co-existing phases area, where the point with x= 0.48 at 25 °C exactly located. But one should be very cautions to compare phases diagram from electrochemical delithiation and chemical delithiation.

In Table 4.10, the first column lists Li contents in three samples. The space groups, percentages of phases and the lattice parameters are listed. The values of lattice parameters *a* (Å) and *c* (Å) of layered structure are pristine sample > medium delithiation sample > high delithiation sample. The second phases are found in both medium and high delithiation samples of 15.5 wt.% and 13.6 wt.%, respectively. The lattice parameters *a* (Å), *b* (Å) and *c* (Å) of monoclinic structure of medium delithiation sample are larger than high delithiation sample.

Table 4.10 Rietveld refinement for X-ray diffraction of the commercial NMC442 and selected delithiated specimens Li_xNMC442.

Li content x	Space group	Lattice parameters			Phase wt.%
		a (Å)	*b* (Å)	*c* (Å)	
1.11	$R\bar{3}m$	2.8769(7)	-	14.2922(0)	-
0.76	$R\bar{3}m$	2.8606(8)	-	14.2926(7)	84.5
	P2/mb	5.5284(8)	2.9837(7)	5.13120(6)	15.5
0.48	$R\bar{3}m$	2.8562(2)	-	14.2722(5)	86.4
	P2/mb	5.2134(2)	2.7321(5)	4.7694(1)	13.6

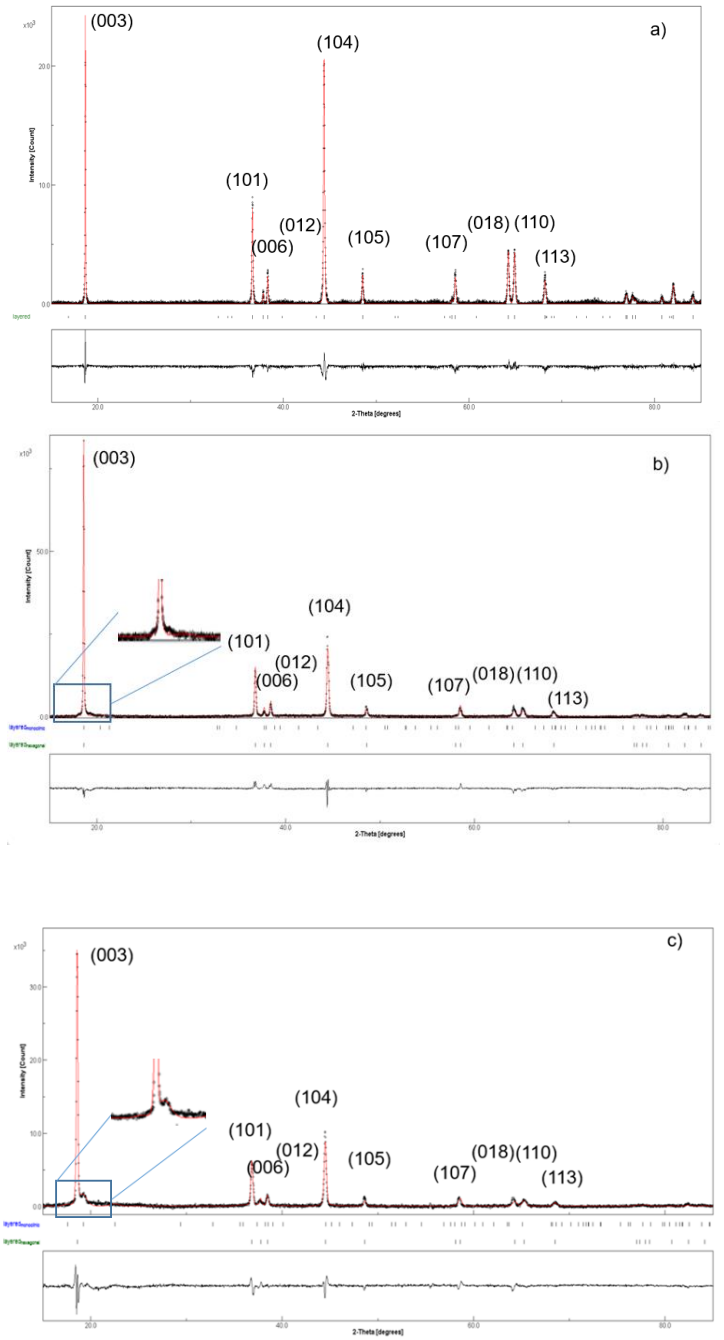

Fig. 4.18: The experimental and calculated XRD patterns of pristine and chemically delithiated commercial $Li_xNMC442$: a) x=1.11, b) x=0.76, c) x=0.48.

Table 4.11 shows the chemical analysis for the three samples, including ICP-OES results of elements in weight percentages. Based on these results, molar ratios of Li and TM and measured composition are calculated with assumption of TM=1. TM ions were partially solved in oxidizing agent along with O, since the O content in pristine and delithiated samples kept same.

Table 4.11 Chemical analysis of the pristine and selected delithiated commercial NMC442 samples. The nominal stoichiometry was calculated based on transition metals' cations equaling to 1 in composition (sum TM=1).

Analyzed elements		**Pristine sample**	**Medium degree delithiated sample**	**High degree delithiated sample**
ICP-OES wt.%	Li	7.68±0.16	5.33±0.11	3.40±0.07
	Ni	24.40±0.37	24.37±0.37	22.43±0.34
	Mn	22.50±0.41	23.30±0.42	25.90±0.47
	Co	10.10±0.19	10.13±0.19	9.75±0.19
	O	33.60±2.99	34.00±3.00	33.70±3.00
Molar ratio	Li/sum TM	1.11	0.76	0.48
	Ni/sum TM	0.42	0.41	0.38
	Mn/sum TM	0.41	0.42	0.46
	Co/sum TM	0.17	0.17	0.16
	O/sum TM	2.08	2.10	2.07
Measured composition		$Li_{1.11}Ni_{0.42}Mn_{0.41}Co_{0.17}O_{2.08}$	$Li_{0.76}Ni_{0.41}Mn_{0.42}Co_{0.17}O_{2.10}$	$Li_{0.48}Ni_{0.38}Mn_{0.46}Co_{0.16}O_{2.07}$

Simultaneous thermal analysis and oxygen release study

Pristine commercial NMC442 materials and selected delithiated commercial NMC442 specimens are investigated in regard of thermal properties by the simultaneous TG-DTA apparatus and mass spectroscopy (STA & MS) combined oxygen detector (SGM 5T, Zitrox Sensoren und Elektronik GmbH Germany) and high temperature oxide melt drop solution calorimeter (Alexsys-1000). The research aims were to reveal the influence of the delithiation degree on the thermal stability. Even though TM ions were also extracted during chemical delithiation process, some tendencies can be derived for electrochemically delithiated samples. The heat flow signal and thermogravimetric analysis of the samples with compositions of $Li_{1.11}Ni_{0.42}Mn_{0.41}Co_{0.17}O_{2.08}$, $Li_{0.76}Ni_{0.41}Mn_{0.42}Co_{0.17}O_{2.10}$ and $Li_{0.48}Ni_{0.38}Mn_{0.46}Co_{0.16}O_{2.07}$, are depicted in Fig. 4.19. The mass loss increases with an increase in the delithiation degree significantly. However, the DTA signals (black curves) in Fig. 4.19 b) and c) for materials with different delithiation degrees are in same range and showing similar multi-reactions. The red curves in Fig. 4.19 are the derivatives of DTA signal, which indicate the heat flux changes. As shown in Fig. a), the differential of heat flux is flat, indicating no reaction. Comparing with the delithiated samples, the pristine sample has the most stable thermal property at high temperatures with only 0.2 % mass loss. This loss might stem from the impurity of the commercial powders, and the purity is listed in Table 4.6. For the delithiated samples in Fig. 4.19 b) and c), there are several peaks on the differential of heat flux. For medium degree delithiated sample, the multi reactions took place at 101 °C, 308 °C, 365 °C, 477 °C and 659 °C, indicated by DTA peaks. The reactions at 308 °C and 477 °C are accompanying with oxygen release, where the phase transitions (equation 4.5 on page 76) occurred. For high degree delithiated sample, the first reaction was at 73 °C, and corresponding mass changes are also observed at approximately 71 °C (Fig. 4.20, when x=0.48). In Fig. 4.20, the blue curves show oxygen concentration measured by oxygen detector, and dash black curves are the differential of mass change. At approximately 218 °C in Fig. 4.20 x=0.76, mass decrease occurs due to oxygen release in both delithiated samples. Fig. 4.20 portrays the first derivative of the mass change percentage versus temperature, and in Fig. 4.20 x=0.76, onset of the peaks at 158 °C and 218 °C indicate reactions with two mass losses accompanying thermal effect in Fig. 4.19 b) on red curve at 101 °C. The peaks at 320 °C and 555 °C are the heat caused by phase transition (equation 4.5) where the oxygen concentration increases (Fig. 4.20, when x=0.76). In Fig. 4.19 c), the reactions at 363 °C, 485 °C and 717 °C are related to phase transition with O_2 release. Beside the phase transition (equation 4.5), there are other reactions, due to the second phase involved reactions or the impurity introduced by oxidizing agent.

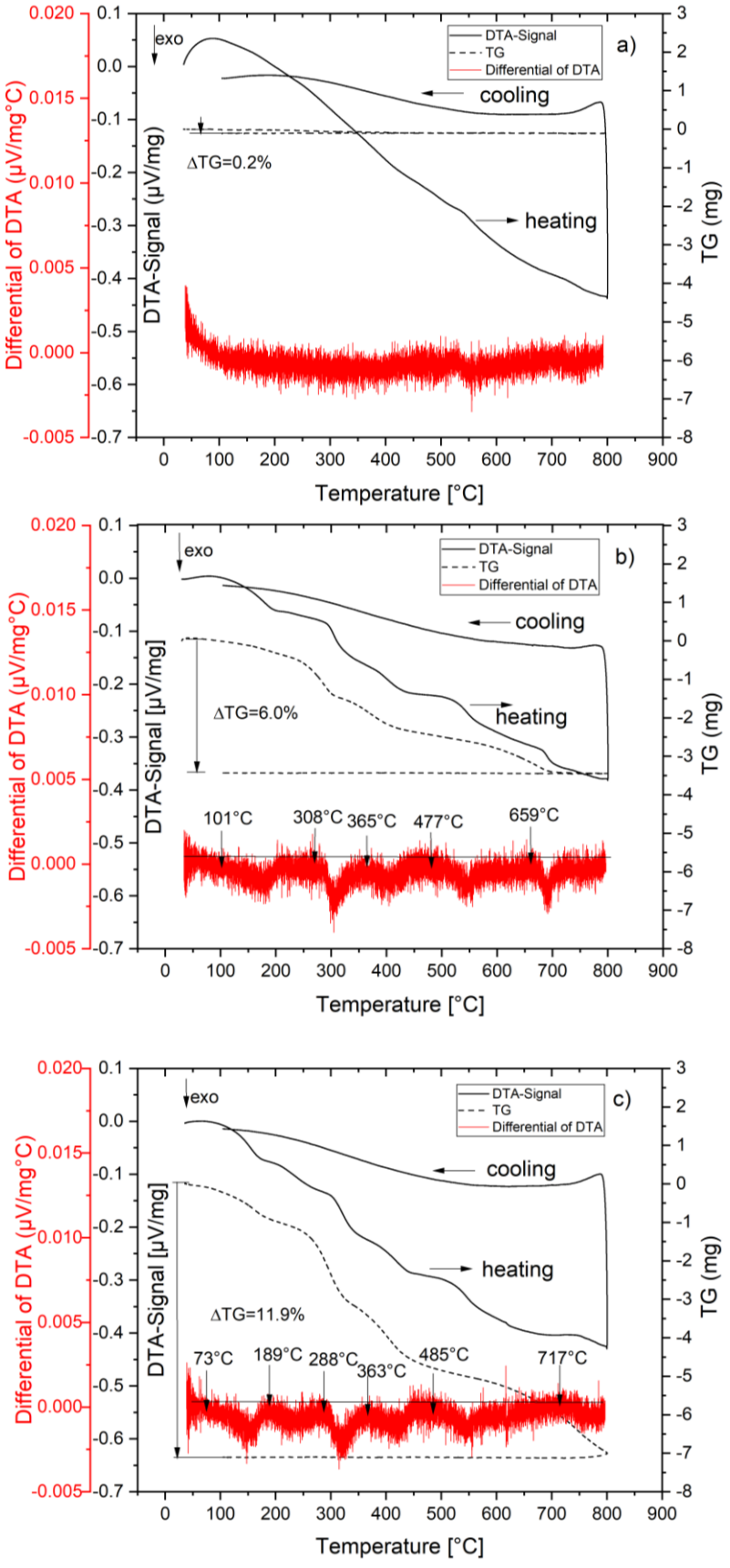

Fig. 4.19: Simultaneous thermal analysis for pristine and chemically delithiated commercial $Li_xNMC442$ samples: a) x=1.11, b) x=0.76, and c) x=0.48.

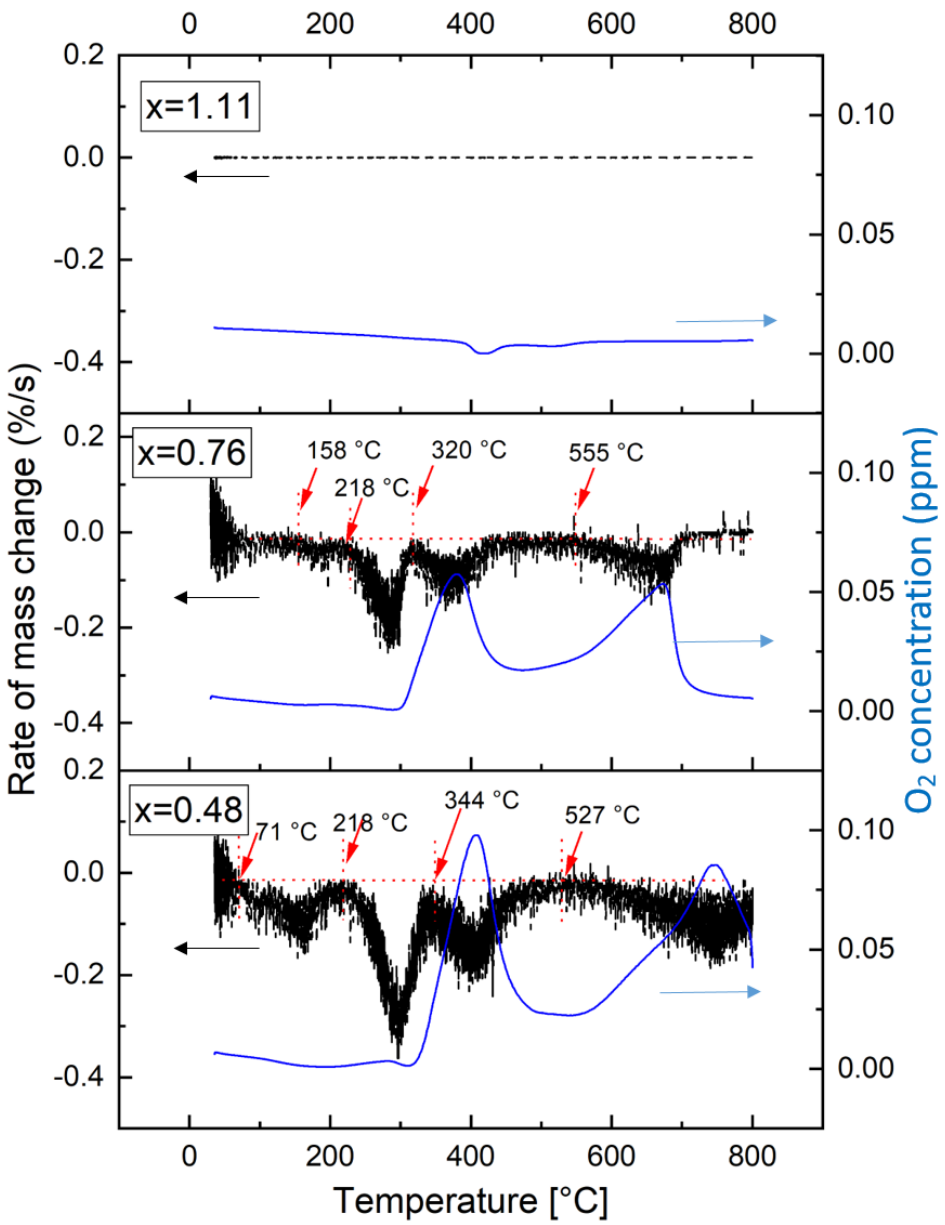

Fig. 4.20: Comparison of selected delithiation degrees by using the first derivative of the mass change percentage with time for commercially available $Li_xNMC442$ samples, regarding the mass loss and oxygen concentration measured by oxygen detector.

From the onset temperatures, rate of mass change and oxygen releasing, the sample with higher delithiated degree is less stable and more oxygen was produced. That indicates according to equation 4.5, as further delithiation, more materials in layered structure phase transfer to spinel and even rock-salt type phase. Similar to equation 4.2, the following phase transition took place [37]:

$$\mathrm{Li}_x\mathrm{TMO}_2\ \text{layered}(R\bar{3}m) \xrightarrow{\text{high temperature}} \mathrm{TM}_3\mathrm{O}_4\ \text{spinel}(Fd\bar{3}m) + \varepsilon\mathrm{O}_2$$

$$\mathrm{TM}_3\mathrm{O}_4\ \text{spinel}(Fd\bar{3}m) \xrightarrow{\text{increasing temperature}} \mathrm{TMO}\ \text{rock} - \text{salt}(Fm3m) + \varepsilon\mathrm{O}_2 \quad (4.5)$$

In addition, Zheng et al. [107] studied the thermal stability of chemically delithiated NMC samples by ab-initio computation and experimental methods TGA and XRD. They focused on

the formation of oxygen vacancies, proposing the reaction: $Li_xTMO_2 \rightarrow Li_xTMO_{2-\delta} + \delta/2 \cdot O_2$. Since pressure P and volume V changes of solids in the equation G=E+P·V-T·S are negligible [108], the Gibbs free energy equation can be simplified by following reaction:

$$\Delta G \approx \Delta H - T \cdot \Delta S \approx -E^0(Li_xTMO_2) + E^0(Li_xTMO_{2-\delta}) + \delta'/2E^*(O_2) - T \cdot \Delta S \qquad (4.6)$$

Here, E^0 and E* are compound's Gibbs energy at 0 K and at 298 K, respectively. These calculations were performed at 0 K, but the standard formation enthalpy were obtained at 298 K. Therefore one potential source of error of this calculation is the enthalpy differences of metal oxides between 0 K and 298 K. This error has been reported to be negligible [108]. They calculated the formation enthalpy of an oxygen vacancy and found that the formation enthalpy is closely correlated to the local coordination structure unit (LCSU), as demonstrated in Fig. 4.21. Fig. 4.21 a) establishes the studied compositions NMC333, NMC622, NMC532, and NMC442. One fully lithiated unit is shown in Fig. 4.21 b), which has one oxygen atom in center, three Li atoms, two Ni atoms and one Co atom around. When the positive electrode charged, Li atoms are extracted from NMC materials, so the Li-O bindings will reduce. The unit of an oxygen and TM bonds are shown in Fig. 4.21 c). For instance, when delithiated, oxygen atom can be surrounded by two Li atoms, and three Ni atoms, which is group named "NNN-2Li" in Table 4.12. Table 4.12 lists onset temperatures and mass losses for LCSU groups' decomposition in different compounds.

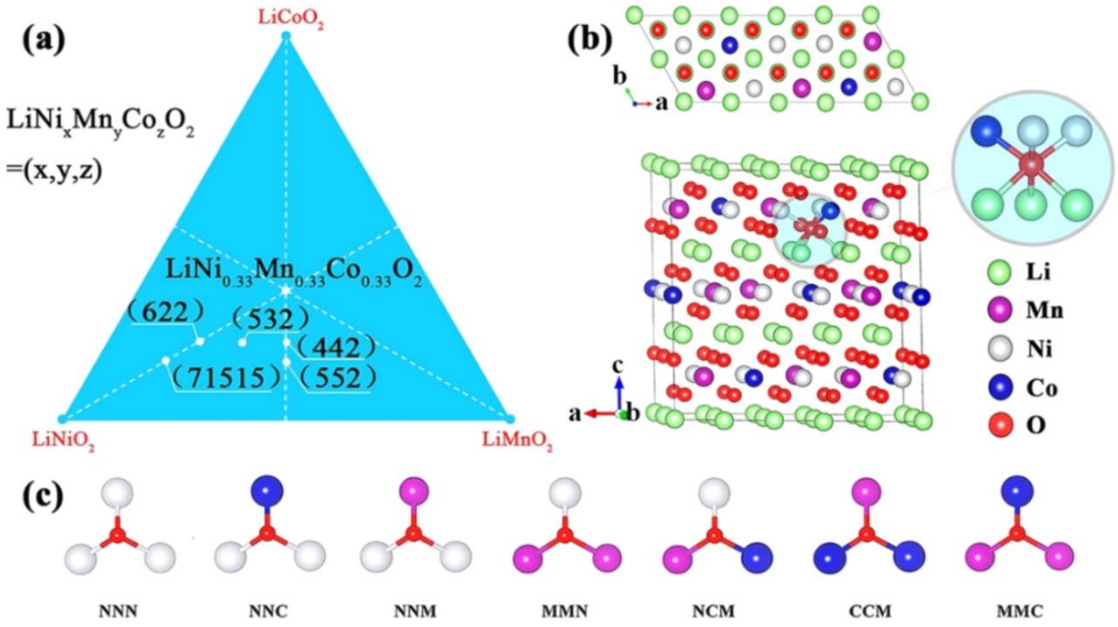

Fig. 4.21: Zheng et al. studied NMC materials: a) compositions in phase triangle, b) schematic illustration of NMC532 structure, and enlargement of one unit with O in center; c) the oxygen and TM bonds in NMC materials. The corresponding names are used in Table 4.12 [107].

In Table 4.12, onset temperature for NNC-2Li group in $Li_{0.75}$NMC442 is 280 °C with mass loss 1.4 %; for $Li_{0.50}$NMC442 is 260 °C with mass loss 2.0 %. The mass losses mentioned here is relative to the NMC materials, while the mass loss ratio in Table 4.12 are relative to the total oxygen content in NMC materials. Since NNC-2Li and NNC-Li groups are energy favorite LCSU, other LCSU groups will decompose following with mass loss and heat release. In Fig. 4.19 and 4.20, the onset temperature of $Li_{0.76}$NMC442 and $Li_{0.48}$NMC442 are 158 °C and 71 °C respectively, lower than the prediction in Table 4.12. The decomposition of the energy favorite LCSU could be one of the reactions corresponding to mass losses and thermal effects at 280 °C

for $Li_{0.76}$NMC442 and at 260 °C for $Li_{0.48}$NMC442. Therefore, heat flux and mass loss in this work, indicate multi-reactions. The accompanying mass change of $Li_{0.76}TMO_2$ and $Li_{0.48}TMO_2$ are 6.0 % and 11.9 %, as illustrated in Fig. 4.19.

Table 4.12 A summary of energy favorite LCSU, corresponding to onset temperature (TG) and weight loss (mass loss ratio relative to the total oxygen content in NMC materials) of the first stage of oxygen loss at SOC25 and SOC50.

$Li_{1-x''}TMO_2$		NMC Compounds			
		333	**442**	**532**	**622**
X''=0.25	LCSU group	NCM-2Li	NNC-2Li	NNM-2Li	NNN-2Li
	TG (°C)	315	280	250	205
	mass loss ratio	0.024	0.042	0.045	0.054
X''=0.5	LCSU group	NCM-Li	NNC-Li	NNM-Li	NNN-Li
	TG (°C)	310	260	210	190
	mass loss ratio	0.042	0.061	0.085	0.115

The produced gases are measured by the mass spectrometer, and the results are presented in volume percentage in Fig. 4.22. Some nitrogen and oxygen are observed at the beginning of the pristine sample measurement, as air may be introduced in the calorimeter. These results measured by MS correspond well to the oxygen concentrations showing in Fig. 4.20, which were measured by oxygen detector. During the course of heating, there are two oxygen peaks detected in both delithiated samples. For $Li_{0.76}$NMC442, the maximum values of oxygen concentration peaks are 0.06 ppm at ~380 °C and 0.05 ppm at ~674 °C in Fig. 4.20 b). In Fig. 4.22 b), the peak of oxygen volume percentage were 6.3 % at 377 °C and 5.2 % at 672 °C. While, for $Li_{0.48}$NMC442 sample, the maximum values of oxygen concentration peaks are 0.10 ppm at ~407 °C and 0.09 ppm at ~742 °C in Fig. 4.20 c), where the oxygen is produced continuously till the terminal of the measurement. In Fig. 4.22, oxygen peaks with volume percentage 11.3 % and 8.7 % were observed at 405 °C and 749 °C. These results by measured MS and Zirox are in very good agreement. Two oxygen peaks are corresponding to the route of the structural variation from layered to spinel structure and from spinel to rock-salt structure (equation 4.5).

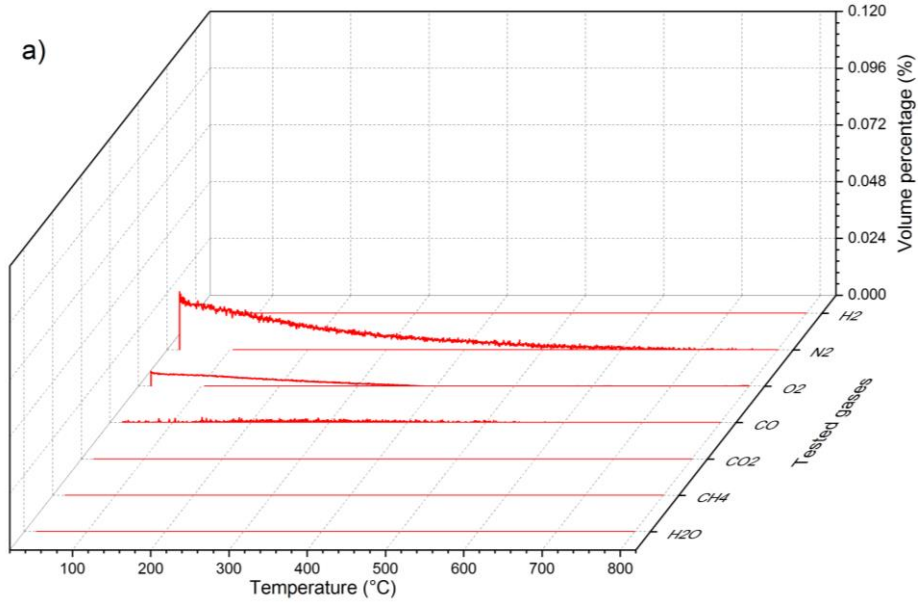

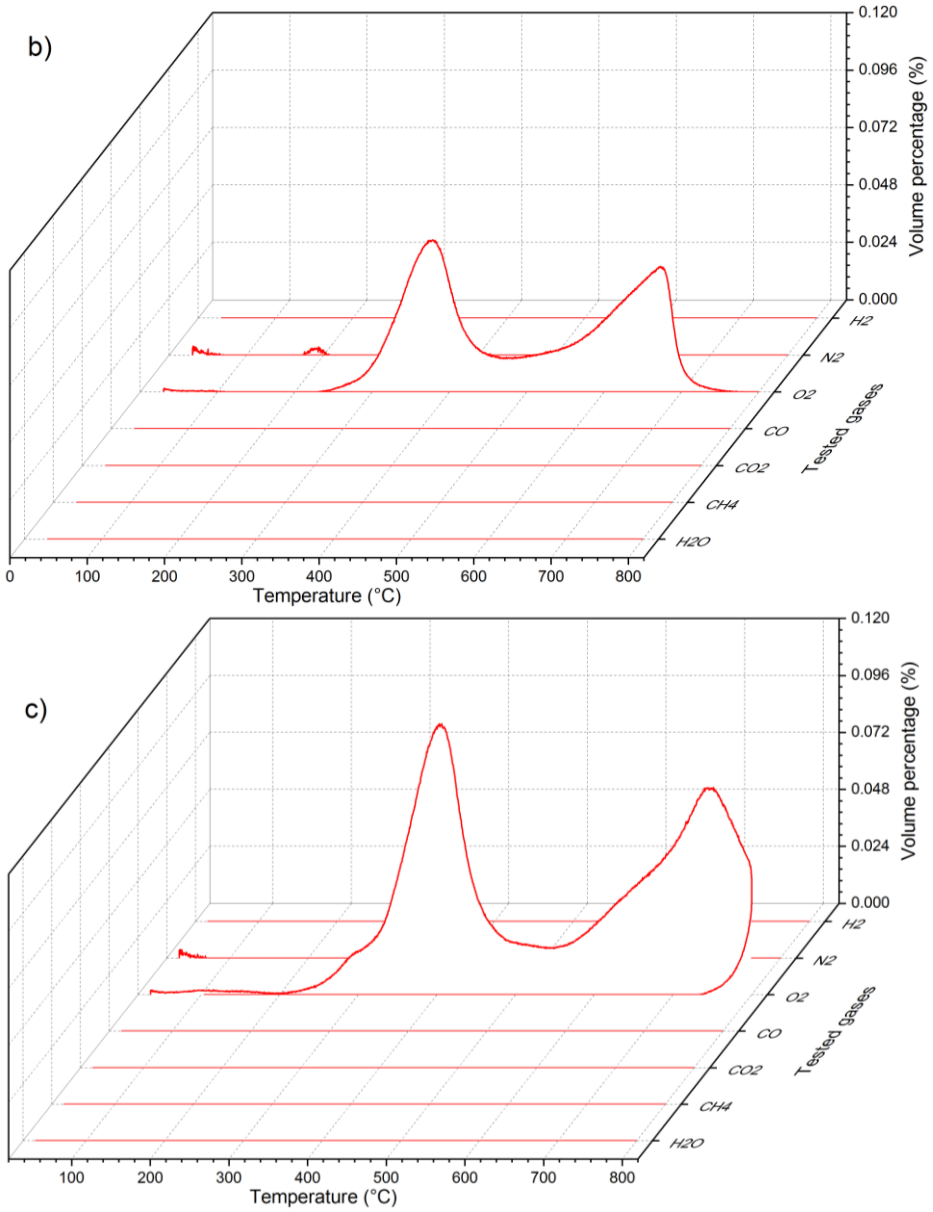

Fig. 4.22: Mass spectroscopy analysis for pristine and chemically delithiated commercial $Li_xNMC442$ samples: a) x=1.11, b) x=0.76, and c) x=0.48.

Since Ni^{2+} and Co^{3+} are the electrochemically active ions in NMC442 positive electrode materials, their oxidation states in the delithiated samples are Ni^{3+}, Ni^{4+}, and Co^{4+}. Upon heating, oxygen vacancies are formed in the structure, and TM cation is reduced to lower oxidation states, in order to maintain the overall charge neutrality [94]. The thermal stability of the NMC442 materials is significantly affected by the amount of Ni^{3+} and Ni^{4+}, which increases with the degree of delithiation. This is the underlying reason of the appearance of a large amount of oxygen vacancies at a high degree of delithiation. However, with additional loss of TM during chemical delithiation, this is all just qualitative explanation.

Complementary results are obtained from XRD investigation to determine the phases of the specimens after STA/MS measurement. Fig. 4.23 shows the results of Rietveld refinement: a) the pristine commercial NMC442 maintains the layered structure. Comparing to the commercial NMC442's structure before STA/MS measurement, the coalescence of the (006)/(012) and (018)/(110) peaks indicate an increase in the lattice parameters a and a decrease in c. The lower intensity ratio of (003)/(104) implies a less cation mixing after heat treatment up to 800 °C. b) Three phases with layered structure (space group $R\bar{3}m$), spinel

structure (space group $Fd\bar{3}m$), and rock-salt structure (space group $Fm\bar{3}m$) are found to be coexistent in the sample. The previous chemical delithiation probably proceeds as an onion model, and the Li ions in core are not extracted, so that the layered structure maintains, qualitatively similar to pristine powders. The intensity of the reflection $(111)_{spinel}$ and $(200)_{rock\text{-}salt}$ demonstrates the proportion of spinel and rock-salt structures, which are approximately 50 % and 46 %, respectively. c) For the deep delithiated sample, spinel structure and rock-salt structure were found, and the maximal reflection $(003)_{layered}$ totally disappeared. The reflection $(200)_{rock\text{-}salt}$ has a much higher intensity than $(111)_{spinel}$, indicating that rock-salt phase proportion increases. The formation of rock-salt phase is positively proportional to the delithiation degree, accompanying with oxygen release.

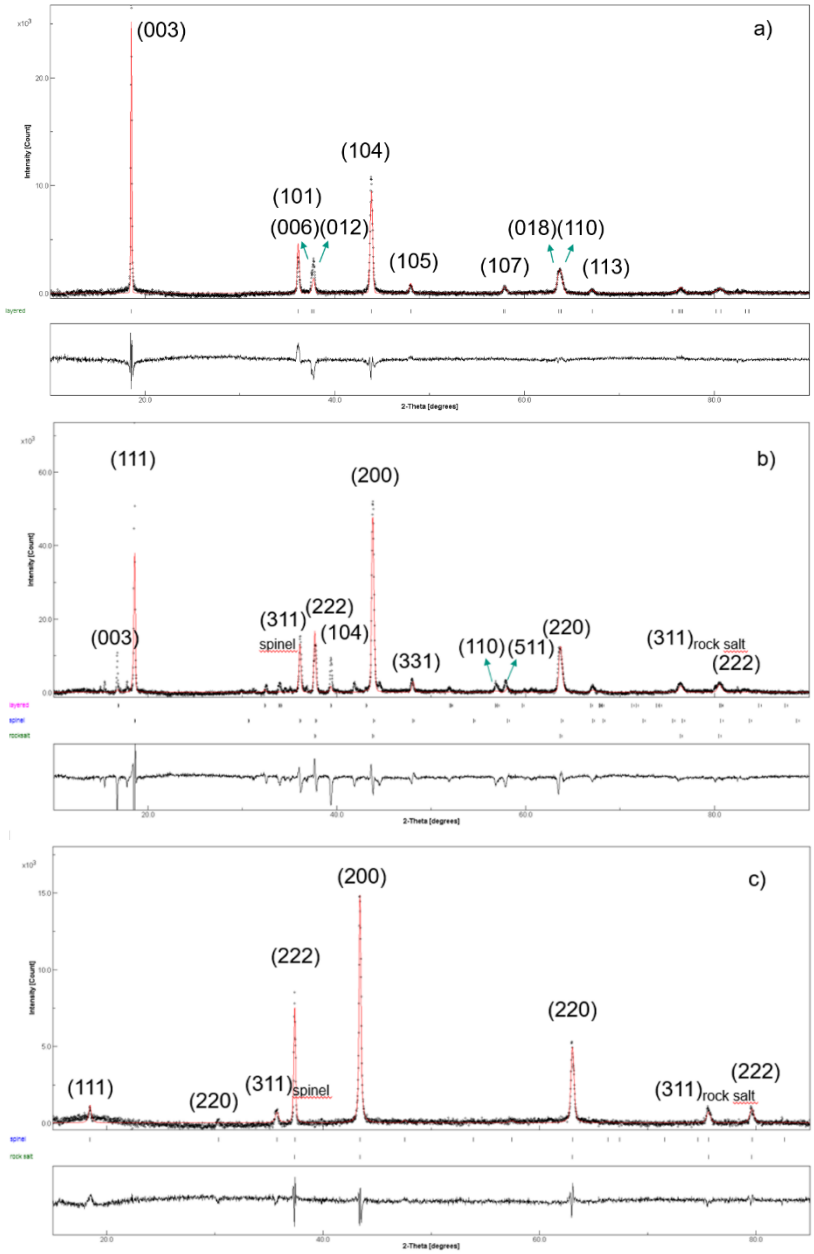

Fig. 4.23: The XRD patterns and Rietveld refinement curves of pristine and chemically delithiated commercial $Li_xNMC442$ after STA/MS measurement with maximum temperature 800 °C (black curve: measured, red curve: refined): a) x=1.11 b) x=0.76 c) x=0.48.

Enthalpy analysis for NMC442 and chemical delithiated NMC

The enthalpy of the drop solution is listed in Table 4.13, with corresponding uncertainties. Enthalpies of the drop solution are increasing with further delithiation in specimens, which are 100.82±0.86 kJ/mol, 101.92±0.77 kJ/mol and 107.56±1.84 kJ/mol for pristine, medium and high degree delithiated specimens, respectively. To calculate enthalpies of formation from the oxides, the oxidation state of TM have to be determined firstly.

Koyama et al. [109] used the first principle to calculate the oxidation states of transition metals' changes when Li is extracted from the positive electrode material. They reported that the oxidation reactions proceeded three stages depending on the Li content x in $Li_{1-x}[Ni_{1/3}Co_{1/3}Mn_{1/3}]O_2$: 0<x<2/3, redox couple $Ni^{2+/3+}$, $Ni^{3+/4+}$ (Ni^{3+} is an unstable interphase); and 2/3<x<1, redox couple $Co^{3+/4+}$. Kim and Chung [110] experimentally investigated the same issues, demonstrating that Ni^{2+} was oxidized to Ni^{4+} at around 3.75 V and the oxidation reactions of $Co^{3+/4+}$ seem to occur in the entire range of charging. Their experimental results could partially prove Koyama's calculations. The disagreement between the experimental and calculated results is because the assumption for the calculation deviates from the actual state of particles, which are in a non-equilibrium heterogeneous state instead of the homogeneous state. The difference is understandable and both could be considered as references.

With increasing Ni content i.e. $LiNi_{0.5}Mn_{0.3}Co_{0.2}O_2$, the transition metal redox evolution in electrodes was found to be similar: charging to 4.2 V, both $Ni^{2+/3+/4+}$ and $Co^{3+/4+}$ redox couples involved; and further charging to 4.5 V, only oxidation of $Co^{3+/4+}$ was observed. At 4.5 V, there remained approximately 20 % of Ni^{2+} on the electrode surface [111]. In this work, the oxidation states of Ni and Co in pristine NMC442 sample are considered as 2+ and 3+. The oxidation states of Ni in delithiated samples are simplified to the mixture of 2+ and 4+. As shown in thermodynamic cycle Fig. 4.24, the enthalpy of formation is calculated based on the oxygen content (measured by ICP-OES). Since Co_2O_3 (Co^{3+}) and Ni_2O_3 (Ni^{3+}) are unstable under normal conditions, the parameters of CoO (Co^{2+}), CoO_2 (Co^{4+}), MnO_2 (Mn^{4+}), Li_2O (Li^+) and NiO (Ni^{2+}), NiO_2 (Ni^{4+}) are used in calculation.

The enthalpy increment from room temperature to 974 K, is calculated using Gibbs energy, according to the calculation for pure elements [112]. For composition $Li_{1-x}Ni_{0.4}Mn_{0.4}Co_{0.2}O_2$, when x=0, the equation for enthalpy of formation from the oxides and elements are summarized in equation 4.7 and 4.8, respectively:

$$\begin{aligned}\Delta_f H^{\theta,oxide}_{Li_{1-x}Ni_{0.4}Mn_{0.4}Co_{0.2}O_2} &= \frac{1-x}{2}\cdot\Delta_{ds}H_{(Li_2O)} + 0.4\cdot\Delta_{ds}H_{(NiO)} + 0.4\cdot\Delta_{ds}H_{(MnO_2)} \\ &+ \frac{0.2}{2}\cdot(\Delta_{ds}H_{(CoO_2)}+\Delta_{ds}H_{(CoO)}) + \frac{0.1}{2}\int_{298}^{974} C_{p(O_2)} \\ &- \Delta_{ds}H_{(Li_{1-x}Ni_{0.4}Mn_{0.4}Co_{0.2}O_2)}\end{aligned} \tag{4.7-1}$$

$$\begin{aligned}\Delta_f H^{\theta,elements}_{Li_\alpha Ni_\beta Mn_\gamma Co_\delta O_\varepsilon} &= \Delta_f H^{\theta,oxides}_{Li_\alpha Ni_\beta Mn_\gamma Co_\delta O_\varepsilon} + \frac{\alpha}{2}\cdot\Delta_f H_{(Li_2O)} + \beta\cdot\Delta_f H_{(NiO)} + \gamma\cdot\Delta_f H_{(MnO_2)} + \frac{\delta}{2} \\ &\cdot(\Delta_f H_{(CoO_2)}+\Delta_f H_{(CoO)})\end{aligned} \tag{4.8-1}$$

Assuming x=0.8 in $Li_{0.2}Ni_{0.4}Mn_{0.4}CoO_2$ material, Ni^{2+} ions are completely oxidized to Ni^{4+}, which ends up with $Li^+_{0.2}Ni^{4+}_{0.4}Mn^{4+}_{0.4}Co^{3+}_{0.2}O_2$ materials. When x>0.8, CoO_2 will replace CoO partially in equation 4.7 and 4.8. When 0<x<0.8, NiO_2 will replace NiO partially. For example, the

medium degree delithiated sample $Li_{0.76}Ni_{0.41}Mn_{0.42}Co_{0.17}O_{2.10}$, will be $Li^{+}_{0.76}Ni^{4+}_{0.12}Ni^{2+}_{0.29}Mn^{4+}_{0.42}Co^{3+}_{0.17}O_2$ (equation 4.7-1) and (equation 4.8-1) are corresponding calculations:

$$\Delta_f H^{\theta,oxide}_{Li_{0.76}Ni_{0.41}Mn_{0.42}Co_{0.17}O_{2.10}} = \frac{0.76}{2}\cdot \Delta_{ds}H_{(Li_2O)} + 0.29\cdot \Delta_{ds}H_{(NiO)} + 0.12\cdot \Delta_{ds}H_{(NiO_2)} + 0.42\cdot \Delta_{ds}H_{(MnO_2)} + \frac{0.17}{2}\cdot (\Delta_{ds}H_{(CoO_2)} + \Delta_{ds}H_{(CoO)}) + \left[2.10 - \left(\frac{0.76}{2} + 0.29 + 0.12\cdot 2 + 0.42\cdot 2 + 0.17\cdot 1.5\right)\right]\cdot \int_{298}^{974} C_{p\left(\frac{1}{2}O_2\right)} - \Delta_{ds}H_{(Li_{0.76}Ni_{0.41}Mn_{0.42}Co_{0.17}O_{2.10})} \quad (4.7\text{-}2)$$

The enthalpy of formation from elements was calculated by using the following equation:

$$\Delta_f H^{\theta,elements}_{Li_{0.76}Ni_{0.41}Mn_{0.42}Co_{0.17}O_{2.10}} = \Delta_f H^{\theta,oxides}_{Li_{0.76}Ni_{0.41}Mn_{0.42}Co_{0.17}O_{2.10}} + \frac{0.76}{2}\cdot \Delta_f H_{(Li_2O)} + 0.29\cdot \Delta_f H_{(NiO)} + 0.12\cdot \Delta_f H_{(NiO_2)} + 0.42\cdot \Delta_f H_{(MnO_2)} + \frac{0.17}{2}\cdot (\Delta_f H_{(CoO_2)} + \Delta_f H_{(CoO)}) \quad (4.8\text{-}2)$$

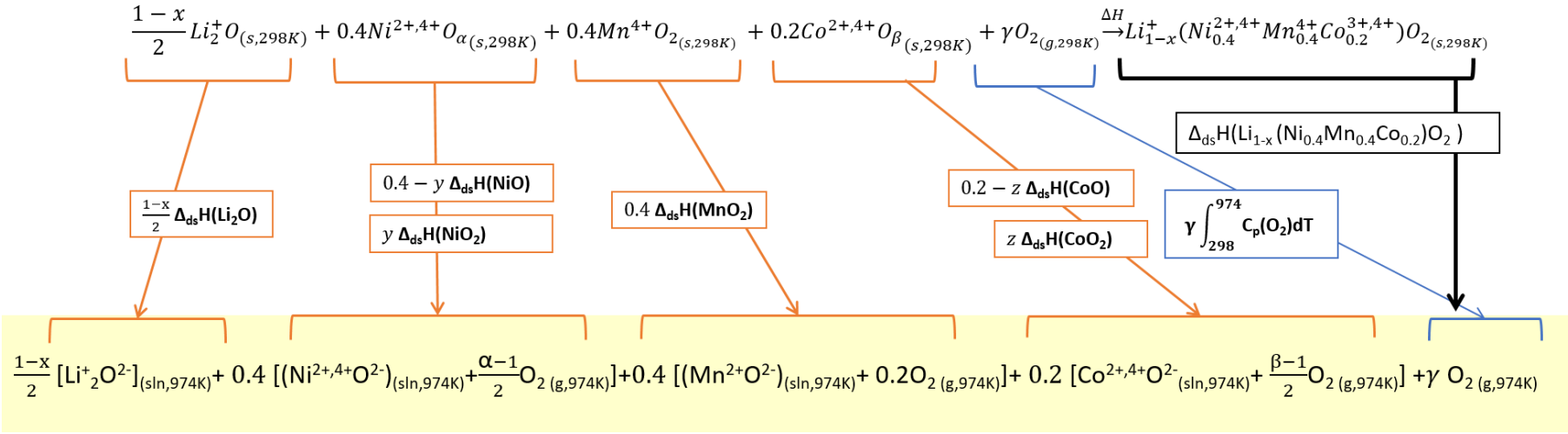

Fig. 4.24: Thermodynamic cycle. First line: the formation enthalpy of various NMC composition from the binary oxides and oxygen. Second line: the measured enthalpies of drop solution of the binary oxides. Last line: the (oxidation) states of the species in the molten solution at 974 K [113].

Table 4.13 Enthalpies of drop solution, enthalpies of formation from the oxides and from the elements at P=0.1 MPa of the investigated specimens, as well as enthalpies of drop solution of binary oxides from literature.

Nominal stoichiometry	Enthalpy of drop solution (kJ/mol)	Enthalpy of formation from the oxides (kJ/mol)	Enthalpy of formation from the elements (kJ/mol)
$Li_{1.11}Ni_{0.42}Mn_{0.41}Co_{0.17}O_{2.08}$	100.82±0.86	-75.88±1.61	-769.46±2.11
$LiNi_{0.4}Mn_{0.4}Co_{0.2}O_2$	98.86±1.09(18)[e]	-75.35±1.65[e]	-726.59±1.72[e]
$Li_{0.76}Ni_{0.41}Mn_{0.42}Co_{0.17}O_{2.10}$	101.92±0.77	-61.88±1.24	-675.95±1.59
$Li_{0.48}Ni_{0.38}Mn_{0.46}Co_{0.16}O_{2.07}$	107.56±1.84	-57.57±1.97	-607.44±2.08
Li_2O	-93.02±2.24[a,b]		-597.935±0.334[c]
MnO_2	128.92±0.91[d]		-521.493±0.836[c]
NiO	35.73±0.95[a]		-239.743±0.543[c]
NiO_2	20.98±0.69[f]		-449.166[f]
CoO	15.35±0.46[a]		-238.906±1.255[c]
CoO_2	70.9±0.8[b]	-44.6±1.0[b]	-283.506±2.255*

The expanded uncertainties U were given behind the symbol ±, which is calculated as U=k*u*.

Here, u is the standard uncertainty and the value of the coverage factor k is 2. Therefore, the confidence interval of U is 95 percent. [a][114] [b][115] [c][116] [d][117] [e][113] [f][118], * calculated by the data from literatures [115] and [116].

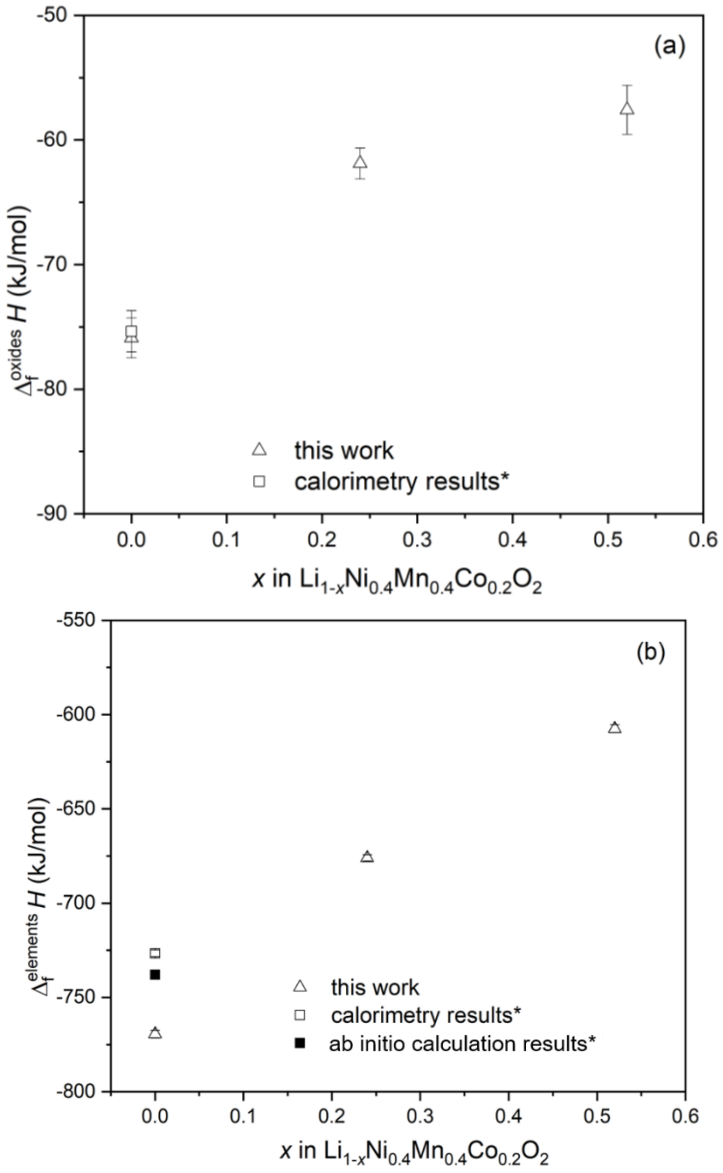

Fig. 4.25: Enthalpy of formation from a) oxides and b) elements versus delithiation degrees, in comparison with *Masoumi et al.'s work [113].

In Fig. 4.25, the enthalpies of formation from oxides and elements are demonstrated, which are in good agreement with Masoumi et al.'s [113] experimentally measured and the ab-initio calculated results [113]. The further delithiated specimens have less negative enthalpy value, which is considered to be less stable. The oxidation states of Ni and Co are complex in thermal cycle's calculation, and introducing different oxides reflects the real energetic trend.

4.4 Conclusion

Synthesis of $LiNi_xMn_{0.8-x}Co_{0.2}O_2$

$LiNi_xMn_{0.8-x}Co_{0.2}O_2$ particles in nano-meter scale were synthesized via sol-gel method. With this method the content of transition metals in samples were well controlled, however, Li loss was found in Ni-rich samples. The calcination temperature was optimized by increasing the heat treatment temperatures with Ni content rise. An improvement of crystallization was observed although losing more Li in the samples.

Evaluation of chemical delithiation with $(NH_4)_2S_2O_8$

It is noteworthy to point out the difference between chemical delithiation and electrochemical delithiation. The pH value of the solution is heedfully controlled to 7, since it impacts the oxidation potential of the redox couples. The redox couple $S_2O_8^{2-}/2SO_4^{2-}$ has a standard oxidation potential 5.05 V versus Li^+/Li, which is much higher than the operating potential 4.2 V. The large over potential is prone to extract Li ions severely, leading to local "Li ions vacuum" and inhomogeneous concentration, which contributes to the particle level heterogeneity according to Ref. [119]. As the NMC particles were immersed in the oxidizing reagent solution, the delithiation process is limited by the bulk diffusion, engendering a uniformity at the bulk level as well. The Ni/Li cation mixing in the pristine specimen might be the reason for Ni cations dissolving in the oxygen reagent. Therefore, the composition of the samples prepared via chemical delithiation depart from the electrical delithiation. Our investigation based on the chemical delithiation samples can only reflect the tendency of thermal stability during chemical delithiation.

5 Thermal behavior studies of LiB under normal operation and thermal abuse scenarios

To improve the thermal stabilities of LiB, the thermal behavior is studied in this chapter. In first part, the specific heat capacity of investigated cells was determined. After that, the thermal behavior under normal operating scenario at different charging/discharging rates was investigated, which deepens the understanding of the heat generation in LiB during cycling. In the last part, thermal runaway measurements were performed to investigate the thermal behavior of LiB under thermal abuse scenario. The experimental determined thermal properties can be used in thermal management system.

5.1 Literature review

The heat generation of LiB during cycling can be separated as reversible and irreversible heats. The reversible heat is generated due to the entropy effects in reversible reactions. The irreversible heat is generated due to the irreversible reactions and impedances during cycling. In the literature review, some researches in this field are introduced. In addition, the thermal runaway measurements are also introduced under thermal abuse conditions. There are some calorimetric studies on the whole cells such as thermal runaway tests, and the calorimetric studies on the components such as electrolyte and electrodes of LiB.

5.1.1 Heat generation and entropy measurements

Saito et al. [120] studied thermal and chemical properties of a lithium secondary battery with $LiCoO_2$ as positive electrode active material using a Tian-Calvet C80 calorimeter. Commercially available cells with a nominal capacity of 500 mAh were investigated. The specific heat capacities of the cell at selected SOCs were measured by the scanning method. The selection of the SOCs was based on the measured curves of the heat flow rate during discharge at critical positions such as a maximum or a minimum, which is demonstrated in Fig. 5.1. Fig. 5.1 shows the heat generation curve of a Lithium-ion battery during discharge under a constant current of 50 mA.

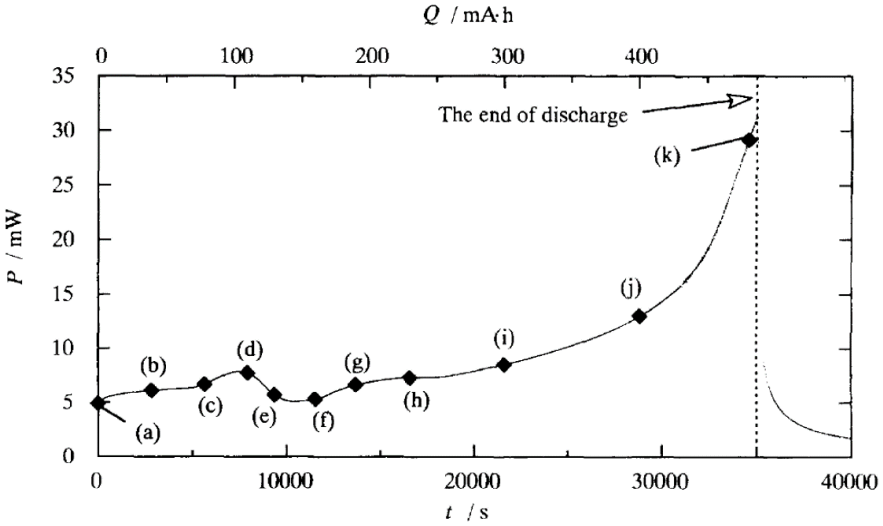

Fig. 5.1: Heat generation curve of a 500 mAh LiB during discharge at 50 mA (C/10 rate) constant current. Q means quantity of electricity discharged from full charged state of the battery. Symbols ◆ on curve are plotted at Q where the apparent specific heat capacity of the battery is evaluated: (a) 0 mAh (SOC100), (b) 40 mAh (SOC92), (c) 80 mAh (SOC84), (d) 110 mAh (SOC78), (e) 130 mAh (SOC74), (f) 160 mAh (SOC68), (g) 190 mAh (SOC62), (h) 230 mAh (SOC54), (i) 300 mAh (SOC40), (j) 400 mAh (SOC20), and (k) 480 mAh (SOC4) [120].

Fig. 5.2 depicts heat flow rates and voltages change against time for cells at various states of charge under same temperature program [120]. Fig. 5.2 (a)-(k) are corresponding to selected points in Fig. 5.1. The cells were measured under a scanning rate of 0.1 K/min in the temperature range of 303 K - 343 K. Endothermic peaks (marked by ○ in Fig. 5.2 (d) and (e)) at positions in (d) and (e), were observed in the heat flow rate curve. Based on the research of Reimers and Dahn [106], Saito suggested that the positive electrode material $LiCoO_2$ had the monoclinic structure at states (d) SOC78 and (e) SOC74. With increasing temperature, the monoclinic structure transformed to the hexagonal structure. Endothermic peaks observed in Fig. 5.2 (d) and (e) indicate this phase transition. The voltage (dot line) has a linear relationship against time, seeing the red line in Fig. 5.2 (b) SOC92. At same time, the temperature is increasing with scanning rate 0.1 K/min. Except at the positions (a) SOC100, (j) SOC20 and (k) SOC4, all voltages decrease linearly with increasing temperature. Since ΔV and ΔT have a linear relationship, the value of ΔV/ΔT is constant. The value of ΔV/ΔT implies the entropy change of reversible reactions, according to equation (2.11). At states (a), (j) and (k), a non-linear behavior is observed because the influence of the lithium ions diffusion dominates at states (a), (j) and (k), where relatively large amount of lithium ions intercalate into or deintercalate from the electrodes.

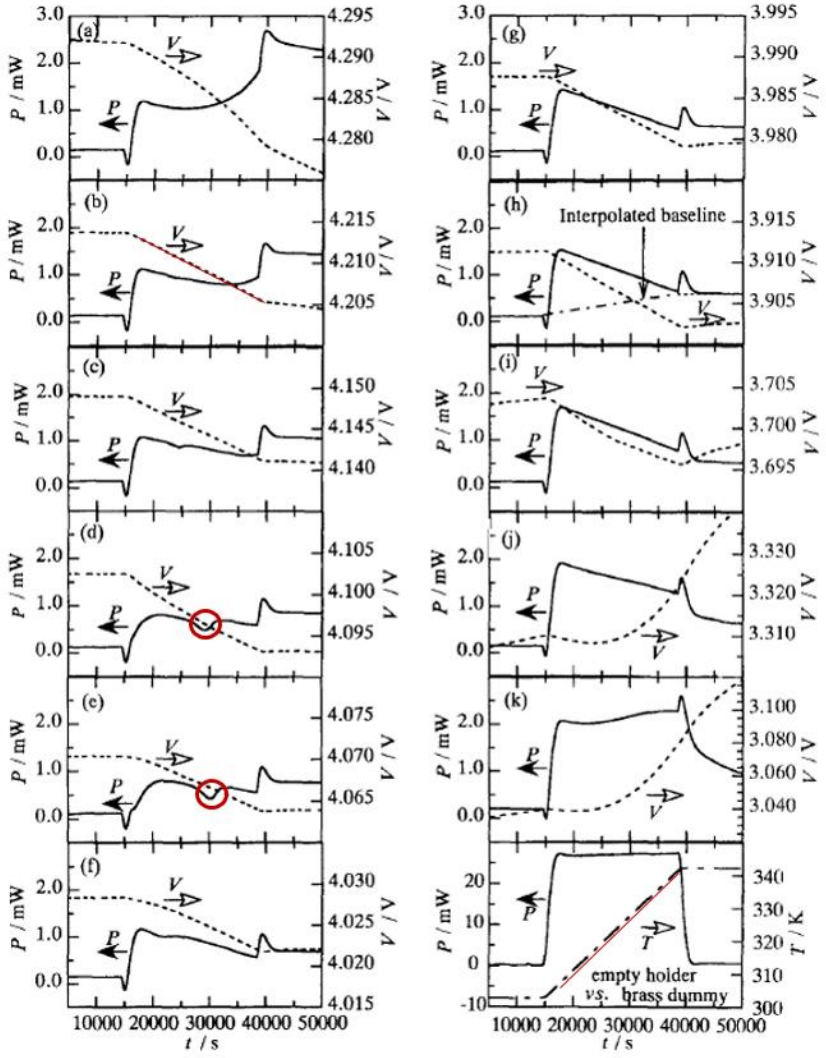

Fig. 5.2: Heat flow rate and its voltages at SOC (a) 100, (b) 92, (c) 84, (d) 78, (e) 74, (f) 68, (g) 62, (h) 54, (i) 40, (j) 20, and (k) 4, and last diagram shows the temperature program [120].

Schmidt et al.'s research [121] also met these difficulties to measure the entropy of the cell at low SOCs, which was due to sluggish diffusion kinetics in their opinion. They measured A123 cells with $LiFePO_4$ and graphite. Murashko et al. [122] explained this phenomenon by the difficulty to reach equilibrium state at low SOCs, since the diffusivity of the Li^+ ions in graphite was increasing with decreasing SOC. A 2.3 Ah A123 cylindrical cell was tested with active materials of $LiFePO_4$. In this work during entropy measurement, it was also observed at high SOCs (100 % and 90 %) or low SOCs (0 % and 10 %), after a 24-hours relaxation that the quasi-equilibrium conditions cannot be reached. Besides all the above causes, Li diffusion was strongly influenced by located lithium concentration at fully charged or fully discharged states [120]. The entropy measurements are performed in the range of SOC80 to SOC20 with an interval of 10 %.

Osswald et al. [45] measured the entropy of commercially available 18650 cells with $LiNi_{1/3}Mn_{1/3}Co_{1/3}O_2$ and $LiNi_{0.8}Co_{0.15}Al_{0.05}O_2$ at a main operating temperature of 30 °C. The relaxation voltages (15 minutes) were measured at temperatures of 25 °C and 20 °C. At temperatures higher than 40 °C, the ageing process was accelerated due to the side reactions [123]. The cells were discharged from SOC100 with C/10 for 15 minutes, the interval thus was 2.5 % of the nominal capacity. A fast methodology for entropy measurements was proposed by subtracting the baseline from OCV curves. The voltages at 30 °C were connected to build as baseline (Fig. 5.3). Fig. 5.3 shows the relaxation behavior of cells at SOC100, SOC87, SOC57 and SOC20. The OCVs were plotted at different temperatures. So the slope $\Delta V/\Delta T$ was determined. In this work, the baseline subtraction was done to reduce the effects of non-equilibrium conditions.

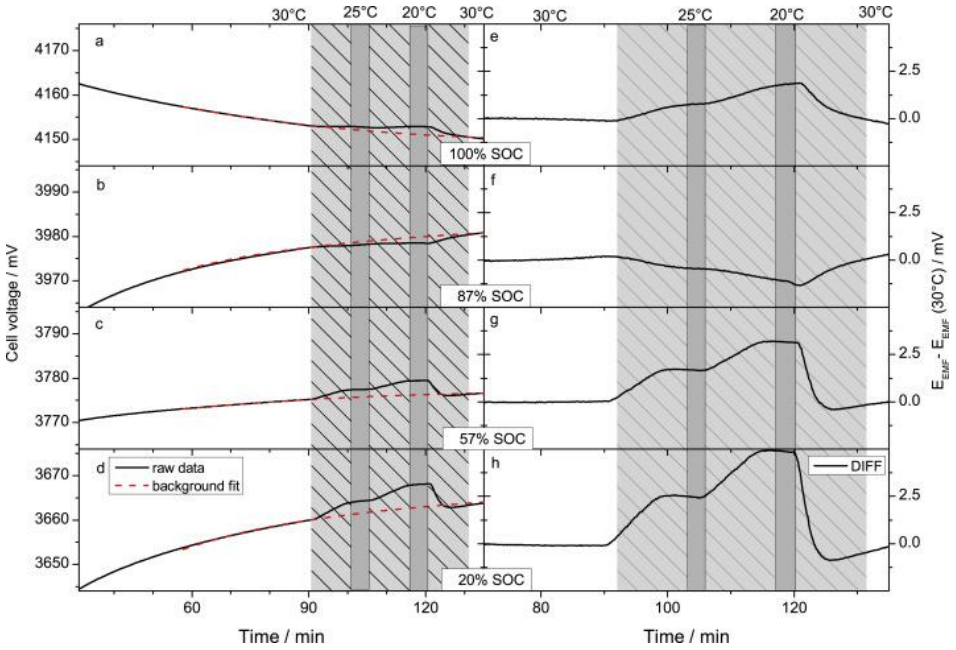

Fig. 5.3: Relaxation behavior of the cell voltage for NMC cell a) SOC100, b) SOC87, c) SOC57, and d) SOC20 including the voltage response of temperature changes to 25 °C and 20 °C respectively plotted with the mathematical fitted background. In e), f), g), h), the resulting subtraction of the measured voltage and the calculated relaxation background for the respective state of charge is shown [45].

Yazami [44] investigated the entropy change of carbonaceous negative electrode materials and $LiCoO_2$ (LCO) and $LiMn_2O_4$ as positive electrode materials by an electrochemical thermodynamic measurement system (ETMS). Half cells with metallic lithium as reference electrode were assembled in an argon glove box. The half cells were either fully charged for

carbon negative electrodes or fully discharged for positive electrodes as the initial state for entropy measurements. The entropy change curve of the natural graphite during discharge and the LCO positive electrode during charging are shown in Fig. 5.4 and Fig 5.5, respectively. In later researches [43, 126], the combined entropy changes were calculated for different positive/negative electrodes combinations based on half cells' entropy change.

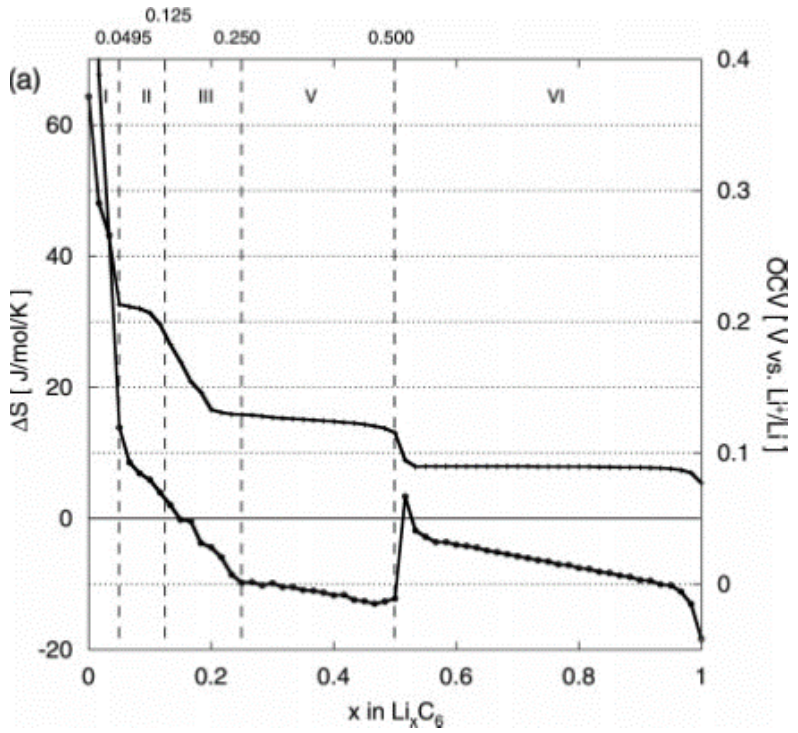

Fig. 5. 4: Entropy and OCV of lithiation during discharge of natural graphite [44].

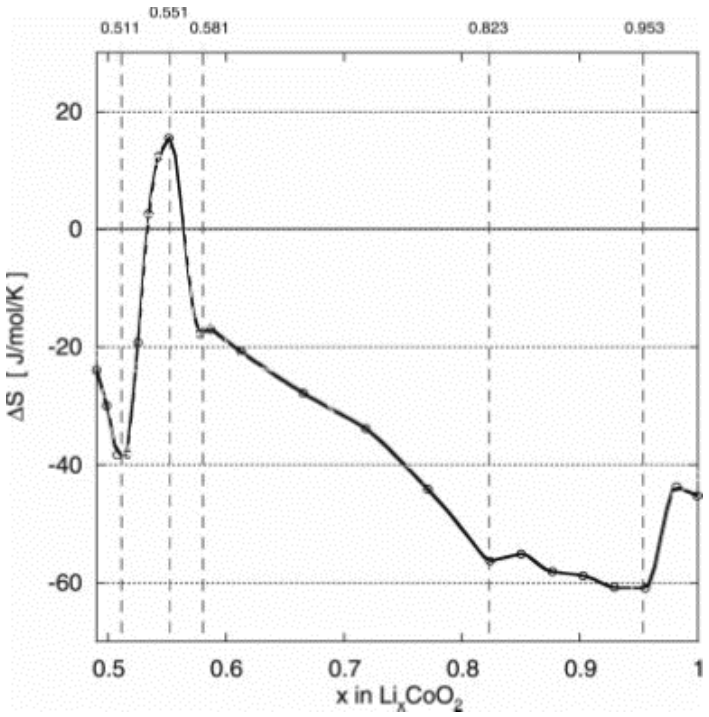

Fig. 5. 5: Entropy of lithium intercalation into Li_xCoO_2 [44].

In another publication of Maher and Yazami [124], the entropy change of full cells of LiBs with

graphite negative electrode and lithium cobalt oxide (LCO) positive electrode were studied. 2032 coin cells with capacity of 44 mAh were tested under C/4 rate current. The cells at different overcharge degree (4.3 V, 4.4 V, 4.5 V, 4.6 V, 4.7 V, 4.8 V and 4.9 V), were investigated through thermodynamic measurements. The entropy profiles are shown in Fig. 5.6. From fully discharged state (2.75 V), the cells were charged with 5 % SOC increments by applying a 6 mA constant current for 20 minutes at the ambient temperature. The relaxation time was not mentioned. When a constant OCV was reached, the temperature was decreased from 25 °C to 10 °C in step of 5 °C. The entropy and enthalpy changes of different overcharged cells (with cut-off voltage (COV): 4.3 V, 4.4 V, 4.5 V, 4.6 V, 4.7 V, 4.8 V and 4.9 V) in the full range of SOCs were compared. In Fig. 5.6, the maximum entropy shifts to lower SOCs as COV goes higher. The entropies at SOC0 increase with increasing COVs. Both phenomenon indicate that the entropy curves are shifting to lower SOCs as COV increasing.

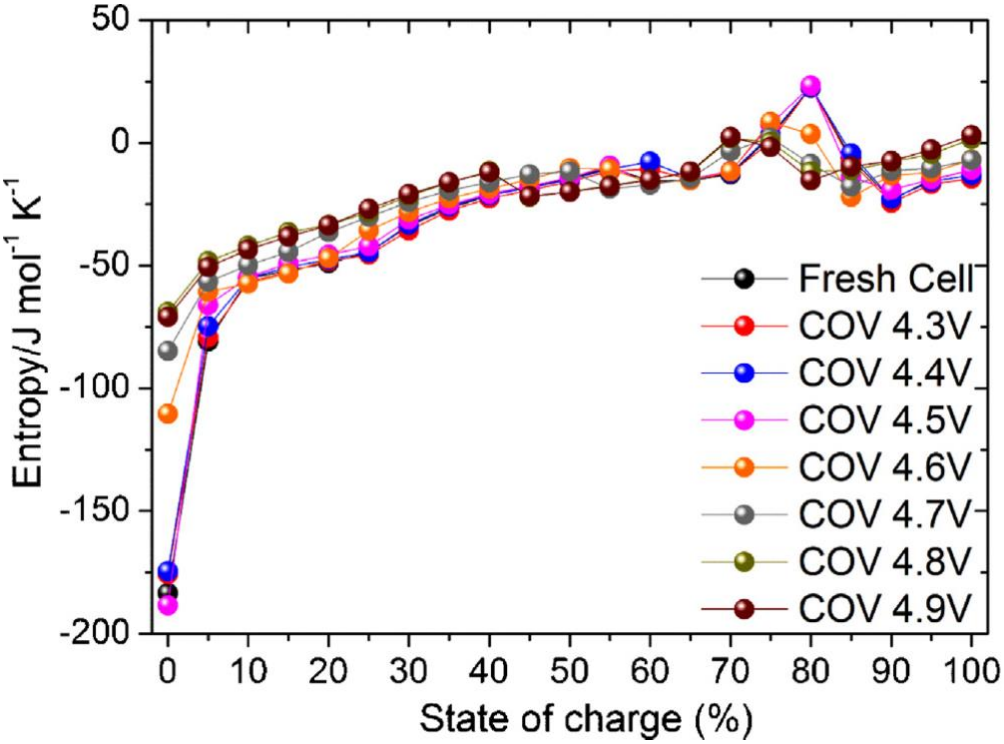

Fig. 5. 6: Entropy profiles of 2032 coin cells with capacity of 44 mAh (LCO/graphite) at different charge cut-off voltage (COV) [124].

Viswanathan et al. [43] investigated the entropy change of half cells with $LiFePO_4$ (LFP) as active material of positive electrode against Li and lithium titanate (LTO) as positive electrode against Li. After 3 cycles, the cells were fully discharged to start the entropy measurement at 35 °C. The charge process was also performed and stabilized at 35 °C. After equalization at 35 °C, 25 °C, and 15 °C, the OCV was defined at the end of the relaxation. They simulated the combined entropy change by the measured results of the negative and positive electrode in half cells.

Williford et al. [125] compared half cells with active materials of LCO and NMC. Similar to Ref. [126], the entropy measurements were performed. The voltages were measured after 15 minutes relaxation at 35 °C, 25 °C and 15 °C to determine entropy change. Fig. 5.7 and 5.8 compare entropy changes versus SOCs of LCO and NMC from the same manufacturer. Two curves as shown in Fig. 5.8 where two entropy measurements carried out on different days, were in good agreement. In conclusion, LCO was found to have a much larger entropy than NMC. NMC was much more thermodynamically stable than LCO.

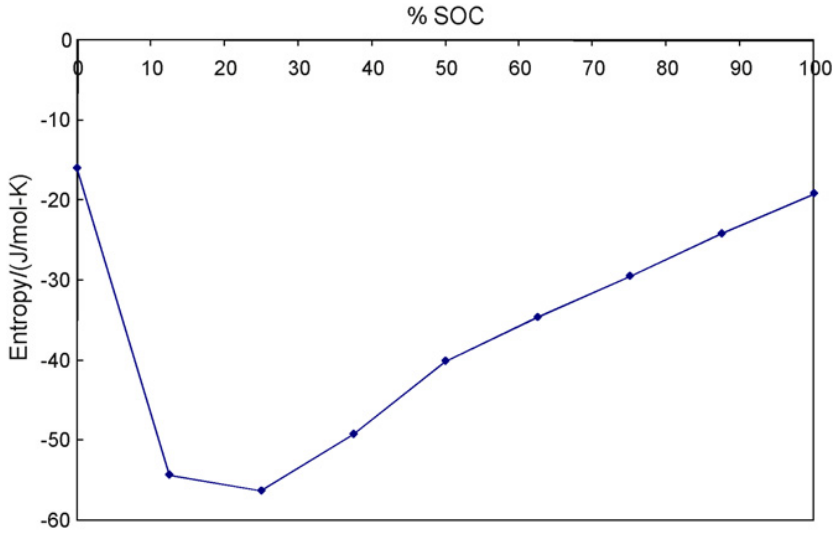

Fig. 5. 7 Entropy changes for commercially available $LiCoO_2$ positive electrode (LICO Technology Corporation) [125].

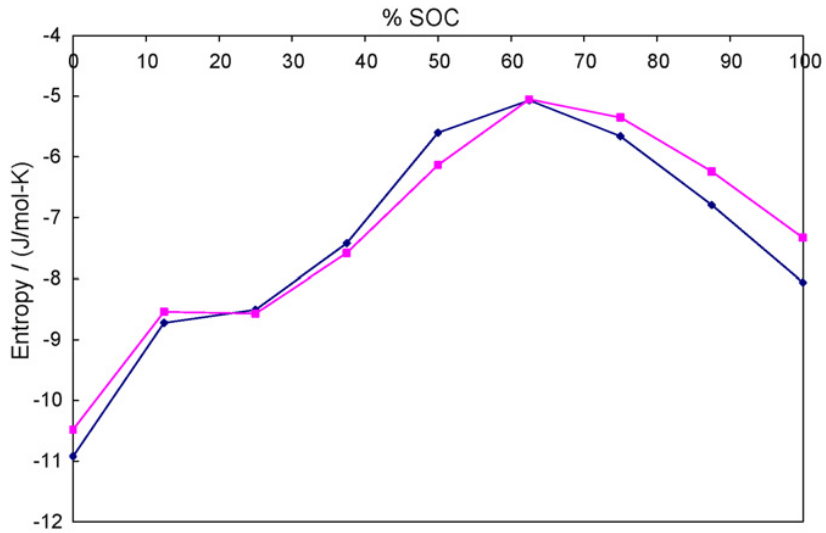

Fig. 5. 8 Entropy changes for commercial available $LiNi_xCo_yMn_zO_2$ (LICO Technology Corporation). The agreement between two runs (shown as two separate curves in the figure) on different days for the same cell is reasonable good [125].

Murashko et al. [122] determined the entropy change profile of A123 System 18650 cylindrical LiBs with LFP positive electrode (nominal capacity 2.3 Ah) by the potentiometric method and by a heat flux sensor. The cell was first discharged to determine the discharge capacity. After the cell was fully charged at 24 °C, the cell was discharged with a constant current of 3 A for 264 s. After reaching the selected SOCs, the relaxation time was 12 h. The OCVs were measured at 30 °C, 25 °C, 20 °C, and 30 °C. For the gradient heat flux sensor (GHFS) method, the cell relaxation period was only 30 min between charging and discharging pulses. The current pulses were charging and discharging 264 s under 3 A. They assume the irreversible heat was identical during charging and discharging. Therefore, based on total heat generation during charging/discharging, equation 2.11: $\dot{Q}_{tot} = \dot{Q}_{rev} + \dot{Q}_{irr}$, the reversible heat flux is half value of the difference of heat fluxes of charging and discharging ($\dot{Q}_{rev} = \frac{\dot{Q}_{dis} - \dot{Q}_{ch}}{2}$). The temperature changes on cell's surface was measured. Moreover, the thermal diffusivity inside the cylindrical cell was calculated by integrating the gradient heat flux (GHF). Based on the

reversible heat flux, the entropy change can be estimated using equation (2.17) $\dot{Q}_{rev} = T \cdot \Delta S \cdot \frac{i}{F}$. The results from the two methods showed a good agreement (Fig. 5.9).

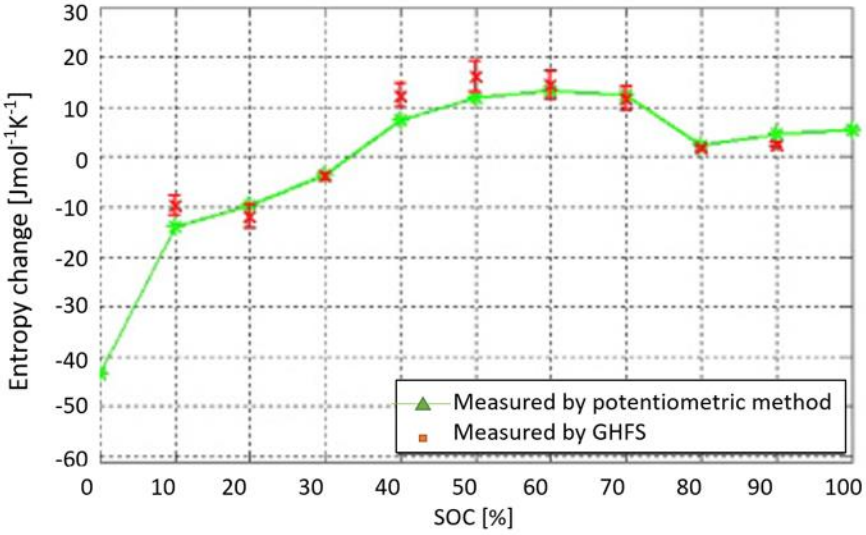

Fig. 5. 9: Entropy change of 18650 cells with capacity of 2.3 Ah (LFP positive electrode) measured by the potentiometric method and by using the gradient heat flux sensor (GHFS) [122].

Jalkanen et al. [126] studied the entropy change influence on the thermal behavior of a LFP/graphite LiB at different SOCs. The tested cells were one prismatic, pouch-type cell with a nominal capacity of 42 Ah, LFP half cells and graphite half cells. The entropy changes of full cells and half cells were measured at 20 °C. After achieving the desired SOC, the cell was stabilized for 20 h at 20 °C. Afterwards, the temperature was increased in steps of 10 °C from 0 °C to 40 °C. For each temperature step, a stabilization time of 1.5 h was chosen, and the average voltage value for the last 30 minutes was used in later calculation, as shown in Fig. 5.10. The entropy change of half cells and full cells were compared in Fig. 5.11. The full cell entropy change can be calculated based on half cells' entropy change:

$$\Delta S_{full\ cell,discharge} = \Delta S_{LFP,reduction} + \Delta S_{graphite,oxidation} = \Delta S_{LFP,reduction} - \Delta S_{graphite,reduction} \quad (5.1)$$

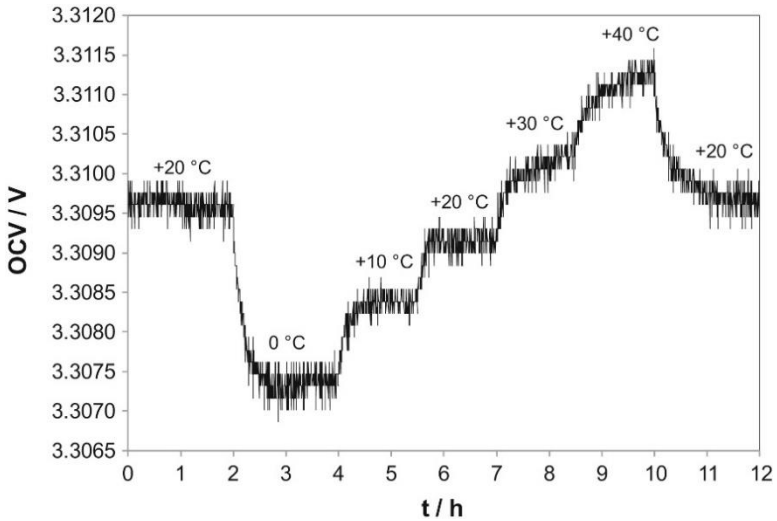

Fig. 5. 10: Potentiometric measurement of pouch cell with a capacity of 42 Ah (LFP/graphite) at SOC70 plotted as open circuit voltage (OCV) vs. time [126].

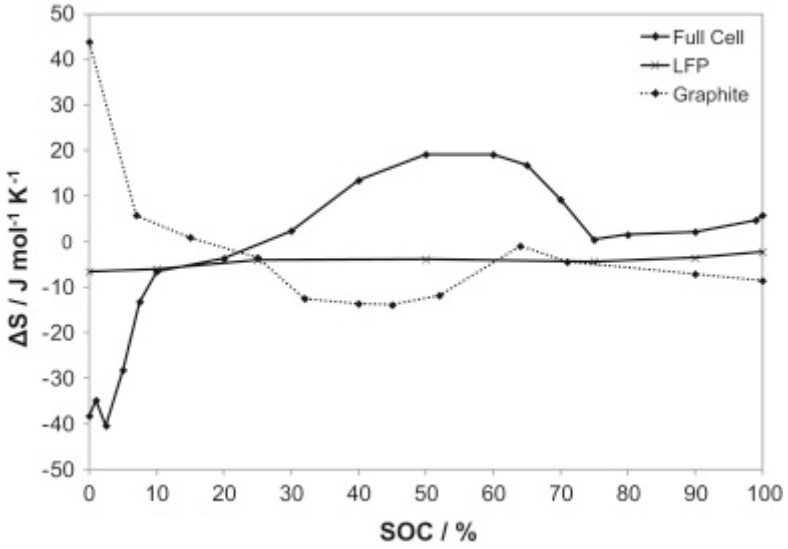

Fig. 5. 11: Entropy changes for the pouch cell with a capacity of 42 Ah (LFP/graphite), LFP half cell and graphite half cell [126].

5.1.2 Thermal runaway studies

Another important issue for the application of LiBs, is the thermal runaway event. Short circuit, overcharging, fast charging/discharging or high ambient temperature can cause uncontrolled self-heating of LiBs [17-19], which is known as a thermal runaway event. In a thermal runaway event, the reactions and their onset temperatures are proposed to be the following [18, 127]:

- 90 - 120 °C decomposition of the SEI layer
- >120 °C exothermic reactions between the electrolyte and the intercalated Li-ions from the negative electrode
- ±130 °C melting point of separator material polyethylene (PE)
- ±168 °C melting point of separator material polypropylene (PP)
- >170 °C exothermic reactions between the electrolyte and the positive electrode
- >200 °C decomposition of the electrolyte.

The anode solid electrolyte interface (SEI) layer mainly consists of e.g. lithium carbonate Li_2CO_3, lithium methyl carbonate (LMC), and lithium ethylene dicarbonate ($(CH_2OCO_2Li)_2$, LEDC), LiF, and lithium alkyl carbonates ($LiOCO_2R$). Spotnitz and Franklin [18] proposed two possible reactions on the metastable composition LEDC:

$$(CH_2OCO_2Li)_2 \rightarrow Li_2CO_3 + C_2H_4 + CO_2 + \frac{1}{2}O_2 \qquad (5.2)$$

or

$$2Li + (CH_2OCO_2Li)_2 \rightarrow 2Li_2CO_3 + C_2H_4 \qquad (5.3)$$

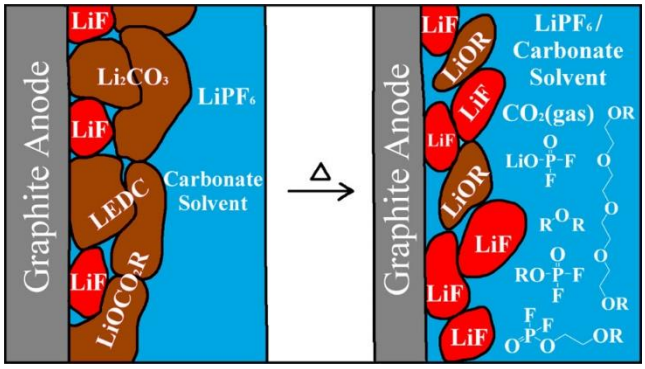

Fig. 5. 12: Decomposition reactions of anode solid electrolyte interphase (SEI) components with $LiPF_6$ [128].

In Fig. 5.12, the results of a recent research about SEI layer decomposition is shown. Parimalam et al. [128] utilized X-ray photoelectron spectroscopy (XPS) and infrared spectroscopy with attenuated total reflectance (IR-ATR) combined with nuclear magnetic resonance (NMR) spectroscopy and gas chromatography with mass selective detection (GC-MS) to study the decomposition reactions of the SEI layer. With increasing temperature at 55 °C, Li_2CO_3 reacts with $LiPF_6$ in DMC as follows:

$$LiPF_6 + 2Li_2CO_3 \rightarrow 2CO_2 + 4LiF + F_2PO_2Li \tag{5.4}$$

The thermal decomposition of LMC is a chain reaction at 55 °C:

$$\begin{gathered} LiPF_6 + 3C_2H_3LiO_3 \rightarrow 4LiF + 3CO_2 + OPF_2(OCH_3) + O(CH_3)_2 \\ OPF_2(OCH_3) + C_2H_3LiO_3 \rightarrow LiF + CO_2 + OPF(OCH_3)_2 \end{gathered} \tag{5.5}$$

The decomposition of LEDC under heating is more complex. The products: CO_2, LiF, CH_3OCH_3, $OP(OCH_3)_3$, $OPF(OCH_3)_2$, $OPF_2(OCH_3)$, and F_2PO_2Li were observed. Once the SEI layer decomposes, there is no protection between the electrolyte and the intercalated Li ions.
In this work Section 5.6.2, the early stage of thermal runaway was investigated. There are multi-reactions observed by thermal effects measured by C80.
Wang et al. [129] studied the thermal behavior of lithiated graphite with 1M $LiPF_6$/EC+DEC by using a Tian-Calvet C80 calorimeter. For SEI decomposition, besides equation 5.2 and 5.3, another reaction equation 5.5 was proposed. After the breakdown of SEI layer, electrolyte can easily reach intercalated Li ions. They defined the following reactions, which generate flammable gases [129, 130]:

$$LiPF_6 \leftrightarrow PF_5 + LiF \tag{5.6}$$

$$2Li + C_3H_4O_3(EC) \rightarrow Li_2CO_3 + C_2H_4 \tag{5.7}$$

Fig. 5.13 shows three heat flow rate curves from research [129], which are electrolyte (—■—), electrolyte with lithiated anode (—▲—) and lithiated anode (—○—). The corresponding heat flow rate curve is represented by “triangle line” with thermic peaks at 101.6 °C, indicating SEI decomposition where reactions of equation 5.1, 5.2 and 5.5 were considered as main reason causing heat effects. The thermic peak at 217.5 °C indicate the reactions between intercalated lithium and electrolyte, which formed a secondary SEI layer. Equation 5.5 and 5.6 were attributed in this process. Thermic peak at 233.3 °C was attributed to the secondary SEI decomposition. Therefore, the intercalated lithium ions reacted with electrolyte again and PVDF had a minimal effect too. These reactions lead to the thermic peak at 248.2 °C.

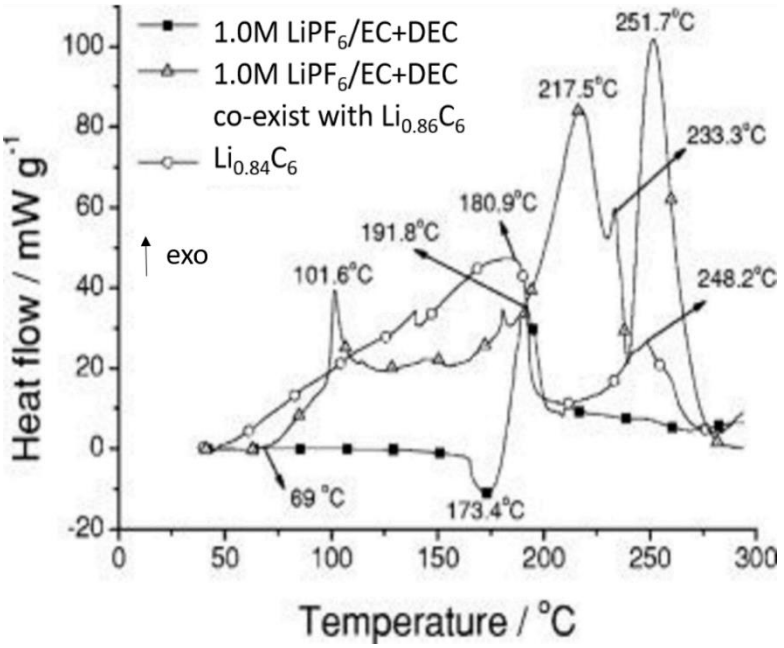

Fig. 5. 13: C80 heat flow curves of lithiated graphite ($Li_{0.84}C_6$), 1.0 M $LiPF_6$/EC+DEC electrolyte, and $Li_{0.86}C_6$ [129].

With increasing temperature, the separator materials PE and PP start to melt, ending up with a short circuit. With higher temperatures, more reactions will be initiated.
Wang et al. [130] investigated the thermal behavior of the electrolyte $LiPF_6$/EC+DEC, and the charged positive electrodes with $LiPF_6$ by a C80 calorimeter. They found $LiPF_6$ reacts with EC in an exothermic reaction by cleaving the ring and generating transesterification products at 212 °C. In the temperature range of 225 °C to 280 °C, a polymerization reaction took place with products of polyethylene oxide polymers and CO_2 [131-132], which was an exothermic reaction. The electrode was rinsed by dimethyl carbonate (DMC) to get rid of electrolyte. DMC could dissolve parts of the organic SEI film.

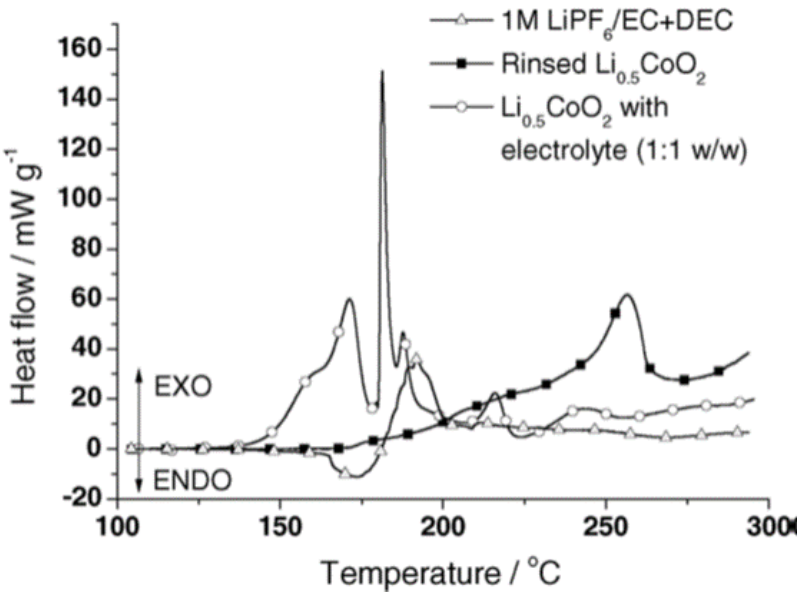

Fig. 5. 14: Heat flow curves of 1 M $LiPF_6$ in EC+DEC, rinsed and their co-existing system at 0.2 °C·min^{-1} in argon [130].

In Fig. 5.14, the heat flow rate curves of electrolyte (—Δ—), rinsed $Li_{0.5}CoO_2$ (—■—) and $Li_{0.5}CoO_2$ with electrolyte (—o—) are plotted versus temperature. The thermal behavior of electrolyte co-existing with delithiated positive electrode material $Li_{0.5}CoO_2$ was studied. As the curve of $Li_{0.5}CoO_2$ with electrolyte showing, the reactions began at 130 °C, much lower than the decomposition of rinsed $Li_{0.5}CoO_2$ and the electrolyte alone. That may be caused by the oxidation in the electrolyte solvent to form CoO [133]. The exothermic reactions were observed and the onset temperature was 170 °C. The decomposition proposed by MacNeil and Dahn [133-134] was:

$$Li_{0.5}CoO_2 \rightarrow \frac{1}{2}LiCoO_2 + \frac{1}{6}Co_3O_4 + \frac{1}{6}O_2 \qquad (5.8)$$

When the electrolyte is added into delithiated $Li_{0.5}CoO_2$, EC and DEC will react with oxygen producing CO_2 and H_2O. The onset temperature was measured to be 130 °C followed by three exothermic reactions (Fig. 5.14). The delithiated positive electrode material's reactions are described by equation 4.1 and 4.2 on page 48. This triggers the thermal runaway event. Beside the reactions between released gases and the electrolyte, flammable gases were also produced from previous reactions. Consequently, a significant amount of heat and an increasingly amount of gases are produced due to the intensive exothermic reactions. The internal pressure of the cell is thus growing.

Accelerating rate calorimeter (ARC) was used to investigate the thermal stability of $Li_{0.81}C_6$ in different electrolyte by Jiang and Dahn [135] (Fig. 5.15). Heat-treated mesocarbon microbeads (MCMB) were used as positive electrode against lithium metal materials. 1 M $LiPF_6$ was dissolved in EC/DEC (1:2, v/v) to build coin cells. Another electrolyte was 0.8 M LiBOB dissolved in EC/DEC (1:2, v/v). After fully lithiation of MCMB, the negative electrode was rinsed. Approximately 100 mg active composite (MCMB, PVDF and carbon black) and the same mass of DMC, DEC or EC/DEC solvent were tested in the ARC from 110 °C to 350 °C. The heat-wait-search mode was used from 110 °C to 350 °C. The heat step was 10 °C at a rate of 5 °C/min, and waiting for 15 min, followed by a 10 min search (self-heating rate sensitivity: 0.04 °C/min).

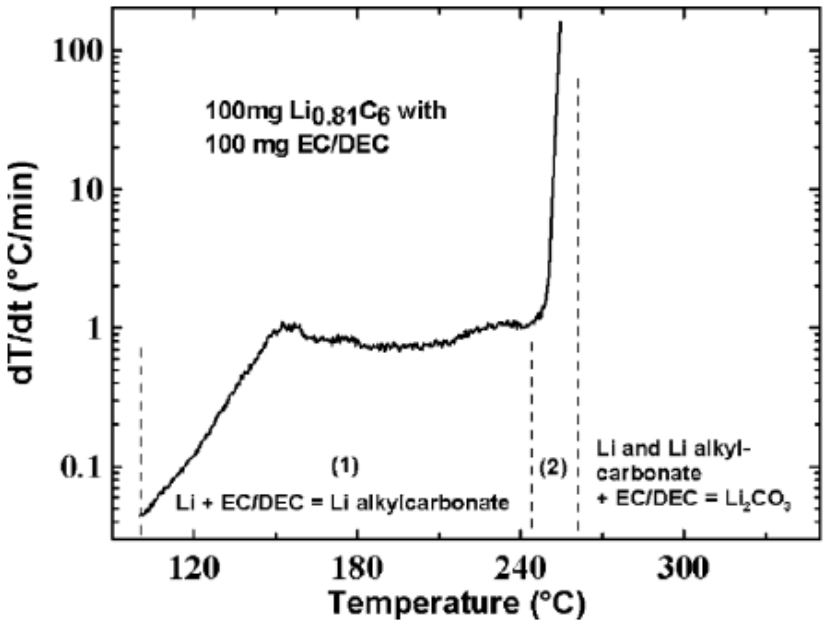

Fig. 5. 15: Proposed reactions between $Li_{0.81}C_6$ and EC/DEC solvent in the temperature range between 110 °C and 260 °C correlated to the accelerating rate calorimeter (ARC) results [135].

Fig. 5.15 shows two parts of the reaction of $Li_{0.81}C_6$ with EC/DEC at elevated temperature: (1) 90 °C - 243 °C, $Li_{0.81}C_6$ and EC/DEC reacting to form Li-alkyl carbonates; (2) > 243 °C, Li-alkyl carbonates and EC/DEC reacted to form Li_2CO_3.

Besides the investigation on the reactions between the lithiated negative electrode and the electrolyte, the thermal stability of delithiated positive electrode material $Li_{1-x}Ni_{1/3}Mn_{1/3}Co_{1/3}O_2$ (NMC) and $Li_{1-x}Ni_{1/3}Co_{1/3}Al_{1/3}O_2$ (NCA) were also investigated using accelerating rate calorimeter (ARC) [136]. NMC and NCA positive electrode materials were used to make 2325-size coin cells with a lithium metal negative electrode. The cells were charged to 4.2 V, and then disassembled in a glove box. The positive electrode was rinsed with dimethyl carbonate (DMC) solvent and dried. 66 mg of delithiated positive electrode powder and 20 mg electrolyte were put into measuring tubes. The samples were weighted before and after measurement to make sure no leak occurred. Since the amount of samples were very little for ARC measurement, the impurity must be very carefully controlled. The sample tubing was sonicated in acetone solution two times for cleaning. The self-heating rate (SHR) and the temperature of exothermic reactions in the temperature range of 100 °C to 380 °C were measured in the ARC tests. The sensitivity was set as 0.03 K/min. The SHR of the reactions between NMC and the electrolyte (EC:DEC volume ratio 1:2) with 0.5 M, 1 M and 1.5 M $LiPF_6$ reached 1 K/min at 250 °C. After that temperature, the SHR increased relatively fast, reaching the maximum values, as shown in Fig. 5.16.

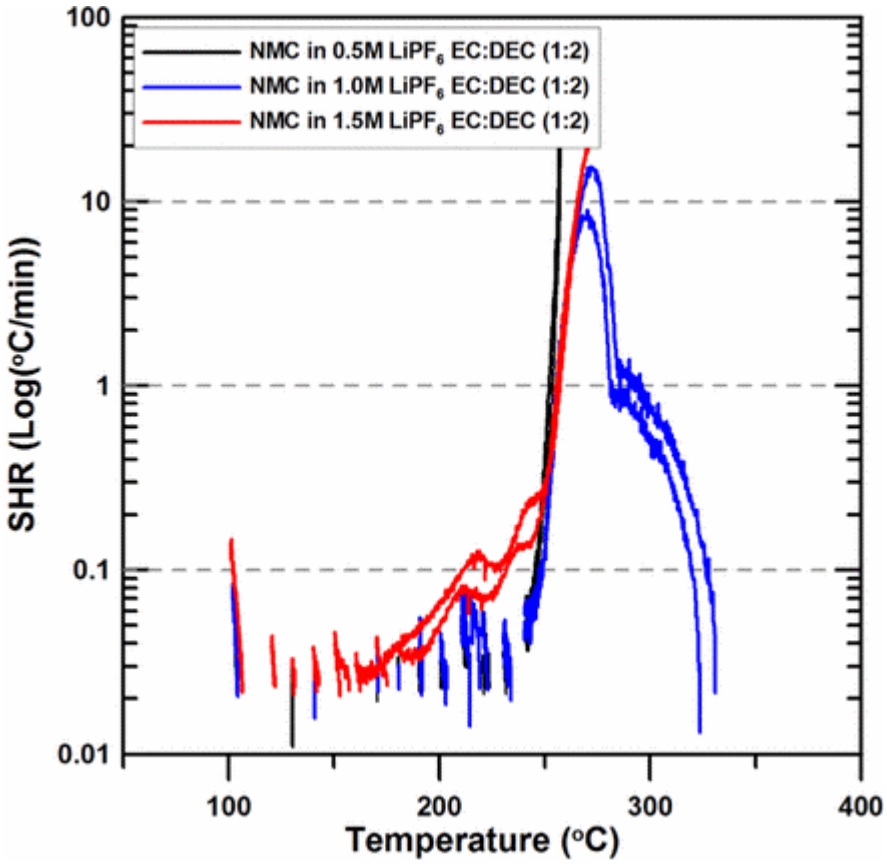

Fig. 5. 16: Self-heating rate vs. temperature: ARC results for ground electrode powder of NMC (66 mg) reacting with 0.5 M, 1.0 M and 1.5 M $LiPF_6$ in EC:DEC (1:2 v/v ratio) electrolyte (20 mg) [136].

The previous thermal stability researches showed that the calorimetric study is a very effective and sensitive method to study thermal properties of single components or inter-reactions between components. Delithiated positive electrode and lithiated negative electrode showed a very unstable thermal performance especially in presence of electrolyte. In this work,

thermal stability of coin cells as well as components were studied by C80 calorimeter and Accelerating Rate Calorimeter (ARC). The cells were charged to different states and disassembled in glovebox. Thermal behavior of the electrodes with electrolyte was investigated up to 150 °C in C80 calorimeter. Thermal runaway tests were performed on full coin cells with selected SOCs by ARC.

5.2 Measurements for thermal behavior study

The two types of calorimetric studies in this section aim at first to investigate and understand the heat generation during cycling; and at second to illustrate the whole picture of thermal runaway of commercial coin cells.

5.2.1 Heat generation determination

Two different methods to determine the heat generation have been compared. Firstly, the heat generation was determined experimentally by measuring the temperature change and the heat flux during cycling. This is achieved by the following procedures:

- measurements to determine the specific heat capacity of coin cells using a C80 calorimeter
- measurements of the temperature change of the whole cells during cycling using a thermocouple
- measurements of the heat flow rates of the whole cells during cycling using a C80 calorimeter

Secondly, the irreversible and reversible heat generation were calculated by the following procedures:

- measurements to determine internal resistances
- measurements of the entropy change of the reversible reaction

5.2.2 Thermal runaway measurements

This work combines ARC and C80 calorimeter to investigate the thermal runaway and its earlier stages by the following procedures:

- measurements of commercial coin cells with SOC0, SOC50 and SOC100 using ARC in the whole temperature range of 50 °C to 450 °C
- measurements of the positive electrodes, negative electrodes, separator and whole cells with SOC0, SOC50 and SOC100 using a C80 calorimeter in the lower temperature range of 60 °C to 150 °C

5.3 Investigated coin cells

The investigated coin cells are commercially available with a diameter of 14 mm and a height of 5.4 mm. The negative electrode material is graphite and the positive electrode material is layered lithium transition metal oxide NMC. The nominal capacity (C) is 85 mAh, which was determined by discharging at 0.2 C from 4.2 V to 3.0 V at 20 °C. The average weight of cells is 2.4 ± 0.2 g.

The standard charge current is 42.5 mA with a constant current constant voltage (CCCV) method. The coin cells were disassembled in a glove box. The positive electrode, the separator and the negative electrode are in this order winded in the coin cell, which are shaped in forms of a long strip and there is a double-sided coating for the electrodes. The chemical composition of the negative and positive electrode was investigated by ICP-OES, as listed in Table 5.1. The active material is $LiNi_{0.6}Mn_{0.2}Co_{0.2}O_2$ (NMC622) with approximately 80 wt.% of the whole positive electrode. The weight proportion of positive electrode is less than 100 %, because mass of binder materials was not taken into account.

Table 5.1 Chemical analysis (ICP-OES) of the positive and negative electrodes in the coin cell.

Components of the electrode	Analyzed elements	ICP-OES wt. %	ICP-OES at. %	Nominal at. % Sum TM=100	Nominal stoichiometry Sum TM=1
Rinsed active material of positive electrode	Li	5.44±1.10	24.14	96	0.96
	Ni	28.8±0.4	15.02	60	0.60
	Mn	8.88±0.16	4.95	20	0.20
	Co	9.57±0.18	4.98	20	0.20
	O	26.6±2.4	50.91	204	2.04
	Sum	79.29±4.24	100		-
Substrate film of positive electrode	Al	5.44±1.1			-
Conductive material	C	4.82±0.40			-
Weight proportion of all investigated elements in the positive electrode		93.40±5.74			-
Negative electrode	Li	4.13±0.10			-
Substrate film of negative electrode	Cu	28.7±0.8			-
Weight proportion of all investigated elements in the negative electrode		32.83±0.90			-

5.4 Measurements of the specific heat capacity of coin cells

The specific heat capacities are measured by continuous and step methods using C80 calorimeter. The measuring temperature range was from 30 °C to 60 °C. The temperature was chosen slightly higher than ambient temperature to maintain an isothermal condition and also below the maximum operating temperature of the tested cells.
The specific heat capacity can be measured by the continuous/scanning method and discontinuous/step method. The step method can help to obtain acceptable values when the scanning method failed [137-138]. The performance of the scanning method and the step method depends highly on the sample's properties. For both methods, an empty measurement and a measurement on sapphire Al_2O_3 (SRM 720, NIST) were carried out as baseline and reference [68, 139], respectively. In this work, both methods were performed to measure specific heat capacity of LiBs using sapphire as reference.

5.4.1 Continuous method

The measurement procedure started with an isothermal condition at 30 °C for 2 h and then heating with 0.1 K/min to 60 °C. At last, the temperature was hold at 60 °C for 2 h. The specific heat capacity at constant pressure of sapphire is given by equation 5.9 [68]:

$$\begin{aligned} c_{p,Ref}(T) = & -0.687717 \cdot 10^2 + 0.7155 \cdot T + 0.145685 \cdot 10^6 \cdot T^{-2} \\ & - 0.596292 \cdot 10^{-5} \cdot T^3 + 0.16912 \cdot 10^{-7} \cdot T^4 \\ & - 0.221044 \cdot 10^{-10} \cdot T^5 + 0.144189 \cdot 10^{-13} \cdot T^6 \\ & - 0.378847 \cdot 10^{-17} \cdot T^7 \end{aligned} \quad (5.9)$$

where temperature T in K, and specific heat capacity in $J \cdot K^{-1} \cdot mol^{-1}$. This polynomial function is suitable for the temperature range 150 K - 900 K. The uncertainty of equation 5.9 for specific capacity of reference is 0.08 %. The equation 5.10 is calculated by the molar mass of reference 101.9613 $g \cdot mol^{-1}$. The specific heat capacity of the samples at a temperature T and constant pressure can therefore be calculated by equation 5.10 [140-141]:

$$c_{p,S}(T) = \frac{\Phi_S(T) - \Phi_0(T)}{\Phi_{Ref}(T) - \Phi_0(T)} \cdot \frac{m_{Ref}}{m_S} \cdot c_{p,Ref}(T) \tag{5.10}$$

where $\Phi_S(T)$, $\Phi_0(T)$, and $\Phi_{Ref}(T)$ denote the measured heat flow rates of samples, baseline, and reference material. $C_{p,Ref}(T)$ is the specific heat capacity of sapphire at the temperature T. Two cells are measured as samples. The measured heat flow rate curves are shown in Fig. 5.17.

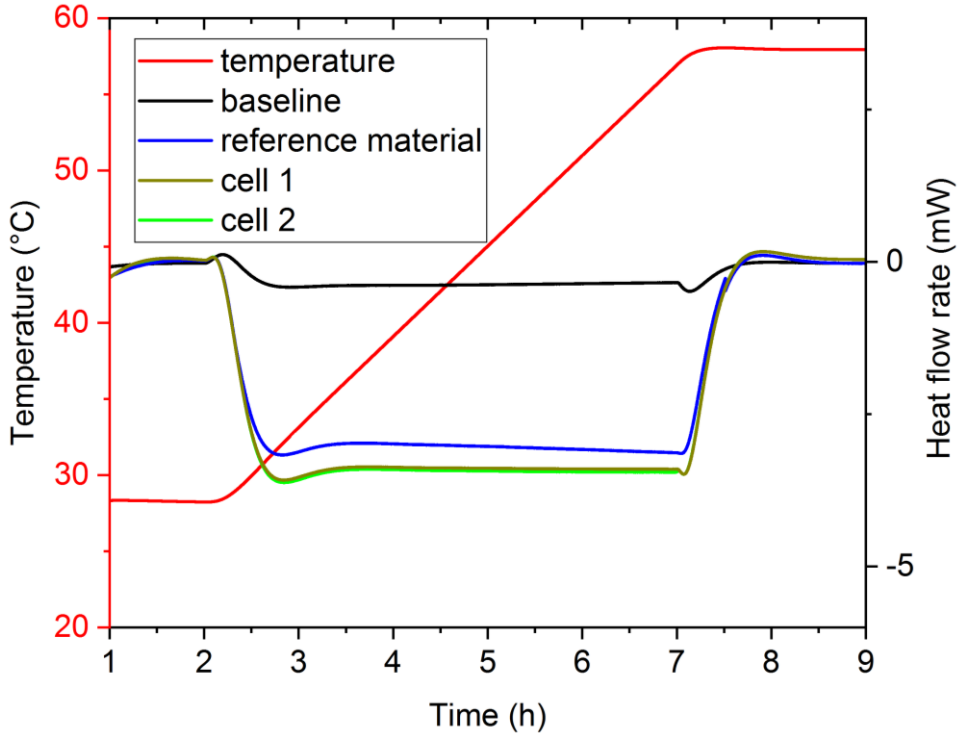

Fig. 5.17: Heat flow rate curves of baseline, reference material, and samples versus time measured by continuous method.

The calculated specific heat capacity of the two cells and their uncertainty are depicted in Fig. 5.18. A polynomial Maier-Kelley function proposed in Ref. [142] for the specific heat capacity of the samples is used to fit the data:

$$c_{p,S} = a + b \cdot T - c \cdot T^{-2} \tag{5.11}$$

The deviation of the two cells is smaller than 1.7 %, so the repeat results are in good agreement.

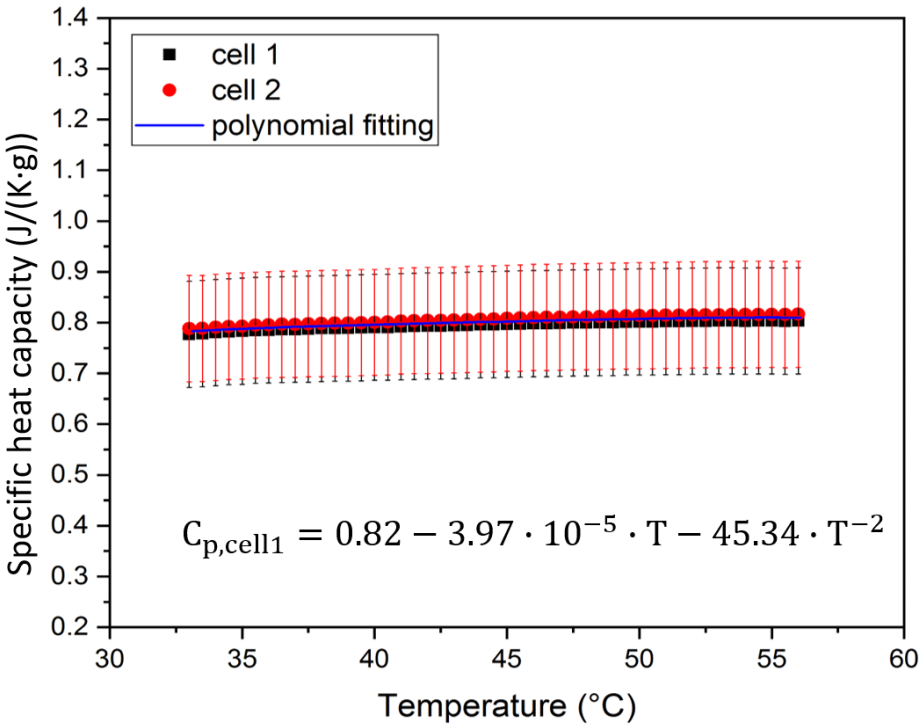

Fig. 5. 18: Specific heat capacity of two cells and their fitting curves and functions in continuous method measurements.

5.4.2 Step method

The step method is performed in the same temperature range from 30 °C to 60 °C by increasing the temperature in 5 °C steps. After reaching the desired temperature, the temperature is held for 2 h to achieve a stable heat flow rate, as shown with the red curve in Fig. 5.19. Afterwards, a scanning rate of 0.3 K/min is applied to reach the next temperature level. The calibration of heat effect for each step is integrated [140] and the specific capacity of the cells is obtained by equation 5.12, which integrates the heat flow rates of samples and references in same temperature ranges over time based on equation 5.10:

$$c_{p,S} = \frac{m_{Ref} \cdot c_{Ref}}{m_S} \cdot \frac{\int(\Phi_S - \Phi_0)dt}{\int(\Phi_{Ref} - \Phi_0)dt} \tag{5.12}$$

The calculated results and the polynomial fittings are plotted in Fig. 5.20, and the deviation of the two cells is less than 1.7 %. The specific heat capacities of the two cells are in a good agreement. However, the uncertainty of the measurements is relatively large compared to the continuous method. The specific heat capacity values at 30 °C are 0.77±0.08 J/K·g and 0.77±0.13 J/K·g according to the results from continuous and step method respectively. Both results are comparable and the continuous method turns out to be more suitable for specific heat capacity measurements in this case. The heat capacity of coin cell in the small temperature of 30 °C to 60 °C is relatively stable. Between each temperature step, the heating step was applied during measurements, and these disturbances may introduce an error into the measurement.

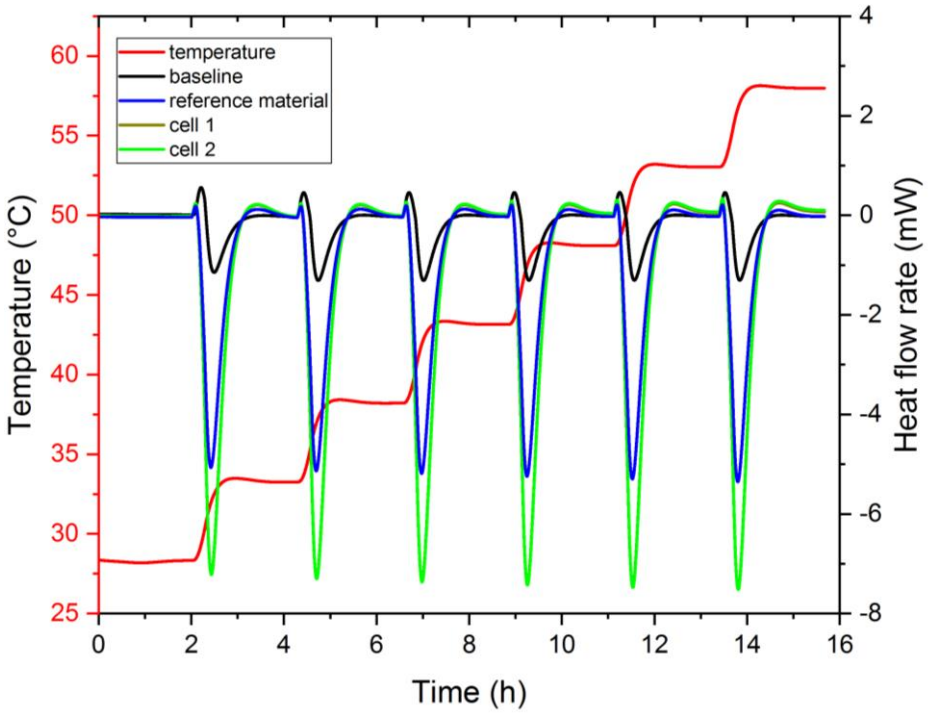

Fig. 5. 19: Heat flow rate curves and temperature change of baseline and sapphire vs. time measured by step method.

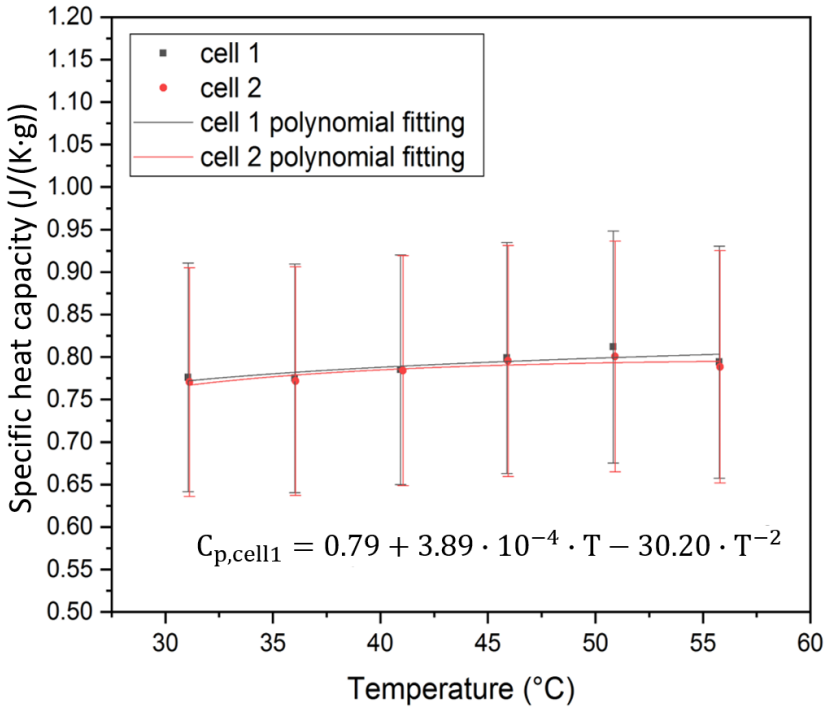

Fig. 5. 20: Specific heat capacity of two cells and their fitting curves and functions in step method measurements.

5.5 Heat generation during cycling

The heat generation during cycling was investigated under various scenarios: operation at 30 °C and 25 °C, cycling with various C-rates, and under adiabatic condition. A Tian-Calvet C80

calorimeter allowed to measure the heat generation accurately and to control the ambient temperature very precisely. Besides heat flow rate measurement, the temperature change was also monitored by additional thermocouples. The thermocouple was introduced into the sample vessel and measuring the temperature change of cell's surface. Temperature changes were measured under isoperibolic condition at 30 °C, while heat flow rates were measured at both 30 °C and 25 °C. The cells were charged by constant current of 0.5, 1, and 2 C (42.5 mA, 85 mA and 170 mA), respectively, and when reaching 4.2 V they were hold at constant voltage (CCCV, till current < C/20) and finally they were discharged with constant current. In order to maintain the measurement temperature at 25 °C, the C80 calorimeter is put in a cooling incubator (Binder GmbH, Germany).

5.5.1 Heat generation determined by temperature measurement

A K-type thermocouple was attached on the surface of the tested coin cells with an isolated glass tape, while another thermocouple was fixed at the bottom of the reference side. The influence of cables on heat flow rate measurements was adjusted by the calibration later. Since the mass of glass tap is relatively small, the heat absorption of glass tap is negligible. The glass tape also isolate thermally conductive between coin cell's surface and the vessel. Therefore, heat dissipation is considered mainly through air convection. The heat flow rates were measured by 3D sensors around vessels. Two ceramic discs with similar weight were placed at the bottom of the sample vessel and the reference vessel respectively to isolate the cells from the metallic vessel's bottom. The set-up of coin cell's measurement is shown in Fig. 5.21, which is the set-up 2 in Fig. 3.6 (page 27). Two cables and K type thermocouple are introduced into the vessel, so the cell is cycling in the vessel measuring the temperature and heat flow rate.

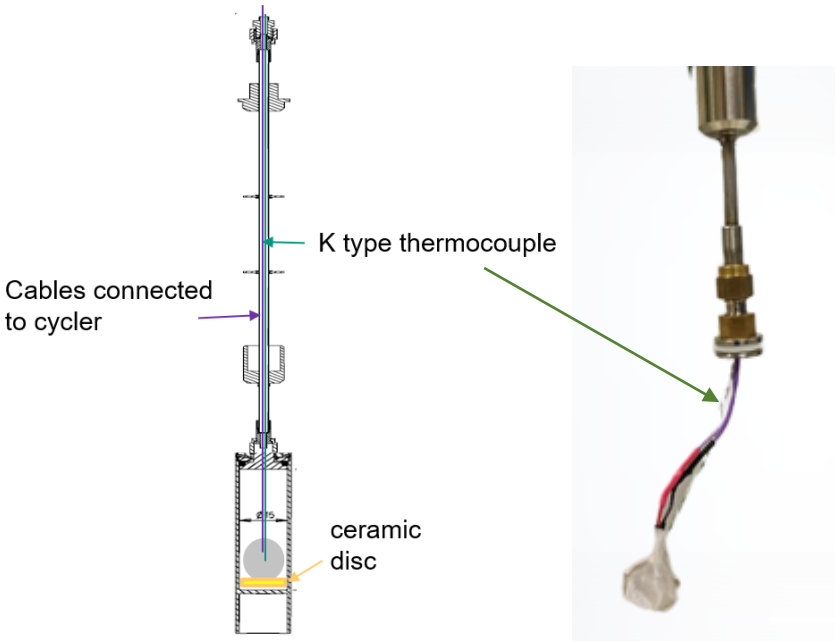

Fig. 5. 21: The internal set-up of coin cell cycling in C80 calorimeter: purple line are the cable connected to cycler, green line represents the K type thermocouple and yellow disc is ceramic disc on bottom of the vessel.

Firstly, the heat dissipation had to be determined. When the current was not applied on the cells, the stored heat in the coin cell started to dissipate into the chamber. The stored heat was the product of the temperature difference and the heat capacity of the cells. The thermal conduction is negligible since glass tape isolates the conduction between cells and the vessel. The dissipation via radiation is very small and negligible, thus the heat dissipation is mainly due to heat convection [143]. This can be described with the following relationship based on

equation 2.24:

$$
\begin{aligned}
m \cdot c_p \cdot dt &= -h \cdot A \cdot (T(t) - T_{env}) \cdot dt \frac{dT}{T(t) - T_{env}} \\
&= -\frac{h \cdot A}{m \cdot C_p} \cdot dt \frac{T(t) - T_{env}}{T_i - T_{env}} \\
&= \exp\left(-\frac{h \cdot A}{m \cdot C_p} \cdot t\right) \Delta \mathrm{T} \\
&= \Delta T_i \cdot \exp\left(-\frac{h \cdot A}{m \cdot C_p} \cdot t\right)
\end{aligned}
\tag{5.13}
$$

where c_p denotes the specific heat capacity of the coin cells ($J \cdot g^{-1} \cdot K^{-1}$), which was measured as described before, T is the temperature (K), and t represents time. A and h are the surface area of the coin cells (m^2), and the heat transfer coefficient between cells and environment ($W \cdot m^{-2} \cdot K^{-1}$). Hence, h can be determined by the exponential function of temperature and time, which is the cooling curve with no power applied. When stopping to discharge and no current applied, the temperature of cells will decrease and heat dissipates from cells to the surroundings. With such cooling curve, the heat transfer coefficient is calculated. In Fig. 5.22, the temperature difference ΔT is the temperature curve minus the base line (30 °C). To simplify the calculation, the mass and heat capacity of glass tape and connected cables were not considered in the analysis. This influence may introduce errors in the temperature measurements. The curves are extracted from maximum temperature to the temperature setting in calorimeter, which is corresponding curve at 22500 s in Fig. 5.23. Fig. 5.22 shows cooling curves at various C-rates and their fitting function, where the constant b is used to calculate the heat transfer coefficient h, and the results are listed in Table 5.2 with:

$$
h = -\frac{b \cdot m \cdot c_p}{A} \tag{5.14}
$$

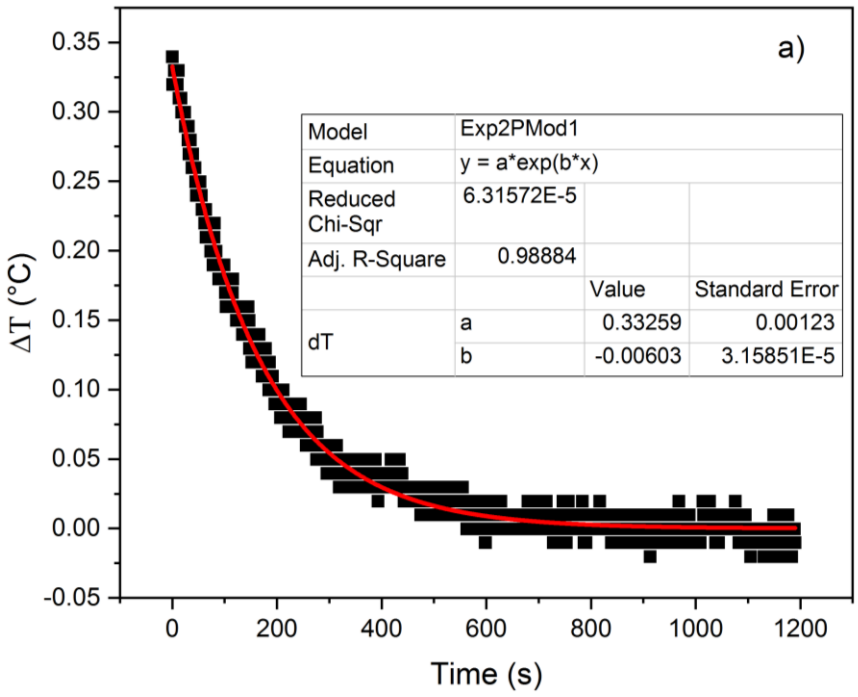

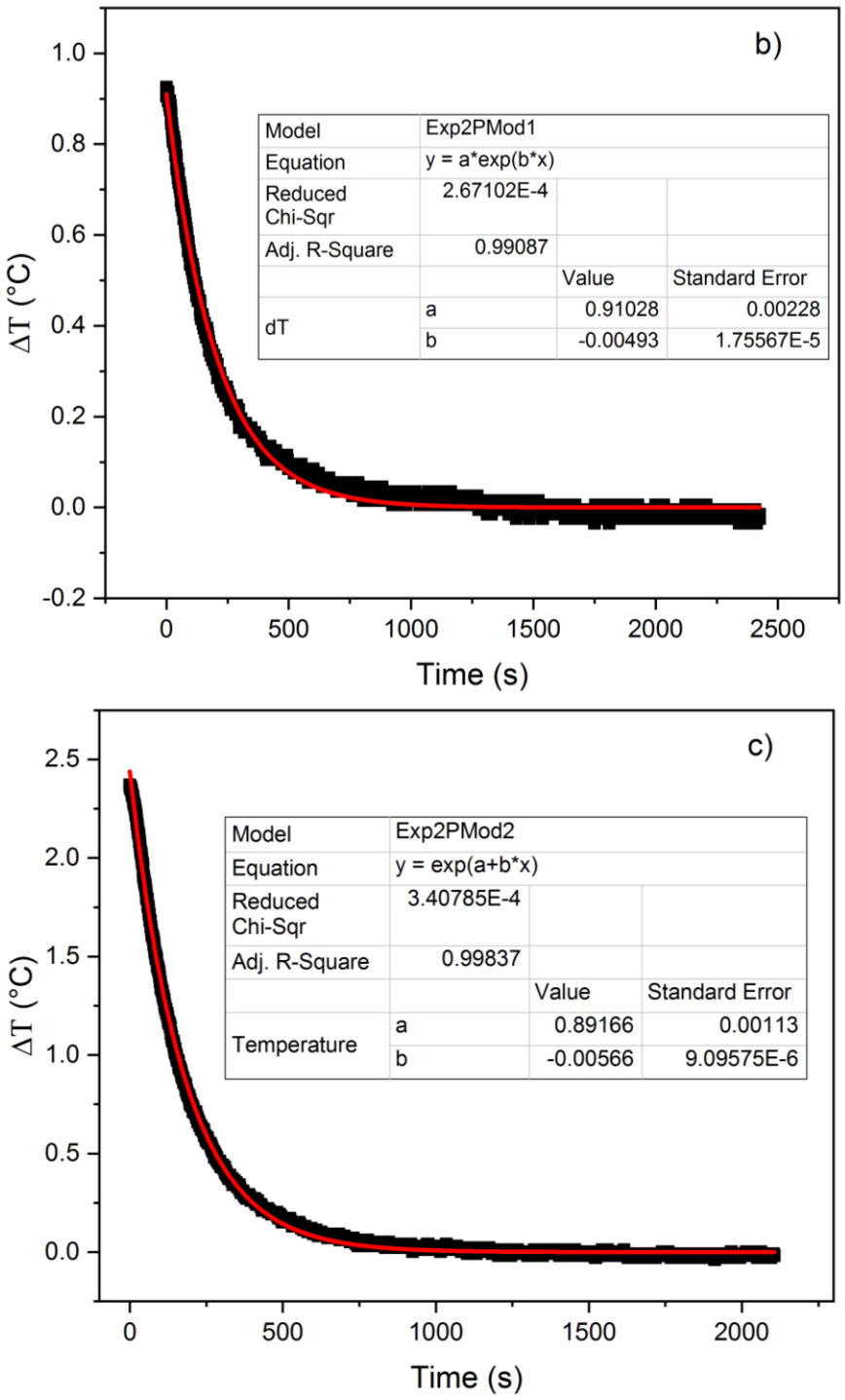

Fig. 5.22: Cooling curves after discharging at various C-rates: a) at 0.5 C, b) at 1 C, c) at 2 C and their fitting functions.

With this heat transfer coefficient, the heat dissipation is obtained by integrating the heat flow rate over time:

$$Q_{diss} = A \cdot h \cdot \int_0^t (T - T_{env}) \cdot dt \tag{5.15}$$

As shown in Fig. 5.23, the temperature increases when the current is applied. The total heat generation consists of the heat stored in the coin cell and the heat dissipated into the

environment (equation 5.16). The red curves present the temperature increasing and heat generation was determined by these values on red curves. The black curves are the temperatures during heat dissipation and cell's relaxation. The dissipation was determined by these values on black curves. The blue curve shows the applied currents. The calculated results are summarized in Table 5.2:

$$Q_t = c_p \cdot m \cdot \Delta T + Q_{diss} \tag{5.16}$$

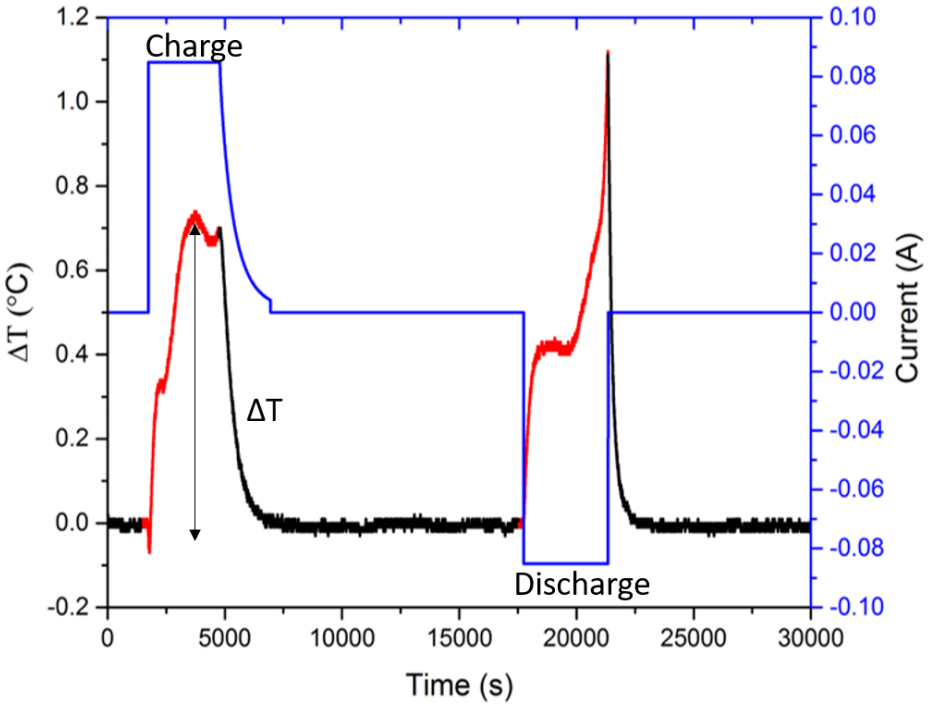

Fig. 5. 23: Temperature curve when cycling at 0.5 C, red curve represents the temperature change used in calculation; blue curve represents the applied current.

Table 5.2 The heat transfer coefficients and the calculated heat generation during cycling at various C-rates.

Current flow C-rates	0.5 C (42.5 mA)	1 C (85 mA)	2 C (170 mA)
h ($W \cdot m^{-2} \cdot K^{-1}$)	20.94	17.12	19.65
Heat generation during charge (J)	12.9±0.5	15.7±1.1	19.7±1.7
Heat generation during discharge (J)	11.2±0.9	15.2±0.8	25.0±1.1

5.5.2 Heat generation determined by heat flow rate measurement

A Joule effect calibration using a standard resistance, was performed before the measurements on the cells, in order to compensate the effects of cables, which are introduced into the calorimeter for the cell cycling. In addition, the glass tape with similar mass in measurements was used too. This means that a defined heat input was applied by a current flow through a resistor with a resistance of 9.85 Ω, measured by a DC resistance digital tester. The current values are adjusted to cover the same range as the typical heat flow rates of the cells (Fig. 5.24). The heat dissipated by the resistor is calculated by integration over time and the comparison with the measured values of the C80 gives the calibration coefficient as the result. The calibration coefficient is defined by the ratio of the electrical energy to the measured heat. Since the cables that connect the cells with the potentiostat/galvanostat Gamry (Reference 3000, C3 Prozess- und Analysentechnik GmbH, Germany) develop heat but dissipate heat simultaneously, the combined heat effects were analyzed by this procedure. As

seen in Table 5.3, the calibration coefficient shows a constant value of 1.03, independent on the current flows. The calibration was repeated three times in order to confirm a good repeatability. This calibration coefficient was thus used to compensate the cable effect in the following measurements on the cells, listed in Table 5.3.

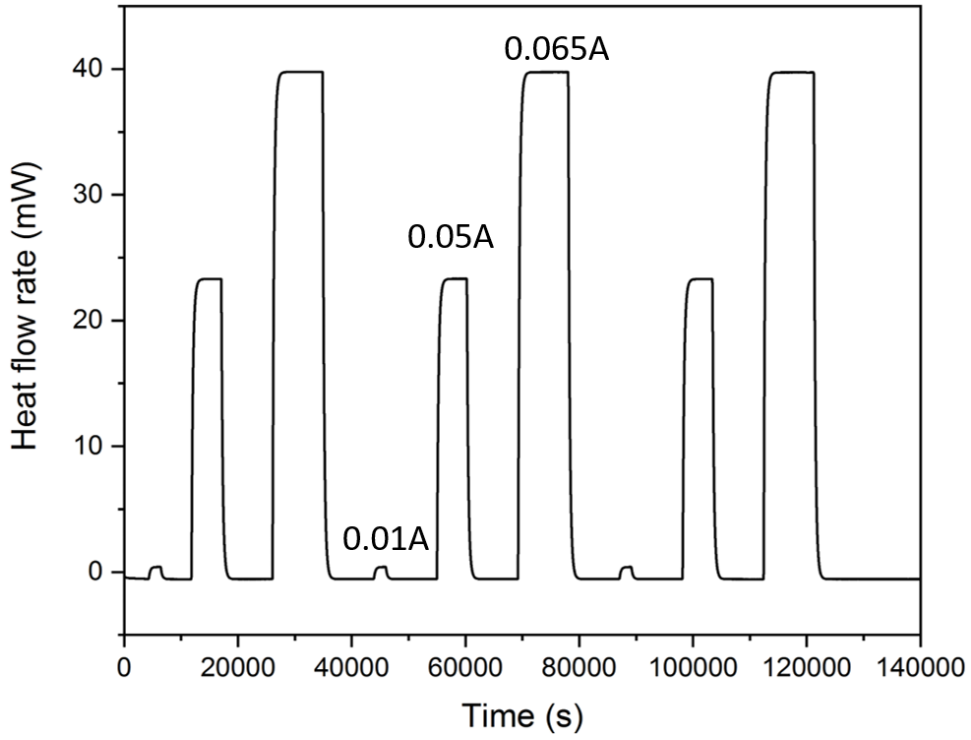

Fig. 5.24: Heat flow rates of joule effect calibration with standard resistance in C80 calorimeter.

Table 5.3 The calibration coefficients for different heat flow rates.

Current flow (A)	Power (mW)	Joule effect (J)	Measured heat effect (J)	Calibration coefficient
0.01	0.99	2.07	2.02	1.03
0.05	24.62	129.17	125.28	1.03
0.065	41.60	366.56	355.57	1.03

The heat flow rates for three cycles with various currents (0.5 C, 1 C, 2 C i.e. 42.5 mA, 85 mA, 170 mA), as measured by C80 calorimeter, are shown in Fig. 5.25. At the beginning of the charging at the lowest rate of 0.5 C, a cooling effect is visible. This cooling effect was also reported in earlier studies [125, 144] and can be explained by the entropy change in early stages of the Li^+ de-intercalation of the positive electrode and the following intercalation of the negative electrode. The beginning and the end of the charging and discharging period, respectively, are obviously generating discriminable peaks in the heat flow rate. Furthermore, the difference between the heat flow characteristics on charging and discharging is caused by the fact that the values of the entropy change and consequently the reversible heat flow rate changes the sign. With higher C-rate, less peaks can be detected and there is only one peak at 2 C. That indicates that the thermal effects overlap by fast charging/discharging, as the reactions tend to happen simultaneously under large driving forces. In addition, the reversible heat effect is usually exceeded by the irreversible heat effect at high current rates, because it deviates more from equilibrium. The measurements at 25 °C (Fig. 5.26) showed a similar

thermal behavior as those at 30 °C. The time-dependent factors, such as charge transfer and solid state diffusion, affect the cycle process increasingly with large current flows.

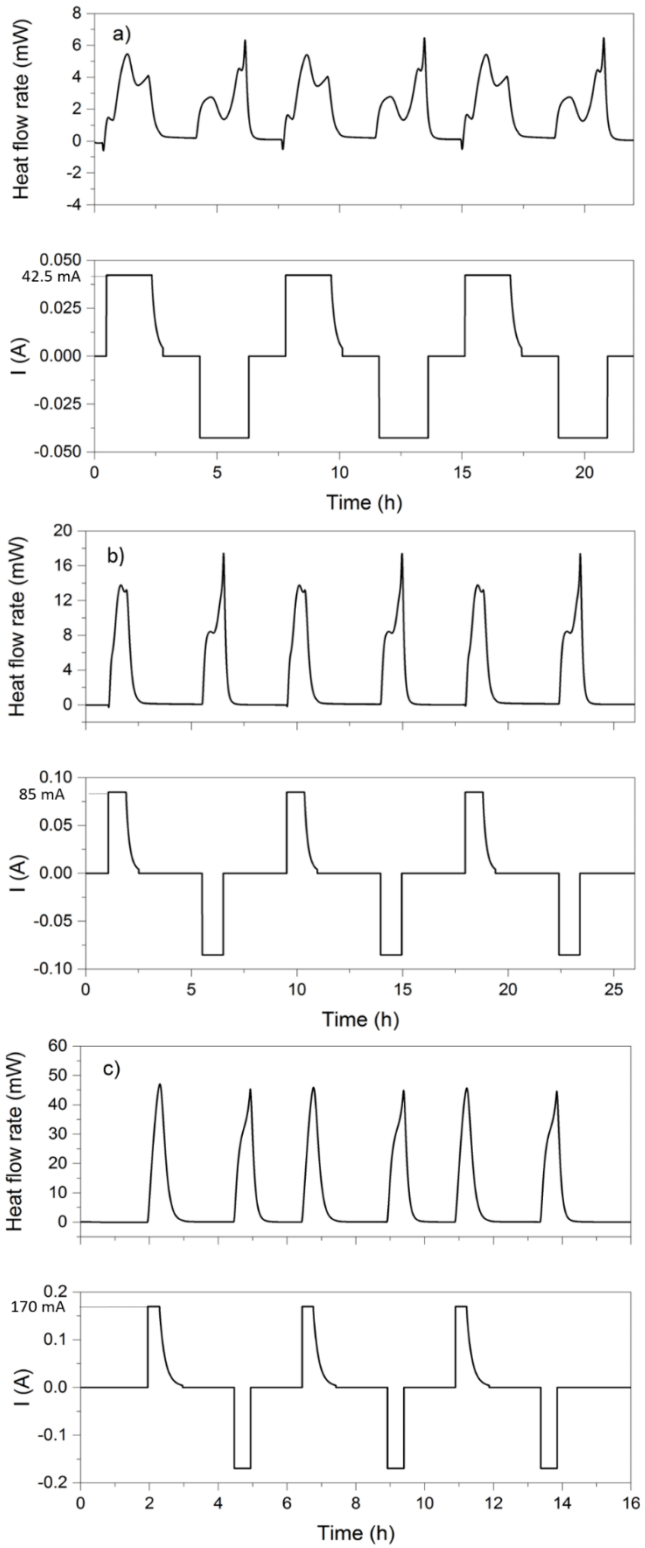

Fig. 5. 25: Heat flow rates measured by C80 calorimeter and applied current flows versus time at 30 °C: a) 0.5 C (42.5 mA), b) 1 C (85 mA) and c) 2 C (170 mA).

The heat generation in charge/discharge process was derived by the integration of the measured heat flow rate over time. In Table 5.4, the total heat generation at 30 °C and 25 °C

is compared. Heat generation at 25 °C was always a little higher than at 30 °C. Since a temperature difference of 5 K has very little effect on the reversible heat generation (equation 2.13), the irreversible heat generation should be critical for the difference. This assumption is later proven by the internal resistance investigation.

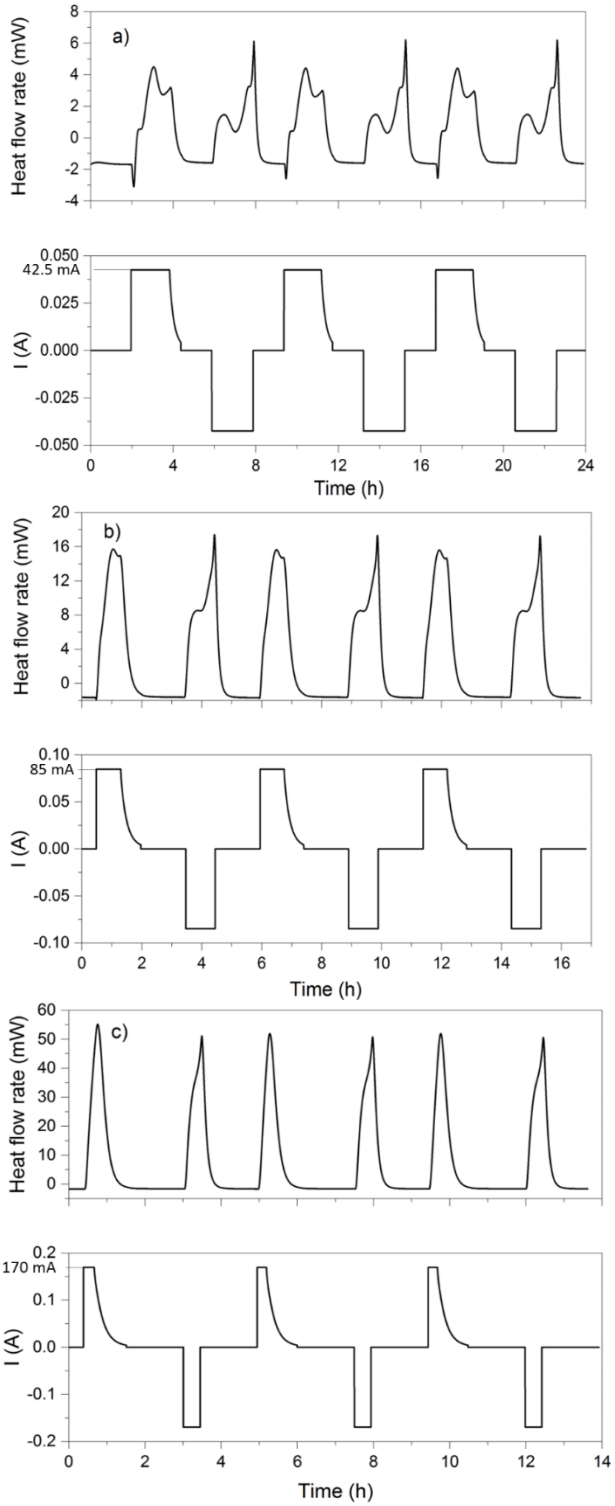

Fig. 5.26: Heat flow rates measured by C80 calorimeter and applied current flows versus time at 25 °C: a) 0.5 C (42.5 mA), b) 1 C (85 mA) and c) 2 C (170 mA).

Table 5.4 Measured total heat generation when cycling with various C-rates at 30 °C and 25 °C.

Current flow (1 C = 85 mA)	Heat determined via C80 calorimeter (J)	
at 30 °C	Charge	Discharge
0.5 C	23.59±1.64	22.18±2.00
1 C	41.60±0.42	38.98±0.78
2 C	65.62±1.54	66.34±0.30
at 25 °C	Charge	Discharge
0.5 C	26.61±1.49	25.35±0.70
1 C	44.28±1.14	43.04±0.64
2 C	69.66±8.08	69.86±4.21

When comparing the results obtained by the temperature measurement and in Section 5.51 the heat flow rate measurement (Fig. 5.27), the differences are large, and even larger with increasing C-rates. In Fig. 5.27, the heat generation measured from temperature measurements (yellow bars) and heat flow rate measurements (green bars) are compared at currents a) 0.5 C, b) 1 C and c) 2 C. The error bar in Fig. 5.27 represents the deviation of the three tested cells. The value from heat flow rate measurements are always larger than temperature measurements. There are several reasons. The cables connected with the coin cells can generate heat as well as dissipate heat, which is not covered by the heat transfer coefficient. The glass tape was used to prevent short and its mass is about 0.1 g, so the thermal influence is not considered. ΔT is defined as the difference between the peak and the starting temperature. However, the temperature increases all the time in the period of charging/discharging, which is time-dependent. The integration of temperature over time has no physical meaning, therefore, a rough calculation is using ΔT. This effect becomes more and more obvious with increasing C-rates. On the contrast, C80 calorimeter measures the heat flow rate all along the measurement with sensitive 3 D Calvet sensor (Chapter 3), which is able to detect the heat much more accurately than the sample temperature measurement. The calorimetric study clearly produces more reliable and accurate results. In the following thermal analysis, the calorimetric investigation results were used.

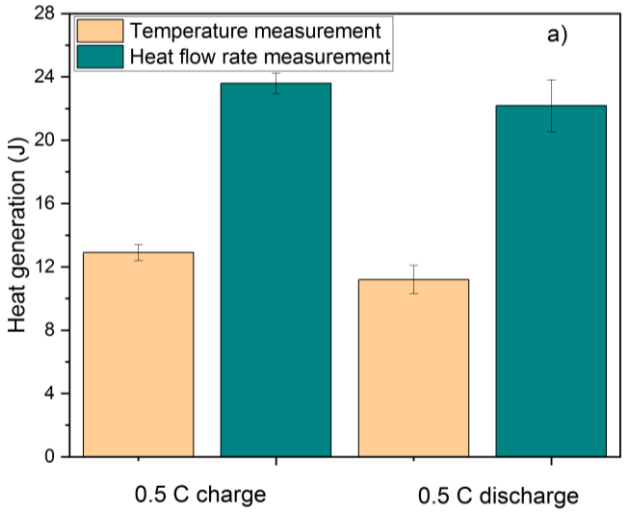

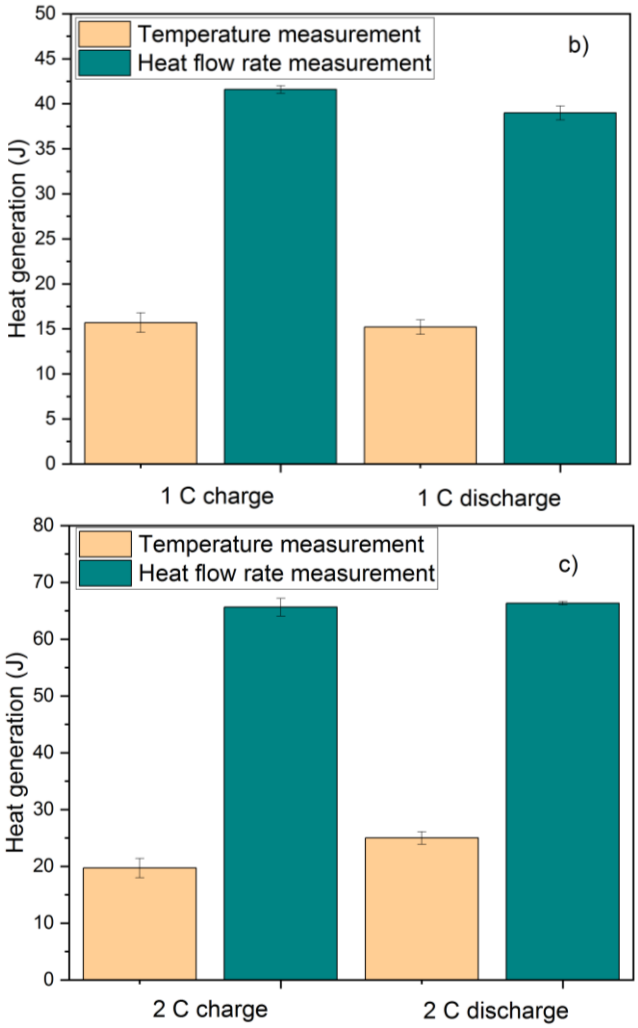

Fig. 5. 27: Comparison of heat generation determined by temperature measurements (Table 5.2) and heat flow rate measurements (Table 5.4) at 30 °C for: a) 0.5 C, b) 1 C and c) 2 C.

5.5.3 Measurement of internal resistances

Electrochemical Impedance Spectroscopy (EIS) measurement

EIS measurement was performed on a coin cell, as introduced in Chapter 2. As shown in Fig. 5.28, the polarization due to a combination of kinetic and diffusion processes is represented at low frequency (right side). The intersection of the diagram with x axis denotes the ohmic resistance at high frequency, which doesn't vary with the SOC values. In the tested cells, the ohmic resistance was 402±2 Ω. The ohmic resistance consists of the electronic/ionic resistance of the two electrodes, the electrolyte and the separator, as well as the current collectors, and the contact resistance between the cells and the holders. The charge transfer resistance and the interfacial resistance due to the formation of the SEI layer are reflected by the semicircle, which is larger at low SOCs (e.g. SOC0, SOC10 and SOC20 in Fig. 5.28). The Warburg impedance corresponds to the nearly straight line at low frequency, which is related to the diffusion of lithium ions on the interface between the active material particles and the electrolyte. Since the current applied in EIS measurement was very small, the charge transfer resistance and diffusion resistance are determined by GITT. The ohmic resistance is used in later heat generation's calculation

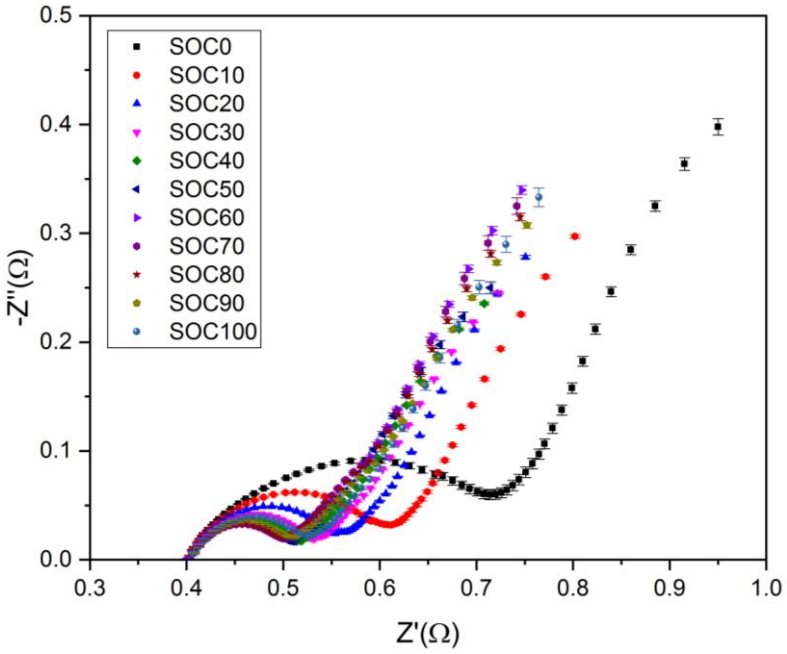

Fig. 5. 28: EIS of coin cells with various SOC at ambient temperature.

Galvanostatic Intermittent Titration Technique (GITT) measurement

The Galvanostatic Intermittent Titration Technique (GITT) measurements were performed at 25 °C and 30 °C on three cells for each temperature in charging and discharging process. The method was already described in Chapter 2. Therefore, the overpotentials due to ohmic resistance, charge transfer and diffusion are defined via GITT. Fig. 5.29 shows a typical result of the GITT measurements, which are used to separate contributions of different overpotentials under a charge pulse. In this work, the charge pulses were 0.5 C (42.5 mA), 1 C (85 mA) and 2 C (170 mA) for 12 minutes, 6 minutes and 3 minutes, respectively. The pauses were 3 h between the charge pulses, measuring at 30 °C and 25 °C. The IR-drop represents the sum of the overpotentials η_Ω and η_{ct}, respectively, due to the effects of the ohmic resistance and charge transfer impedance.
Since the total overpotential η is caused by ohmic losses, charge transfer resistance and limitations in the mass transport due to limited diffusion, the irreversible heat generation rate in cells can be also expressed with the individual contributions:

$$\begin{aligned} \dot{Q}_\Omega &= I \cdot \eta_\Omega \\ \dot{Q}_{ct} &= I \cdot \eta_{ct} \\ \dot{Q}_D &= I \cdot \eta_D \end{aligned} \tag{5.17}$$

where η_Ω, η_{ct} and η_D are the ohmic potential drop, the activation overpotential due to the charge transfer and the diffusion overpotential, respectively. I is the applied current for charging and discharging processes. According to equation 2.20, the three parts of the irreversible heat can be determined by integrating the heat flow rate over time.

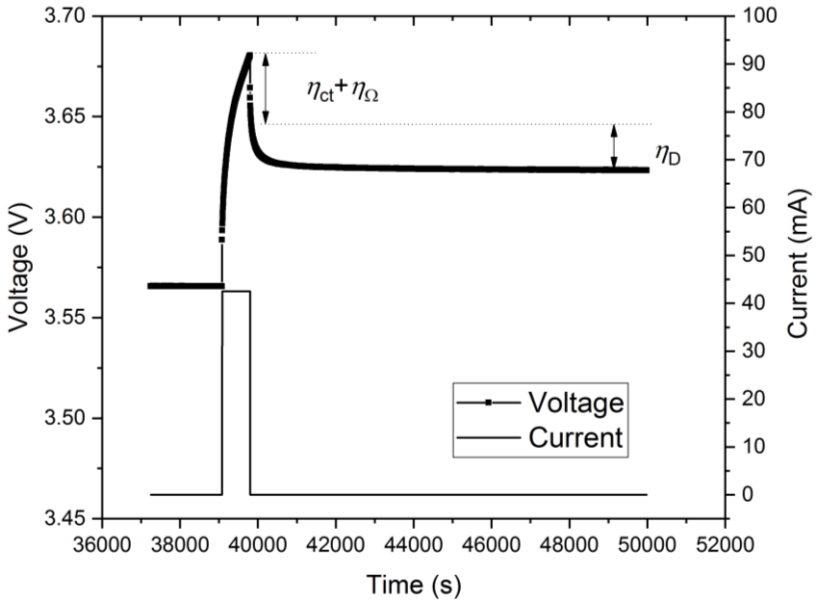

Fig. 5. 29: Charging pulse (42.5 mA) followed by relaxation time of 3 h.

The SOC and DOD (depth of discharge) values were defined by comparing with the nominal capacity of 85 mAh. Before and after the GITT measurements, the capacity of the cells is determined to be 85 mAh - 87 mAh, and no capacity fade is observed after the GITT measurements. The irreversible heat flow rates due to ohmic losses, charge transfer and ionic diffusion during charge and discharge process at 30 °C are shown in Fig. 5.30 a) – f) for different charging and discharging rates. The heat flow rates over SOCs are plotted in Fig. 5.30 and Fig. 5.31 for 30 °C and 25 °C, respectively. The error bars represent the differences of measured values for three tested cells. The values of SOC and DOD (depth of discharge) are defined with respect to the nominal capacity of 85 mAh at equilibrium conditions, i.e. for very low C-rates. The reachable capacities for 0.5 C, 1 C and 2 C are reduced to 98 %, 93 % and 85 %, respectively. In Fig. 5.30 and Fig. 5.31 a), c) and e), the heat is generated sustainedly in the whole SOC range in the charge process. In Fig. 5.30 and Fig. 5.31 b), d) and f), the diffusion heat flow rates in the discharge process, however, have a maximum value at the deeply discharged state. The corresponding maximum heat flow rates for 0.5 C, 1 C and 2 C are all higher than for the charge process. Similarly, the charge transfer heat flow rates are also very stable during charging and reach the maximum values at deep discharged state.

In Fig. 5.30 and Fig. 5.31 b), d) and f) shown, the maximum heat flow rates due to the charge transfer are increasing with rising C-rates, and the heat flow rate at deep discharge is critical, which has a relatively high value. The heat generation caused by ohmic resistance is the Joule effect, which is proportional to the current flow regardless reaction's direction. The values for the heat generation due to the diffusion resistance and the charge transfer increased dramatically with larger currents. The influences of the current flow on the three heat generations follow the ordering for both charge and discharge $\dot{Q}_{ct}>\dot{Q}_D>\dot{Q}_{\Omega}$. The heat due to the diffusion resistance dominates at 0.5 C, and shows thermal effects in the same range as the charge transfer resistance at 1 C. At 2 C, the heat effect due to the charge transfer is even larger than the effect due to the diffusion resistance in the discharge process (Fig. 5.30 f)). The heat generation values due to diffusion and charge transfer are extremely different for charging and discharging. For diffusion heat flow rates during the charge process, there are 3 peaks whose maximum value rise by faster charging/discharging, as listed in Table 5.5.

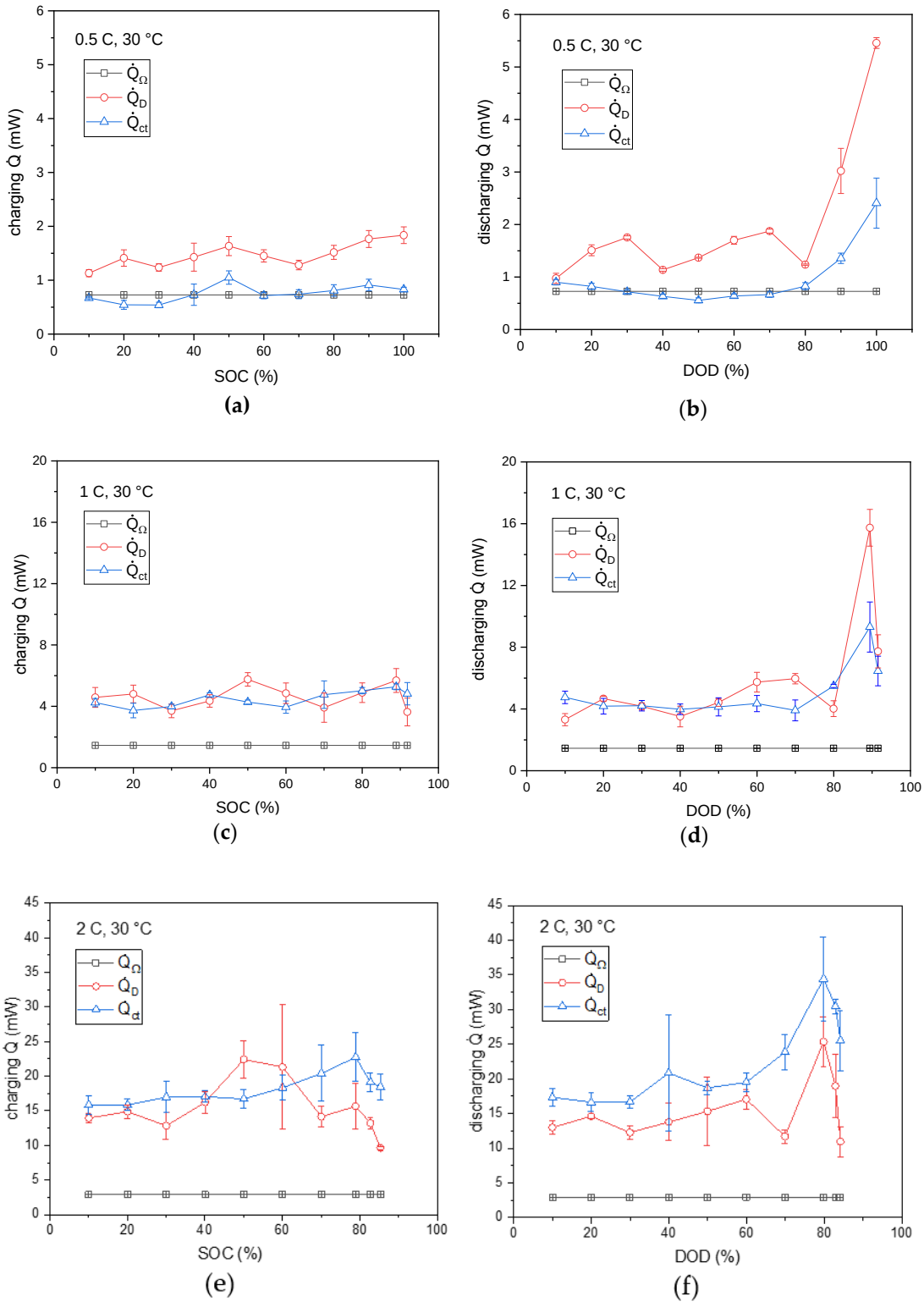

Fig. 5. 30: Irreversible heat flow rates due to ohmic, charge transfer and diffusion impedances during charging and discharging with different C-rates versus SOC and DOD at 30 °C: (a, b) 0.5 C, (c, d) 1 C and (e, f) 2 C.

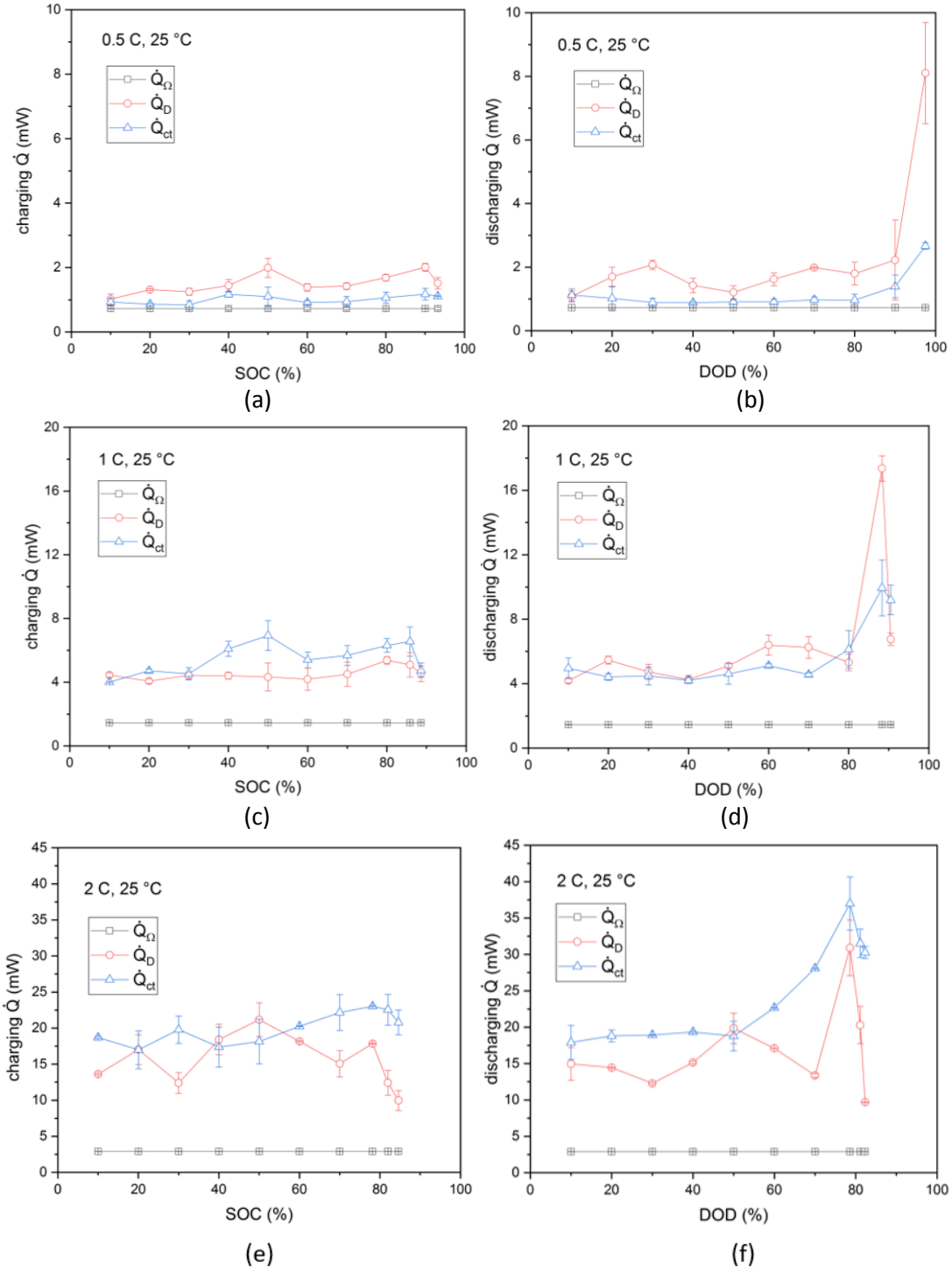

Fig. 5. 31: Irreversible heat flow rates due to ohmic, charge transfer and diffusion impedances during charging and discharging with different C-rates versus SOC and DOD at 25 °C: (a, b) 0.5 C, (c, d) 1 C and (e, f) 2 C.

Table 5.5 The maximum heat flow rates due to diffusion and charge transfer impedance in charge/discharge process at 30 °C and 25 °C.

	Max. heat flow rate in charge process at 30 °C (mW)			Max. heat flow rate in discharge process at 30 °C (mW)		
Current flow	0.5 C	1 C	2 C	0.5 C	1 C	2 C
$\dot{Q}_D$	1.8±0.3	5.8±0.4	22.4±2.7	5.5±0.2	15.7±1.2	25.4±3.5
$\dot{Q}_{ct}$	1.0±0.1	5.3±0.2	22.7±3.5	2.40±0.03	9.3±1.6	34.4±6.0
	Max. heat flow rate in charge process at 25 °C (mW)			Max. heat flow rate in discharge process at 25 °C (mW)		
Current flow	0.5 C	1 C	2 C	0.5 C	1 C	2 C
$\dot{Q}_D$	2.0±0.1	6.9±0.9	21.2±2.3	8.1±1.6	17.4±0.8	30.9±3.8
$\dot{Q}_{ct}$	1.2±0.2	5.4±0.2	23.0±0.1	2.7±0.1	9.9±1.7	37.0±3.7

At 25 °C, the C-rate influences on the heat generation caused by charge transfer is larger than at 30 °C. There is less heat generated at 30 °C than at 25 °C. That might be because the process for diffusion and charge transfer are impeded more at 25 °C than at 30 °C.

In Fig. 5.32 and Fig. 5.33, comparing the total irreversible heat generation at various C-rates, there is nearly the same trend. Interestingly, the heat flow rate's curves shift towards lower SOC/DOD with increasing C-rates for both charge and discharge process. Moreover, the heat effects are much stronger at high C-rates. It is similar to the differential scanning calorimetry (DSC) measurement, when with higher scanning rate, the thermal effects will shift and meanwhile the effects will be larger. In Fig. 5.32 a) shown, the total irreversible heat flow rates are about 3 mW, 10 mW and 45 mW at 0.5 C, 1 C and 2 C at 30 °C. The heat flow rates at 25 °C are in the same range (Fig. 5.33 a)). As shown in Fig. 5.32 b) and Fig. 5.33 b), there will be dramatically more heat generated at the deeply discharged state. At 2 C-rates, the heat flow rates during discharge reach a maximum value of ca. 65 mW at 30 °C and ca. 72 mW at 25 °C, where the DOD are 80 %. The heat flow rates in Fig. 5.32 b) and 5.33 b) at 0.5 C and 1 C- rates also reach the maximum values at high DODs. Therefore, in discharge process, the irreversible heat can be effectively reduced by preventing deep discharge.

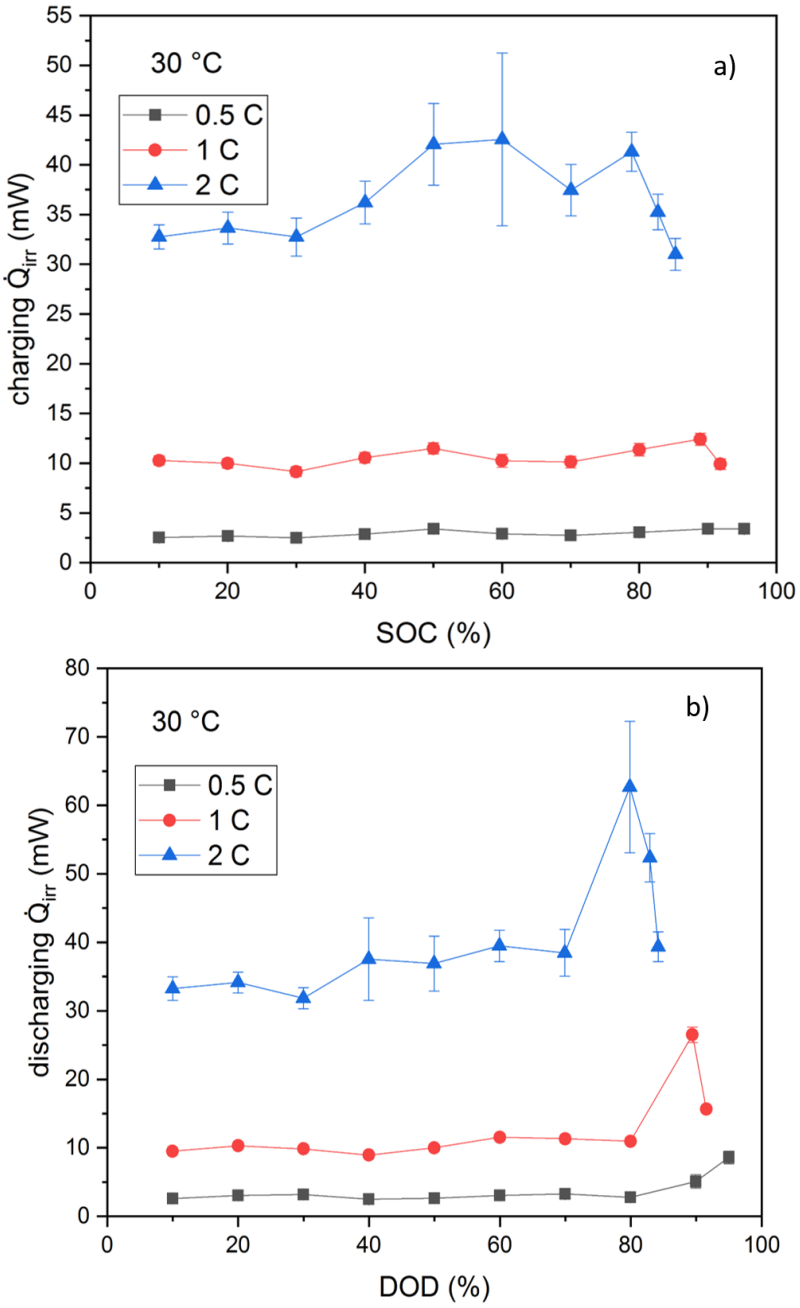

Fig. 5. 32: The total irreversible heat flow rates with various C-rates versus SOC and DOD at 30 °C: a) charging, b) discharging.

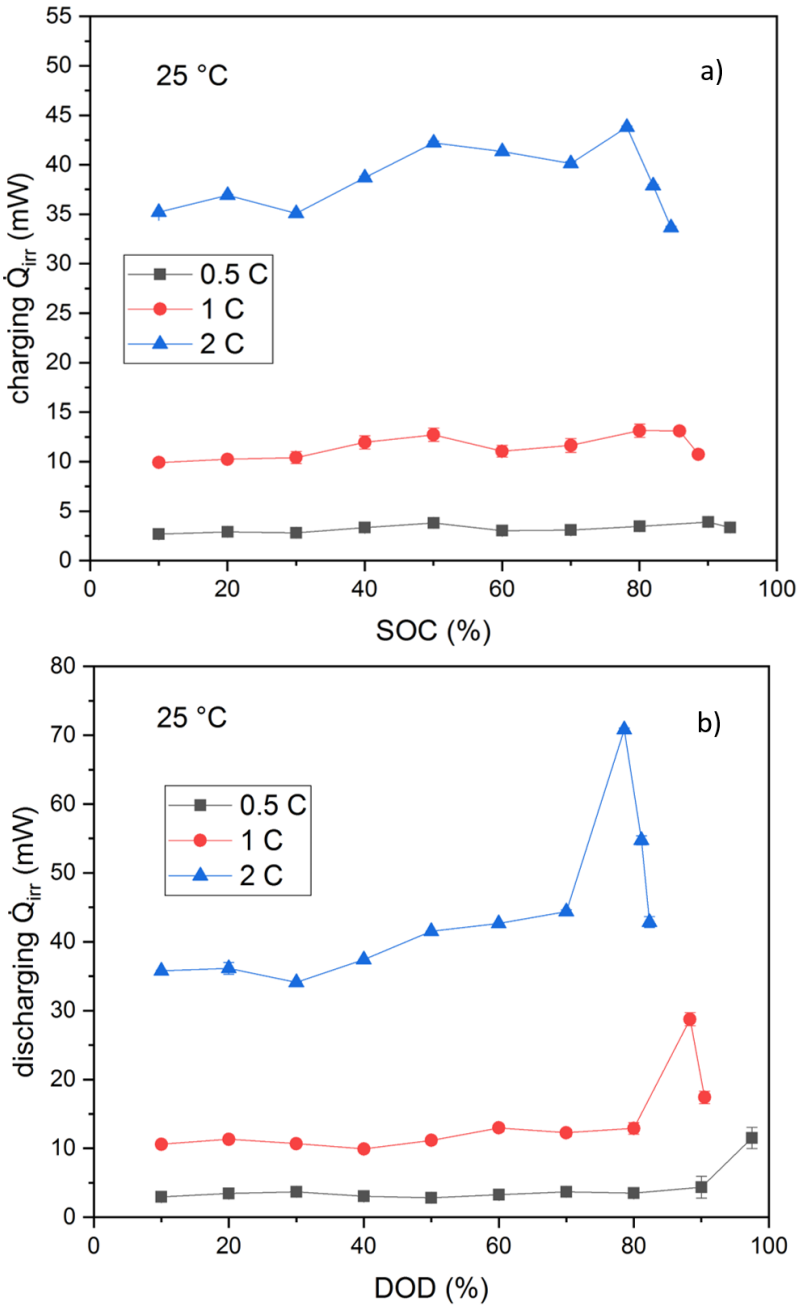

Fig. 5. 33: The total irreversible heat flow rates with various C-rates versus SOC and DOD at 25 °C: a) charging, b) discharging.

5.5.4 Measurement of entropy change

At a certain SOC, under ideal conditions, the change of entropy can be determined by measuring the OCVs under various temperatures according to equation 2.13 in Chapter 2 [41, 43, 44].

$$\Delta S(x) = \mathrm{F} \cdot \left(\frac{\partial U^0(x,T)}{\partial T}\bigg|_x \right) \tag{2.13}$$

The dependence of OCVs on temperature is ideally linear (see e.g. Fig. 5.34 b)). The product of the slope of this linear function with the Faraday constant is the entropy change at certain SOC. Analogously, the variation of the enthalpy is obtained by equation (2.14) [41, 43].

$$\Delta H(x) = \mathrm{F} \cdot \left(-U^0(x,T) + T \cdot \left. \frac{\partial U^0(x,T)}{\partial T} \right|_x \right) \tag{2.14}$$

The total changes in the entropy and enthalpy are achieved via the integration between two electrode compositions, as described by equation 2.15 and equation 2.16 [44].

$$\Delta S|_{x_1}^{x_2} = F \cdot \left(\int_{x_1}^{x_2} \left. \frac{\partial U^0(x,T)}{\partial T} \right|_x \cdot dx \right) \tag{2.15}$$

$$\Delta H|_{x_1}^{x_2} = F \cdot \int_{x_1}^{x_2} \left(-U^0(x,T) + T \cdot \left. \frac{\partial U^0(x,T)}{\partial T} \right|_x \cdot dx \right) \tag{2.16}$$

As the entropy change will be determined based on the relationship between OCVs and temperatures, two temperature ranges are carefully compared. One measurement is performed in large range from 45 °C to 5 °C; the other is in small temperature range of 35 °C - 15 °C.

Δ S measurement in the temperature range of 45 °C to 5 °C (large range)

Three coin cells are firstly charged to SOC100 at 25 °C, and OCVs are measured in 10 % SOC steps. For each SOC step, the cells are relaxed for 3 h at temperatures: 45 °C, 40 °C, 35 °C, 30 °C, 25 °C, 20 °C, 15 °C, 10 °C and 5 °C. In order to achieve selected SOCs, the cells are discharged with 0.5 C for 0.2 h. The OCVs in the last 30 minutes of relaxation, where the voltages are considered to be in equilibrium, are taken to calculate the average value at selected temperatures.

Ideally, as the temperature changes stepwise with time, the OCVs should exhibit corresponding stepwise behavior with linearly visible plateaus, as can be seen in Fig. 5.34 a) for SOC40. In this case, the dependence of OCVs on temperatures is linear (Fig. 5.34 b)). According to equation 2.13, the entropy change of reversible reaction at SOC40 is obtained.

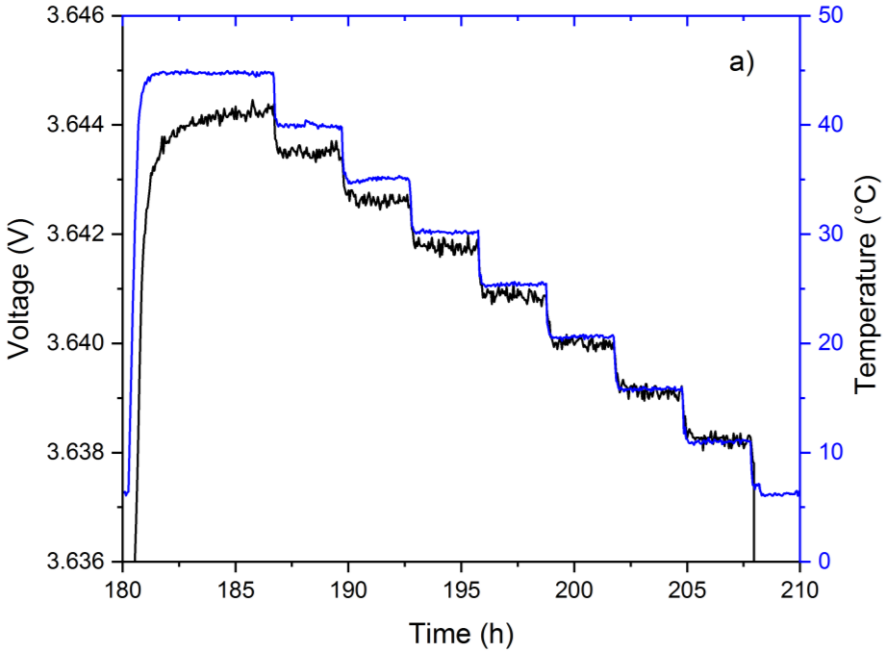

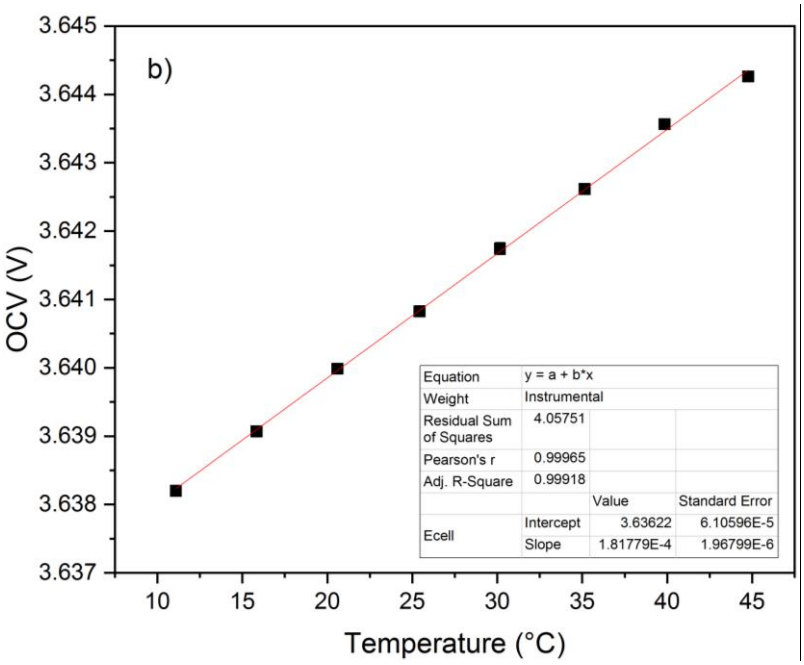

Fig. 5.34: The results from entropy measurements in this work: a) the voltage curve at various temperatures at SOC40 and b) OCV versus temperature and the fitting function at SOC40.

Fig. 5.35 is showing the temperature and voltage changes and the corresponding fitting curve for SOC100. On the contrary to SOC40, at SOC100, the equilibrium states are hard to reach, since both the charge transfer and the mass transfer are fairly slow. As a consequence, the measured voltages deviate from the equilibrium values and do not show a stepwise behavior with plateaus (Fig. 5.35 a)). Hence, in this case, the linearity of the dependence of OCVs on temperatures (Fig. 5.35 b)) is not as good as that in Fig. 5.34 b). For the convenience of calculating the entropy change, a linear fit is also adopted for the dependence of OCVs on temperatures. It is noteworthy that only the temperatures less than 30 °C are employed for the fitting in this case. In this work, when the voltage drops to less than 0.01 V, it is considered to as reaching an equilibrium from the temperature of 30 °C. The voltages in the first 10 hours of relaxation are not stable since the higher temperatures accelerate the self-discharge and side reactions inside cells. As the voltage stabilizes from 30 °C, the OCVs from 30 °C to 10 °C are used to fit the function. At SOC100, the active materials on the positive electrode are in a metastable phase due to deep delithiation. At boundary of stable/metastable phase, the equilibrium is thus relatively difficult to achieve.

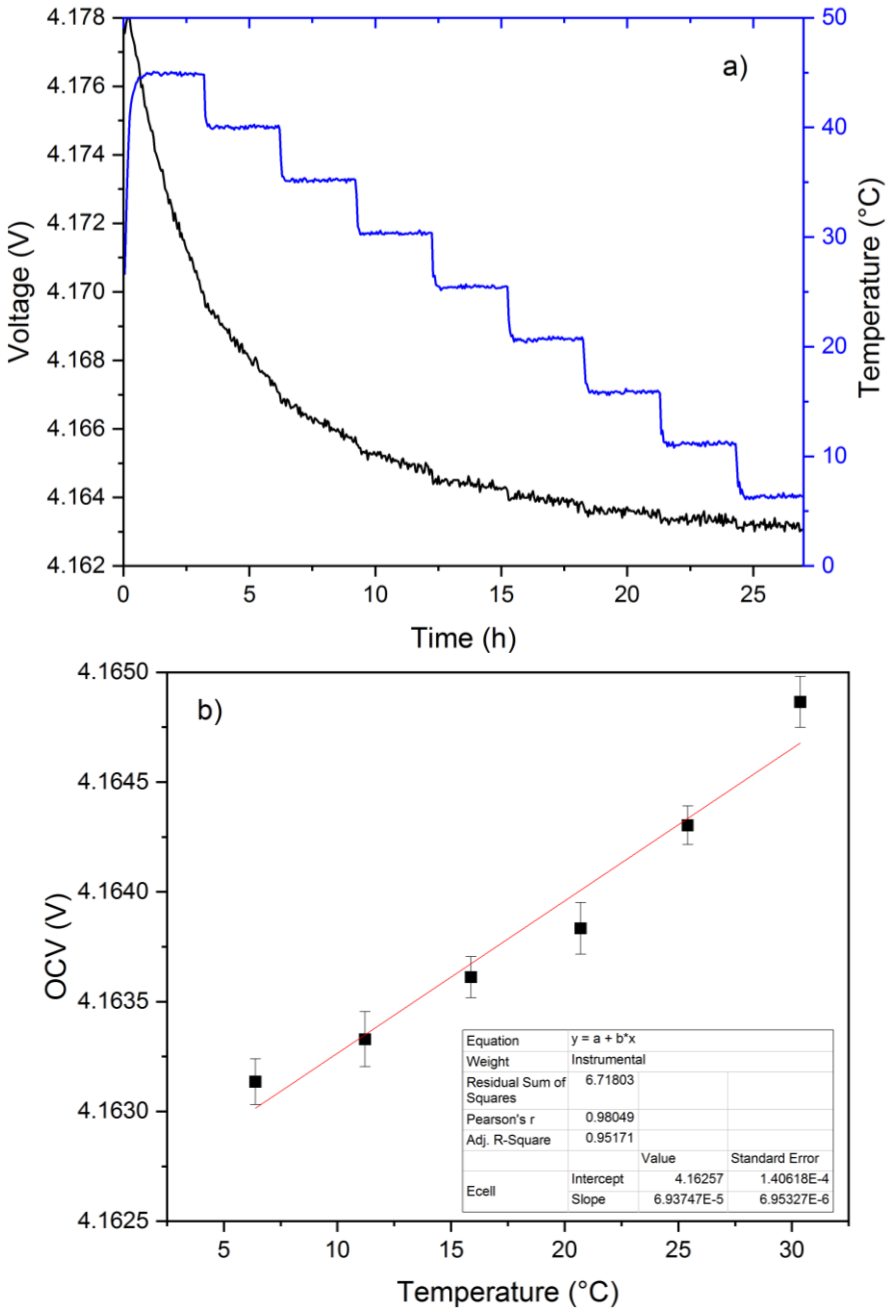

Fig. 5.35: The results from entropy measurements in this work: a) The voltage curve under various temperatures at SOC100 and b) OCV versus temperature and the fitting function at SOC100.

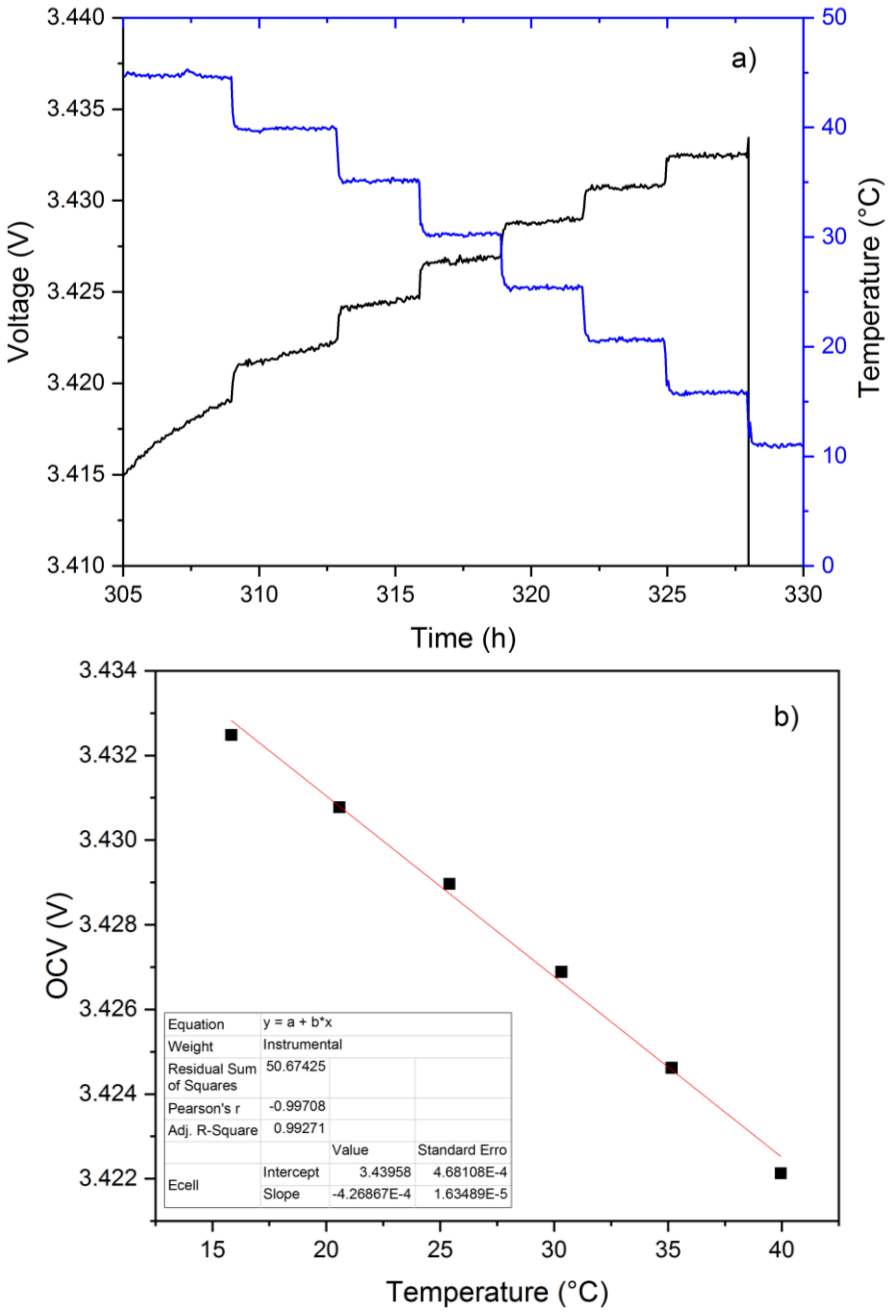

Fig. 5.36: The results from entropy measurements in this work: a) The voltage curve under various temperatures at SOC0 and b) OCV versus temperature and the fitting function at SOC0.

Fig. 5.36 shows the measurement at SOC0, taking longer relaxation time to achieve an equilibrium than at SOC40. Therefore, the fitting is from OCVs at 40 °C. The results of entropy change measurements on three cells are demonstrated in Fig. 5.37 a), and the three measurements are in good agreement. Fig. 5.37 b) demonstrates that the results are very comparable with Viswanathan et al.'s work [43] and Yazami's work [145], which measured LiBs with similar positive electrode materials. With help of equation 2.13, the enthalpy change of the reversible reaction is calculated. Discharging from SOC90 to SOC60, the entropy change are slightly decreasing, and positive values indicate another order to disorder phase transfer. Further discharging in SOC60 - 40, the maximal value 20 J/(mol·K) of entropy change is reached at SOC50, and the minimal value is at about 0 J/(mol·K) at SOC60. The phases are changing

towards disorder phases. In SOC range 0 - 30, the phases in cells are changing towards higher order. At SOC0 in discharge process, the entropy change was negative value indicating exothermic effects of reversible heat will be observed in cells when cell's SOC is between SOC0 and SOC30.

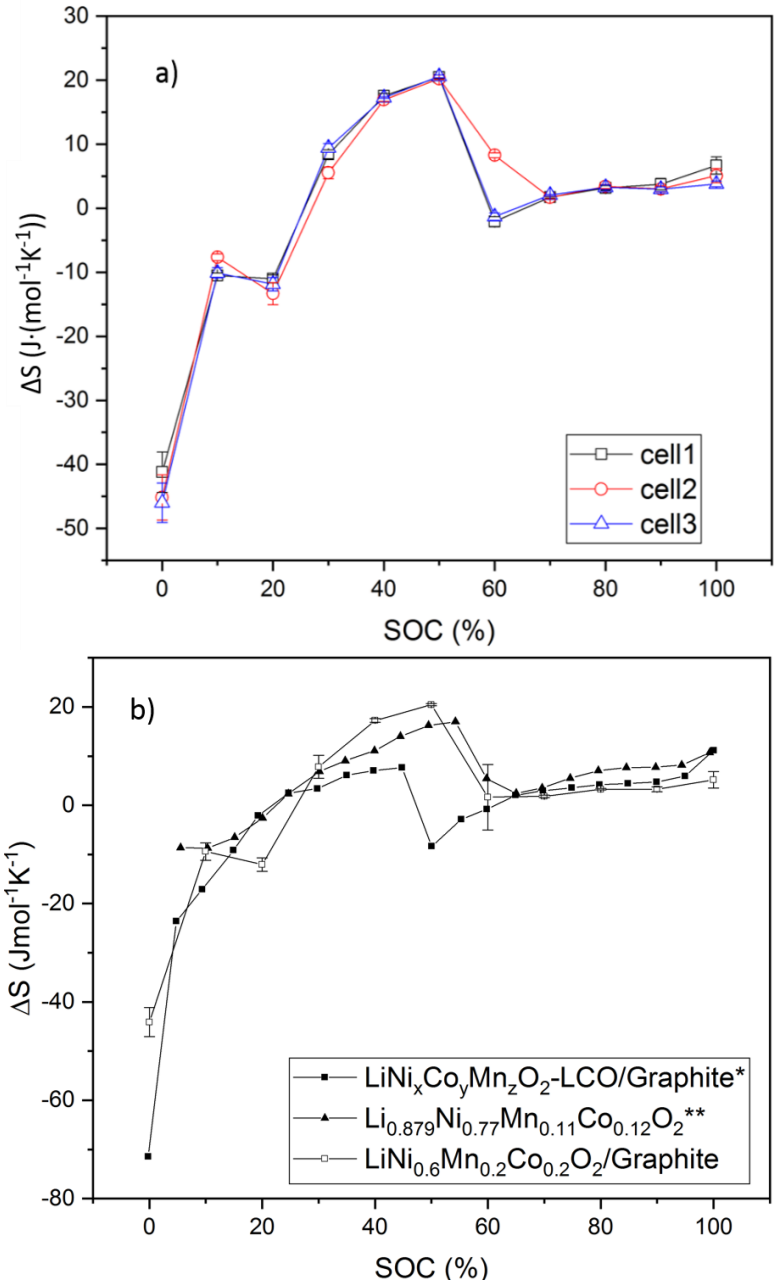

Fig. 5.37: Entropy change vs. SOC: a) the entropy change versus SOC of three cells. b) The comparison of this work measured in large temperature range with *the results from Ref. [43] and ** the results from Ref. [145].

An empirical relationship between SOC, entropy change and enthalpy change of the reversible reaction is proposed by Yazami [145]:

$$\mathrm{SOC} = \alpha + \beta \cdot \Delta S + \gamma \cdot \Delta H \tag{5.18}$$

Table 5.6 The fitting parameters and R-square for the function of SOC, entropy change and enthalpy change, according to equation 5.18.

α	β	γ	R^2
-35.53	-1.34	0.64	0.98

These fitting parameters have been determined in this work for the commercial coin cells. The resulting plot is shown in Fig. 5.38.

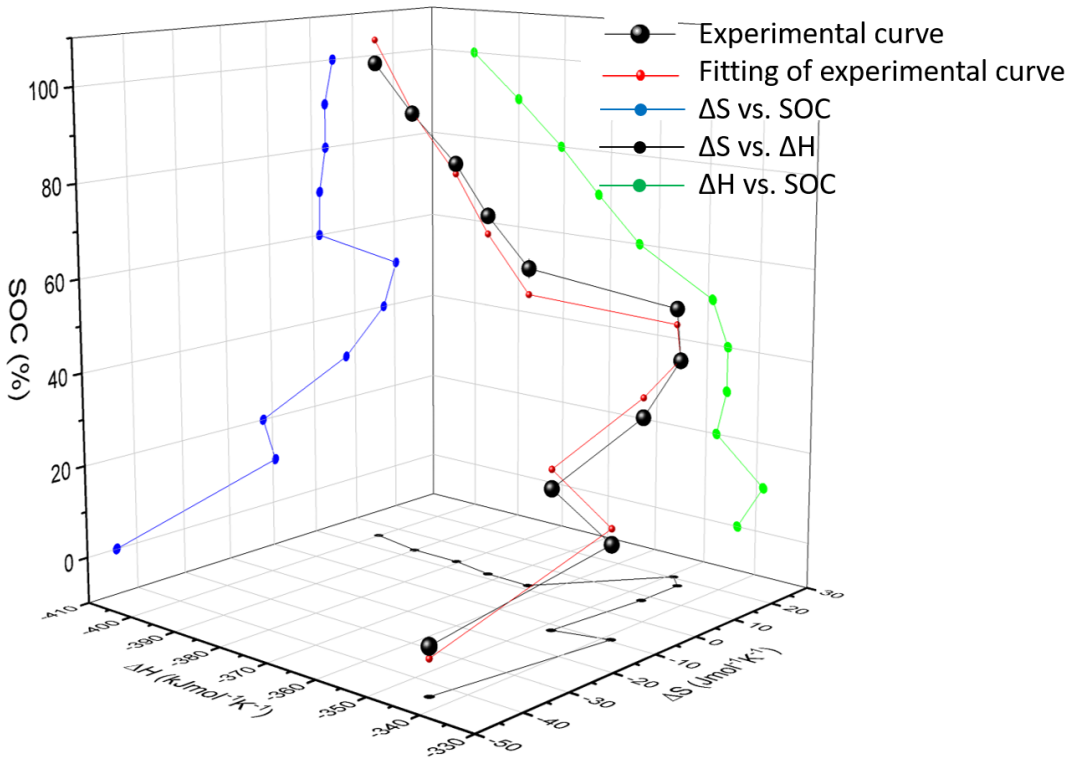

Fig. 5.38: The function of ΔS, ΔH, and SOC three-dimensional plots measured in large temperature range, and the data are listed in Appendix III.

ΔS measurement in the temperature range of 35 °C to 15 °C (small range)

The side reactions, such as self-discharge in LiBs and electrolyte decomposition have a considerable impact on the entropy measurements when the temperature dramatically deviates from 25 °C [45, 123]. Hence, entropy change measurement was optimized by measuring in a smaller temperature range of 35 °C to 15 °C with 5 °C interval. Due to the difficulty to obtain equilibrium at SOC100 and SOC0, the measuring range was limited from SOC90 to SOC10. The applied discharge current between the SOCs steps was reduced from 0.5 C to 0.1 C. Since the current is smaller, the disturbance to the system is smaller, so the equilibrium can be achieved easier and faster. A similar baseline correction as in Ref. [45] was applied at 25 °C, therefore the OCV at 25 °C was measured 3 times. The baseline is defined by a function fitting to the OCV curves at 25 °C. The temperature profile is shown in Fig. 5.39, according to the method proposed by Ref. [43, 45]. Each temperature step will be 3 h.

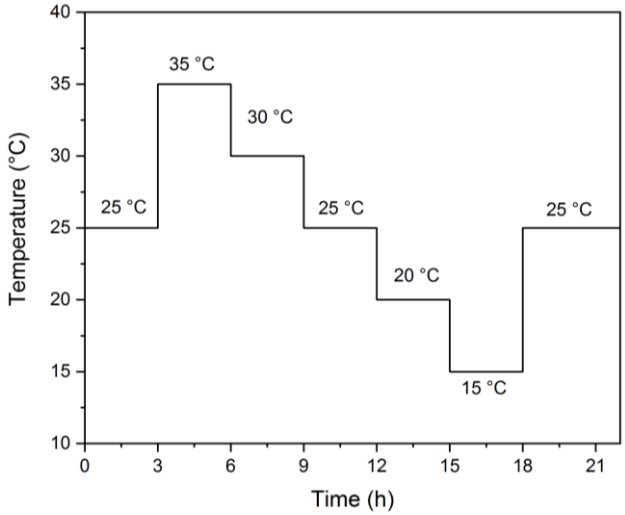

Fig. 5.39: The temperature profile for ΔS measurement.

In ideal case, when the baseline function is perfect fitting the OCVs curves, the baseline subtraction can help to reduce the potential drift from equilibrium. However, when the baseline function is not perfect fitting, such as the difference between the red fitting curve and black measured curve, highlighted by the blue circle in Fig. 5.40 b), an extra error will be introduced in the measurements.

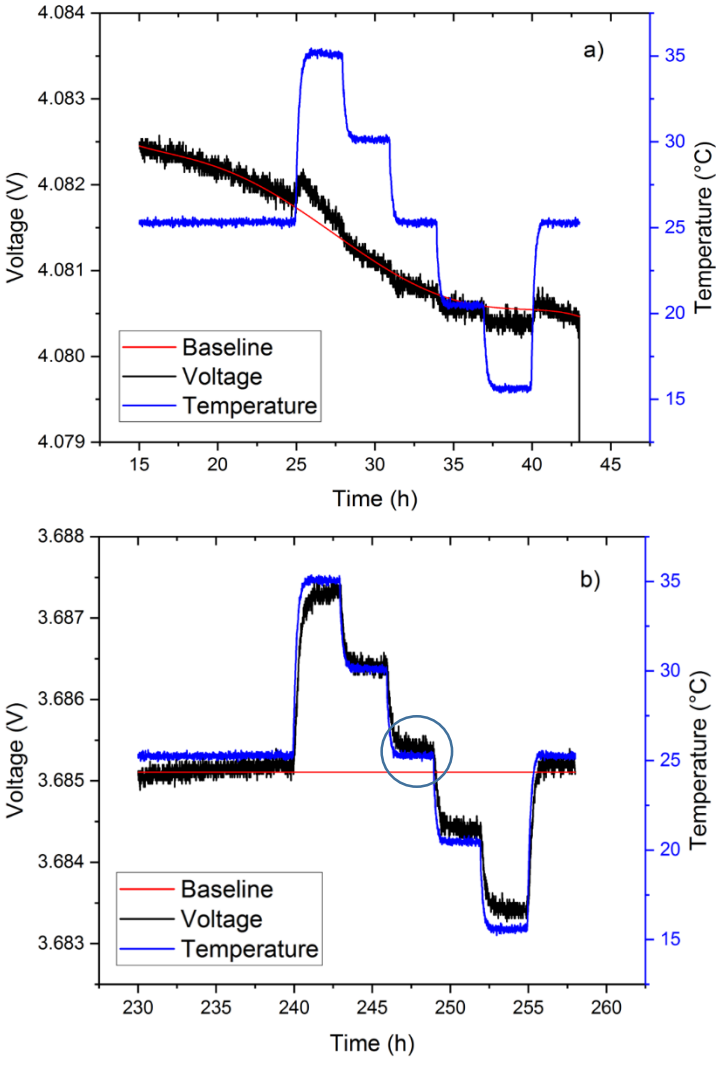

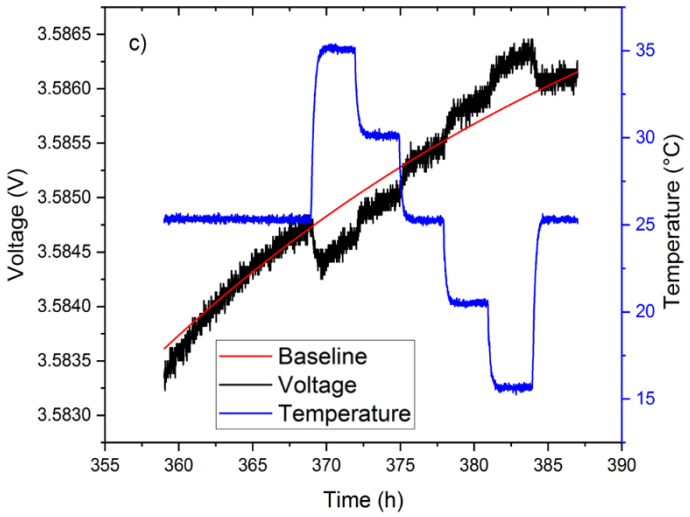

Fig. 5.40: The voltage curve under various temperatures with its baseline: a) at SOC90, b) at SOC40 and c) at SOC10.

Comparing the average ΔS for three cells, the difference due to subtraction are shown at SOC10, SOC20 and SOC60 in Fig. 5.41. The high temperature measurement (black curve) is in a good agreement with the baseline measurement, and the curve lies between the other two curves with a small uncertainty. The entropy change at SOC60 has a large uncertainty, where the blue curve deviates dramatically from the others. As Fig. 5.37 shows, the turning point at about SOC60 shifts, which may relate to a phase transformation. Hence, the results at this point show a large deviation. Another reason is not reaching equilibrium, which is corrected by baseline. With baseline correction, the red line is in good agreement with black line. Therefore, the high temperature measurement results (black line) are used in the later thermal analysis.

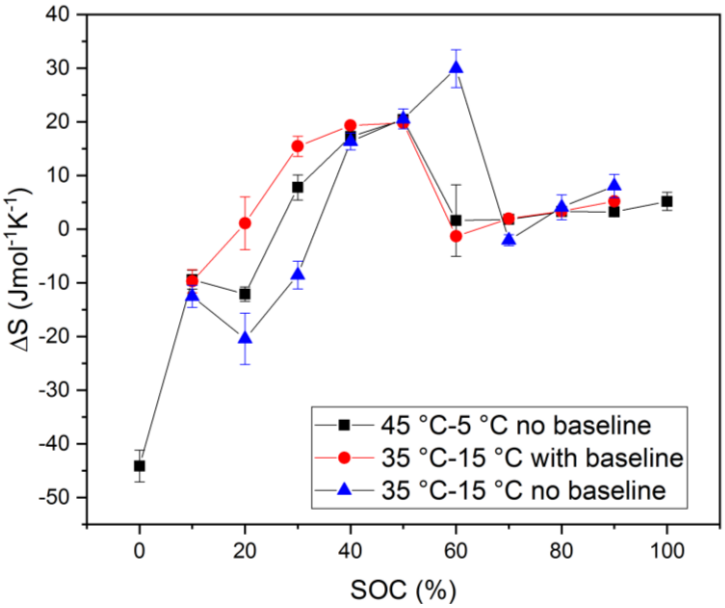

Fig. 5.41: The comparison of average value of three cells' ΔS for measurements with/without baseline subtraction.

5.5.5 Comparison of calculated heat generation with measured data

As the irreversible heat flow rates were determined by using the values for the internal resistances, the reversible heat flow rates were determined by the entropy change as well. Using the equation 2.10 and equation 2.16, the total heat flow rates can be computed.

$$\dot{Q}_{tot} = \dot{Q}_{rev} + \dot{Q}_{irr} \tag{2.10}$$

$$\dot{Q}_{rev} = T \cdot \Delta S \cdot \frac{i}{F} \tag{2.16}$$

Here, $\dot{Q}_{irr}$: irreversible heat flow rate; $\dot{Q}_{rev}$: reversible heat flow rate; T: temperature; ΔS: reversible entropy change; i: current flow; F Faraday constant (96485 Coulomb per equivalent).

The total heat flow rates have been computed for the different SOC values at 30 °C and 25 °C under different C-rates as shown by open symbols in Fig. 5.42 (at 30 °C) as well as in Fig. 5.43 (at 25 °C). These values are compared with the curves from the C80 measurements as solid curve in Fig. 5.42 (at 30°C) as well as in Fig. 5.43 (at 25 °C). As the heat flow rate in blue circle in Fig. 5.42 a) showing, an endothermic effect is observed at beginning of the charging process with 0.5 C, which was also reported by Williford et al. [125] and Hong et al.[144]. This cooling effect is due to the positive value (endothermic effect) of entropy change in reversible reaction during charging (opposite reaction in discharge process in Fig. 5.37 page 124) at low SOCs. When cells are charged at 1 C and 2 C rates, the cooling effect decreases and vanishes (in Fig. 5.42 and 5.43). The reversible heat effect dominates the charging process at low currents. The standard CCCV method, as mentioned before, was adopted in C80 calorimeter measurements, while the entropy change and internal resistance were using CC method for reaching each SOC step. The CCCV in charging process is mainly to compensate for self-discharge, so the total energy in charging equals to the energy in discharging. Thermal effects in CV phase was negligible and wasn't considered in calculation. The computed heat flow rates deviate more from the measured heat flow at 1 C and 2 C. One reason is that charging with CCCV method can reach a higher capacity, meanwhile more heat is generated.

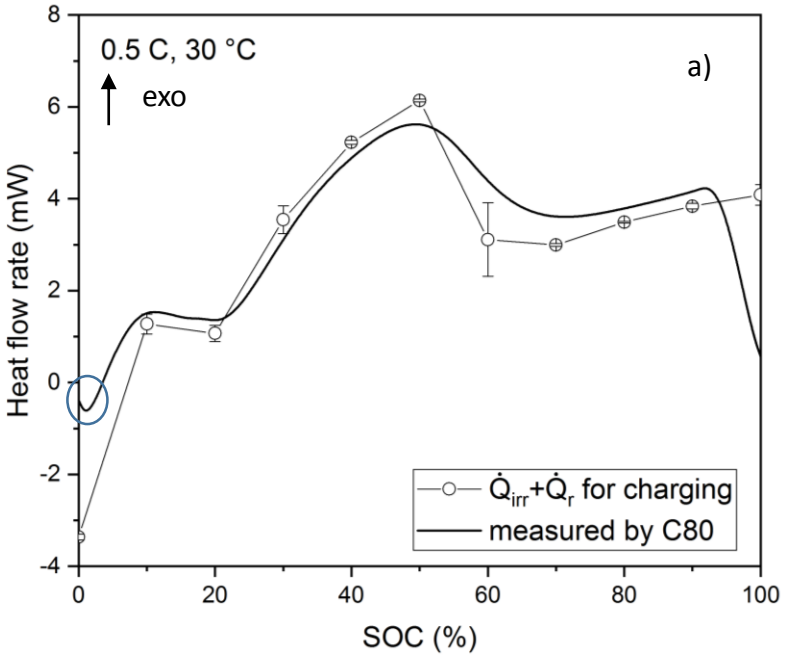

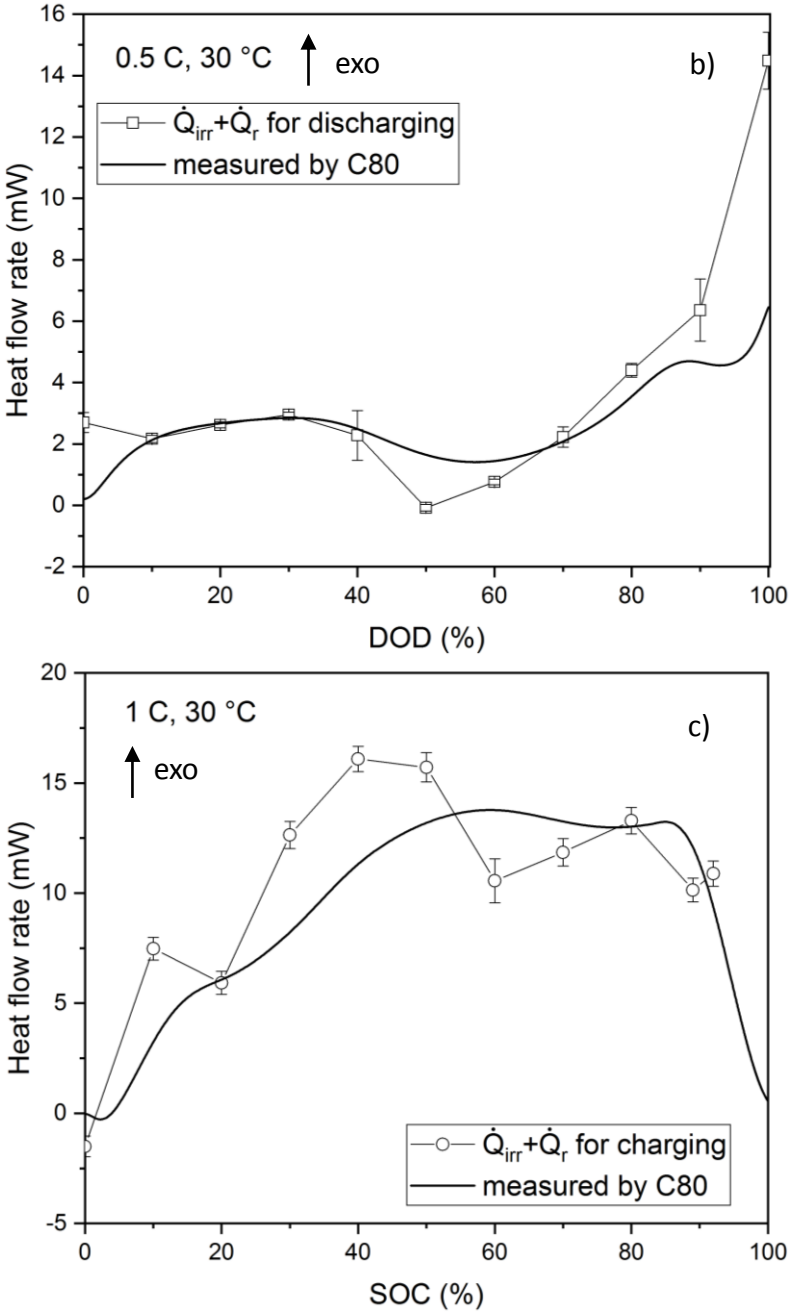
0.5 C, 30 °C
exo
b)
$\dot{Q}_{irr}+\dot{Q}_r$ for discharging
measured by C80
Heat flow rate (mW)
DOD (%)
1 C, 30 °C
exo
c)
$\dot{Q}_{irr}+\dot{Q}_r$ for charging
measured by C80
Heat flow rate (mW)
SOC (%)

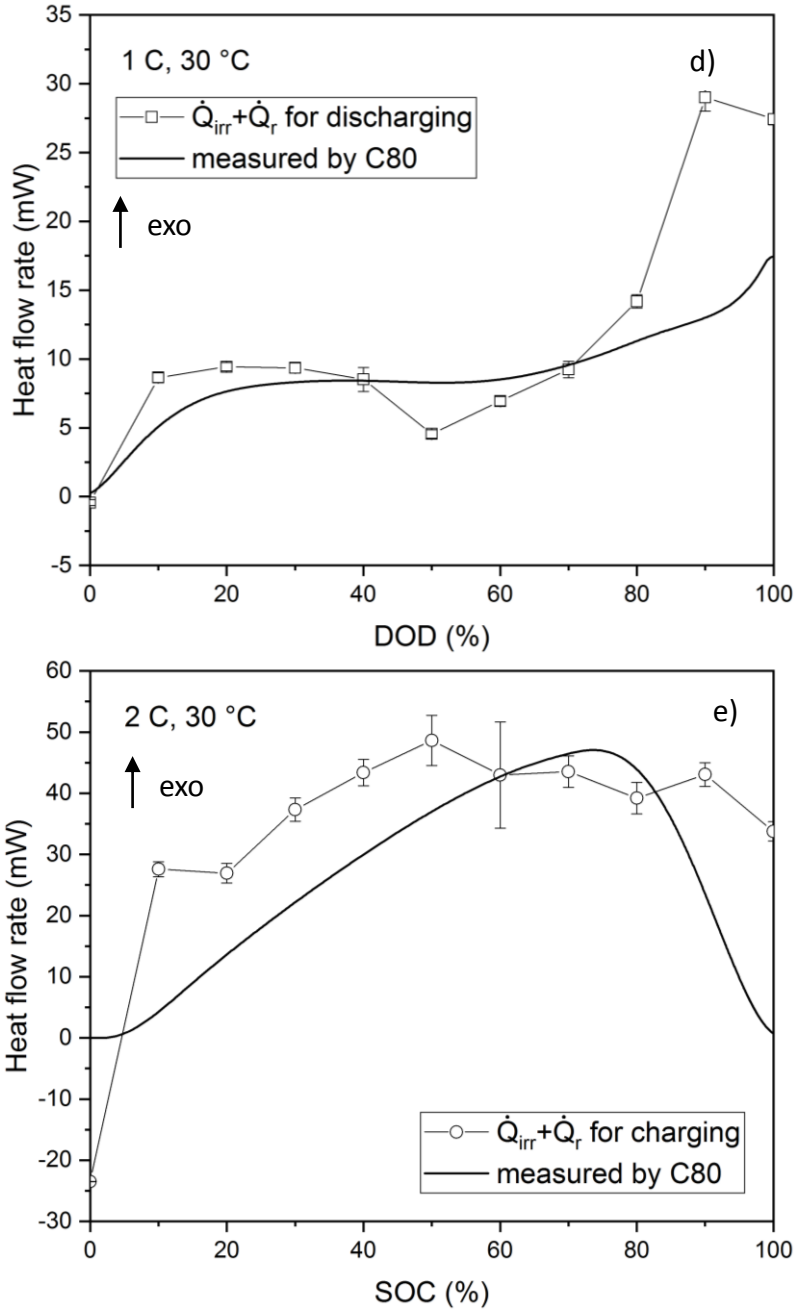
1 C, 30 °C
d)
$\dot{Q}_{irr}+\dot{Q}_r$ for discharging
measured by C80
exo
Heat flow rate (mW)
DOD (%)
2 C, 30 °C
e)
exo
$\dot{Q}_{irr}+\dot{Q}_r$ for charging
measured by C80
Heat flow rate (mW)
SOC (%)

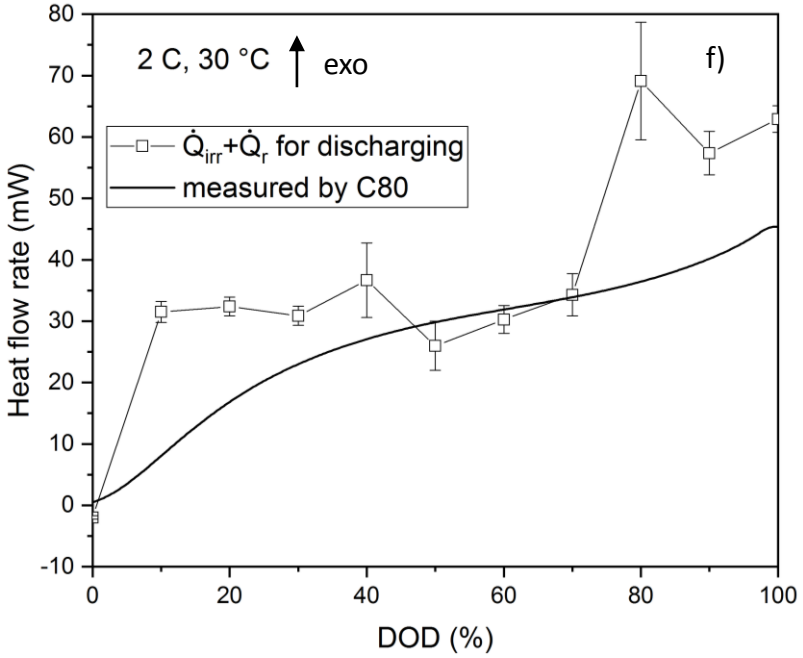

Fig. 5. 42: The comparison of computed heat flow rates from irreversible and reversible heat flow rates; and the total heat flow rates measured by C80 calorimeter versus SOC/DOD under different C-rates at 30 °C: a) charging at 0.5 C (42.5 mA), b) discharging at 0.5 C (42.5 mA), c) charging at 1 C (85 mA), d) discharging at 1 C (85 mA), e) charging at 2 C (170 mA), f) discharging at 2 C (170 mA).

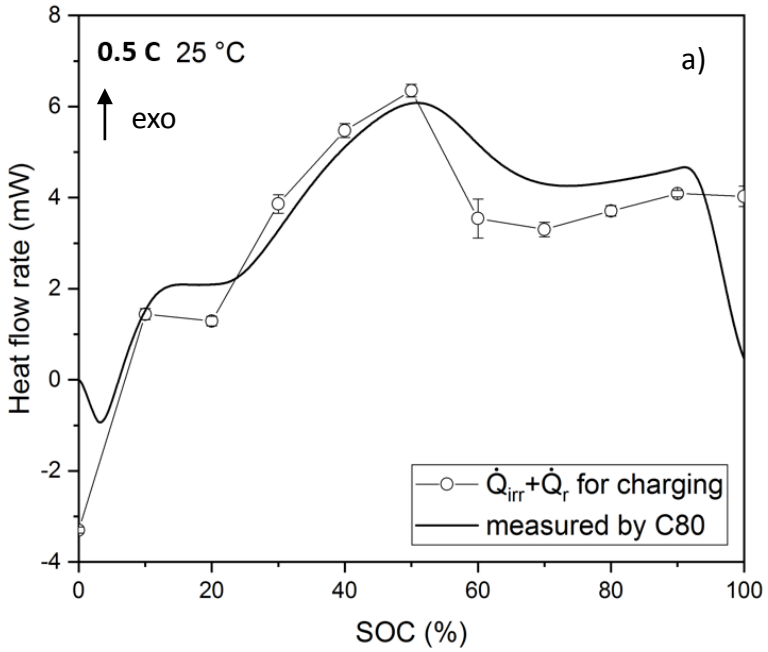

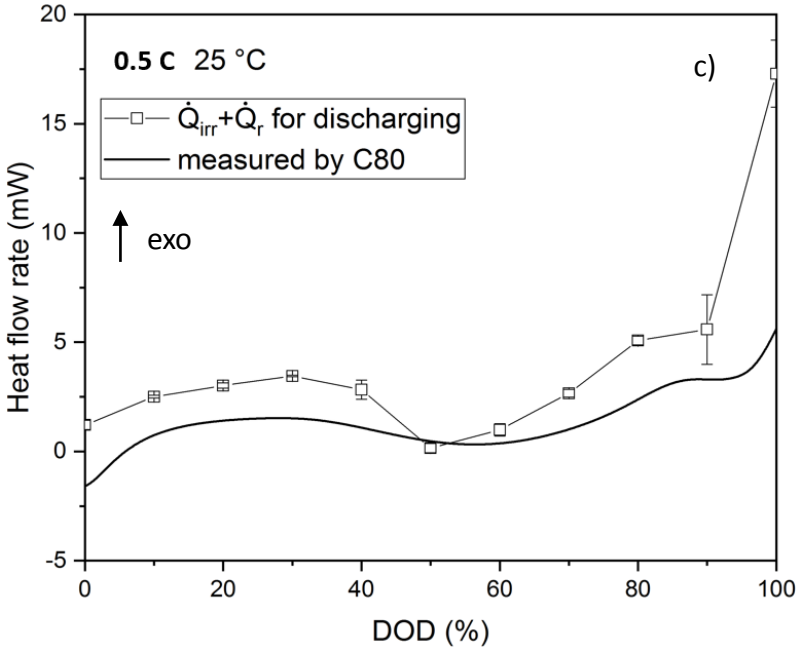
0.5 C 25 °C
c)
$\dot{Q}_{irr}+\dot{Q}_r$ for discharging
measured by C80
exo
Heat flow rate (mW)
DOD (%)

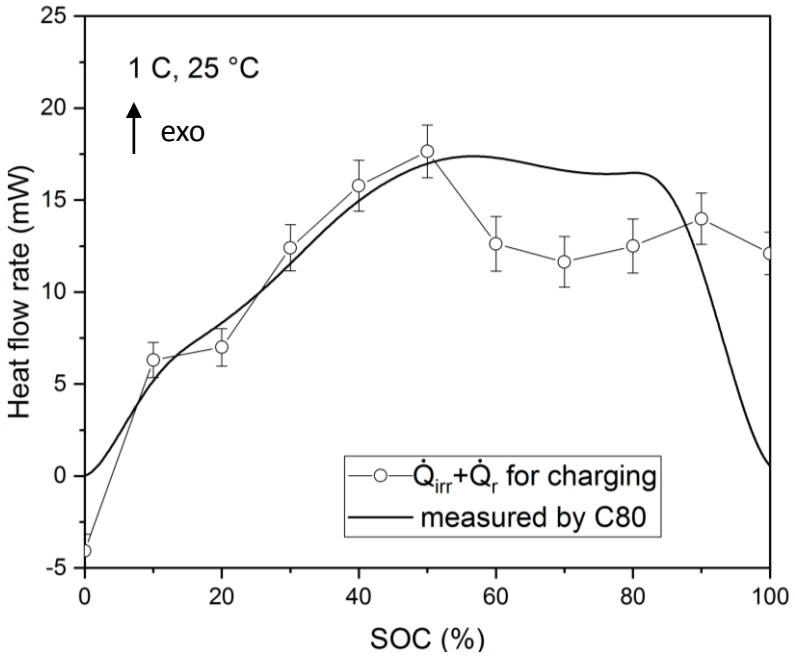
1 C, 25 °C
exo
$\dot{Q}_{irr}+\dot{Q}_r$ for charging
measured by C80
Heat flow rate (mW)
SOC (%)

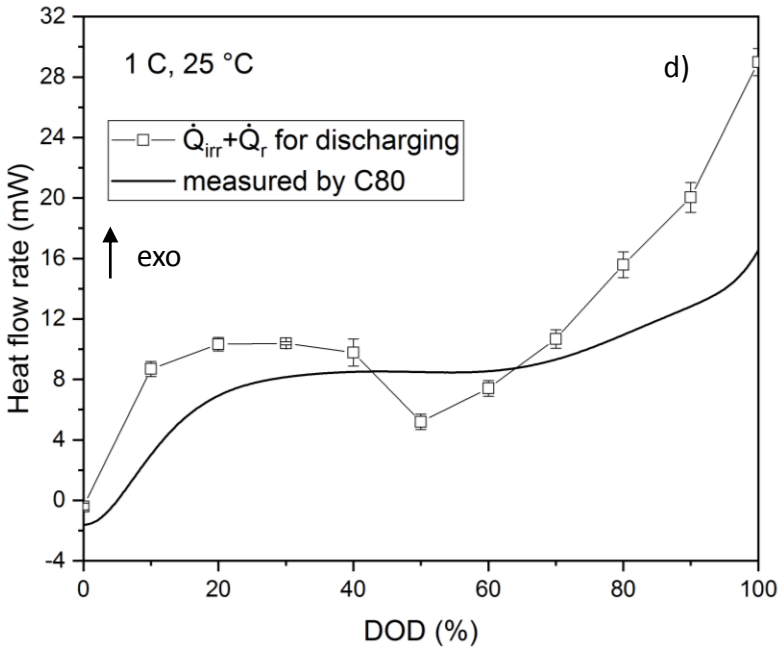
1 C, 25 °C
d)
$\dot{Q}_{irr}+\dot{Q}_r$ for discharging
measured by C80
exo
Heat flow rate (mW)
DOD (%)

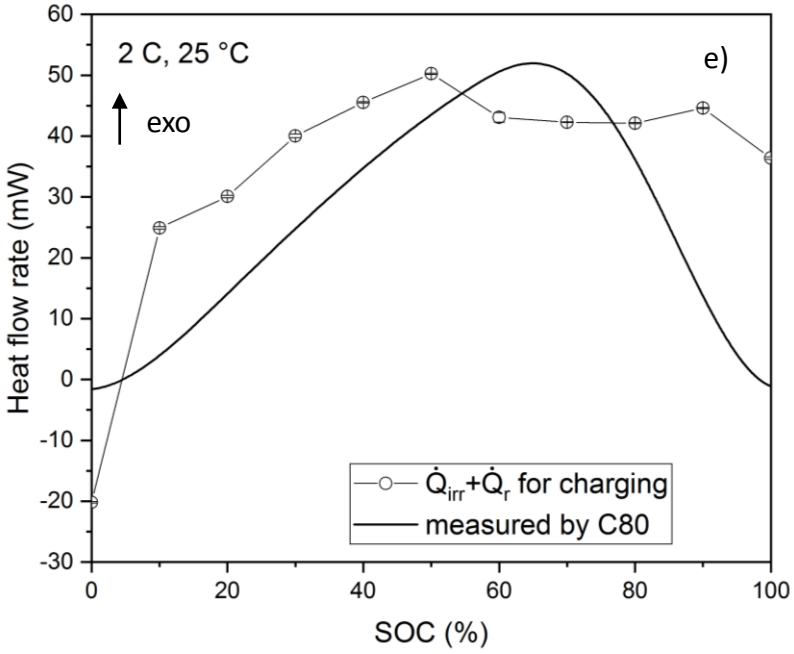
2 C, 25 °C
e)
exo
$\dot{Q}_{irr}+\dot{Q}_r$ for charging
measured by C80
Heat flow rate (mW)
SOC (%)

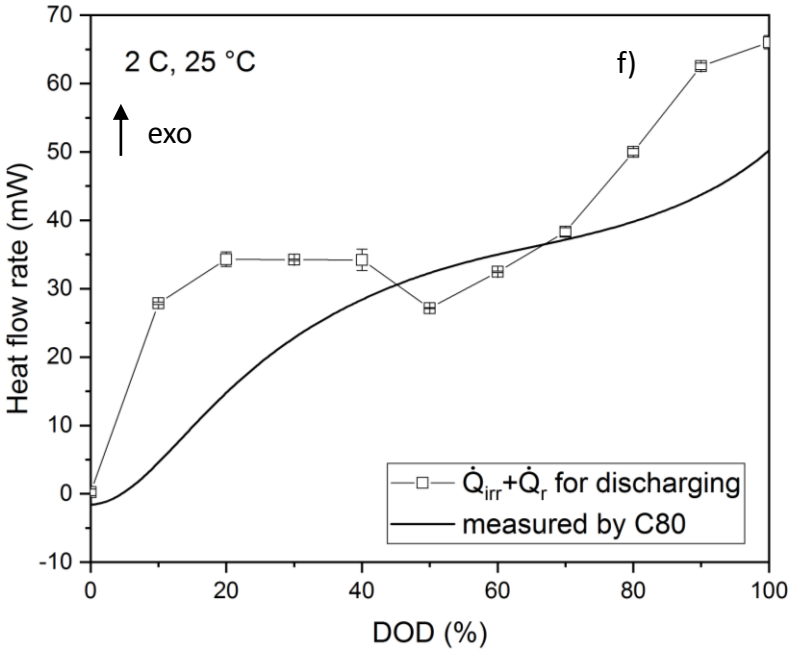

Fig. 5. 43: The comparison of computed heat flow rates from irreversible and reversible heat flow rates; and the total heat flow rates measured by C80 calorimeter versus SOC/DOD under different C-rates at 25 °C: a) charging at 0.5 C (42.5 mA), b) discharging at 0.5 C (42.5 mA), c) charging at 1 C (85 mA), d) discharging at 1 C (85 mA), e) charging at 2 C (170 mA), f) discharging at 2 C (170 mA).

According to equation (2.18) and (2.20), the reversible and irreversible heat can be computed by integration and the summary of the total heat is obtained.

$$Q_{rev} = T \cdot \Delta S|_{x_1}^{x_2} \tag{2.18}$$

$$Q_{irr} = |U_i - OCV| \cdot \int_{t_1}^{t_2} i \cdot dt \tag{2.20}$$

Comparing the computed and measured total heat generation, the computed values are normally lower than the measured values (Fig. 5.44). The total computed heat for discharge equals to Q_{irr} value (green part) minus Q_{rev} value (yellow part). For charge process, the total heat generation is the sum of the Q_{irr} and Q_{rev} values. For discharge process, the total heat generation is the value of Q_{irr} subtracted Q_{rev}. In Fig. 5.42 a) and Fig. 5.43 a), the computed curves in range of SOC0 - 10, are clearly lower than the measured results, which leads to a large deviation of the computed results from the measured data of -9.97 % and -9.62 % at 30 °C and 25 °C, respectively (Table 5.7). The irreversible heat effect dominates the shape of the curves with increasing C-rates. The problem is that by Galvanostatic Intermittent Titration Technique (GITT) the current flow is interrupted and equilibrium states are added between each SOC step, which is different in comparison to the states under current flowing. This deviation might be another reason for the deviation of computed heat generation at 0.5 C rate. The computed results show the deviations of -7.50 % and -8.56 % (Table 5.7) at 1 C rate at 30 °C and 25 °C, respectively. The deviations become smaller when larger current applied in charge process. The heat generation during charging can be better predicted at larger currents. However, in discharge process, the deviations of computed heat are irrelevant to applied currents.

In Table 5.7, the heat generation values due to charging and discharging are similar, and increase approximately linear with increasing current flow. On the contrast, the difference of the heat generation between charge and discharge processes decreases with increasing

current flow. The reason is that the share of reversible heat is reduced with larger current flows. Since the reversible heat has opposite signs during charging and discharging, the heat difference due to charge and discharge process reflects the influence of reversible heat. The deviations of computed heat during discharging are all lower than ±6 %, which is a good prediction for thermal effects.

Table 5.7 Computed and measured total heat generation when cycling with various C-rates at 30 °C and 25 °C.

Current flow	Computed total heat generation (J)		Heat determined via C80 calorimeter (J)		Deviation of computed heat from measured heat (%)	
At 30 °C	Charge	Discharge	Charge	Discharge	Charge	Discharge
0.5 C	22.35±1.69	23.22±2.40	24.82±1.60	22.34±3.92	-9.97	3.92
1 C	64.40±5.16	68.20±6.43	64.14±2.87	67.36±1.28	-7.50	2.54
2 C	64.40±5.16	68.20±6.43	64.14±2.87	67.36±1.28	-4.08	1.24
At 25 °C	Charge	Discharge	Charge	Discharge	Charge	Discharge
0.5 C	24.05±1.50	25.57±3.25	26.61±1.49	25.35±0.70	-9.62	0.88
1 C	40.49±1.30	40.46±2.55	44.28±1.14	43.04±0.64	-8.56	-6.00
2 C	66.77±0.89	67.36±1.13	69.66±8.08	69.86±4.21	-4.15	-3.58

The given standard deviation suggests an expanded uncertainty with 95 % confidence.

As demonstrated in Fig. 5.30 (page 115), the diffusion and charge transfer influence are especially large at deep discharge, therefore the equilibration of cells needs extremely long time. This raises the difficulties in the entropy change and internal resistances measurement at low SOCs as well as high DODs. The accuracy of the thermal behavior analysis strongly relies on the achieved level of equilibrium. In Table 5.7 and Fig. 5.44, computed total heat generation is evaluated by comparing with measured heat. The computed values for charging process, are always lower than the C80 measurement regardless of the current rates. On the contrast, the values for the discharging process, are always larger than those from the direct measurements. At 2 C rate, the deviations of computed values for charge and discharge processes reach their minimum values. Since the reversible heat has opposite heat effect in charge and discharge process, and the influence of reversible heat effect decreases with increasing current flow, the deviation of the computed values comes mainly from the reversible heat determination. The deviation of computed values is less than 10 % at all C-rates, even < 5 % at 2 C. The two heats generation values from the computation and the direct measurements, are absolutely comparable, especially considering the uncertainty of the measurements, seeing the error bars in Fig. 5.44 and Fig. 5.45.

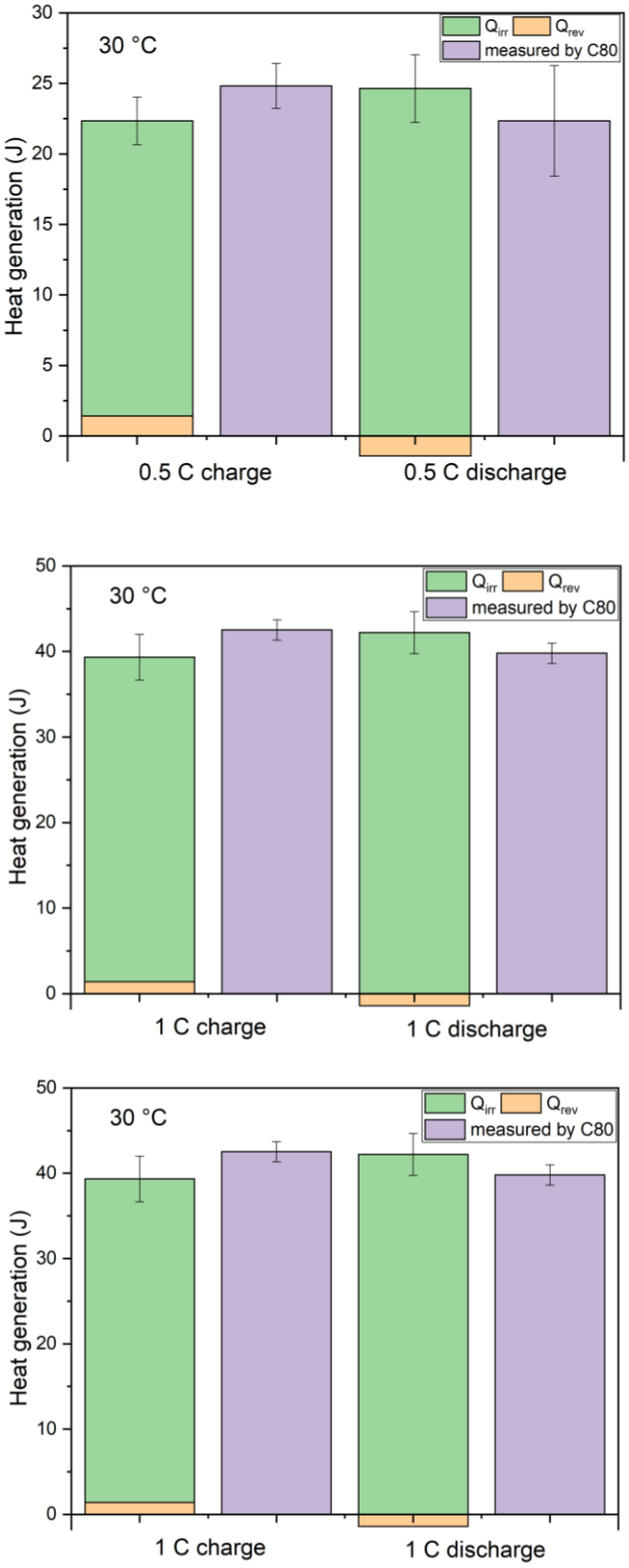

Fig. 5. 44: The comparison of the computed values of total heat generation and those measured by C80 for various C-rates at 30 °C.

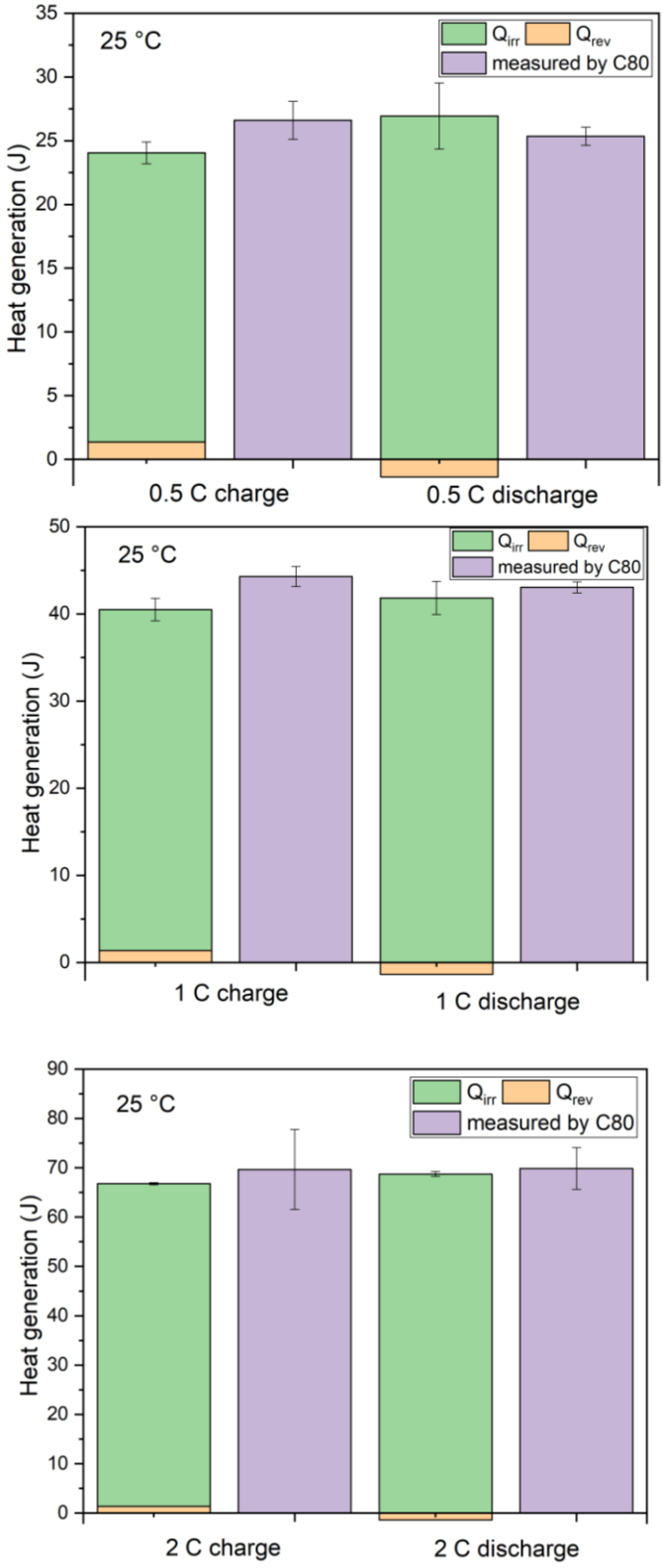

Fig. 5. 45: The comparison of the computed values of total heat generation and those measured by C80 for various C-rates at 25 °C.

5.5.6 Conclusion

The heat generation during cycling is determined by calculation and calorimetric study. The computed heat generations are considerably acceptable to predict thermal behavior with the deviation less than 10 % at various C-rates. The computed heat flow rates can provide a

reasonable prediction of thermal behavior during cycling. For the irreversible heat effect, heat flow rates are separated into heat generation due to charge transfer, ohmic resistance and diffusion. The diffusion and charge transfer contribute the main part of the irreversible heat. More irreversible heat is generated in discharge process than charge process. The achievement of equilibrium is critical to measure the entropy change accurately, which is extremely difficult at low SOCs. Therefore, the computed heat flows deviate from the measured curves dramatically at low SOCs or high DODs.

5.6 Combined thermal runaway investigation with ARC and C80 calorimeter

Thermal runaway and early stage of thermal runaway events are investigated via a novel approach by combining of the ARC and the C80 calorimeter. After charging to selected SOC, the cells are tested under quasi-adiabatic condition using the heat-wait-seek (HWS) method in the ARC. As Fig. 5.46 shows, the system is heating stepwise by 5 °C in heat mode. For each step, the temperature is stabilized for 15 minutes, which is the so-called wait mode. At the end of the wait mode, the seek mode starts, where the temperature change rate (dT/dt) is detected and compared with the set sensitivity value of 0.02 °C/min. If the sample temperature is relatively stable, and dT/dt smaller than 0.02 °C/min, the system will switch back to the heat mode. The HWS loop will continue until an interruption occurs by either reaching the maximum temperature of 450 °C or dT/dt exceeding 0.02 °C/min. The system will switch to cool mode or exotherm mode in the two cases respectively. Cool mode will be activated when the temperature / temperature rate is higher than set maximum values, in considering the safety. Exotherm mode will be activated when temperature rate is higher than set sensitivity value, where is considered as an exothermic reaction taking place. Another special case is not demonstrated in Fig. 5.46. When temperature drops more than 25 °C, the cool mode will be activated too, assuming the measurement finished. Under cool mode, the calorimeter is cooled down by pressurized gas. Exotherm mode is operation under a quasi-adiabatic condition. During exotherm mode, the temperature difference between the sample and the calorimeter, which is measured by the bomb sensor and the middle sensor respectively, will be driven to zero by controlling the heaters around the calorimeter (Fig. 5.47).

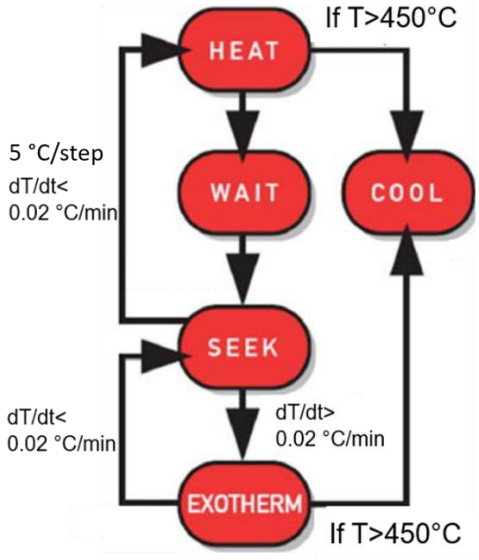

Fig. 5. 46: Schematic illustration of the HWS measurement program with modes and conditions [146].

By the ARC's HWS method, the onset temperature and the maximum temperature rate during thermal runaway are determined. A small temperature drop is observed in the early stage of

thermal runaway events. The reason could be cell's venting due to high internal pressure or an endothermic reaction. However, the ARC is not capable to follow all details in thermal runaway event completely. Therefore, in a C80 calorimeter, not only the full cells but also the disassembled components (the positive electrode, negative electrode and separator) were analyzed with the help of a scanning method. In addition, the morphology of the positive, negative electrodes and separator of fresh and tested cells are investigated with help of scanning electron microscope. Furthermore, the microstructure and the chemical composition of the individual components were investigated by X-ray diffraction (XRD) and inductively coupled plasma with optical emission spectroscopy (ICP-OES), respectively.

5.6.1 Thermal runaway investigation for a large temperature range using ARC

Experimental

The commercial coin cells are cycled 3 times to determine the capacity. The standard charge method is adopted, which is CCCV with 0.5 C current charging to 4.2 V. For each selected SOC (SOC0, SOC50, and SOC100), three cells are prepared for the thermal runaway measurements. The temperature range was set between 30 °C and 450 °C. The sensitivity of the detection for exothermic reactions was 0.02 °C/min.
The set-up for thermal runaway measurements is established in Fig. 5.47, and the coin cell is attached on the holder with glass cloth tape (3M industrial business, USA) which isolates tested cell, locating in the middle of the reacting chamber. Since the mass of glass tape is small, the heat absorption of glass tape is not considered. The N-type thermocouples (Omega Newport Electronics GmbH, Germany) are used as temperature sensors, attaching on the surface of coin cells and placing in the top, side and bottom of the reacting chamber. As shown in Fig. 5.47, there are heaters in top and in the jacket and on the bottom of the chamber. After the first measurements on cells with SOC100, the start temperature was adjusted to 50 °C, since cell's operating temperature up to 60 °C, there should be no reaction below 50 °C.

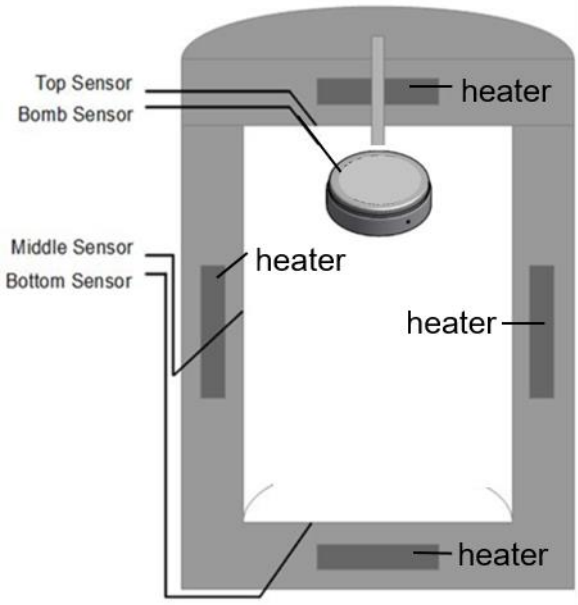

Fig. 5. 47: Schematic set-up for the thermal runaway measurement in the ARC.

Results and discussion

Fig. 5.48 demonstrates the results of thermal runaway measurements of 3 fully charged coin cells. All tested cells reach the maximum measuring temperature of 450 °C, therefore the

cooling mode was activated and stopped the measurement. There are some plateaus, which have longer waiting and seeking time, caused by temperature drift, so the temperature rate varies below or higher than 0.02 °C/min. The time difference between cell 1's measurement and those of cell 2, cell 3, is due to the heating power in cell 1's measurement higher than cell 2 and cell 3. The 5 °C steps were faster than cell 2 and cell 3. Since the comparison of cell 1, cell 2 and cell 3 is based on temperature, the time of each step has no influence on results.

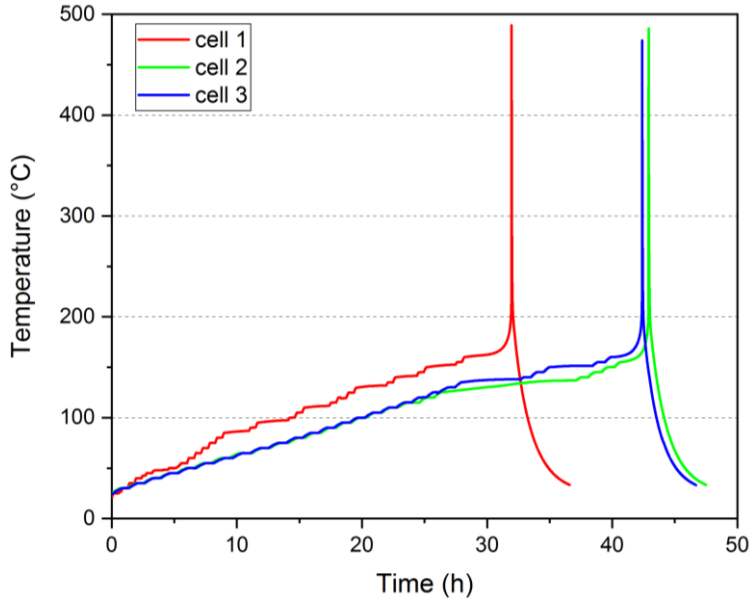

Fig. 5. 48: Temperature vs. time curves for thermal runaway measurements of three cells with SOC100 measured by the ARC using HWS method.

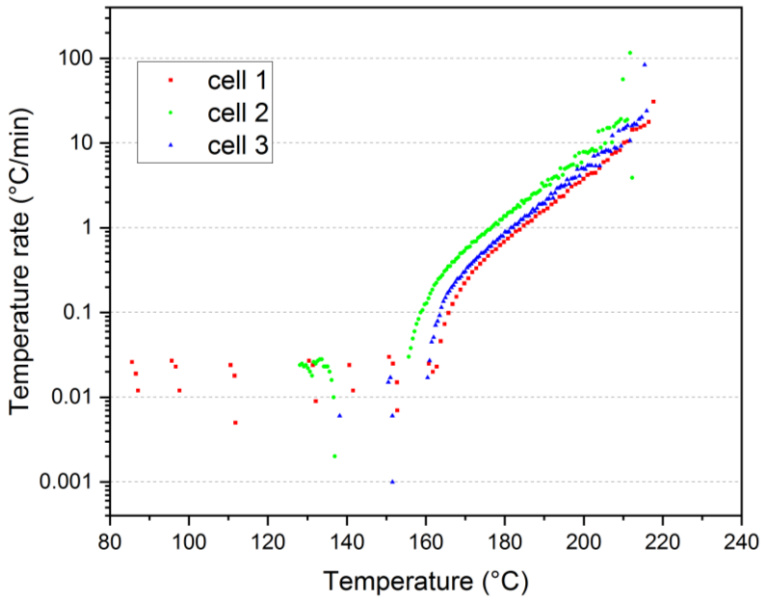

Fig. 5. 49: Temperature rate versus temperature curves for thermal runaway measurements of three cells with SOC100 measured by the ARC.

From Fig. 5.49, we can see the strongly self-heating exothermic reaction takes place at 164 °C (cell 1, red points), 157 °C (cell 2, green points), and 161 °C (cell 3, blue points), respectively, where the system switches to exotherm mode and the temperature rate increased from threshold sensitivity 0.02 °C/min to over 10 °C/min. Hence, these temperatures symbolize the

onset of thermal runaway. The measured points of cell 1 (red points) in Fig. 5.49, reveal a system error caused by the heaters in the ARC from 80 °C to 150 °C, where the heating rate is detected to be over 0.02 °C/min due to an overshooting of the heaters but not due to self-heating of the cell. This effect could be reduced by increasing the wait time. The onset temperature of cell 3, was around 150 °C, where an exothermic effect was observed with temperature rate larger than 0.02 °C/min, as shown in Fig. 5.49. This could be the decomposition of solid electrolyte interface (SEI) layer [23] or the exothermic reactions between electrolyte [147] and electrodes. The hazard reaction of the fully charged cells can lead to a self-heating up to 480 °C with a maximum temperature rate of 100 °C/min.

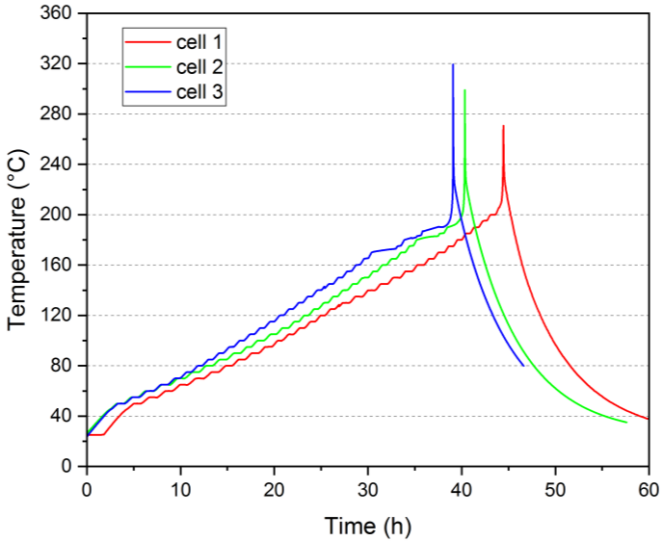

Fig. 5.50: Temperature vs. time curves for thermal runaway measurements of three cells with SOC50 measured by the ARC using HWS method.

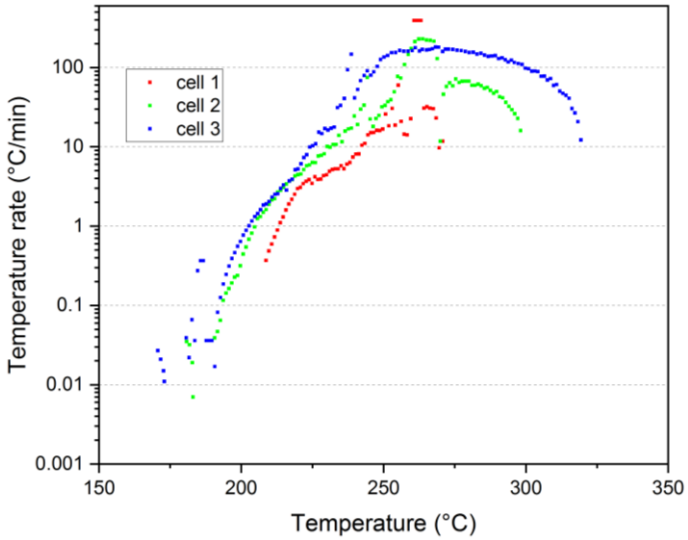

Fig. 5.51: Temperature rate vs. temperature curves for thermal runaway measurements of three cells with SOC50 measured by the ARC.

Fig. 5.50 and Fig. 5.51 display the temperature change and the temperature rate for exothermic reactions of cells with SOC50. Compared with the cells of SOC100, the onset temperatures are higher, and reach about 208 °C (cell 1, red curve), 180 °C (cell 2, green curve), and 170 °C (cell 3, blue curve). The maximum temperatures are lower with 250 °C, 300 °C and 320 °C. However, as Fig. 5.51 shown, the temperature rate can increase as fast to more than 100 °C/min.

Three cells with SOC0 were tested in ARC and the temperature changes against time were plotted in Fig. 5.52. There were no dramatically temperature increase in all three tests. Between 180 °C and 240 °C, exothermic effects were observed. Interestingly, as temperature becomes higher than 240 °C, no exothermic reaction was observed until the end of tests. The cells with SOC0 have the best safety performance, as is demonstrated in Fig. 5.52. This is not surprising, because in this case the cells had the lowest delithiation degree of positive electrode material. Therefore, the phase transition as shown in equation 4.5 (page 76) would not take place. Cell 2 and cell 3 had plateaus but not cell 1, because the temperature drifts occurs after long time operation. The temperature drift can be calibrated as described in Chapter 3. Fig. 5.53 shows the temperature rates of three cells with SOC0. In Fig. 5.53, the three cells show a similar behavior: the onset temperatures were 180 °C (cell 1, red points), 190 °C (cell 2, green points and cell 3, blue points); the maximum temperature rates of all three cells were around 1 °C/min.

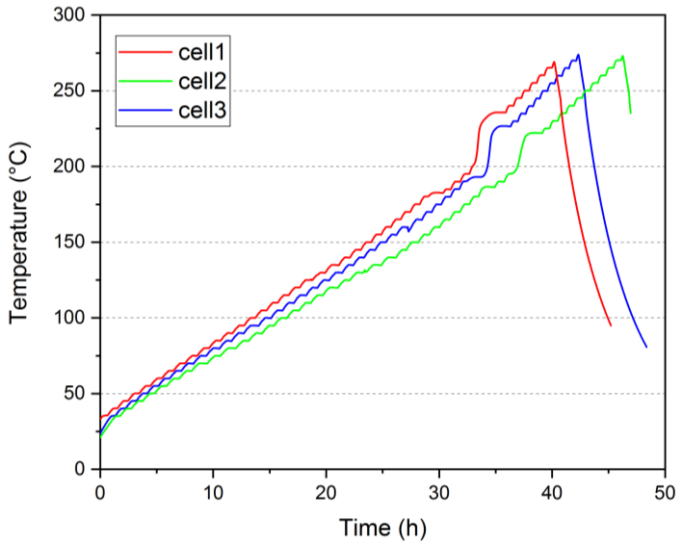

Fig. 5. 52: Temperature vs. time curves for thermal runaway measurements of three cells with SOC0 measured by the ARC using HWS method.

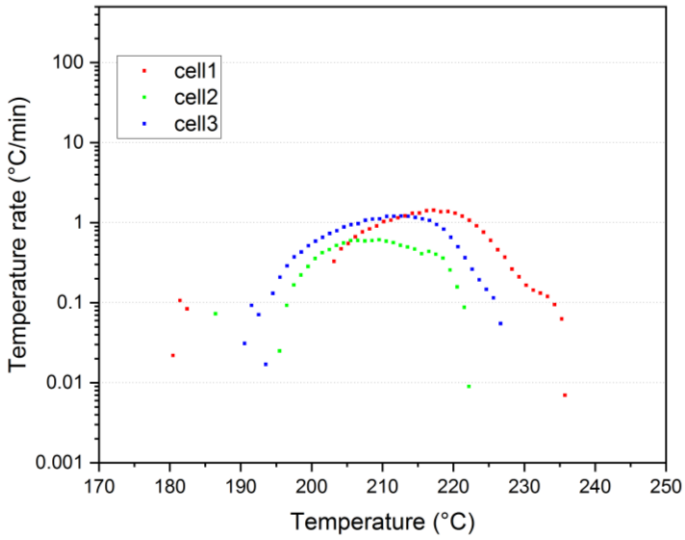

Fig. 5. 53: Temperature rate vs. temperature curves for thermal runaway measurements of three cells with SOC0 measured by the ARC.

Fig. 5.54 shows a comparison of the selected cells with SOC0 (cell 3), SOC50 (cell 2) and SOC100 (cell 3). The selected cells for this representation were those, whose curves lie in the middle among the three cells with same SOC, to represent the thermal behaviors with different SOCs. In Fig. 5.54 a) shown, the maximum temperatures in measurements are SOC100 (blue curve) > SOC50 (red curve) > SOC0 (black curve). The temperature increases of SOC100 and SOC50 were accelerated due to the self-heating, resulting in two sharp peaks. While, the thermal runaway of the cell with SOC0 shows no peak. In Fig. 5.54 b), the temperature rates are compared: SOC100 > SOC50 > SOC0. SOC0 points show a clearly decrease trend after 210 °C, which indicates the self-heating was much less severe than that of SOC50 and SOC100.

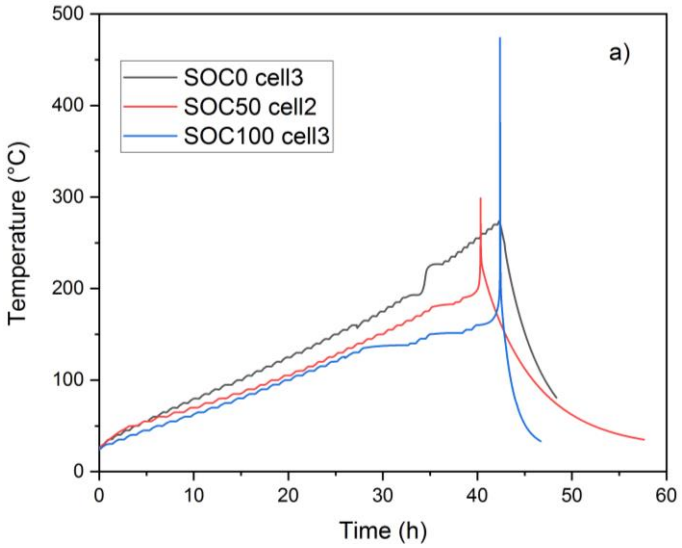

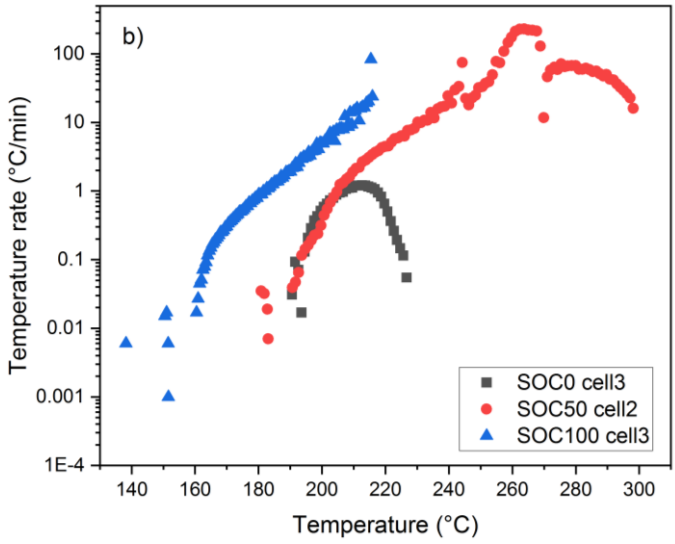

Fig. 5. 54: The comparison between SOC0, SOC50 and SOC100: a) Temperature vs. time curves for thermal runaway measurements with SOC0, SOC50 and SOC100 measured by the ARC using HWS method. b) Temperature rate vs. temperature curves for thermal runaway measurements with SOC0, SOC50 and SOC100 measured by the ARC.

Arrhenius equation describes the temperature dependence of reaction rates [92, 148-149] and the temperature rate under adiabatic conditions can be calculated by:

$$\frac{dT}{dt} = \Delta T_{ad} A e^{\frac{-E_a}{k_B T}} \cdot (1-\mu)^n \tag{5.19}$$

Where ΔT_{ad}, E_a, μ and n represent the adiabatic temperature rise, the activation energy, the degree of conversion, and the reaction order respectively, and A denotes the frequency factor of the Arrhenius equation. k_B is the Boltzmann constant with a value of $8.6173 \cdot 10^{-5}$ eV/K. The values of μ are much smaller and negligible, so assuming $(1-\mu)^n$ equals to 1. Thus, the function for the temperature rate and the activation energy can be simplified as [11, 148-149]:

$$\ln\left(\frac{dT}{dt}\right) \approx ln\Delta T_{ad} \cdot A - \frac{E_a}{k_B T} \tag{5.20}$$

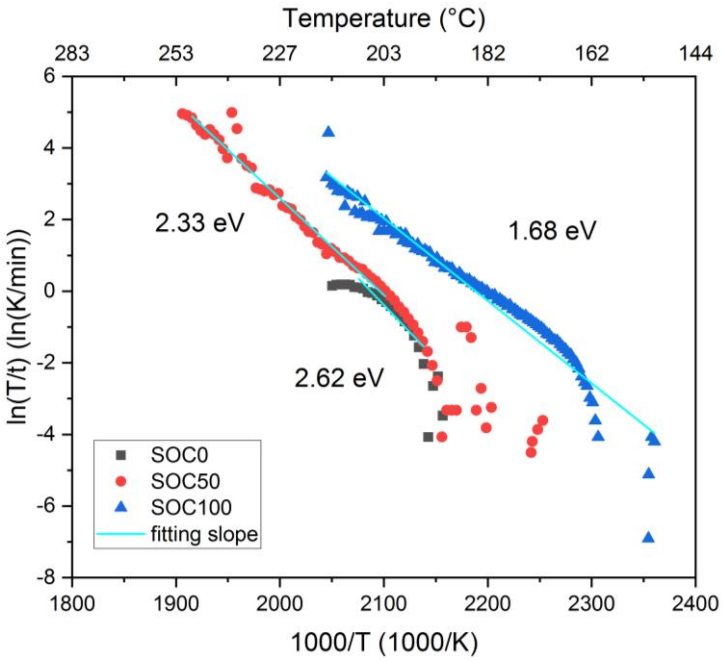

Fig. 5. 55: The functions of natural logarithm of temperature increasing rate and reciprocal temperature, and the E_a of reactions is calculated from the fitting slope.

Hence, the slope of the natural logarithm of the temperature rate vs. 1/T is the product of the activation energy of the reactions divided by k_B. In Fig. 5.55, the natural logarithm of the temperature rates of the cells at SOC0, SOC50 and SOC100 versus 1000/T are plotted. The activation energies E_a are 1.68 eV ($2.69 \cdot 10^{-19}$J), 2.33 eV ($3.73 \cdot 10^{-19}$J), and 2.62 eV ($4.20 \cdot 10^{-19}$J), for cells with SOC100, SOC50 and SOC0 during thermal runaway, which indicates that the energy barrier of reactions is increasing with decreasing SOC.

In the early stage of thermal runaway measurements, a possible endothermic reaction was observed in all three cells. Fig. 5.56 suggests that a temperature decrease happens between 110 °C and 125 °C. The temperature rate decreases to approximately -0.5 °C/min. In Fig. 5.56, temperature and temperature rate are plotted against time, and a) b) and c) are the measurements for three fully charged cells by using HWS method in ARC. The negative values of temperature rate were observed at 1095 min in a), at 1381 min in b) and at 1550 min in c), where the temperature drop occurred, which implies the endothermic effect. In order to investigate this phenomenon, the same experiment was conducted on a forth cell and was terminated at the time where the temperature drops (red line in Fig. 5.57) and the temperature rate negative (blue points in Fig. 5.57). Then tested cell was disassembled in a glove box, and its materials were investigated. The XRD analysis revealed the phase transformation during the thermal runaway events, as shown in Fig. 5.58.

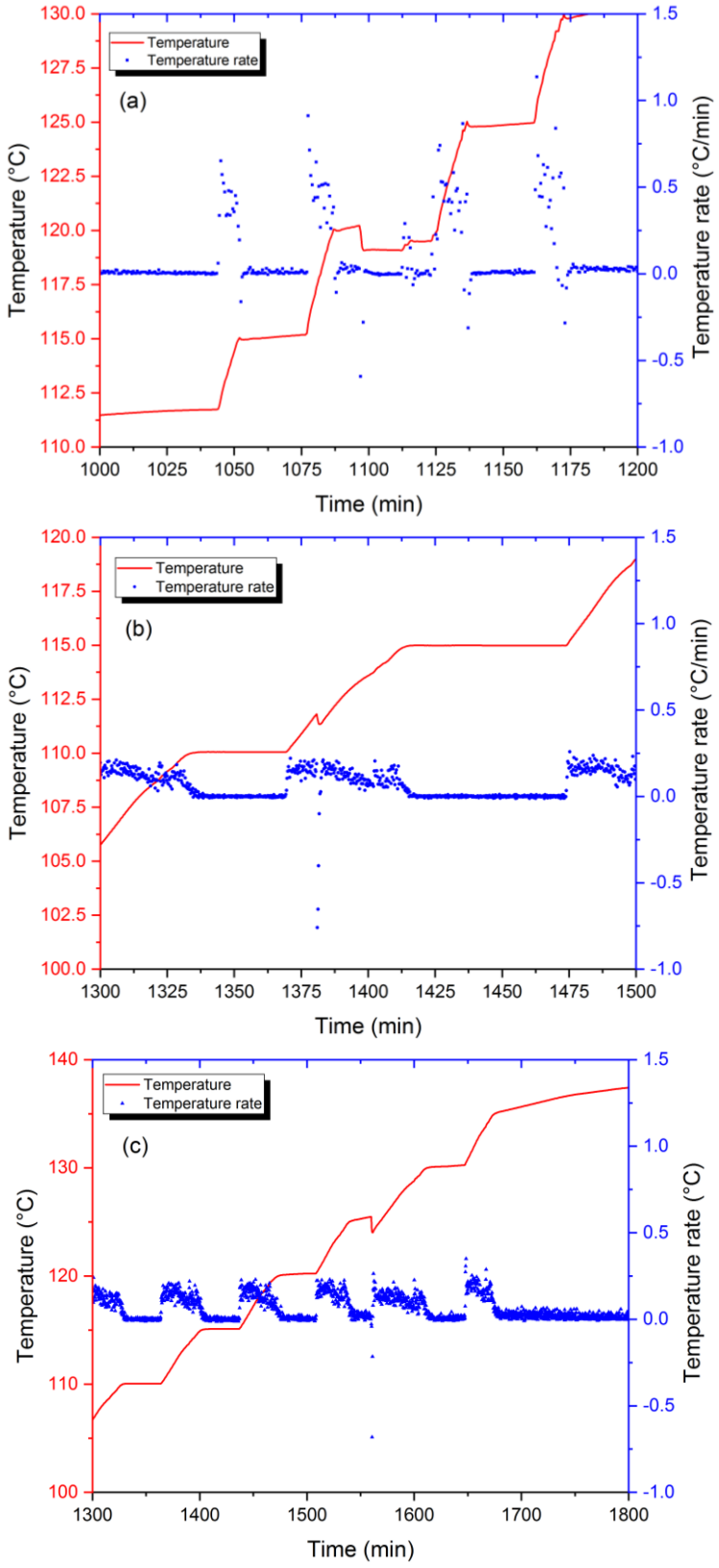

Fig. 5. 56: Early stage of thermal runaway: temperature drop of the measurement on (a) cell 1, (b) cell 2, (c) cell 3.

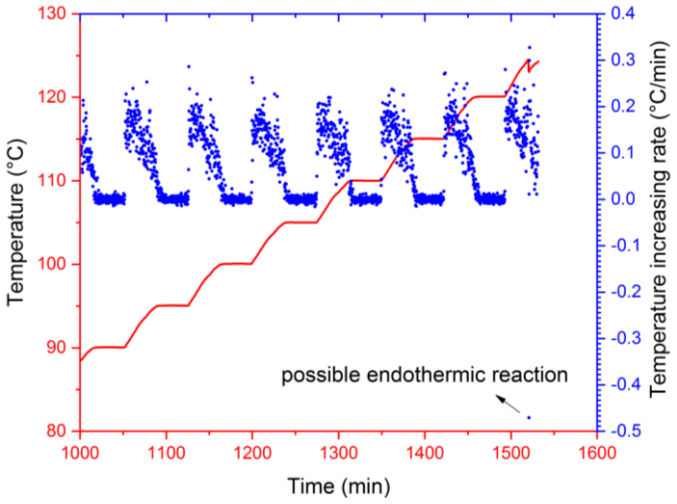

Fig. 5. 57: Early stage thermal runaway measurement of fully charged cell by ARC: the temperature and the temperature rate vs. time.

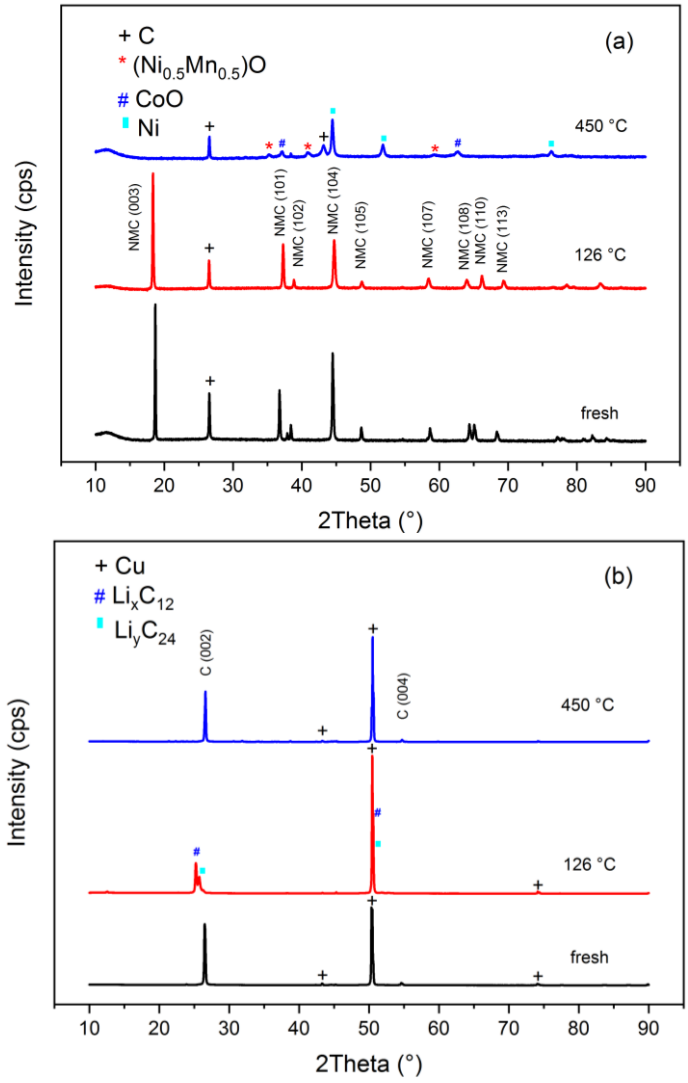

Fig. 5. 58: XRD patterns of (a) the positive electrodes and (b) the negative electrodes after 450 °C thermal runaway measurement, 126 °C early stage thermal runaway measurement and fresh cell.

In the fresh cell with 3.5 V (~SOC6), as expected, the positive electrode material exhibits α-$NaFeO_2$ layered structure [105, 106], and carbon black as conducting agent was observed in the pattern. The XRD pattern of the negative electrode shows that it consists of the graphite coating on the Cu current collector. When the cell was heated up to 126 °C, no phase transformation was observed at the positive electrode. After 3 cycles and charged to SOC100, the Li-ions were found to be intercalated into the negative electrode (Fig. 5.58 b)). Therefore, the positive electrode was delithiated as Li_xTMO_2 (TM represents Ni, Co and Mn) with x<1. In the thermal runaway measurement, the cells are heated up to 450 °C, and the phase of the positive electrode material NMC622 is completely transformed from layered structure to rock-salt structure. Dahn et al. [32] proposed that the delithiated layered structure Li_xCoO_2 (x<1) positive electrode material decomposes to rock-salt structure Co_3O_4 and produces oxygen, which is already discussed in detail in Chapter 4. With less intercalated Li ions, the positive electrode material is more prone to release oxygen. This explains the dependence of the behavior of thermal runaway event on the SOC. Since the cells with SOC100 have the smallest amount of x, the onset temperature is the lowest and the maximum temperature is the highest. In LiBs, the thermal stability of the delithiated positive electrode is most essential problem. In addition, intercalated Li in negative electrode is active too. The decreasing or even vanishing of the intercalated Li in the negative electrode after thermal runaway measurement is because of the following reactions [23]:

$$2\mathrm{Li} + \mathrm{C_3H_6O_3(DMC)} \rightarrow \mathrm{Li_2CO_3} + \mathrm{C_2H_6} \tag{5.21}$$

In addition, the SEM images exhibit the morphological properties of the positive electrodes and negative electrodes in Fig. 5.59 and Fig. 5.60. Comparing the negative electrode materials in Fig. 5.59 (b) with (a), there are more broken particles than in Fig. 5.59 (a). While, the most particles in Fig. 5.59 (c) have cracks, which makes the interface between negative electrode and electrolyte larger. The particles of the positive electrodes crack after heating up to 126 °C, and more dramatically after thermal runaway measurement. On the other hand, the particles of the negative electrodes establish a relatively stable form after heating (Fig. 5.60). After thermal runaway measurement, there are cracks and small particles on the surface, which might be the products from the reactions as discussed later on page 153 and 155.

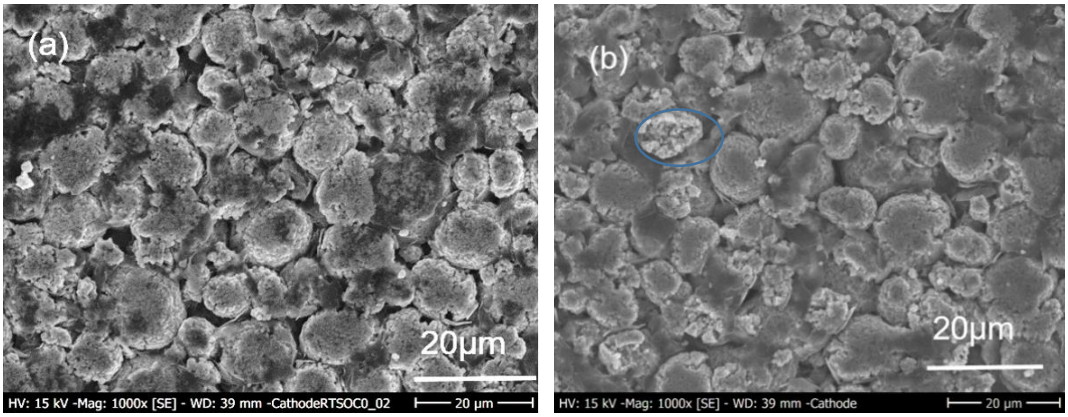

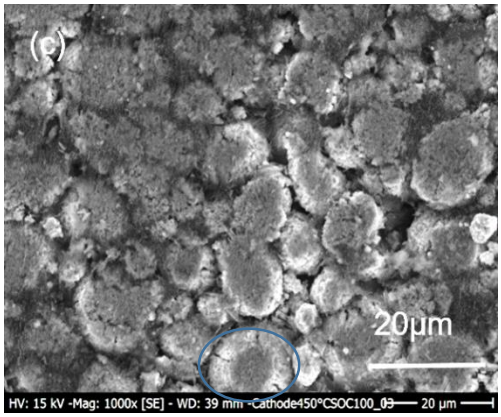

Fig. 5.59: SEM images of the positive electrodes from (a) fresh cell, (b) the cell heated up to 126 °C, and (c) the cell heated up to 450 °C.

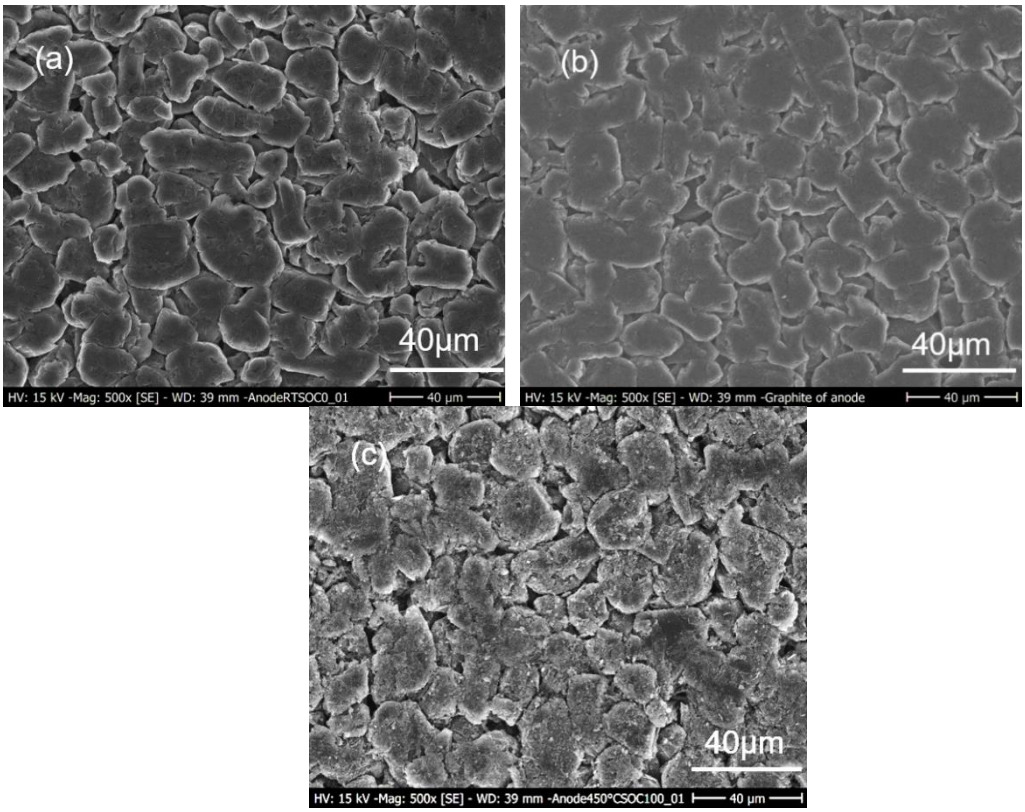

Fig. 5.60: SEM images of the negative electrodes from (a) fresh cell, (b) the cell heated up to 126 °C, and (c) the cell heated up to 450 °C.

Fig. 5.61 demonstrates the SEM images of the separator from the fresh cell and from the early stage of thermal runaway cell. The melting of the separator can be clearly seen in Fig. 5.61(b). The pores are closed and the particles are attached on the surface due to the decomposition of the electrode materials.

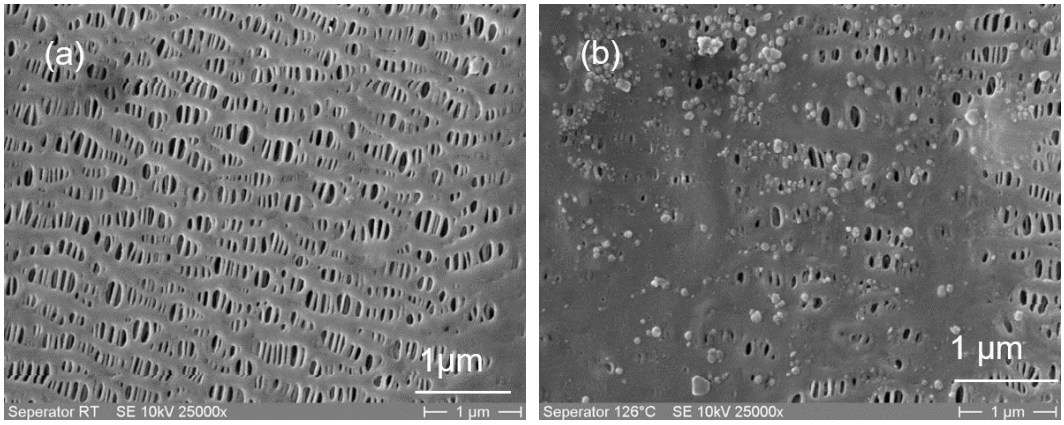

Fig. 5. 61: SEM images of the separators from (a) fresh cell and (b) the cell heated up to 126 °C.

The chemical analysis is shown in Table 5.8. In the fresh cell, the voltage was ~3.5 V, approximately at SOC6. The Li-ions intercalate mostly at the positive electrode, and the molar ratio of Ni: Mn: Co is 3:1:1, which suggests that the active material is $LiNi_{0.6}Mn_{0.2}Co_{0.2}O_2$ of the coin cell. The molar ratio remains constant in the tested cells. Since there is no reaction at the Al current conductor, the dramatically increasing weight percentage from the fresh cell to the tested cells reveals the consumption of active materials under heating. The tested cells have more Li-ions intercalated at the negative electrode, because they were in fully charged state. Vice versa, in the fresh cell, most Li-ions are in the positive electrode rather than in the negative electrode. The conducting agent material carbon black at the positive electrode should also participate in the reactions resulting in less content in the tested cell. The carbon content in the tested cell heated up to 450 °C, was not measured. For the negative electrode, the sums of the weight percentage of Li ions and Cu are between 33 % and 34 %, and the rest of the mass, which is the mass of the graphite, changes only by a small amount. Hence, graphite is supposed to be not involved in the reactions, which is indicated by XRD pattern, too. The Li-ions content decreases while the Cu content increases with elevated temperature, and these data reveal that the reaction of intercalated Li-ions proceeds further at higher temperature, which confirms the observation in XRD measurements.

Table 5.8 Chemical analysis (ICP-OES) of the positive electrode materials and negative electrode materials in fresh cell and tested cells.

Analyzed elements	Fresh cell	Fresh cell	Heat up to 126°C	Heat up to 126°C	Heat up to 450°C	Heat up to 450°C
	wt.%	Atom ratio TM=1	wt. %	Atom ratio TM=1	wt.%	Atom ratio TM=1
Positive electrode						
Li	5.44±1.10	0.99	2.51±0.06	0.42	3.17±0.08	0.47
Ni	28.8±0.4	0.60	30.8±0.5	0.60	34.4±0.6	0.60
Mn	8.88±0.16	0.20	9.69±0.20	0.20	11.00±0.23	0.20
Co	9.57±0.18	0.20	10.29±0.22	0.20	11.50±0.24	0.20
Al	9.29± 0.17		11.5±0.3		12.3±0.4	
C	4.82± 0.40		3.51±0.27		-	
Continue Table 5.8						
Negative electrode						
Li	0.598±0.010		4.13±0.10		2.95±0.07	
Cu	32.7±0.9		28.7±0.8		31.5±0.9	

5.6.2 Investigation of early stages of thermal runaway using C80 calorimeter

Experimental

To complete the whole picture of the thermal runaway, the early stage of thermal runaway is studied by a C80 calorimeter. Since the C80 calorimeter has a higher sensitivity, the small exothermic and endothermic reactions and other details can be investigated. For safety reasons, the maximum measuring temperature is set to 150 °C, which is just below the onset temperature of thermal runaway at SOC100. The measurement started at 60 °C with a scanning rate of 0.1 K/min. A fresh cell was disassembled in the glove box, and separator, positive electrode and negative electrode were rinsed with dimethyl carbonate (DMC) with purity of 99 % and dried for 24 h at room temperature under vacuum conditions, to get rid of electrolyte. Positive electrode or negative electrode with 15 µL electrolyte of 1 M $LiPF_6$ in 1:1 (by weight) EC/DMC (LP30, BASF, Germany) are put into Al crucibles in the glove box, and the Al lids and Al crucibles were sealed by applying pressure on the metal model. To exclude the possible reactions between negative electrode and Al crucible, the temperature measurements for the negative electrode from cells with SOC0 and SOC100 are repeated with stainless steel crucibles. A ceramic disc was placed in the bottom of the vessel to prevent the short circuit of the tested cells. The schematic of the two set-ups is shown in Fig. 5.62.

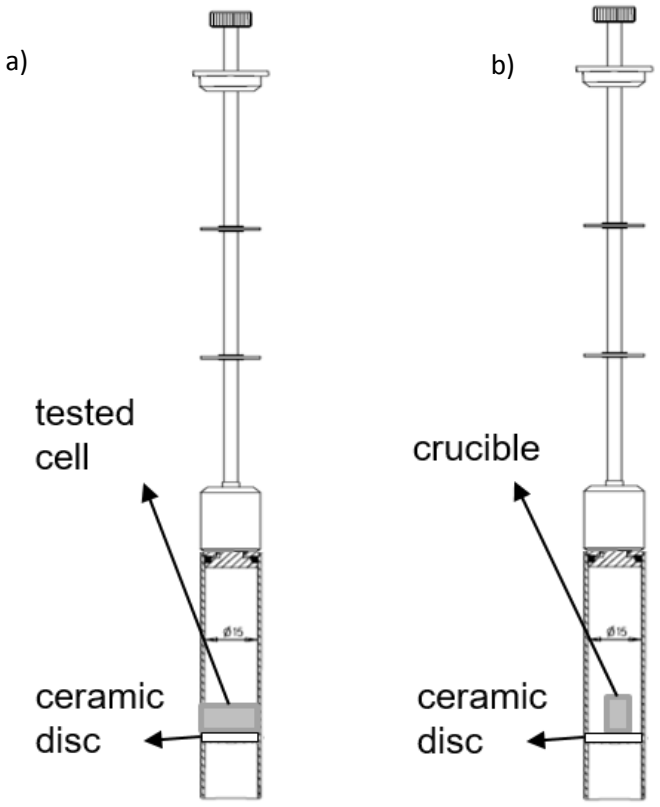

Fig. 5. 62: Schematic set-ups for the temperature measurement in C80 calorimeter of a) full cell and b) individual components.

Results and discussion

In temperature 60 °C - 150 °C, multi-reactions are taking place in cells, as introduced in literature review. Firstly, SEI decomposes, so the protection between negative electrode and electrolyte vanished. Therefore, intercalated Li in negative electrode starts to react with electrolyte, which are the main reactions before 150 °C [127, 129-130]. Meanwhile, the

electrolyte becomes thermal instable. Thermal effects due to the reactions of components on the inter surface are measured and analyzed in this work.
The produced gases due to the reactions will raise the pressure in the cells, ending up with the opening of the coin cells. Some studies [11, 150] have revealed the significant impact of gases releasing during thermal runaway event. After the measurements, the cells were by expanded 20 % in height. Fig. 5.63 and Fig. 5.64 show the heat flow rate for the measurement of three cells with SOC100 and the comparison of the cells with SOC100, SOC50 and SOC0. There are clearly endothermic heat effects on the tested cells, and the onset temperature varied from 110 °C to 135 °C. Produced gases caused cell's venting, and endothermic effect was caused by gas releasing. The cell 1 (red curve) in Fig. 5.63 with SOC100 showed a relative large heat effect compared with the other tested cells, which could reflect the melting of the separator. In Fig. 5.65, the melting of polyethylene (PE) and polypropylene (PP) are observed at 132.4±2.5 °C and 166.8±0.4 °C, respectively. The melting enthalpies are 33.9±1.9 J/g for polyethylene and 20.3±1.1 J/g for polypropylene. These results are relatively comparable to the literature data: the polyethylene and polypropylene melting took place at 135±1 °C and 159 °C with the melting enthalpy of 32.4 J/g and 23.6 J/g, respectively [151]. Hence, materials of the separator can be defined, which is a trilayer structure PP/PE/PP film.

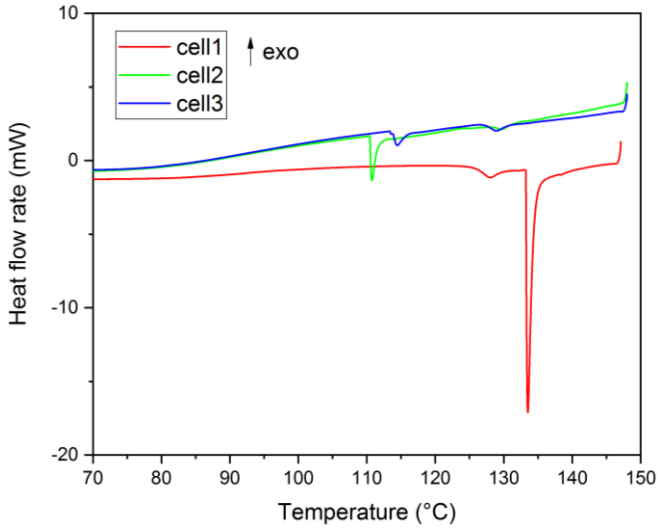

Fig. 5.63: The heat flow rate of 3 cells with SOC100 vs. temperature.

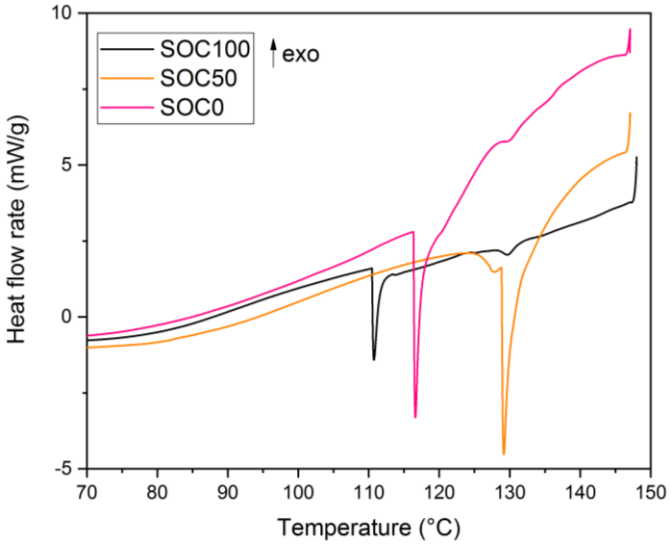

Fig. 5.64: The heat flow rate of cells with selected SOCs vs. temperature.

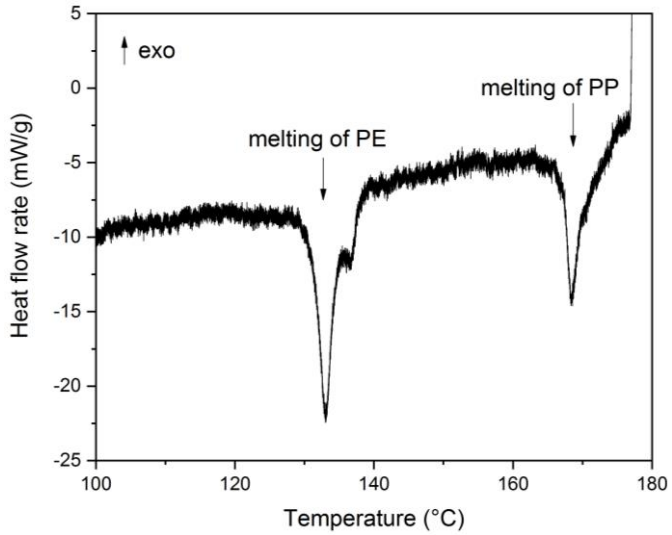

Fig. 5.65: The heat flow rate during trilayer separator melting vs. temperature.

As shown in Fig. 5.66, the measured heat effects (blue curve) were broken down to multi thermal peaks (black curves) by modeling with Gaussian peaks. The computed curve (red curve) fits the measured data very well with R-squared R^2=0.97.
First exothermic peak is observed at approximately 73 °C. This reaction is supposed to be SEI decomposition. One reason is the onset temperature fitting the results from Ref. [129, 130]. Another reason is the cells with SOC100 and SOC0 show stronger effects than fresh cell. SOC100 and SOC0 cells have more SEI layer as the SEI layer is growing during cycling [152]. One reaction in the decomposition of SEI is [153]:

$$CH_3CH_2OCOOLi + 6Li \rightarrow C + 3Li_2O + CH_3CH_2Li \qquad (5.22)$$

The first black peak, which is the exothermic heat due to SEI decomposition is 44.1 mJ/g. The thermal stability of EC is better than DMC thank to its stronger binding energy of covalent bond in the cyclic carbonate [154]. The exothermic peaks at 86 °C, 96 °C and 108 °C are supposed to be the reactions between LiC_6 and DMC [154]. At approximately 120 °C, the exothermic peak due to the reaction of intercalated lithium ions and EC is observed, which is in a good agreement with literature [129]. $LiPF_6$ salt can also react in the solvent [130]:

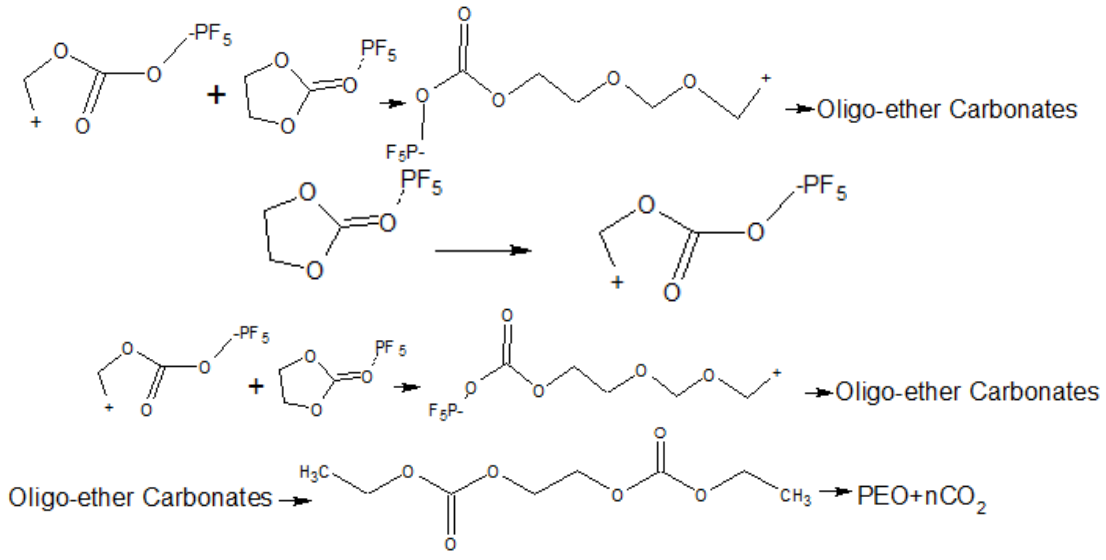

Based on the measured curves, the heat generations in the negative electrode due to reactions of DMC and EC are 691.6 mJ/g and 341.7 mJ/g, respectively.

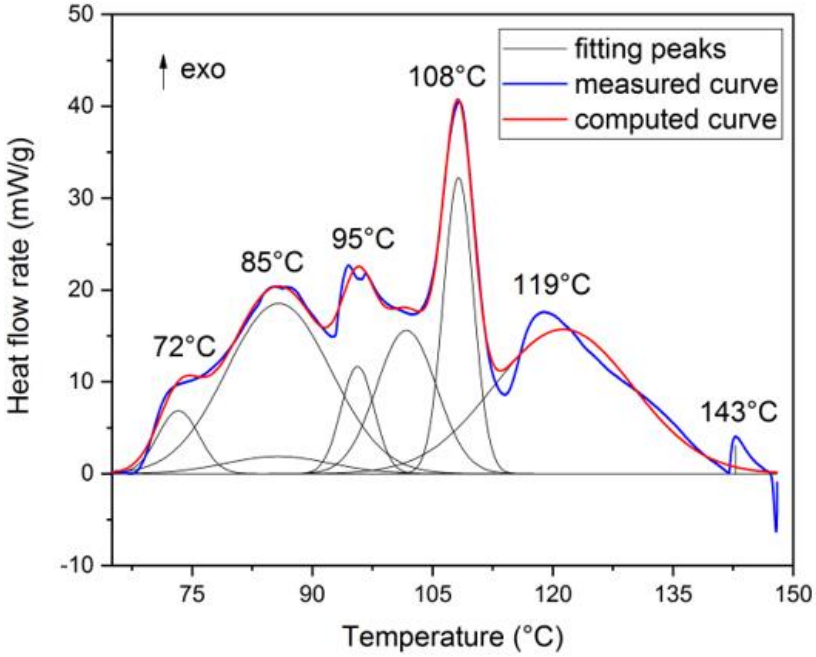

Fig. 5.66: The measured heat flow rate (blue curve), the fitting peaks (black curves) and the computed curve for the negative electrode with electrolyte from a cell with SOC100 vs. temperature.

Table 5.9 Modeling data for multi thermal peaks in Fig. 5.66.

Peak index	Max. temperature °C	Area fit mJ/g	Max. height mW/g
1	73	44.1	6.85
2	86	30.8	1.88
3	86	303.2	18.53
4	96	60.5	11.67
5	102	146.1	15.60
6	108	151.0	32.23
7	121	341.7	15.71
8	143	$3.4575 \cdot 10^{-7}$	3.07

The heat flow rates of the negative electrodes from fresh cell, the cell with SOC0 and the cell with SOC100 (identical to Fig. 5.66) are compared in Fig. 5.67. Before shipping, commercial cells are normally cycled to form the SEI layer (formation procedure), and the voltage is approximately 3.4 V. The onset temperatures of the SEI decomposition are 71 °C for SOC0, and 69 °C for both SOC100 and fresh cell. In the temperature range of 108 °C - 150 °C, there are many exothermic peaks in the curve for the fresh cell. Since the lithium ion content is lower than in the fully charged cell, the heat effects are noticeably smaller. In case of the cell with SOC0, the heat effect can be barely observed.

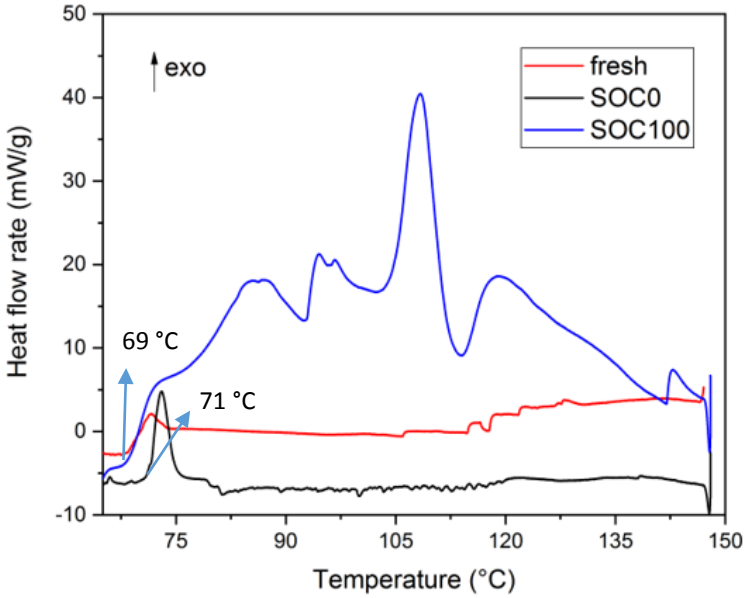

Fig. 5.67: The heat flow rate of the negative electrodes with selected SOCs versus the temperature.

The heat flow rates of full cell, positive/negative electrodes with electrolyte and separator were measured in temperature range of 80 °C - 145 °C, and plotted in Fig. 5.68. In the full cell with SOC100 measurement, no exothermic reactions are detected. That might be because the electrolyte of coin cells is more thermally stable than LP30. The large endothermic heat effect of the fully charged cell is corresponding to the melting of the separator. Meanwhile, the opening of the coin cell can also cause an endothermic heat effect. The endothermic heat is 11.53 J/g. This could be the temperature drop detected by ARC in the early stage thermal runaway. Due to SEI layer decomposition and evaporation of the electrolyte, the produced gases will raise the pressure inside the cells, ending up with the opening of the cell. No thermal effect is found on the positive electrode by heating to 150 °C. Another endothermic effect due to decomposition of separator can be hardly observed, because multi reactions took place.

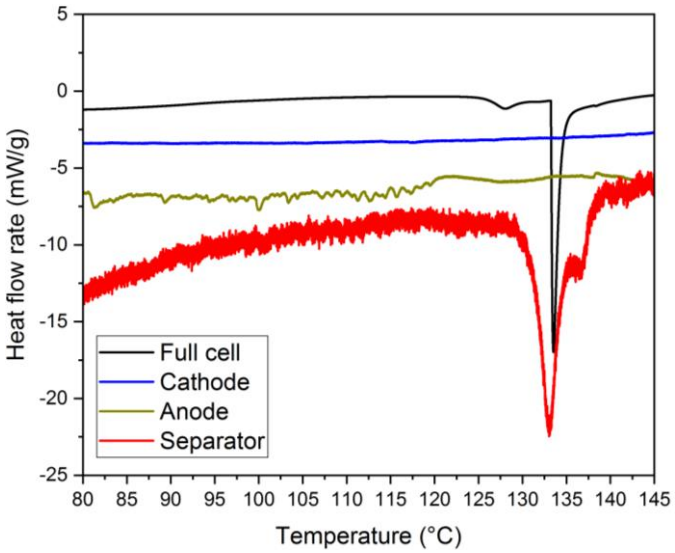

Fig. 5.68: The heat flow rate of the components and the full cell at SOC100 vs. temperature.

5.6.3 Conclusion

This work combined ARC and C80 calorimeter to provide a novel approach to studying the thermal properties of Li-ion coin cells at high temperature. The tested cells were commercial coin cells with 85 mAh, and had $LiNi_{0.6}Mn_{0.2}Co_{0.2}O_2$ as positive electrode materials and graphite as negative electrode materials. In the early stage of thermal runaway, the intercalated Li-ions at the negative electrode dominate the heat generation. On the other hand, the delithiated positive electrode $Li_xNi_{0.6}Mn_{0.2}Co_{0.2}O_2$ is relative stable; no phase transformation and no heat effect are observed. The melting of the separator could affect the full cell in some cases. The main reason for the endothermic effect of the cell is the pressure release through the cell's opening. The separator melting was another endothermic effect which was observed by C80 calorimeter. The thermal behavior in thermal runaway events depends on the state of charge of tested cells strongly. For the cells with SOC100, the onset temperature is approximately 161 °C in average. During thermal runaway, the phase transformation at the delithiated active materials layered structure took place, ending with rock-salt structure. Simultaneously, oxygen was produced accompanied by the heat generation. The cells could self-heat to over 450 °C, and the maximum temperature rate of could reach 100 °C/min. For the cells with SOC50, the onset temperature increases to nearly 200 °C. Although the maximum temperature rate reaches over 100 °C/min. For the cells with SOC0, no thermal runaway event took place. The temperature increasing rate of the cells with SOC0 is even below 1 °C/min. The activation energy of reactions increases with decreasing SOCs, implying the energy barrier is larger at lower SOCs.

6 Summary and outlook

In this work, thermal properties and thermal behavior of LiBs with active materials NMC were investigated. A novel approach was adopted by combining materials analysis and electrochemical-calorimetric study. The whole production of LiBs was studied in aspects of materials, components and cells. The main results are summarized regarding materials and coin cells.

The first part was the investigation on active material level. For the layered structure NMC with various compositions, the synthesis and calcination temperature were optimized. In order to investigate the delithiated NMC active materials, a chemical delithiation were performed on both sol-gel self-made and commercial NMC442. The samples with different delithiation degrees and constant molar ratio of transition metals (remaining Ni:Mn:Co=2:2:1) were selected and their thermal effects and gases releasing during phase transition of selected samples were analyzed.

The other part of this work is thermal behavior of commercial NMC-based cells during cycling. The heat flow rates of cells were measured by C80 calorimeter, as well as the thermal effects of components with increasing temperatures were investigated by C80 calorimeter. Thermal runaway tests of whole cells were performed by ARC, and the onset temperatures and the temperature rates were defined. The combination of C80 and ARC gives a full picture of thermal runaway.

In the outlook, some suggestions to complete or deepen the understanding are given in scope of this work.

6.1 NMC active material investigations

Series active materials $LiNi_xMn_{0.8-x}Co_{0.2}O_2$, x=0.4, 0.5, 0.6, 0.7 and 0.8 were synthesized by sol-gel method. When all compositions were sintered at 800 °C, the NMC materials with higher Ni content show a better crystallization of particles. The particle sizes decrease from NMC802 to NMC442. With increasing Ni content, the Ni^{2+} migration from transition-metal layer to the lithium layer will be more critical, since the ionic radius of Ni^{2+} (0.69 Å) is similar to the ionic radius of Li^+ (0.76 Å). An appropriate calcination temperature is a compromise between the suppression of the cation mixing and a good structural crystallinity. The optimized calcination temperatures for NMC442, NMC532, NMC622 and NMC712 were determined as 900 °C, 875 °C, 850 °C and 825 °C, respectively. Raw materials of Li source were designed to be 3 at.% extra Li to compensate the loss for the preparation of all samples. The aimed compositions were achieved and the crystal structure establishes a pure $R\bar{3}m$ group layer structure.

An attempt to chemically delithiation of NMC442 was performed by utilizing oxidizing agent $(NH_4)_2S_2O_8$. Various reaction periods and two different amounts of oxidizing agent were applied on sol-gel made and commercial NMC442 powders. Li atoms were successfully extracted, however, transition metals were also found to be dissolved in the agent. In deep delithiated samples, a second phase was found. The delithiated samples were carefully selected for the further studies. The molar ratio of transition metals should remain, with derivation ≤ 2 at.% according to chemical stoichiometry formula. Li contents of the samples were middle delithiation with around 76 at.% and deep delithiation with around 48 at.%. The structure of delithiated samples were found to be layered and monoclinic structure. According to the results of Rietveld refinement, lattice parameter *a* decreased with less Li content.

In STA measurements, the heat flow rates and mass loss were measured in temperature range of room temperature to 800 °C. The chemically delithiated NMC442 showed a considerably unstable thermal behavior at high temperature. The deep delithiated sample had the lowest onset temperature for exothermic reactions at approximately 71 °C, while the onset temperature of middle delithiated sample was 158 °C. The pristine NMC442 sample was very

stable in the measurement. Main reactions were supposed to be phase transitions from the phase with layered structure to spinel and then to rock-salt structure. Simultaneously, mass loss and oxygen release were observed during the phase transitions. Two oxygen releasing peaks were corresponding to the two phase transitions. With increasing delithiation states, more oxygen was released from the sample.
With help of the high temperature oxide melt drop solution calorimetry, the enthalpy of drop solution for delithiated samples were measured. Based on these results and the thermodynamic cycle, enthalpy of formation for three NMC442 samples with different Li contents was calculated. The formation enthalpy was found to decrease with rising of Li vacancies due to the thermal instability of delithiated NMC. For pristine NMC442, enthalpy of formation from the oxides and elements were -75.88 kJ/mol and -769.46 kJ/mol, respectively. Middle and deep delithiated samples had -61.88 kJ/mol and -57.57 kJ/mol for enthalpy of formation form the oxides, respectively; and -726.59 kJ/mol and -675.95 kJ/mol for enthalpy of formation from the elements, respectively.

6.2 Coin cell investigations

The commercial coin cells with NMC622 were investigated. Specific heat capacity of investigated coin cells were determined by continuous and step method in C80 calorimeter. The measurements were performed in temperature range of room temperature to 60 °C, which is maximal operating temperature for the tested commercial coin cells. The results from the two methods were in good agreement, resulting in 0.77±0.08 $J \cdot K^{-1} \cdot g^{-1}$ from continuous method, and 0.77±0.13 $J \cdot K^{-1} \cdot g^{-1}$ from step method, respectively. This value was used to determine the heat generation during cycling based on the temperature change measurements.
Coin cells were cycled in C80 calorimeter at 30 °C and 25 °C and the temperature changes and heat flow rates were measured. To stabilize the temperature of measuring system in C80 calorimeter at 25 °C, the calorimeter was put in a temperature incubator. During cycling, different C-rates 0.5 C (42.5 mA), 1 C (85 mA) and 2 C (170 mA) were used. Charging process was applied with CCCV method up to 4.2 V, and discharging process was applied with CC method with lower cut-off voltage 3 V. The cables influence was eliminated by a calibration coefficient, which was defined via Joule effect at three heat flow rates. The glass tape was used to isolate thermal and electrical conduction of cells, and its thermal influence was not considered in the results.
The values of heat calculated from the specific heat capacity and temperature changes, were much smaller than measured values from the calorimeter measurements. For example, heat generation for changing at 0.5 C were 12 J determined by temperature change measurements, and 24 J determined by heat flow rate measurements. The difference was even larger at higher C-rates cycling. For 2 C charging, the heat determined by temperature measurements was 20 J, while, 70 J determined by heat flow rate measurements. There are several error resources in the results from temperature change measurements. Firstly, the specific heat capacities of glass tape and cables were not considered in heat generation calculation. Secondly, the heat transfer coefficient was determined only based on geometry of the coin cells, and surface area and mass of the cables and glass tape were not considered. At last, the temperature was measured on one surface of coin cell, which was not the average temperature of the whole cells. On the other hand, C80 calorimeter has 3 D heat flow sensors, and the influences of glass tape and cables were adjusted in the calculation. Therefore, the calorimetric study provides an extremely sensitive and precise way to analyze the heat generation during cycling. To break down the heat flow rates in cycling, the irreversible and reversible heats were analyzed by internal resistances measurements and entropy measurements.
The reversible heat is generated from reversible reaction, which is the Li intercalation and deintercalation process. Since there is a relationship between the dependence of OCVs on

temperatures and reversible entropy change, the reversible entropy changes were determined at different SOC. Two temperature ranges were used. In addition, in order to achieve the OCVs under equilibrium, the OCVs at same temperature were measured three times (before/in/after measurement), so an OCV baseline (at 25 °C) at a certain SOC to be determined. However, when the function for baseline is not perfect fitting to three OCVs' curves, an extra error is introduced. After the optimization of the entropy change measurement, the entropy changes and enthalpy changes of reversible reaction in charging/discharging process were determined, and the corresponding reversible heat generation was determined too.
The irreversible heat is generated by internal resistances. Firstly, with help of EIS measurements, the ohmic resistance of tested cell was determined. Using GITT method, the internal resistances were measured at 0.5 C, 1 C and 2 C during charging and discharging at different SOCs. Moreover, the internal resistance were separately investigated for charge transfer, ohmic resistance and diffusion, and the corresponding heats were determined too. The heat flow rate as well as the total heat generation at various C-rates in charging and discharging processes were computed by summarizing the reversible and irreversible heat generation. The computed and measured heat flow rates had similar shape of curves and in the same range. The deviation of the computed heat flow rate to measured one varies from 10 % to 0.9 %, and the deviation comes mainly from the inaccuracy of entropy change measurements and GITT measurements due to the deviation from equilibrium states. The computed heat flow rate of discharge process fits better than charge process. The total heat generation from computed and measured results were in very good agreement.
The thermal runaway of coin cells with SOC0, SOC50 and SOC100 were investigated by C80 calorimeter and ARC. Firstly, the components, including negative, positive electrode with electrolyte and separator were separately investigated in C80 calorimeter to analyze the early stage of thermal runaway up to 150 °C. Thermal effects due to the reactions in negative electrode were critical at early stage of thermal runaway, which produce gases. Furthermore, the opening of coin cells and the separator melting were observed in the measurement of C80 calorimeter.
Secondly, the coin cells were heated to 450 °C in ARC. The endothermic effects were also observed before thermal runaway, where the temperature rate had a negative value. When the temperature rates were higher than 0.02 °C/min, exotherm mode would be active, which is a quasi-adiabatic condition. The heaters worked so that the temperature in chamber was the same as the cell's temperature. There was no heat dissipation of tested cells, so the self-heating could be defined by the value of temperature increase rate. Comparing the temperature increase rates of SOC100, SOC50 and SOC0 against temperature, the developments of self-heating were very clear: onset temperature, maximal temperature rate, most severer heat release, etc. The onset temperature for cells with SOC100, SOC50 and SOC0 were around 160 °C, 180 °C, 195 °C, respectively. The maximal temperature rate were 110 °C/min and 1 °C/min for cells with SOC50 and SOC0, respectively. The temperature rate of cells with SOC100 hasn't reached the maximal value in measurement because it stopped by cooling mode at 450 °C. The temperatures for the most severer heat release took place at 270 °C for cells with SOC50 and 210 °C - 220 °C for cells with SOC0. For cells with SOC100, the heat was released so fast, which heated the cells from 220 °C to over 500 °C in very short time. With higher SOC values tend to have a more violent behavior in thermal runaway, showing lower onset temperatures and higher temperature rate.

6.3 Outlook

In future, for Ni-rich NMC synthesis, the calcination can be optimized by applying an oxygen atmosphere to suppress the formation of oxygen vacancies and keep Ni at high oxidation state 3+. The influence of calcination temperature on electrochemical performance can be investigated especially during the growth of primary particles could result in the internal strain.

The electrochemical performance of sol-gel made NMC materials with different Ni contents can be compared. Since Ni-rich NMC is very sensitive to humidity, the process of slurry coating on Al foils should be performed either in a glovebox or in a dry room.

The chemical delithiation in this work extracted not only Li but also transition metals and removed oxygen. In Sekizawa et al.'s research [155], $LiNi_{0.5}Mn_{0.5}O_2$ was chemically delithiated by $(NH_4)_2S_2O_8$ solution for 0.5 - 4 hours under air. They also found the removal of oxygen. However, in Chebiam et al.'s research [156], the chemical delithiation was performed on $LiCoO_2$ and $LiMn_2O_4$ with various quantities oxidizing agent NO_2PF_6 or NO_2BF_4. There was no oxygen removal took place in $Li_xMn_2O_4$. From these results, we know the delithiation behavior varies by different combinations of a sample and an oxidizing agent. For Ni-rich active materials, the reaction $2Ni^{3+} \rightarrow Ni^{4+}+Ni^{2+}$ could occur and Ni^{2+} would dissolved in acid leaching process [157]. In Ref. [157], $LiNiO_2$ was also chemical delithiated by two methods: $NOPF_6$ as oxidizer and acid leaching. With $NOPF_6$ solution as oxidizer, $Li_{0.6}NiO_2$ was obtained. Further delithiated samples were $Li_{0.5}NiO_2$ achieved by acetic acid, $Li_{0.2}NiO_2$ by phosphoric acid and $Li_{0.1}NiO_2$ by sulfuric acid. In other research [101], $LiCoO_2$ active materials were chemical delithiated by Cl_2, Br_2, I_2 and sulfuric acid. Cl_2 was found to be too strong leading to a dissolution of samples. Sulfuric acid method resulted in a disorder between Li and Co in samples, and Co was prone to be extracted too. In Ref. [158], layered $LiCoO_2$ and $Li_xNi_{2-x}O_2$ ($0.6<x<1$) were chemically delithiated by acid. H and Li exchange was found in delithiation process, ending up with $Li_{1-x-y}H_yCoO_2$ sample. For layered $Li_xNi_{2-x}O_2$ ($0.6<x<1$), because of cation mixing between Li and Ni, partially Ni in LiO_2-layer was extracted. In the future work, the choose of oxidizing agent depends on the aiming delithiation degree, active composition. When aiming to a low Li content in samples, the acid leaching delithiation is more suitable than $NOBF_4$ or $NOPF_6$ solutions. With increasing Ni content in sample, the lower oxidizing power should be chosen to minimize Ni^{2+} dissolving. According to sample's oxidation potentials, the suitable oxidizing power should be chosen.

Intercalated Li in negative electrode material is prone to react with electrolyte, which contributes to the early stage thermal runaway. Chemical lithiation can be performed on negative electrode, and the thermal properties of lithiated negative electrode can be investigated by calorimeters. The interface reactions, such as SEI formation can be investigated for samples with different Li contents.

To compare with chemical delithiation / lithiation, the cells can be disassembled after cycling. The reactions between electrochemical delithiated positive electrode materials / lithiated negative electrode materials and electrolyte can be investigated by STA and MS. The released gases can be analyzed. Similarly, in the thermal runaway tests, the gases can be collected and analyzed. Since the micro- strain and micro-cracks in positive electrode material's particles are formed during Li intercalation and deintercalation, the reactions between positive electrode and electrolyte take place. The thermal stability of aging cells is a very critical problem. The aging cells can be disassembled and the thermal properties of components can be investigated by calorimeters.

The influence of morphology on thermal stabilities of positive electrode materials can be investigated in the future. Single crystalline positive electrode materials have lower initial capacity but longer cycling life and high stability at high voltage than polycrystalline positive electrode materials [159-160]. Noh et al. [161] reported gradient materials had high energy and good safety performance. The mechanism of reactions for positive electrode materials with different morphologies can be investigated by calorimeters.

In aspect of cell's format influence, for prismatic or pouch cells, the heat flow rates cannot be measured by C80 calorimeter because of the size. The reversible entropy change and internal resistance can be determined by entropy change measurements and GITT measurements, respectively. The computed heat flow rates can give a prediction to find the critical SOC with the maximal heat flow rate. The total heat generation can also be calculated. From the

individual cell, these results can be expanded in battery packs. Especially for fast charging process, the safety problems can be effectively controlled by thermal management system.
To improve the thermal stability, there are different approaches on material's level, cell's level and battery module's level. In scope of material development, artificial SEI, atomic layer deposition (ALD) coating and substitution are reported to improve the thermal stabilities [162-164]. The application of additives in electrolyte, optimization of electrode preparation, format of cells etc. in cell design are very promising and effect methods too. On battery module's level, the thermal management system in BMS can monitor and control the thermal stabilities. The cooling system, dissipation of battery module and circuit design can be investigated and improve the thermal stabilities of batteries.
The calorimetric study on LiBs provides a novel approach to investigate the thermal effects and heat generation. This method can apply on batteries with different materials, helping to evaluate the performance in consideration of thermal stability and safety. Since fast charging becomes an urgent demand for electrical devices and EVs, battery thermal management especially at high C-rates can help to improve the safety of LiBs. Based on the correlation between thermal properties and electrochemical properties, the thermal behavior of LiBs could be predicted and the safety issues can be noticed and managed immediately. Moreover, the storage of batteries should also be carefully monitored and controlled, which needs to investigate experimentally to understand and prevent battery's self-heating.

Bibliography

[1] Korosec, K.: *Tesla vehicle fire in Shanghai caused by single battery module.* Join Extra Crunch, News on website https://techcrunch.com/, June 28, 2019.

[2] Nedelea, A.: *The incident occurred while the car was being charged at a dealership in Prague*. INSIDEEVs, News on website https://insideevs.de/, July 01, 2020.

[3] Mayer, H.: *Air pollution in cities.* Atmospheric Environment, 33 (24-25), pp. 4029-4037, 1999.

[4] Zubi, G.; Dufo-López, R.; Carvalho, M. and Pasaoglu, G.: *The lithium-ion battery state of the art and future perspectives.* Renewable and Sustainable Energy Reviews, 89, pp. 292-308, 2018.

[5] Wang, Y. and Cao, G.: *Developments in nanostructured cathode materials for high-performance lithium-ion batteries.* Advanced Materials, 20 (12), pp.2251-2269, 2008.

[6] Kang, K.; Meng, Y. S.; Bréger, J.; Grey, C. P. and Ceder, G.: *Electrodes with high power and high capacity for rechargeable lithium batteries.* Science, 311 (5763), pp. 977-980, 2006.

[7] Thackeray, M. M.; David, W. I. F.; Bruce, P. G. and Goodenough, J. B.: *Lithium insertion into manganese spinels.* Materials Research Bulletin, 18 (4), pp.461-472, 1983.

[8] Luo, W.; Zhou, F.; Zhao, X.; Lu, Z.; Li, X. and Dahn, J. R.: *Synthesis characterization and thermal stability of* $LiNi_{1/3}Mn_{1/3}Co_{1/3-z}Mg_zO_2$, $LiNi_{1/3-z}Mn_{1/3}Co_{1/3}Mg_zO_2$ *and* $LiNi_{1/3}Mn_{1/3-z}Co_{1/3}Mg_zO_2$. Chemistry of Materials, 22 (3), pp. 1164-1172, 2010.

[9] Chung, S. Y.; Bloking, J. T. and Chiang, Y. M.: *Electronically conductive phospho-olivines as lithium storage electrodes*. Nature Materials, 1 (2), pp. 123, 2002.

[10] Tang, A. and Huang, K.: *Electrochemical properties and structural characterization of layered* $Li_xNi_{0.35}Co_{0.3}Mn_{0.35}O_{2+\delta}$ *cathode materials*. Materials Science and Engineering: B, 122 (2), pp. 115-120, 2005.

[11] Lei, B.; Zhao, W.; Ziebert, C.; Uhlmann, N.; Rohde, M. and Seifert, H. J.: *Experimental analysis of thermal runaway in 18650 cylindrical Li-ion cells using an accelerating rate calorimeter*. Batteries, 3 (2), pp. 14-28, 2017.

[12] Huang, Q.; Ma, L.; Liu, A.; Ma, X.; Li, J.; Wang, J. and Dahn, J. R.: *The reactivity of charged positive* $Li_{1-n}[Ni_xMn_yCo_z]O_2$ *electrodes with electrolyte at elevated temperatures using accelerating rate calorimetry*. Journal of Power Sources, 390, pp. 78-86, 2018.

[13] Ma, L.; Nie, M.; Xia, J. and Dahn, J. R.: *A systematic study on the reactivity of different grades of charged* $Li[Ni_xMn_yCo_z]O_2$ *with electrolyte at elevated temperatures using accelerating rate calorimetry*. Journal of Power Sources, 327, pp. 145-150, 2016.

[14] Levy S. C and Bro, P.: *Battery hazards and accident prevention.* Springer Science & Business Media, New York, USA, 1994.

[15] Accident report: *Boeing 787 battery on fire.* National transportation safety board accident investigations, https://www.ntsb.gov/investigations/pages/boeing_787.aspx, July 1st 2013.

[16] Ruiz, V.; Pfrang, A.; Kriston, A.; Omar, N.; Van den Bossche, P. and Boon-Brett, L.: *A review of international abuse testing standards and regulations for lithium ion batteries in electric and hybrid electric vehicles*. Renewable and Sustainable Energy Reviews, 81 (1), pp. 1427-1452, 2018.

[17] Saito, Y.; Takano, K. and Negishi, A.: *Thermal behaviors of lithium-ion cells during overcharge.* Journal of Power Sources, 97-98, pp. 693-696, 2001.

[18] Spotnitz, R. and Franklin, J.: *Abuse behavior of high-power lithium-ion cells*. Journal of Power Sources, 113 (1), pp. 81-100, 2003.

[19] Ping, P.; Wang, Q.; Huang, P.; Li, K.; Sun, J.; Kong, D. and Chen, C.: *Study of the fire behavior of high-energy lithium-ion batteries with full-scale burning test.* Journal of Power Sources, 285, pp. 80-89, 2015.

[20] Goodenough, J. B. and Kim, Y.: *Challenges for rechargeable Li batteries*. Chemistry of materials, 22 (3), pp. 587-603, 2010.

[21] Thackeray, M. M.; Wolverton, C. and Isaacs, E. D.: *Electrical energy storage for*

transportation—approaching the limits of, and going beyond, lithium-ion batteries. Energy & Environmental Science, 5 (7), pp. 7854-7863, 2012.
[22] Balakrishnan, P. G.; Ramesh, R. and Kumar, T. P.: *Safety mechanisms in lithium-ion batteries.* Journal of Power Sources, 155 (2), pp. 401-414, 2006.
[23] Wang, Q.; Ping, P.; Zhao, X.; Chu, G.; Sun, J. and Chen, C.: *Thermal runaway caused fire and explosion of lithium ion battery*. Journal of Power Sources, 208, pp. 210-224, 2012.
[24] Golubkov, A. W.; Fuchs, D.; Wagner, J.; Wiltsche, H.; Stangl, C.; Fauler, G.; Voitic, G.; Thaler, A. and Hacker, V.: *Thermal-runaway experiments on consumer Li-ion batteries with metal-oxide and olivin-type cathodes*. RSC Advances, 4 (7), pp. 3633-3642, 2014.
[25] Ouyang, D.; Chen, M.; Huang, Q.; Weng, J.; Wang, Z. and Wang, J.: *A review on the thermal hazards of the lithium-ion battery and the corresponding countermeasures.* Applied Sciences, 9 (12), pp. 2483-2528, 2019.
[26] Huggins, R. A.: *Advanced Batteries.* Springer Science & Business Media, New York, USA, 2009.
[27] Yuvaraj, S.; Selvan, R. K. and Lee, Y. S.: *An overview of AB_2O_4- and A_2BO_4-structured negative electrodes for advanced Li-ion batteries.* RSC Advances, 6 (26), pp. 21448-21474, 2016.
[28] Broussely, M.; Biensan, P. and Simon, B.: *Lithium insertion into host materials: the key to success for Li ion batteries.* Electrochimica Acta, 45 (1-2), pp. 3-22, 1999.
[29] Manthiram, A.: *An outlook on lithium ion battery technology.* ACS central science, 3 (10) pp. 1063-1069, 2017.
[30] Manthiram, A.: *A reflection on lithium-ion battery cathode chemistry*. Nature Communications, 11 (1), pp. 1-9, 2020.
[31] Liu, H.; Li, J.; Zhang, Z.; Gong, Z. and Yang, Y.: *The effects of sintering temperature and time on the structure and electrochemical performance of $LiNi_{0.8}Co_{0.2}O_2$ cathode materials derived from sol-gel method*. Journal of Solid State Electrochemistry, 7 (8), pp. 456-462, 2003.
[32] Dahn, J. R.; Fuller, E. W.; Obrovac, M. and Von Sacken, U.: *Thermal stability of Li_xCoO_2, Li_xNiO_2 and λ-MnO_2 and consequences for the safety of Li-ion cells.* Solid State Ionics, 69 (3-4), pp. 265-270, 1994.
[33] Davidson, I. J.; McMillan, R. S.; Murray, J. J. and Greedan, J. E.: *Lithium-ion cell based on orthorhombic $LiMnO_2$.* Journal of Power Sources, 54 (2), pp. 232-235, 1995.
[34] Reynaud, M. and Casas-Cabanas, M.: *Order and disorder in NMC layered materials: a FAULTS simulation analysis.* Powder Diffraction, 32, pp. 213-220, 2017.
[35] MacNeil, D. D.; Lu, Z. and Dahn, J. R.: *Structure and electrochemistry of $Li[Ni_xCo_{1-2x}Mn_x]O_2$ $(0\leq x\leq 1/2)$*. Journal of the Electrochemical Society, 149 (10), pp. A1332-A1336, 2002.
[36] Jung, R.; Metzger, M.; Maglia, F.; Stinner, C. and Gasteiger, H.: *Oxygen release and its effect on the cycling stability of $LiNi_xMn_yCo_zO_2$ (NMC) cathode materials for Li-ion batteries.* Journal of the Electrochemical Society, 164 (7), pp. A1361-A1377, 2017.
[37] Noh, H. J.; Youn, S.; Yoon, C. S. and Sun, Y. K.: *Comparison of the structural and electrochemical properties of layered $Li[Ni_xCo_yMn_z]O_2$ (x=1/3, 0.5, 0.6, 0.7 ,0.8 and 0.85) cathode material for lithium-ion batteries*. Journal of Power Sources, 233, pp. 121-130, 2013.
[38] Huang, Z.; Gao, J.; He, X.; Li, J. and Jiang, C.: *Well-ordered spherical $LiNi_xCo_{1-2x}Mn_xO_2$ cathode materials synthesized from cobalt concentration-gradient precursors.* Journal of Power Sources, 202, pp. 284-290, 2012.
[39] Kosova, N. V.; Devyatkina, E. T. and Kaichev, V. V.: *$LiNi_{1-x-y}Co_xMn_yO_2$ (x = y = 0.1, 0.2, 0.33) cathode materials prepared using mechanical activation: structure, state of ions, and electrochemical performance.* Inorganic Materials, 43 (2), pp. 185-193, 2007.
[40] Shizuka, K.; Kobayashi, T.; Okahara, K.; Okamoto, K.; Kanzaki, S. and Kanno, R.: *Characterization of $Li_{1+y}Ni_xCo_{1-2x}Mn_xO_2$ positive active materials for lithium ion batteries.* Journal of Power Sources, 146 (1-2), pp. 589-593, 2005.
[41] Berndt, D.: *Maintenance-free batteries based on aqueous electrolyte - A handbook of*

battery technology. 3rd Edition, Research studies press LTD., Baldock, UK, 2003.
[42] Zhu, Y. and Wang, C.: *Galvanostatic intermittent titration technique for phase-transformation electrodes.* Journal of Physical Chemistry C, 114 (6), pp. 2830-2841, 2010.
[43] Viswanathan, V. V.; Choi, D.; Wang, D.; Xu, W.; Towne, S.; Williford, R. E.; Zhang, J.; Liu, J. and Yang, Z.: *Effect of entropy change of lithium intercalation in cathodes and anodes on Li-ion battery thermal management.* Journal of Power Sources, 195 (11), pp. 3720-3729, 2010.
[44] Yazami, R.: *Thermodynamics of electrode materials for lithium-ion batteries.* Editor: Ozawa, K.: *Lithium ion rechargeable batteries: materials, technology, and new applications.* Wiley Online Library, pp. 67-102, Weinheim, Germany, 2009.
[45] Osswald, P. J.; del Rosario, M.; Garche, J.; Jossen, A. and Hoster, H. E.: *Fast and accurate measurement of entropy profiles of commercial lithium-ion cells.* Electrochimica Acta, 177, pp. 270-276, 2015.
[46] Lisbona, D. and Snee, T.: *A review of hazards associated with primary lithium and lithium-ion batteries.* Process Safety and Environmental Protection, 89 (6), pp. 434-442, 2011.
[47] Abada, S.; Marlair, G.; Lecocq, A.; Petit, M.; Sauvant-Moynot, V. and Huet, F.: *Safety focused modeling of lithium-ion batteries: A review.* Journal of Power Sources, 306, pp. 178-192, 2016.
[48] Mandal, B. K.; Padhi, A. K.; Shi, Z.; Chakraborty, S. and Filler, R.: *Thermal runaway inhibitors for lithium battery electrolytes.* Journal of Power Sources, 161 (2), pp. 1341-1345, 2006.
[49] Gao, S.; Lu, L.; Ouyang, M.; Duan, Y.; Zhu, X.; Xu, C.; Ng, B.; Kamyab, N.; White, E. R. and Coman, T.: *Experimental study on module-to-module thermal runaway-propagation in a battery pack.* Journal of the Electrochemical Society, 166 (10), pp. A2065-A2073, 2019.
[50] Spotnitz, R. M.; Weaver, J.; Yeduvaka, G.; Doughty, D. H. and Roth, E. P.: *Simulation of abuse tolerance of lithium-ion battery packs.* Journal of Power Sources, 163 (2), pp. 1080-1086, 2007.
[51] Semenov, N. N.: *Some problems in chemical kinetics and reactivity. Vol. 2, Chap. 8,* Princeton University Press, New Jersey, USA, 1959.
[52] Wang, Q.; Sun, J. and Chu, G.: *Lithium ion battery fire and explosion.* Fire Safety Science, 8, pp. 375-382, 2005.
[53] Torabi, F. and Esfahanian, V.: *Study of thermal--runaway in batteries I. theoretical study and formulation.* Journal of the Electrochemical Society, 158 (8), pp. A850-A858, 2011.
[54] Kumaresan, K.; Sikha, G. and White, R. E.: *Thermal model for a Li-ion cell.* Journal of the Electrochemical Society, 155 (2), pp. A164-A171, 2007.
[55] Kim, G. H.; Pesaran, A. and Spotnitz, R.: *A three-dimensional thermal abuse model for lithium-ion cells*. Journal of Power Sources, 170 (2), pp. 476-489, 2007.
[56] Wang, Q.; Ping, P. and Sun, J.: *Catastrophe analysis of cylindrical lithium ion battery.* Nonlinear Dynamics, 61 (4), pp. 763-772, 2010.
[57] Sarge, S. M.; Höhne, G. W. and Hemminger, W.: *Calorimetry fundamentals, instrumentation and applications.* John Wiley & Sons, New York, USA, 2014.
[58] Sharma, R.; Bisen, D. P.; Shukla, U. and Sharma, B. G.: *X-ray diffraction: a powerful method of characterizing nanomaterials*. Recent research in science and technology, 4 (8), pp. 77-79, 2012.
[59] Chang, B. Y. and Park, S. M.: *Electrochemical impedance spectroscopy.* Annual Review of Analytical Chemistry, 3, pp. 207-229, 2010.
[60] Zha, Z.; Co-supervisor: Ziebert, C.; supervisor: Seifert, H. J.: *Parametrierung, Simulation und Validierung eines Equivalentschaltkreismodells fuer ein 4S1P Batteriepack*. Master thesis, Karlsruhe Institute of Technology (KIT), Institute for Applied Materials-Applied Material Physics (IAM-AWP), Karlsruhe, Germany, 2017.
[61] Heubner, C. M.; Schneider, M. and Michaelis, A.: *Detailed study of heat generation in porous $LiCoO_2$ electrodes*. Journal of Power Sources, 307, pp. 199-207, 2016.
[62] Zhao, W.; Rohde, M.; Mohsin, I. U.; Ziebert, C. and Seifert, H. J.: *Heat generation in*

NMC622 coin cells during electrochemical cycling: separation of reversible and irreversible heat effects. Batteries, 6 (4), pp. 55-67, 2020.
[63] Höhne, G.; Hemminger, W. F. and Flammersheim, H. J.: *Differential scanning calorimetry*. 2nd Edition, Springer Science & Busniess Media, New York, USA, 2003.
[64] Gmelin, E. and Sarge, S. M.: *Temperature, heat and heat flow rate calibration of differential scanning calorimeters.* Thermochimica Acta, 347, pp. 9-13, 2000.
[65] Preston-Thomas, H.: *The international temperature scale of 1990 (ITS-90)*. metrologia, 27 (1), 1990.
[66] Fellmuth, B.: *Guide to the realization of ITS-90*. Physikalisch-Technische Bundesanstalt, Berlin, Germany, 2018.
[67] Stølen, S. and Grønvold, F.: *Critical assessment of the enthalpy of fusion of metals used as enthalpy standards at moderate to high temperatures.* Thermochimica Acta, 327 (1-2), pp. 1-32, 1999.
[68] Della Gatta, G.; Richardson, M. J.; Sarge, S. M. and Stølen, S.: *Standards, calibration, and guidelines in microcalorimetry part 2. Calibration standards for differential scanning calorimetry.* Pure and Applied Chemistry, 78 (7), pp. 1455-1476, 2006.
[69] Jendoubi, H.; Hellali, D.; Zamali, H. and Jemal, M.: *The phase diagram of KNO_3-$RbNO_3$.* Journal of Thermal Analysis and Calorimetry, 111, pp. 877-883, 2013.
[70] Hemminger, W. F. and Cammenga, H. K.: *Methoden der thermischen Analyse (Vol. 1).* Springer-Verlag Berlin, Heidelberg, Germany, 1989.
[71] Höhne, G. W. H.; Cammenga, H. K.; Eysel, W.; Gmelin, E. and Hemminger, W. F.: *The temperature calibration of scanning calorimeters.* Thermochimica Acta, 160 (1), pp. 1-12, 1990.
[72] Boettinger, W. J.; Kattner, U. R. and Moon, K. W.: *DTA and heat-flux DSC measurements of alloy melting and freezing.* NIST recommended practice guide special publication, 960, pp. 1-90, 2006.
[73] Kostyrko, K. and Skoczylas, M.: *Temperature standard reference materials for thermal analysis*. Journal of Thermal Analysis, 38 (9), pp. 2181-2188, 1992.
[74] Navrotsky, A.: *Progress and new directions in high temperature calorimetry.* Physics and Chemistry of Minerals, 2 (1), pp. 89-104, 1977.
[75] Navrotsky, A.: *Progress and new directions in high temperature calorimetry revisited.* Physics and Chemistry of Minerals, 24 (3), pp. 222-241, 1997.
[76] Lilova, K. I. and Rock, P. A.: Presentation: *AlexSYS operation: Phasmatic apparatus or "The ghost in the machine"*. Thermochemistry Laboratory and NEAT ORU, University of California at Davis, 2010.
[77] Manual: *Alexsys 1000 ARDE09009 Karlsruher Institut für Technologie Commissioning*. Setaram Instrumentation, September 2010.
[78] Cupid, D. M.; Reif, A. and Seifert, H. J.: *Enthalpy of formation of $Li_{1+x}Mn_{2-x}O_4$ (0<x<0.1) spinel phases.* Thermochimica Acta, 599, pp. 35-41, 2015.
[79] JCGM: *Evaluation of measurement data—Guide to the expression of uncertainty in measurement.* International Organization for Standardization Geneva ISBN, 50, 2008.
[80] Lu, C. H. and Wei-Cheng, L.: *Reaction mechanism and kinetics analysis of lithium nickel oxide during solid-state reaction*. Journal of Materials Chemistry, 10 (6), pp. 1403-1407, 2000.
[81] Caurant, D.; Baffier, N.; Garcia, B. and Pereira-Ramos, J. P.: *Synthesis by a soft chemistry route and characterization of $LiNi_xCo_{1-x}O_2$ (0≤x≤1) cathode materials.* Solid State Ionics, 91 (1-2), pp. 45-54, 1996.
[82] Zheng, J.; Yan, P.; Estevez, L.; Wang, C. and Zhang, J. G.: *Effect of calcination temperature on the electrochemical properties of Ni-rich $LiNi_{0.76}Mn_{0.14}Co_{0.10}O_2$ cathodes for lithium-ion batteries*. Nano Energy, 49, pp. 538-548, 2018.
[83] Santhanam, R. and Rambabu, B.: *High rate cycling performance of $Li_{1.05}Ni_{1/3}Co_{1/3}Mn_{1/3}O_2$ materials prepared by sol-gel and co-precipitation methods for lithium-ion batteries.* Journal of Power Sources, 195 (13), pp. 4313-4317, 2010.

[84] Sivaprakash, S. and Majumder, S. B.: *Synthesis and electrochemical characteristics of $Li(Ni_{0.375}Mn_{0.375}Co_{0.25})O_2$—$Li(Li_{1/3}Mn_{2/3})O_2$ cathode materials for Li rechargeable batteries.* Journal of the Electrochemical Society, 157 (4), pp. A418-A422, 2010.
[85] Singh, G.; Sil, A.; Ghosh, S. and Panwar, A.: *Effect of citric acid content on synthesis of $LiNi_{1/3}Mn_{1/3}Co_{1/3}O_2$ and its electrochemical characteristics.* Ceramics International, 36 (6), pp. 1831-1836, 2010.
[86] Xu, J.; Chou, S. L.; Gu, Q. F.; Liu, H. K. and Dou, S. X.: *The effect of different binders on electrochemical properties of $LiNi_{1/3}Mn_{1/3}Co_{1/3}O_2$ cathode material in lithium ion batteries.* Journal of Power Sources, 225, pp. 172-178, 2013.
[87] Kızıltaş-Yavuz, N.; Herklotz, M.; Hashem, A. M.; Abuzeid, H. M.; Schwarz, B.; Ehrenberg, H.; Mauger, A. and Julien, C. M.: *Synthesis, structural, magnetic and electrochemical properties of $LiNi_{1/3}Mn_{1/3}Co_{1/3}O_2$ prepared by a sol-gel method using table sugar as chelating agent.* Electrochimica Acta, 113, pp. 313-321, 2013.
[88] Kabi, S. and Ghosh, A.: *Microstructure of $Li(Mn_{1/3}Ni_{1/3}Co_{1/3})O_2$ cathode material for lithium ion battery: Dependence of crystal structure on calcination and heat-treatment temperature.* Materials Research Bulletin, 48 (9), pp. 3405-3410, 2013.
[89] Gan, C.; Hu, X.; Zhan, H. and Zhou, Y.: *Synthesis and characterization of $Li_{1.2}Ni_{0.6}Co_{0.2}Mn_{0.2}O_{2+\delta}$ as a cathode material for secondary lithium batteries.* Solid State Ionics, 176 (7-8), pp. 687-692, 2005.
[90] Kang, K. and Ceder, G.: *Factors that affect Li mobility in layered lithium transition metal oxides.* Physical Review B, 74 (9), pp. 94-105, 2006.
[91] Röder, P.; Baba, N. and Wiemhöfer, H. D.: *A detailed thermal study of a $Li[Ni_{0.33}Co_{0.33}Mn_{0.33}]O_2/LiMn_2O_4$-based lithium ion cell by accelerating rate and differential scanning calorimetry.* Journal of Power Sources, 248, pp. 978-987, 2014.
[92] Chen, W. C.; Wang, Y. W. and Shu, C. M.: *Adiabatic calorimetry test of the reaction kinetics and self-heating model for 18650 Li-ion cells in various states of charge.* Journal of Power Sources, 318, pp. 200-209, 2016.
[93] Sharifi-Asl, S.; Soto, F. A.; Nie, A.; Yuan, Y.; Asayesh-Ardakani, H.; Foroozan, T.; Yurkiv, V.; Song, B.; Mashayek, F.; Klie, R. F.; Amine, K.; Lu, J.; Balbuena, P. B. and Shahbazian-Yassar, R.: *Facet-dependent thermal instability in $LiCoO_2$.* Nano Letters, 17 (4), pp. 2165-2171, 2017.
[94] Bak, S. M.; Hu, E.; Zhou, Y.; Yu, X.; Senanayake, S. D.; Cho, S. J.; Kim, K. B.; Chung, K. Y.; Yang, X. Q. and Nam, K. W.: *Structural changes and thermal stability of charged $LiNi_xMn_yCo_zO_2$ cathode materials studied by combined in-situ time-resolved XRD and mass spectroscopy.* ACS Applied Materials & Interfaces, 6 (24), pp. 22594-22601, 2014.
[95] Tang, W.; Kanoh, H. and Ooi, K.: *Lithium ion extraction from orthorhombic $LiMnO_2$ in ammonium peroxodisulfate solutions.* Journal of Solid State Chemistry, 142 (1), pp. 19-28, 1999.
[96] Belharouak, I.; Lu, W.; Vissers, D. and Amine, K.: *Safety characteristics of $Li(Ni_{0.8}Co_{0.15}Al_{0.05})O_2$ and $Li(Ni_{1/3}Co_{1/3}Mn_{1/3})O_2$*. Electrochemistry Communications, 8, pp. 329-335, 2006.
[97] Chen, C. H.; Hwang, B. J.; Chen, C. Y.; Hu, S. K.; Chen, J. M.; Sheu, H. S. and Lee, J. F.: *Soft X-ray absorption spectroscopy studies on the chemically delithiated commercial $LiCoO_2$ cathode material.* Journal of Power Sources, 174 (2), pp. 938-943, 2007.
[98] McCalla, E.; Carey, G. H. and Dahn, J. R.: *Lithium loss mechanisms during synthesis of layered $Li_xNi_{2-x}O_2$ for lithium ion batteries.* Solid State Ionics, 219, pp. 11-19, 2012.
[99] Zhang, X.; Jiang, W. J.; Mauger, A.; Gendron, F. and Julien, C. M.: *Minimization of the cation mixing in $Li_{1+x}(NMC)_{1-x}O_2$ as cathode material.* Journal of Power Sources, 195 (5), pp. 1292-1301, 2010.
[100] Kosova, N. V.; Devyatkina, E. T. and Kaichev, V. V.: *Optimization of Ni^{2+}/Ni^{3+} ratio in layered Li(Ni, Mn, Co)O_2 cathodes for better electrochemistry*. Journal of Power Sources, 174 (2), pp. 965-969, 2007.
[101] Gupta, R. and Manthiram, A.: *Chemical extraction of lithium from layered $LiCoO_2$.* Journal

of Solid State Chemistry, 121 (2), pp. 483-491, 1996.
[102] Venkatraman, S. and Manthiram, A.: *Structural and chemical characterization of layered $Li_{1-x}Ni_{1-y}Mn_yO_{2-\delta}$ (y=0.25 and 0.5, and 0≤(1–x)≤1) oxides.* Chemistry of Materials, 15 (26), pp. 5003-5009, 2003.
[103] Labrini, M.; Scheiba, F.; Almaggoussi, A.; Larzek, M.; Braga, M. H.; Ehrenberg, H. and Saadoune, I.: *Delithiated $Li_yCo_{0.8}Ni_{0.1}Mn_{0.1}O_2$ cathode materials for lithium-ion batteries: structural, magnetic and electrochemical studies.* Solid State Ionics, 289, pp. 207-213, 2016.
[104] Abdel-Ghany, A.; Zaghib, K.; Mauger, A.; Eid, F.; Abbas, H.; Hashem, A.; Ramana, C. V. and Julien, C.: *Electrochemical features of $LiNi_yMn_yCo_zO_2$ cathodes for Li-ion batteries*. ECS Transactions, 3 (27), pp. 131-138, 2007.
[105] Labrini, M.; Saadoune, I.; Almaggoussi, A.; Elhaskouri, J. and Amoros, P.: *The $Li_yNi_{0.2}Mn_{0.2}Co_{0.6}O_2$ electrode materials: A structural and magnetic study.* Materials Research Bulletin, 47 (4), pp. 1004-1009, 2012.
[106] Reimers, J. N. and Dahn, J. R.: *Electrochemical and in situ X-ray diffraction studies of lithium intercalation in Li_xCoO_2.* Journal of the Electrochemical Society, 139 (8), pp. 2091-2097, 1992.
[107] Zheng, J.; Liu, T.; Hu, Z.; Wei, Y.; Song, X.; Ren, Y.; Wang, W.; Rao, M.; Lin, Y.; Chen, Z. and Lu, J.: *Tuning of thermal stability in layered $Li(Ni_xMn_yCo_z)O_2$.* Journal of the American Chemical Society, 138 (40), pp. 13326-13334, 2016.
[108] Kim, Y.; Kim, D. and Kang, S.: *Experimental and first-principles thermodynamic study of the formation and effects of vacancies in layered lithium nickel cobalt oxides.* Chemistry of Materials, 23 (24), pp. 5388-5397, 2011.
[109] Koyama, Y.; Tanaka, I.; Adachi, H.; Makimura, Y. and Ohzuku, T.: *Crystal and electronic structures of superstructural $Li_{1-x}[Co_{1/3}Ni_{1/3}Mn_{1/3}]O_2$ (0≤x≤1).* Journal of Power Sources, 119, pp. 644-648, 2003.
[110] Kim, J. M. and Chung, H. T.: *The first cycle characteristics of $Li[Ni_{1/3}Co_{1/3}Mn_{1/3}]O_2$ charged up to 4.7 V.* Electrochimica Acta, 49 (6), pp. 937-944, 2004.
[111] Qiao, R.; Liu, J.; Kourtakis, K.; Roelofs, M. G.; Peterson, D.; Duff, J. P.; Deibler, D.; Wray, L. and Yang, W.: *Transition-metal redox evolution in $LiNi_{0.5}Mn_{0.3}Co_{0.2}O_2$ electrodes at high potentials*. Journal of Power Sources, 360, pp. 294-300, 2017.
[112] Dinsdale, A. T.: *SGTE data for pure elements.* Calphad, 15 (4), pp. 317-425, 1991.
[113] Masoumi, M.; Cupid, D. M.; Reichmann, T. L.; Denis Music, K. C.; Schneider, J. M. and Seifert, H. J.: *Enthalpies of formation of layered $LiNi_xMn_xCo_{1-2x}O_2$ compounds as promising Li-ion battery cathode materials.* International Journal of Materials Research, 108, pp. 1-10, 2017.
[114] Wang, M. and Navrotsky, A.: *Enthalpy of formation of $LiNiO_2$, $LiCoO_2$ and their solid solution, $LiNi_{1-x}Co_xO_2$.* Solid State Ionics, 166 (1-2), pp. 167-173, 2004.
[115] Wang, M.; Navrotsky, A.; Venkatraman, S. and Manthiram, A.: *Enthalpy of formation of Li_xCoO_2 (0.5≤x≤1.0)*. Journal of the Electrochemical Society, 152 (7), pp. J82-J84, 2005.
[116] Glushko, V. P. and Medvedev, V. A.: *Thermal constants of substances.* John Wiley & Sons, New York, USA, 1990.
[117] Wang, M. and Navrotsky, A.: *Thermochemistry of $Li_{1+x}Mn_{2-x}O_4$ (0≤x≤1/3) spinel.* Journal of Solid State Chemistry, 178 (4), pp. 1182-1189, 2005.
[118] Idemoto, Y. and Matsui, T.: *Thermodynamic stability, crystal structure, and cathodic performance of $Li_x(Mn_{1/3}Co_{1/3}Ni_{1/3})O_2$ depend on the synthetic process and Li content.* Solid State Ionics, 179 (17-18), pp. 625-635, 2008.
[119] Kuppan, S.; Xu, Y.; Liu, Y. and Chen, G.: *Phase transformation mechanism in lithium manganese nickel oxide revealed by single-crystal hard X-ray microscopy.* Nature communications, 8 (1), pp. 1-10, 2017.
[120] Saito, Y.; Kanari, K.; Takano, K. and Masuda, T.: *A calorimetric study on a cylindrical type lithium secondary battery by using a twin-type heat conduction calorimeter.* Thermochimica Acta, 296 (1-2), pp. 75-85, 1997.

[121] Schmidt, J. P.; Weber, A. and Ivers-Tiffée, E.: *A novel and precise measuring method for the entropy of lithium-ion cells: ΔS via electrothermal impedance spectroscopy.* Electrochimica Acta, 137, pp. 311-319, 2014.
[122] Murashko K. A.; Mityakov, A. V.; Mityakov, V. Y. Sapozhnikov, S. Z., Jokiniemi, J. and Pyrhönen, J.: *Determination of the entropy change profile of a cylindrical lithium-ion battery by heat flux measurements.* Journal of Power Sources, 330, pp. 61-69, 2016.
[123] Bandhauer, T. M.; Garimella, S. and Fuller, T. F.: *A critical review of thermal issues in lithium-ion batteries.* Journal of the Electrochemical Society, 158 (3), pp. R1-R25, 2011.
[124] Maher, K. and Yazami, R.: *Effect of overcharge on entropy and enthalpy of lithium-ion batteries.* Electrochimica Acta, 101, pp. 71-78, 2013.
[125] Williford, R. E.; Viswanathan, V. V. and Zhang, J. G.: *Effects of entropy changes in anodes and cathodes on the thermal behavior of lithium ion batteries.* Journal of Power Sources, 189 (1), pp. 101-107, 2009.
[126] Jalkanen, K. Aho, T. and Vuorilento, K.: *Entropy change effects on the thermal behavior of a $LiFePO_4$/graphite lithium-ion cell at different states of charge.* Journal of Power Sources, 243, pp. 354-360, 2013.
[127] Melcher, A.; Ziebert, C.; Rohde, M. and Seifert, H.: *Modeling and simulation of the thermal runaway behavior of cylindrical Li-ion cells—computing of critical parameters.* Energies, 9 (4), pp. 292-301, 2016.
[128] Parimalam, B. S.; MacIntosh, A. D.; Kadam, R. and Lucht, B. L.: *Decomposition reactions of anode solid electrolyte interphase (SEI) components with $LiPF_6$.* The Journal of Physical Chemistry C, 121 (41), pp. 22733-22738, 2017.
[129] Wang, Q.; Sun, J.; Yao, X. and Chen, C.: *Thermal behavior of lithiated graphite with electrolyte in lithium-ion batteries.* Journal of the Electrochemical Society, 153 (2), pp. A329-A333, 2005.
[130] Wang, Q.; Sun, J.; Yao, X. and Chen, C.: *Thermal stability of $LiPF_6$/EC + DEC electrolyte with charged electrodes for lithium ion batteries.* Thermochimica Acta, 437 (1-2), pp. 12-16, 2005.
[131] Sloop, S. E.; Kerr, J. B. and Kinoshita, K.: *The role of Li-ion battery electrolyte reactivity in performance decline and self-discharge.* Journal of Power Sources, 119, pp. 330-337, 2003.
[132] Moshkovich, M.; Cojocaru, M.; Gottlieb, H. E. and Aurbach, D.: *The study of the anodic stability of alkyl carbonate solutions by in situ FTIR spectroscopy, EQCM, NMR and MS.* Journal of Electroanalytical Chemistry, 497 (1-2), pp. 84-96, 2001.
[133] MacNeil, D. D. and Dahn, J. R.: *The reaction of charged cathodes with nonaqueous solvents and electrolytes: I. $Li_{0.5}CoO_2$.* Journal of the Electrochemical Society, 148 (11), pp. A1205-A1210, 2001.
[134] MacNeil, D. D. and Dahn, J. R.: *The reactions of $Li_{0.5}CoO_2$ with nonaqueous solvents at elevated temperatures.* Journal of the Electrochemical Society, 149 (7), pp. A912-A919, 2002.
[135] Jiang, J. and Dahn, J. R.: *Effects of solvents and salts on the thermal stability of LiC_6.* Electrochimica Acta, 49 (26), pp. 4599-4604, 2004.
[136] Kim, G. Y. and Dahn, J. R.: *ARC Studies of the effects of electrolyte additives on the reactivity of delithiated $Li_{1-x}[Ni_{1/3}Mn_{1/3}Co_{1/3}]O_2$ and $Li_{1-x}[Ni_{0.8}Co_{0.15}Al_{0.05}]O_2$ positive electrode materials with electrolyte.* Journal of the Electrochemical Society, 161 (9), pp. A1394-A1398, 2014.
[137] Schrödle, S.; Königsberger, E.; May, P. M. and Hefter, G.: *Heat capacities of aqueous solutions of sodium hydroxide and water ionization up to 300 °C at 10 MPa.* Geochimica et Cosmochimica Acta, 72 (13), pp. 3124-3138, 2008.
[138] Páramo, R.; Zouine, M. and Casanova, C.: *New batch cells adapted to measure saturated heat capacities of liquids.* Journal of Chemical & Engineering Data, 47 (3), pp. 441-448, 2002.
[139] Archer, D. G.: *Thermodynamic properties of synthetic sapphire (α-Al_2O_3), standard reference material 720 and the effect of temperature-scale differences on thermodynamic*

properties. Journal of Physical and Chemical Reference data, 22 (6), pp. 1441-1453, 1993.
[140] Sarge, S. M.; Gmelin, E.; Höhne, G. W.; Cammenga, H. K.; Hemminger, W. and Eysel, W.: *The caloric calibration of scanning calorimeters*. Thermochimica Acta, 247 (2), pp. 129-168, 1994.
[141] Ramakumar, K. L.; Saxena, M. K. and Deb, S. B.: *Experimental evaluation of procedures for heat capacity measurement by differential scanning calorimetry*. Journal of Thermal Analysis and Calorimetry, 66 (2), pp. 387-397, 2001.
[142] Maier, C. G. and Kelley, K. K.: *An equation for the representation of high-temperature heat content data 1.* Journal of the American Chemical Society, 54 (8), pp. 3243-3246, 1932.
[143] Bergman, von T. L.; Incropera, F. P.; Lavine, A. S. and Dewitt, D. P.: *Introduction to heat transfer.* 6th Edition, John Wiley & Sons Inc., Hoboken, USA, pp. 2-10, 2011.
[144] Hong, J. S.; Maleki, H.; Al Hallaj, S.; Redey, L. and Selman, J. R.: *Electrochemical-calorimetric studies of lithium-ion cells.* Journal of the Electrochemical Society, 145 (5), pp. 1489-1501, 1998.
[145] Yazami, R.: Presentation: *Addressing key battery issues from a thermodynamics perspective.* Conference: International Battery Seminar & Exhibit, Fort Lauderdale, USA, 2018.
[146] Manual: *The accelerating rate calorimeter EV+ ARC operations manual.* Thermal Hazard Technology (THT), Bletchley, UK, 2013.
[147] Lopez, C. F.; Jeevarajan, J. A. and Mukherjee, P. P.: *Characterization of lithium-ion battery thermal abuse behavior using experimental and computational analysis.* Journal of the Electrochemical Society, 162 (10), pp. A2163-A2173, 2015.
[148] Jhu, C. Y.; Wang, Y. W.; Wen, C. Y. and Shu, C. M.: *Thermal runaway potential of $LiCoO_2$ and $Li(Ni_{1/3}Co_{1/3}Mn_{1/3})O_2$ batteries determined with adiabatic calorimetry methodology.* Applied Energy, 100, pp. 127-131, 2012.
[149] Jhu, C. Y.; Wang, Y. W.; Shu, C. M.; Chang, J. C. and Wu, H. C.: *Thermal explosion hazards on 18650 lithium ion batteries with a VSP2 adiabatic calorimeter*. Journal of Hazardous Materials, 192 (1), pp. 99-107, 2011.
[150] Somandepalli, V.; Marr, K. and Horn, Q.: *Quantification of combustion hazards of thermal runaway failures in lithium-ion batteries.* SAE International Journal of Alternative Powertrains, 3 (1), pp. 98-104, 2014.
[151] Love, C. T.: *Thermomechanical analysis and durability of commercial micro-porous polymer Li-ion battery separators.* Journal of Power Sources, 196 (5), pp. 2905-2912, 2011.
[152] McArthur, M. A.; Trussler, S. and Dahn, J. R.: *In situ investigations of SEI layer growth on electrode materials for lithium-ion batteries using spectroscopic ellipsometry.* Journal of the Electrochemical Society, 159 (3), pp. A198-A207, 2011.
[153] Zhuang, G.; Chen, Y. and Ross, P. N.: *The reaction of lithium with dimethyl carbonate and diethyl carbonate in ultrahigh vacuum studied by X-ray photoemission spectroscopy.* Langmuir, 15 (4), pp. 1470-1479, 1999.
[154] Wang, Q.; Sun, J.; Chen, X.; Chu, G. and Chen, C.: *Effects of solvents and salt on the thermal stability of charged $LiCoO_2$.* Materials Research Bulletin, 44 (3), pp. 543-548, 2009.
[155] Sekizawa, O.; Hasegawa, T.; Kitamura, N. and Idemoto, Y.: *Crystal and electronic structure change determined by various method for delithiation process of $Li_x(Ni, Mn)O_2$-based cathode material.* Journal of Power Sources, 196 (16), pp. 6651-6656, 2011.
[156] Chebiam, R. V.; Kannan, A. M.; Prado, F. and Manthiram, A.: *Comparison of the chemical stability of the high energy density cathodes of lithium-ion batteries*. Electrochemistry Communications, 3 (11), pp. 624-627, 2001.
[157] Arai, H. and Sakurai, Y.: *Characteristics of Li_xNiO_2 obtained by chemical delithiation*. Journal of Power Sources, 81-82, pp. 401-405, 1999.
[158] Zhecheva, S. and Stoyanova, R.: *New phases obtained by acid delithiation of layered $LiMO_2$ (M=Co, Ni)*. Materials Science Forum, 152-153, pp. 259-262, 1994.
[159] Li, J.; Cameron, R.; Li. H.; Glazier, S.; Xiong, D.; Chatzidakis, M.; Allen, J.; Botton, G. A. and

Dahn, J. R.: *Comparison of single crystal and polycrystalline $LiNi_{0.5}Mn_{0.3}Co_{0.2}O_2$ positive electrode materials for high voltage Li-ion cells.* Journal of the Electrochemical Society, 164 (7), pp. A1534-A1544, 2017.
[160] Zhang, F.; Lou, S.; Li, S.; Yu, Z.; Liu, Q.; Dai, A.; Cao, C.; Toney, M. F.; Ge, M.; Xiao, X.; Lee, W. K.; Yao, Y.; Deng, J.; Liu, T.; Tang, Y.; Yin, G.; Lu, J.; Su, D. and Wang, J.: *Surface regulation enables high stability of single-crystal lithium-ion cathodes at high voltage.* Nature Communications, 11 (1), pp. 1-11, 2020.
[161] Noh, H. J.; Chen, Z.; Yoon, C. S.; Lu, J.; Amine, K. and Sun, Y. K.: *Cathode material with nanorod structure- an application for advanced high-energy and safe lithium batteries*. Chemistry of Materials, 25 (10), pp. 2109-2115, 2013.
[162] Menkin, S.; Golodnitsky, D. and Peled, E.: *Artificial solid-electrolyte interphase (SEI) for improved cycleability and safety of lithium-ion cells for EV applications*. Electrochemistry Communications, 11 (9), pp. 1789-1791, 2009.
[163] Meng, X.; Yang, X. Q. and Sun, X.: *Emerging applications of atomic layer deposition for lithium-ion battery studies*. Advanced Materials, 24 (27), pp. 3589-3615, 2012.
[164] Woo, S. W.; Myung, S. T.; Bang, H.; Kim; D. W. and Sun, Y. K.: *Improvement of electrochemical and thermal properties of $Li[Ni_{0.8}Co_{0.1}Mn_{0.1}]O_2$ positive electrode materials by multiple metal (Al, Mg) substitution*. Electrochimica Acta, 54 (15), pp. 3851-3856, 2009.

List of Figures

FIG. 1.1: SPIDER DIAGRAMS OF MAIN CHARACTERISTICS OF COMMERCIAL LI-ION BATTERIES [4]. 2
FIG. 1.2: PRODUCTION STRUCTURE OF THE LI-ION BATTERY INDUSTRY [4]. 3

FIG. 2.1: SCHEMATICS OF A LI-ION BATTERY DURING CHARGE [27]. 5
FIG. 2.2: POSITIONS OF THE VARIOUS REDOX COUPLES RELATIVE TO THE OXYGEN 2P BAND [29]. 7
FIG. 2.3: IDEAL LAYER STRUCTURE OF NMC111 (SPACE GROUP R3M). 8
FIG. 2.4: LOCATIONS OF NMC COMPOSITIONS ON THE GIBBS TRIANGLE, SHOWING 20 AT. %-$LICOO_2$ AND $LINI_{0.5}MN_{0.5}O_2$ CONCENTRATION LINES. 10
FIG. 2.5: AN EXAMPLE OF CHARGE/DISCHARGE GITT CURVES [42]. 12
FIG. 2.6: ENTROPY OF LITHIUM INTERCALATION INTO LI_XCOO_2 [44]. 13
FIG. 2.7: HEAT BALANCE BETWEEN HEAT DUE TO AN EXOTHERMIC REACTION AND HEAT LOSS FROM A VESSEL, AT VARIANT AMBIENT TEMPERATURES A, B, AND C [51]. 17
FIG. 2.8: SCHEMATIC DESIGN OF A CALORIMETER AND ITS SURROUNDINGS UNDER ISOTHERMAL/ADIABATIC/ISOPERIBOLIC CONDITIONS [57]. 19
FIG. 2.9: SCHEMATIC DESIGN OF A CALORIMETER UNDER SCANNING OPERATION [57]. 20

FIG. 3.1: SOLID/LIQUID SPECIMEN'S PREPARATION FOR ICP-OES MEASUREMENTS. 22
FIG. 3.2: INTERFACE OF ELECTRODE AND ELECTROLYTE: A) SCHEMATIC DIAGRAM OF DOUBLE-LAYER STRUCTURE. B) AN ELECTRICAL EQUIVALENT CIRCUIT ACCORDINGLY [59]. 23
FIG. 3.3: CHARGING PULSE FOLLOWED BY A RELAXATION TIME OF 3 H IN THIS WORK [62]. 24
FIG. 3.4: INTERNAL VIEW OF C80 CALORIMETER, DETAILED INFORMATION FOR ALL THE SECTIONS IS INTRODUCED IN THE APPENDIX. 25
FIG. 3.5: 3D HEAT FLOW SENSOR OF C80 CALORIMETER: EACH SENSOR WITH 19 THERMOCOUPLES; TWO IDENTICAL SYSTEMS. 26
FIG. 3.6: TWO SET UPS FOR C80 MEASUREMENTS: A) SET-UP 1 FOR NO CABLE MEASUREMENTS, B) SET-UP 2 FOR CABLE NEEDED MEASUREMENTS. 27
FIG. 3.7: APPLIED POWER EXTERNALLY AND CORRESPONDING VOLTAGES OUTPUTS OF C80 CALORIMETER AGAINST TIME. 28
FIG. 3.8: SENSITIVITY FACTORS UNDER SELECTED TEMPERATURES AND POLYNOMIAL FITTING. 28
FIG. 3.9: DEFINITION OF TERMS FOR DESCRIBING MEASURED CURVES WITH THE PEAK REPRESENTING A TRANSITION OR REACTION IN THE SAMPLE (SUBSCRIPT 'MEAS' DENOTES MEASURED QUANTITIES) IN A PLOT OF HEAT FLOW RATE AND TEMPERATURE AGAINST TIME, [68] PAGE 1460. 30
FIG. 3.10: INTERFACE OF SETARAM SOFTWARE FOR EVALUATION OF HEAT FLOW RATE (SUBTRACTED BASELINE). 31
FIG. 3.11: EXTRAPOLATED PEAK ONSET TEMPERATURE Te AS A FUNCTION OF HEATING RATE B AND MEASURED Te VALUES OF IN FOR BOTH SET-UPS. 32
FIG. 3.12: MEASURED TEMPERATURES AND THEIR UNCERTAINTIES OF IN CALIBRATION WITH DIFFERENT MASSES AND CRUCIBLES. 32
FIG. 3.13: EXTRAPOLATED PEAK ONSET TEMPERATURE Te AS A FUNCTION OF HEATING RATE B AND MEASURED Te VALUES OF KNO_3 FOR BOTH SET-UPS. 33
FIG. 3.14: EXTRAPOLATED PEAK ONSET TEMPERATURE Te AS A FUNCTION OF HEATING RATE B AND MEASURED Te VALUES OF GA FOR BOTH SET-UPS. 34
FIG. 3.15: ENTHALPY CALIBRATION FACTOR PLOTTED AGAINST THE TRANSITION TEMPERATURE $Ttrs$ FOR TWO SET-UPS, AND A KH(T) FUNCTION OF THE TRANSITION TEMPERATURE. 35
FIG. 3.16: ACCELERATING RATE CALORIMETER: A) OVERVIEW; B) INTERNAL VIEW OF THE CALORIMETER'S CHAMBER. 36
FIG. 3.17: PROCESSES OF HEAT-WAIT-SEEK METHOD IN ARC. 36
FIG. 3.18: ALEXSYS-1000 CALORIMETER (A) INTERNAL VIEW, (B) SCHEMATIC DIAGRAM OF ONE THERMOPILE WITH 8 RINGS, SURROUNDING BY 8 PT-PT13RH-THERMAL COUPLES (C) ENLARGEMENT DIAGRAM OF CALORIMETER CELL [76, 77]. 39
FIG. 3.19: SCHEMATIC VIEWS OF SIMULTANEOUS THERMAL ANALYZER STA-449 F3 JUPITER: (A) THE INTERNAL SECTIONAL VIEW, (B) COMBINATION OF DTA AND TGA SIMPLIFIED SCHEMATIC DIAGRAM. 41

FIG. 4.1: SCHEMATIC DIAGRAM OF Li^+ MOVEMENT'S PATH IN ELECTROCHEMICAL DELITHIATION PROCESS [90]. 48
FIG. 4.2: ABOVE: DURING MEASUREMENT, THE PRESSURE OF OXYGEN WAS MEASURED AND ANALYZED BY MASS SPECTROSCOPY; BELOW: THE PHASE TRANSITION TEMPERATURES WERE DEFINED BY IN SITU TIME-RESOLVED X-RAY DIFFRACTION (TR-XRD) MEASUREMENTS [94]. 49
FIG. 4.3: SEM IMAGES OF SPECIMENS SINTERING AT 800 °C: A) NMC442 B) NMC532 C) NMC622 D) NMC712 E) NMC802. 51
FIG. 4.4: XRD PATTERNS OF NMC SPECIMENS CALCINATION AT 800 °C WITH INCREASING NI CONTENT NMC442 TO NMC802. 52
FIG. 4.5: XRD PATTERNS OF SPECIMENS AFTER CALCINATION AT 800 °C AND OPTIMIZED CALCINATION A) NMC442 SAMPLES AT 900 °C AND 800 °C, B) NMC532 SAMPLES AT 875 °C AND 800 °C, C) NMC622 SAMPLES AT 850 °C AND 800 °C, D) NMC712 SAMPLES AT 825 °C AND 800 °C. 53
FIG. 4.6: RIETVELD REFINEMENT RESULTS OF SPECIMENS AFTER CALCINATION AT 800 °C AND OPTIMIZED CALCINATION A) LATTICE PARAMETER *A*, B) LATTICE PARAMETER *C*, C) CRYSTAL UNIT VOLUME. 54
FIG. 4.7: LI AND TM CONTENTS MEASURED BY ICP-OES OF SPECIMENS: A) NOMINAL STOICHIOMETRY OF SAMPLES AFTER PRE-CALCINATION AT 450 °C. SAMPLES OF VARIOUS COMPOSITIONS AFTER CALCINATION AT 800 °C AND OPTIMIZED CALCINATION: B) LI CONTENTS, C) NI CONTENTS, D) MN CONTENTS, E) CO CONTENTS. 55
FIG. 4.8: XRD PATTERN OF COMMERCIAL NMC442 AND SOL-GEL MADE NMC442. 56
FIG. 4.9: ELECTROCHEMICAL TESTS ON COMMERCIAL AND SOL-GEL MADE NMC442: A) TYPICAL CHARGE-DISCHARGE CHARACTERISTICS OF COMMERCIAL AND SOL-GEL MADE NMC442, B) CYCLE PERFORMANCE OF COMMERCIAL AND SOL-GEL MADE NMC442 AT 0.05 C. 57
FIG. 4.10: CYCLE RETENTION OF COIN CELLS WITH COMMERCIAL NMC442 POSITIVE ELECTRODE MATERIAL AT VARIOUS C-RATES. 58
FIG. 4.11: DELITHIATED SPECIMEN BY ONE-PORTION OXIDIZING REAGENT A) MOLAR RATIO OF LI/SUMMATION OF TRANSITION METALS VERSUS DELITHIATION TIME. B) MOLAR RATIO OF MN/CO, MN/NI AND CO/NI VERSUS DELITHIATION TIME. 61
FIG. 4. 12: DELITHIATED SPECIMEN BY DOUBLE-PORTION OXIDIZING REAGENT. A) MOLAR RATIOS OF LI/SUMMATION OF TRANSITION METALS VERSUS DELITHIATION TIME. B) MOLAR RATIOS OF MN/CO, MN/NI AND CO/NI VARYING WITH DELITHIATION TIME. 62
FIG. 4.13: THE XRD PATTERNS AND RIETVELD REFINEMENT CURVES OF PRISTINE AND CHEMICALLY DELITHIATED COMMERCIAL NMC442 MATERIALS BY ONE-PORTION OXIDIZING REAGENT (BLACK CURVE: MEASURED, RED CURVE: REFINED): A) PRISTINE MATERIAL; DELITHIATED SAMPLES: B) 4 H, C) 16 H, D) 24 H, E) 48 H, F) 72 H, G) 96 H. 66
FIG. 4.14: COMPARISON OF LOCAL XRD PATTERNS FOR PRISTINE AND CHEMICALLY DELITHIATED COMMERCIAL NMC442 BY ONE-PORTION OXIDIZING REAGENT: A) SELECTED 2Θ REGIONS OF THE REFLECTION (003), B) SELECTED 2Θ REGIONS OF THE REFLECTIONS (018) AND (110). 66
FIG. 4.15: THE LATTICE PARAMETERS OF DELITHIATED COMMERCIAL NMC442 SAMPLES BY ONE-PORTION OXIDIZING REAGENT: A) A_{HEX} VARYING WITH THE CHEMICAL DELITHIATION TIME. B) C_{HEX} VARYING WITH THE CHEMICAL DELITHIATION TIME. C) C/A RATIO VERSUS CHEMICAL DELITHIATION TIME. 67
FIG. 4.16: THE XRD PATTERNS AND RIETVELD REFINEMENT CURVES OF PRISTINE AND CHEMICALLY DELITHIATED COMMERCIAL NMC442 BY DOUBLE-PORTION OXIDIZING REAGENT (BLACK CURVE: MEASURED, RED CURVE: REFINED, *: $NICO_2S_4$): A) PRISTINE MATERIAL, B) 4 H DELITHIATED SAMPLE, C) 16 H DELITHIATED SAMPLE, D) 24 H DELITHIATED SAMPLE, E) 48 H DELITHIATED SAMPLE, F) 72 H DELITHIATED SAMPLE, G) 96 H DELITHIATED SAMPLE. 70
FIG. 4.17: PHASES FOUND BY IN-SITU X-RAY DIFFRACTION FOR THE LITHIUM ION ORDERING/DISORDERING PHASES IN LI_XCOO_2 IN TERMS OF TEMPERATURE AND CELL VOLTAGE [106]. 71
FIG. 4.18: THE EXPERIMENTAL AND CALCULATED XRD PATTERNS OF PRISTINE AND CHEMICALLY DELITHIATED COMMERCIAL LIXNMC442: A) X=1.11, B) X=0.76, C) X=0.48. 72
FIG. 4.19: SIMULTANEOUS THERMAL ANALYSIS FOR PRISTINE AND CHEMICALLY DELITHIATED COMMERCIAL LI_XNMC 442 SAMPLES: A) X=1.11, B) X=0.76, AND C) X=0.48. 75
FIG. 4.20: COMPARISON OF SELECTED DELITHIATION DEGREES BY USING THE FIRST DERIVATIVE OF THE

MASS CHANGE PERCENTAGE WITH TIME FOR COMMERCIALLY AVAILABLE $LI_XNMC442$ SAMPLES, REGARDING THE MASS LOSS AND OXYGEN CONCENTRATION MEASURED BY OXYGEN DETECTOR. 76
FIG. 4.21: ZHENG ET AL. STUDIED NMC MATERIALS: A) COMPOSITIONS IN PHASE TRIANGLE, B) SCHEMATIC ILLUSTRATION OF NMC532 STRUCTURE, AND ENLARGEMENT OF ONE UNIT WITH O IN CENTER; C) THE OXYGEN AND TM BONDS IN NMC MATERIALS; THE CORRESPONDING NAMES ARE USED IN TABLE 4.12 [107]. 77
FIG. 4.22: MASS SPECTROSCOPY ANALYSIS FOR PRISTINE AND CHEMICALLY DELITHIATED COMMERCIAL $LI_XNMC442$ SAMPLES: A) X=1.11, B) X=0.76, AND C) X=0.48. 79
FIG. 4.23: THE XRD PATTERNS AND RIETVELD REFINEMENT CURVES OF PRISTINE AND CHEMICALLY DELITHIATED COMMERCIAL $LI_XNMC442$ AFTER STA/MS MEASUREMENT WITH MAXIMUM TEMPERATURE 800°C (BLACK CURVE: MEASURED, RED CURVE: REFINED): A) X=1.11 B) X=0.76 C) X=0.48. 80
FIG. 4.24: THERMODYNAMIC CYCLE. FIRST LINE: THE FORMATION ENTHALPY OF VARIOUS NMC COMPOSITION FROM THE BINARY OXIDES AND OXYGEN. SECOND LINE: THE MEASURED ENTHALPIES OF DROP SOLUTION OF THE BINARY OXIDES. LAST LINE: THE (OXIDATION) STATES OF THE SPECIES IN THE MOLTEN SOLUTION AT 974 K [113]. 83
FIG. 4.25: ENTHALPY OF FORMATION FROM A) OXIDES AND B) ELEMENTS VERSUS DELITHIATION DEGREES, IN COMPARISON WITH *MASOUMI'S WORK [113]. 85

FIG. 5.1: HEAT GENERATION CURVE OF A 500 MAH LIB DURING DISCHARGE AT 50 MA (C/10 RATE) CONSTANT CURRENT. Q MEANS QUANTITY OF ELECTRICITY DISCHARGED FROM FULL CHARGED STATE OF THE BATTERY. SYMBOLS ON CURVE ARE PLOTTED AT Q WHERE THE APPARENT SPECIFIC HEAT CAPACITY OF THE BATTERY IS EVALUATED: (A) 0 MAH (SOC100), (B) 40 MAH (SOC92), (C) 80 MAH (SOC84), (D) 110 MAH (SOC78), (E) 130 MAH (SOC74), (F) 160 MAH (SOC68), (G) 190 MAH (SOC62), (H) 230 MAH (SOC54), (I) 300 MAH (SOC40), (J) 400 MAH (SOC20), AND (K) 480 MAH (SOC4) [120]. 87
FIG. 5.2: HEAT FLOW RATE AND ITS VOLTAGES AT SOC (A) 100, (B) 92, (C) 84, (D) 78, (E) 74, (F) 68, (G) 62, (H) 54, (I) 40, (J) 20, AND (K) 4, AND LAST DIAGRAM SHOWS THE TEMPERATURE PROGRAM [120]. 88
FIG. 5.3: RELAXATION BEHAVIOR OF THE CELL VOLTAGE FOR NMC CELL A) SOC100, B) SOC87, C) SOC57, AND D) SOC20 INCLUDING THE VOLTAGE RESPONSE OF TEMPERATURE CHANGES TO 25 °C AND 20 °C RESPECTIVELY PLOTTED WITH THE MATHEMATICAL FITTED BACKGROUND. IN E), F), G), H), THE RESULTING SUBTRACTION OF THE MEASURED VOLTAGE AND THE CALCULATED RELAXATION BACKGROUND FOR THE RESPECTIVE STATE OF CHARGE IS SHOWN [47]. 89
FIG. 5. 4: ENTROPY AND OCV OF LITHIATION DURING DISCHARGE OF NATURAL GRAPHITE [45]. 90
FIG. 5. 5: ENTROPY OF LITHIUM INTERCALATION INTO LI_XCOO_2 [45]. 90
FIG. 5. 6: ENTROPY PROFILES OF 2032 COIN CELLS WITH CAPACITY OF 44 MAH (LCO/GRAPHITE) AT DIFFERENT CHARGE CUT-OFF VOLTAGE (COV) [124]. 91
FIG. 5. 7 ENTROPY CHANGES FOR COMMERCIALLY AVAILABLE $LICOO_2$ POSITIVE ELECTRODE (LICO TECHNOLOGY CORPORATION) [125]. 92
FIG. 5. 8 ENTROPY CHANGES FOR COMMERCIAL AVAILABLE $LINI_XCO_YMN_ZO_2$ (LICO TECHNOLOGY CORPORATION). THE AGREEMENT BETWEEN TWO RUNS (SHOWN AS TWO SEPARATE CURVES IN THE FIGURE) ON DIFFERENT DAYS FOR THE SAME CELL IS REASONABLE GOOD [125]. 92
FIG. 5. 9: ENTROPY CHANGE OF 18650 CELLS WITH CAPACITY OF 2.3 AH (LFP POSITIVE ELECTRODE) MEASURED BY THE POTENTIOMETRIC METHOD AND BY USING THE GRADIENT HEAT FLUX SENSOR (GHFS) [122]. 93
FIG. 5. 10: POTENTIOMETRIC MEASUREMENT OF POUCH CELL WITH A CAPACITY OF 42 AH (LFP/GRAPHITE) 93
FIG. 5. 11: ENTROPY CHANGES FOR THE POUCH CELL WITH A CAPACITY OF 42 AH (LFP/GRAPHITE), LFP HALF-CELL AND GRAPHITE HALF-CELL [126]. 94
FIG. 5. 12: DECOMPOSITION REACTIONS OF ANODE SOLID ELECTROLYTE INTERPHASE (SEI) COMPONENTS WITH $LIPF_6$ [128]. 95
FIG. 5. 13: C80 HEAT FLOW CURVES OF LITHIATED GRAPHITE ($LI_{0.84}C_6$), 1.0 M $LIPF_6$/EC+DEC ELECTROLYTE, AND $LI_{0.86}C_6$ [129]. 96
FIG. 5. 14: HEAT FLOW CURVES OF 1 M $LIPF_6$ IN EC+DEC, RINSED AND THEIR CO-EXISTING SYSTEM AT 0.2 °C·MIN^{-1} IN ARGON [130]. 96

FIG. 5. 15: PROPOSED REACTIONS BETWEEN $LI_{0.81}C_6$ AND EC/DEC SOLVENT IN THE TEMPERATURE RANGE BETWEEN 110 °C AND 260 °C CORRELATED TO THE ACCELERATING RATE CALORIMETER (ARC) RESULTS [135]. 97
FIG. 5. 16: SELF-HEATING RATE VS. TEMPERATURE: ARC RESULTS FOR GROUND ELECTRODE POWDER OF NMC (66 MG) REACTING WITH 0.5 M, 1.0 M AND 1.5 M $LIPF_6$ IN EC:DEC (1:2 V/V RATIO) ELECTROLYTE (20 MG) [136]. 98
FIG. 5.17: HEAT FLOW RATE CURVES OF BASELINE, REFERENCE MATERIAL, AND SAMPLES VERSUS TIME MEASURED BY CONTINUOUS METHOD. 101
FIG. 5. 18: SPECIFIC HEAT CAPACITY OF TWO CELLS AND THEIR FITTING CURVES AND FUNCTIONS IN CONTINUOUS METHOD MEASUREMENTS. 102
FIG. 5. 19: HEAT FLOW RATE CURVES AND TEMPERATURE CHANGE OF BASELINE AND SAPPHIRE VS. TIME MEASURED BY STEP METHOD. 103
FIG. 5. 20: SPECIFIC HEAT CAPACITY OF TWO CELLS AND THEIR FITTING CURVES AND FUNCTIONS IN STEP METHOD MEASUREMENTS. 103
FIG. 5. 21: THE INTERNAL SET-UP OF COIN CELL CYCLING IN C80 CALORIMETER: PURPLE LINE ARE THE CABLE CONNECTED TO CYCLER, GREEN LINE REPRESENTS THE K TYPE THERMOCOUPLE AND YELLOW DISC IS CERAMIC DISC ON BOTTOM OF THE VESSEL. 104
FIG. 5.22: COOLING CURVES AFTER DISCHARGING AT VARIOUS C-RATES: A) AT 0.5 C, B) AT 1 C, C) AT 2 C AND THEIR FITTING FUNCTIONS. 106
FIG. 5. 23: TEMPERATURE CURVE WHEN CYCLING AT 0.5 C, RED CURVE REPRESENTS THE TEMPERATURE CHANGE USED IN CALCULATION; BLUE CURVE REPRESENTS THE APPLIED CURRENT. 107
FIG. 5.24: HEAT FLOW RATES OF JOULE EFFECT CALIBRATION WITH STANDARD RESISTANCE IN C80 CALORIMETER. 108
FIG. 5. 25: HEAT FLOW RATES MEASURED BY C80 CALORIMETER AND APPLIED CURRENT FLOWS VERSUS TIME AT 30 °C: A) 0.5 C (42.5 MA), B) 1 C (85 MA) AND C) 2 C(170 MA). 109
FIG. 5.26: HEAT FLOW RATES MEASURED BY C80 CALORIMETER AND APPLIED CURRENT FLOWS VERSUS TIME AT 25 °C: A) 0.5 C (42.5 MA), B) 1 C (85 MA) AND C) 2 C (170 MA). 110
FIG. 5. 27: COMPARISON OF HEAT GENERATION DETERMINED BY TEMPERATURE MEASUREMENTS (TABLE 5.2) AND HEAT FLOW RATE MEASUREMENTS (TABLE 5.4) AT 30 °C FOR: A) 0.5 C, B) 1 C AND C) 2 C. 112
FIG. 5. 28: EIS OF COIN CELLS WITH VARIOUS SOC AT AMBIENT TEMPERATURE. 113
FIG. 5. 29: CHARGING PULSE FOLLOWED BY RELAXATION TIME OF 3 H. 114
FIG. 5. 30: IRREVERSIBLE HEAT FLOW RATES DUE TO OHMIC, CHARGE TRANSFER AND DIFFUSION IMPEDANCES DURING CHARGE AND DISCHARGE WITH DIFFERENT C-RATES VERSUS SOC AND DOD AT 30 °C: (A, B) 0.5 C, (C, D) 1 C AND (E, F) 2 C. 115
FIG. 5. 31: IRREVERSIBLE HEAT FLOW RATES DUE TO OHMIC, CHARGE TRANSFER AND DIFFUSION IMPEDANCES DURING CHARGE AND DISCHARGE WITH DIFFERENT C- RATES VERSUS SOC AND DOD AT 25 °C: (A, B) 0.5 C, (C, D) 1 C AND (E, F) 2 C. 116
FIG. 5. 32: THE TOTAL IRREVERSIBLE HEAT FLOW RATES WITH VARIOUS C-RATES VERSUS SOC AND DOD AT 30 °C: A) CHARGE, B) DISCHARGE. 118
FIG. 5. 33: THE TOTAL IRREVERSIBLE HEAT FLOW RATES WITH VARIOUS C-RATES VERSUS SOC AND DOD AT 25 °C: A) CHARGE, B) DISCHARGE. 119
FIG. 5.34: THE RESULTS FROM ENTROPY MEASUREMENTS IN THIS WORK: (A) THE VOLTAGE CURVE AT VARIOUS TEMPERATURES AT SOC40 AND (B) OCV VERSUS TEMPERATURE AND THE FITTING FUNCTION AT SOC40. 121
FIG. 5.35: THE RESULTS FROM ENTROPY MEASUREMENTS IN THIS WORK: A) THE VOLTAGE CURVE UNDER VARIOUS TEMPERATURES AT SOC100 AND B) OCV VERSUS TEMPERATURE AND THE FITTING FUNCTION AT SOC100. 122
FIG. 5.36: THE RESULTS FROM ENTROPY MEASUREMENTS IN THIS WORK: A) THE VOLTAGE CURVE UNDER VARIOUS TEMPERATURES AT SOC0 AND B) OCV VERSUS TEMPERATURE AND THE FITTING FUNCTION AT SOC0. 123
FIG. 5.37: ENTROPY CHANGE VS. SOC: A) THE ENTROPY CHANGE VERSUS SOC OF THREE CELLS. B) THE COMPARISON OF THIS WORK MEASURED IN LARGE TEMPERATURE RANGE WITH *THE RESULTS FROM REF. [44] AND ** THE RESULTS FROM REF. [145]. 124
FIG. 5.38: THE FUNCTION OF ΔS, ΔH, AND SOC THREE-DIMENSIONAL PLOTS MEASURED IN LARGE TEMPERATURE RANGE, AND THE DATA ARE LISTED IN APPENDIX III. 125

FIG. 5. 39: THE TEMPERATURE PROFILE FOR ΔS MEASUREMENT. 126
FIG. 5.40: THE VOLTAGE CURVE UNDER VARIOUS TEMPERATURES WITH ITS BASELINE: A) AT SOC90, B) AT SOC40 AND C) AT SOC10. 127
FIG. 5. 41: THE COMPARISON OF AVERAGE VALUE OF THREE CELLS' ΔS FOR MEASUREMENTS WITH/WITHOUT BASELINE SUBTRACTION. 127
FIG. 5. 42: THE COMPARISON OF COMPUTED HEAT FLOW RATES FROM IRREVERSIBLE AND REVERSIBLE HEAT FLOW RATES; AND THE TOTAL HEAT FLOW RATES MEASURED BY C80 CALORIMETER VERSUS SOC/DOD UNDER DIFFERENT C-RATES AT 30 °C: A) CHARGING AT 0.5 C (42.5 MA), B) DISCHARGING AT 0.5 C (42.5 MA), C) CHARGING AT 1 C (85 MA), D) DISCHARGING AT 1 C (85 MA), E) CHARGING AT 2 C (170 MA), F) DISCHARGING AT 2 C (170 MA). 131
FIG. 5. 43: THE COMPARISON OF COMPUTED HEAT FLOW RATES FROM IRREVERSIBLE AND REVERSIBLE HEAT FLOW RATES; AND THE TOTAL HEAT FLOW RATES MEASURED BY C80 CALORIMETER VERSUS SOC/DOD UNDER DIFFERENT C-RATES AT 25 °C: A) CHARGING AT 0.5 C (42.5 MA), B) DISCHARGING AT 0.5 C (42.5 MA), C) CHARGING AT 1 C (85 MA), D) DISCHARGING AT 1 C (85 MA), E) CHARGING AT 2 C (170 MA), F) DISCHARGING AT 2 C (170 MA). 134
FIG. 5. 44: THE COMPARISON OF THE COMPUTED VALUES OF TOTAL HEAT GENERATION AND THOSE MEASURED BY C80 FOR VARIOUS C-RATES AT 30 °C. 136
FIG. 5. 45: THE COMPARISON OF THE COMPUTED VALUES OF TOTAL HEAT GENERATION AND THOSE MEASURED BY C80 FOR VARIOUS C-RATES AT 25 °C. 137
FIG. 5. 46: SCHEMATIC ILLUSTRATION OF THE HWS MEASUREMENT PROGRAM WITH MODES AND CONDITIONS [146]. 138
FIG. 5. 47: SCHEMATIC SET-UP FOR THE THERMAL RUNAWAY MEASUREMENT IN THE ARC. 139
FIG. 5. 48: TEMPERATURE VS. TIME CURVES FOR THERMAL RUNAWAY MEASUREMENTS OF THREE CELLS WITH SOC100 MEASURED BY THE ARC USING HWS METHOD. 140
FIG. 5. 49: TEMPERATURE RATE VS. TEMPERATURE CURVES FOR THERMAL RUNAWAY MEASUREMENTS OF THREE CELLS WITH SOC100 MEASURED BY THE ARC. 140
FIG. 5.50: TEMPERATURE VS. TIME CURVES FOR THERMAL RUNAWAY MEASUREMENTS OF THREE CELLS WITH SOC50 MEASURED BY THE ARC USING HWS METHOD. 141
FIG. 5.51: TEMPERATURE RATE VS. TEMPERATURE CURVES FOR THERMAL RUNAWAY MEASUREMENTS OF THREE CELLS WITH SOC50 MEASURED BY THE ARC. 141
FIG. 5. 52: TEMPERATURE VS. TIME CURVES FOR THERMAL RUNAWAY MEASUREMENTS OF THREE CELLS WITH SOC0 MEASURED BY THE ARC USING HWS METHOD. 142
FIG. 5. 53: TEMPERATURE RATE VS. TEMPERATURE CURVES FOR THERMAL RUNAWAY MEASUREMENTS OF THREE CELLS WITH SOC0 MEASURED BY THE ARC. 143
FIG. 5. 54: THE COMPARISON BETWEEN SOC0, SOC50 AND SOC100: A) TEMPERATURE VS. TIME CURVES FOR THERMAL RUNAWAY MEASUREMENTS WITH SOC0, SOC50 AND SOC100 MEASURED BY THE ARC USING HWS METHOD. B) TEMPERATURE RATE VS. TEMPERATURE CURVES FOR THERMAL RUNAWAY MEASUREMENTS WITH SOC0, SOC50 AND SOC100 MEASURED BY THE ARC. 144
FIG. 5. 55: THE FUNCTIONS OF NATURAL LOGARITHM OF TEMPERATURE INCREASING RATE AND RECIPROCAL TEMPERATURE, AND THE E_A OF REACTIONS IS CALCULATED FROM THE FITTING SLOPE. 145
FIG. 5. 56: EARLY STAGE OF THERMAL RUNAWAY: TEMPERATURE DROP OF THE MEASUREMENT ON (A) CELL 1, (B) CELL 2, (C) CELL 3. 146
FIG. 5. 57: EARLY STAGE THERMAL RUNAWAY MEASUREMENT OF FULLY CHARGED CELL BY ARC: THE TEMPERATURE AND THE TEMPERATURE RATE VS. TIME. 147
FIG. 5. 58: XRD PATTERNS OF (A) THE POSITIVE ELECTRODES AND (B) THE NEGATIVE ELECTRODES AFTER 450 °C THERMAL RUNAWAY MEASUREMENT, 126 °C EARLY STAGE THERMAL RUNAWAY MEASUREMENT AND FRESH CELL. 147
FIG. 5.59: SEM IMAGES OF THE POSITIVE ELECTRODES FROM (A) FRESH CELL, (B) THE CELL HEATED UP TO 126 °C, AND (C) THE CELL HEATED UP TO 450 °C. 149
FIG. 5.60: SEM IMAGES OF THE NEGATIVE ELECTRODES FROM (A) FRESH CELL, (B) THE CELL HEATED UP TO 126 °C, AND (C) THE CELL HEATED UP TO 450 °C. 149
FIG. 5. 61: SEM IMAGES OF THE SEPARATORS FROM (A) FRESH CELL AND (B) THE CELL HEATED UP TO 126 °C. 150
FIG. 5. 62: SCHEMATIC SET-UPS FOR THE TEMPERATURE MEASUREMENT IN C80 CALORIMETER OF (A) FULL CELL AND (B) INDIVIDUAL COMPONENTS. 151

FIG. 5.63: THE HEAT FLOW RATE OF 3 CELLS WITH SOC100 VS. TEMPERATURE. 152
FIG. 5.64: THE HEAT FLOW RATE OF CELLS WITH SELECTED SOCS VS. TEMPERATURE. 152
FIG. 5.65: THE HEAT FLOW RATE DURING TRILAYER SEPARATOR MELTING VS. TEMPERATURE. 153
FIG. 5.66: THE MEASURED HEAT FLOW RATE (BLUE CURVE), THE FITTING PEAKS (BLACK CURVES) AND THE COMPUTED CURVE FOR THE NEGATIVE ELECTRODE WITH ELECTROLYTE FROM A CELL WITH SOC100 VS. TEMPERATURE. 154
FIG. 5.67: THE HEAT FLOW RATE OF THE NEGATIVE ELECTRODES WITH SELECTED SOCS VERSUS THE TEMPERATURE. 155
FIG. 5.68: THE HEAT FLOW RATE OF THE COMPONENTS AND THE FULL CELL AT SOC100 VS. TEMPERATURE. 155

List of Tables

TABLE 2. 1: COMPARISON OF THE CHARACTERISTICS OF MN, CO, AND NI IN NMC CATHODES [30]. 9

TABLE 3. 1 REFERENCE MATERIALS: THE TRANSITION TEMPERATURES T_{TRS} AND ENTHALPIES $\Delta_{TRS}H$ IN J/G AND $\Delta_{TRS}H$ IN J/MOL. 29
TABLE 3. 2 CHEMICALS TABLE OF HIGH TEMPERATURE OXIDE MELT DROP CALORIMETER'S MEASUREMENTS. 39

TABLE 4. 1 CHARACTERISTICS OF NMC PREPARED BY DIFFERENT SYNTHETIC PATHWAYS. 47
TABLE 4. 2 CHEMICALS OF NMC SYNTHESIS VIA SOL-GEL METHOD IN THIS WORK. 50
TABLE 4. 3 LATTICE PARAMETERS OF SOL-GEL MADE NMC MATERIALS WITH VARIOUS COMPOSITIONS. 53
TABLE 4. 4 NOMINAL STOICHIOMETRY OF NMC MATERIALS WITH VARIOUS COMPOSITIONS. 56
TABLE 4. 5 THE LATTICE PARAMETERS AND ANALYTICAL COMPOSITIONS OF COMMERCIAL AND SOL-GEL MADE NMC442 CATHODE MATERIALS. 57
TABLE 4. 6 CHEMICAL TABLE FOR CHEMICAL DELITHIATION EXPERIMENTS: COMMERCIAL NMC442 CATHODE MATERIALS AND OXIDIZING REAGENT $(NH_4)_2S_2O_8$. 59
TABLE 4. 7 ANALYTICAL COMPOSITION OF $LI_XNI_YMN_ZCO_\Delta O_H$ DELITHIATED BY ONE-PORTION OXIDIZING REAGENT, AND MEASURED COMPOSITION WAS NOMINALIZED BY THE ASSUMPTION SUM OF TRANSITION METALS EQUALING TO 1 (SUM TM=1). 60
TABLE 4. 8 ANALYTICAL COMPOSITION OF THE OXIDIZING REAGENT FILTRATE. 62
TABLE 4. 9 ANALYTICAL COMPOSITION OF $LI_XNI_YMN_ZCO_\Delta O_H$ DELITHIATED BY DOUBLE-PORTION OXIDIZING REAGENT, MEASURED COMPOSITION WITH ASSUMPTION SUM OF TRANSITION METALS EQUALING TO 1 (SUM TM=1). 62
TABLE 4. 10 RIETVELD REFINEMENT FOR X-RAY DIFFRACTION OF THE COMMERCIAL NMC442 AND SELECTED DELITHIATED SPECIMENS LI_XNMC442. 71
TABLE 4. 11 CHEMICAL ANALYSIS OF THE PRISTINE AND SELECTED DELITHIATED COMMERCIAL NMC442 SAMPLES. THE NOMINAL STOICHIOMETRY WAS CALCULATED BASED ON TRANSITION METALS' CATIONS EQUALING TO 1 IN COMPOSITION (SUM TM=1). 73
TABLE 4. 12 A SUMMARY OF ENERGY FAVORITE LCSU, CORRESPONDING TO ONSET TEMPERATURE (TG) AND WEIGHT LOSS (MASS RATIO IN TERMS OF THE TOTAL OXYGEN CONTENT IN NMC MATERIALS) OF THE FIRST STAGE OF OXYGEN LOSS AT SOC25 AND SOC50. 78
TABLE 4. 13 ENTHALPIES OF DROP SOLUTION, ENTHALPIES OF FORMATION FROM THE OXIDES AND FROM THE ELEMENTS AT P=0.1 MPA OF THE INVESTIGATED SPECIMENS, AS WELL AS ENTHALPIES OF DROP SOLUTION OF BINARY OXIDES FROM LITERATURE. 84

TABLE 5. 1 CHEMICAL ANALYSIS (ICP-OES) OF THE POSITIVE AND NEGATIVE ELECTRODES IN THE COIN CELL. 100
TABLE 5. 2 THE HEAT TRANSFER COEFFICIENTS AND THE CALCULATED HEAT GENERATION DURING CYCLING AT VARIOUS C-RATES. 107
TABLE 5. 3 THE CALIBRATION COEFFICIENTS FOR DIFFERENT HEAT FLOW RATES. 108
TABLE 5. 4 MEASURED TOTAL HEAT GENERATION WHEN CYCLING WITH VARIOUS C-RATES AT 30 °C AND 25 °C. 111
TABLE 5. 5 THE MAXIMUM HEAT FLOW RATES DUE TO DIFFUSION AND CHARGE TRANSFER IMPEDANCE IN CHARGE/DISCHARGE PROCESS AT 30 °C AND 25 °C. 117
TABLE 5. 6 THE FITTING PARAMETERS AND R-SQUARE FOR THE FUNCTION OF SOC, ENTROPY CHANGE AND ENTHALPY CHANGE, ACCORDING TO EQUATION (5.17). 125
TABLE 5. 7 COMPUTED AND MEASURED TOTAL HEAT GENERATION WHEN CYCLING WITH VARIOUS C-RATES AT 30 °C AND 25 °C. 135
TABLE 5. 8 CHEMICAL ANALYSIS (ICP-OES) OF THE POSITIVE ELECTRODE MATERIALS AND NEGATIVE ELECTRODE MATERIALS IN FRESH CELL AND TESTED CELLS. 150

Appendix

Appendix I The parts of C80 calorimeter

1. The "Measurement" fluxmeter
2. The "Reference" fluxmeter
3. The calorimetric block which is the thermostat
4. Pt100 Platinum probe to measure the calorimetric sample temperature; another probe, a Pt200 Platinum one, to control the temperature, is also in the block
5. A peripheral heating element
6. A sleeve surrounding the thermostat block. Inside the sleeve, cooling air can circulate, pulsed by a fan.
7. A heat insulator, limited by the external wall surrounding the air circulation sleeve. At the bottom of the wall, there are air admissions through which ventilation air escapes.
8. The upper section of the block comprises an internal chamber
9. A cover
10. Four (4) screws to fix the cover
11. Two (2) support guides fitted to the block
12. Screws to attach the guides to the block. These guides constitute a thermostated buffer to the area occupied by the cells. They act as thermal protectors and define the preheating zone when the cells are placed inside.
13. A cylindrical space above the cover used by the heat insulating stopper.
14. A heat insulating stopper represented in the figure in the lifted-up position.
15. Two wells.
16. An upper plate.
17. Four (4) knurled screws attaching the upper plate on the outer unit.
18. Two sliding stops may obturate the wells partially: they are aimed at holding in place rods or tubes linked to cells.
19. Two metallic tubes which connect directly the upper plate to the guides (11). Sometimes (for reversal cells), they are replaced by two long stoppers (not shown in the figure).
20. A support base, fixed with 6 screws.
21. At the rear of the body, a device for fixing the calorimeter on the reversal fitting can be found. A 3-position switch (manual – 0 – automatic) and its light control the fan.

Appendix II The raw data of ICP-OES results

Table 1: The raw data for Table 4.4: Measured composition of NMC materials with various compositions.

Samples	Li element wt.%	Ni element wt.%	Mn element wt.%	Co element wt.%
NMC442 800°C	7.30±0.02	23.80±0.12	22.50±0.07	12.10±0.06
NMC442 900°C	7.09±0.03	23.60±0.02	22.40±0.02	12.10±0.01
NMC532 800°C	7.24±0.01	29.40±0.02	16.60±0.01	11.90±0.01
NMC532 875°C	6.96±0.01	30.00±0.05	17.00±0.01	12.10±0.03
NMC622 800°C	7.16±0.03	35.30±0.12	11.00±0.05	11.90±0.05
NMC622 850°C	6.92±0.02	35.70±0.06	11.20±0.05	12.00±0.02
NMC712 800°C	7.08±0.03	41.40±0.23	5.53±0.03	11.90±0.07
NMC712 825°C	6.59±0.01	42.40±0.10	5.65±0.01	12.30±0.03
NMC802 800°C	6.77±0.03	47.50±0.12	<0.4	12.00±0.05

Table 2: The raw data for Table 4.7: Analytical composition of $Li_xNi_yMn_zCo_\delta O_\eta$ delithiated by one-portion oxidizing reagent, measured composition with assumption sum of transition metals equaling to 1 (sum TM=1)..

Reaction time h	Li element wt.%	Ni element wt.%	Mn element wt.%	Co element wt.%
0	7.68±0.01	24.40±0.05	22.50±0.58	10.10±0.07
4	7.07±0.10	24.89±0.04	22.55±0.04	10.25±0.02
16	6.21±0.09	24.67±0.04	23.33±0.04	10.21±0.02
24	6.19±0.04	24.80±0.02	23.02±0.02	10.28±0.01
48	5.84±0.04	24.10±0.02	23.82±0.02	10.16±0.01
72	5.37±0.04	23.50±0.02	24.40±0.02	10.07±0.01
96	5.23±0.03	23.60±0.02	24.14±0.02	10.08±0.01

Table3: The raw data for Table 4.8: Analytical composition of the oxidizing reagent filtrate.

.

Reaction time h	Li element mg/kg	Ni element mg/kg	Mn element mg/kg	Co element mg/kg
4	35.1±0.2	42.7±0.1	39.8±0.1	17.4±0.1
16	77.5±0.7	96.2±0.1	87.5±0.1	39.1±0.1
48	88.4±0.3	112.3±0.5	45.0±0.1	96.0±0.1

Table 4: The raw data for Table 4.9: Analytical composition of $Li_xNi_yMn_zCo_\delta O_\eta$ delithiated by double-portion oxidizing reagent, measured composition with assumption sum of transition metals equaling to 1 (sum TM=1).

Reaction time h	Li element wt.%	Ni element wt.%	Mn element wt.%	Co element wt.%
0	7.68±0.01	24.40±0.05	22.50±0.58	10.10±0.07
4	6.41±0.02	25.59±0.05	22.60±0.06	10.45±0.02
16	5.69±0.01	24.26±0.06	24.12±0.05	10.13±0.02
24	5.15±0.01	24.32±0.17	24.25±0.20	10.23±0.05
48	4.35±0.01	22.96±0.23	25.79±0.29	10.02±0.03
72	4.33±0.02	24.64±0.11	24.06±0.02	10.34±0.03
96	3.41±0.01	22.45±0.09	25.84±0.04	9.79±0.02

Appendix III The raw data of the function of ΔH, ΔS and SOCs in Fig. 5.38

ΔH	ΔS	SOC	ΔH in fitting curve	ΔS in fitting curve	SOC in fitting curve
kJ/K·mol	J/K·mol	%	kJ/K·mol	J/K·mol	%
-343.5	-44.1	0	-343.5	-44.1	-2.4
-338.7	-9.4	10	-338.7	-9.4	13.3
-348.0	-12.1	20	-348.0	-12.1	24.1
-346.1	7.8	30	-346.1	7.8	34.3
-346.0	17.3	40	-346.0	17.3	40.3
-349.1	20.4	50	-349.1	20.4	46.5
-364.0	1.6	60	-364.0	1.6	54.4
-372.6	1.8	70	-372.6	1.8	66.0
-380.6	3.3	80	-380.6	3.3	77.8
-390.0	3.2	90	-390.0	3.2	90.4
-400.1	5.2	100	-400.1	5.2	105.2